Designing of Optically Active Self-Assembled Nanostructures toward Environmental Remediation and Catalysis

Ph.D. Thesis

By

Shivendra Singh

DEPARTMENT OF CHEMISTRY

INDIAN INSTITUTE OF TECHNOLOGY INDORE

JULY 2024

Designing of Optically Active Self-Assembled Nanostructures toward Environmental Remediation and Catalysis

A THESIS

Submitted in partial fulfillment of the
requirements for the award of the degree
of
DOCTOR OF PHILOSOPHY

by
SHIVENDRA SINGH

DEPARTMENT OF CHEMISTRY

INDIAN INSTITUTE OF TECHNOLOGY INDORE

JULY 2024

INDIAN INSTITUTE OF TECHNOLOGY INDORE

I hereby certify that the work which is being presented in the thesis entitled **Designing of Optically Active Self-Assembled Nanostructures toward Environmental Remediation and Catalysis** in the partial fulfillment of the requirements for the award of the degree of **DOCTOR OF PHILOSOPHY** and submitted in the **DEPARTMENT OF CHEMISTRY, Indian Institute of Technology Indore**, is an authentic record of my own work carried out during the time period from **JULY 2019** to **JULY 2024** under the supervision of **Dr. Tushar Kanti Mukherjee**, Professor, and Head, Department of Chemistry, IIT Indore.

The matter presented in this thesis has not been submitted by me for the award of any other degree of this or any other institute.

21/10/2024

Signature of the student with date

(SHIVENDRA SINGH)

This is to certify that the above statement made by the candidate is correct to the best of my knowledge.

21/10/2024

Signature of Thesis Supervisor with date

(PROF. TUSHAR KANTI MUKHERJEE)

SHIVENDRA SINGH has successfully given his/her Ph.D. Oral Examination held on 18/10/2024

21/10/2024

Signature of Thesis Supervisor with date

(PROF. TUSHAR KANTI MUKHERJEE)

Acknowledgements

I take this opportunity to thank all the people who have helped me carry out the work leading to this thesis and make my days memorable during my Ph.D. First and foremost, I express my sincere respect and deep gratitude to my supervisor, Prof. Tushar Kanti Mukherjee, for his significant guidance, constant support, and encouragement throughout my research period. His dedication, keen insights, and unyielding attitude toward research and his students have been greatly responsible for completing my research work. His timely scholarly advice, meticulous scrutiny, and scientific approach have assisted me greatly in accomplishing this thesis.

I sincerely thank my PSPC members, Prof. Satya S. Bulusu and Prof. Anjan Chakraborty, for their fruitful discussions, invaluable suggestions, and motivation during my PhD. I also express my immense gratitude to Prof. Suhas S. Joshi, Director, IIT Indore, for his continuous support in every panorama. Also, I would like to acknowledge IIT Indore for providing excellent academic facilities and Sophisticated Instrumentation Center (SIC) for instrumental facilities.

I profusely thank Prof. Chayan Kanti Nandi, Dr. Tridib Kumar Sarma, Dr. Chethana, and Ms. Vidhi Agarwal for their collaborative work, cooperation, and scientific discussions during my projects. Further, I would like to thank Prof. Anindya Datta and Mr. Arkaprava Chowdhury, IIT Bombay, for their help in fluorescence up-conversion measurements. I would also like to thank Prof. Saptarshi Mukherjee and Mr. Paritosh for their help in EPR experiments. I would also like to thank Dr. Dipak Kumar Roy and Mr. Rahul Kumar Yadav for their help in electrochemical measurements. I extend my gratitude to all the faculty members of the chemistry department IIT Indore for their timely help and guidance during different activities. I also thank all the staff members, Mr. Manish Kushwaha, Ms. Vinita Kothari, Mr. Rameshwar Dauhare, and Mr. Souvik, for their help and support during my PhD.

Dedicated to

My Beloved Parents

& Family

Abstract

Nature utilizes cellular and subcellular compartmentalization to efficiently drive many complex biochemical transformations via spatiotemporal regulations *[1]*. In this context, designing new multifunctional self-assembled nanostructures has found tremendous importance in recent times. Artificial protocell models are self-assembled nanostructures that mimic one or more functions of natural cells. Moreover, they tend to sequester a wide range of biologically active molecules in their architecture. Previously, extensive efforts have been made to design and formulate a diverse range of functional assemblies such as micelles, liposomes, polymersomes, plasmonic vesicles, dendrimers, hydrogels, metal-organic frameworks, polymeric nanoparticles, and coacervate droplets to mimic the properties and functions of cellular bodies *[2]*. In the present thesis, the unique properties of micelles and membraneless coacervates have been utilized to explore chemical reactivity inside these self-assembled nanocomposites.

Among them, micelles are the simplest self-assembled structures that mimic the natural self-assembled organelles *[3]*. Normally, amphiphilic surfactants self-assemble into micelles above their critical micellar concentration (CMC). The hydrophobic region of micelles can trap/encapsulate a wide range of molecules while their charged aqueous interface (CAI) can host oppositely charged molecules. CAIs can dramatically modulate many chemical and photochemical reactions that are otherwise inefficient in bulk medium. Apart from confinement, CAIs provide unique electric fields that align probe dipoles with respect to the interface and facilitate product selectivity. The micellar interface provide a unique microenvironment to solubilize both hydrophilic and hydrophobic probes at distinct locations in the micellar scaffold, bringing them in close proximity, which is particularly important for diffusion-controlled bimolecular reactions. At the same time, the interfacial charges on the surface of micelles dictate their interactions

with the charged molecules. These unique properties of micelles make them highly promising for a wide range of applications.

Another important class of protocell model is the membraneless coacervates. Coacervates are spherical self-assembled droplets formed via liquid–liquid phase separation (LLPS) phenomenon in aqueous dispersion of a wide range of solutes such as proteins, polypeptides, and polymers [4]. Coacervates can be broadly classified into biomolecular, synthetic organic, and synthetic hybrid coacervates. Biomolecular condensates mainly involve the coacervation of biomolecules such as (ribonucleic acid) RNA, proteins, etc., while the LLPS of organic macroions, including polypeptides, polyelectrolytes, biopolymers, amphiphilic polymers, and surfactants, form synthetic organic coacervates via noncovalent interactions [4, 5]. In contrast, synthetic hybrid coacervates are formed from oppositely charged organic polyelectrolytes and inorganic nanoparticles (NPs) such as metal clusters, polyoxometalate, quantum dots (QDs), carbon dots (CDs), etc., in aqueous medium [6].

Coacervates offer unique advantages over other self-assembled systems due to their inherent membraneless architecture and preferential sequestration of a wide range of solutes, including dyes, sugars, proteins, enzymes, nucleic acids, and nanoparticles [4, 7]. Notably, the physicochemical properties of coacervates can be easily tuned by varying the stochiometric ratio of its constituents, equilibration time, pH, and ionic strength of the medium. Although synthetic organic coacervates have been extensively explored toward protocell research and various enzymatic transformations, very little is known about their hybrid counterparts. The presence of optically active units in hybrid coacervates makes them highly promising for a wide range of applications such as photocatalysis, bioimaging, sensing, and environmental remediation. In this thesis, we have fabricated a unique class of intrinsically luminescent hybrid coacervates via simple electrostatic complexation of negatively charged CdTe quantum dots

(QDs) and positively charged polymer poly(diallyldimethylammonium chloride) (PDADMAC). The electrostatic attraction between the oppositely charged inorganic and organic counterparts is the primary force driving the formation of hybrid coacervates. Moreover, the favorable entropy change from the release of counterions and solvated water also facilitates coacervation. Interestingly, the NP-embedded hybrid coacervates retain all the unique features of synthetic organic coacervates while inheriting the optoelectronic properties of embedded NPs inside their membraneless architecture.

In this thesis, the CAIs of cetyltrimethylammonium bromide (CTAB) micelles have been utilized for the photocatalytic oxidative coupling of arylamines to azoaromatics in aqueous medium under ambient conditions. In the next study, the membraneless architecture and the optoelectronic properties of QD-embedded coacervates have been utilized for the ultrasensitive detection and removal of Hg^{2+}. Next, QD- and CD-embedded coacervates (QD- and CD-Ds) have been utilized for the visible-light-driven photo redox conversion of ferricyanide to ferrocyanide. QD-Ds were then utilized for the photocatalytic degradation of rhodamine B (RhB) and methylene blue (MB) as model organic pollutants. Finally, the QD-Ds have been utilized as a stable scaffold for the in situ formation of Au NPs to fabricate a new type of plexcitonic coacervates (Au@QD-Ds) without any capping and reducing agent. The Au@QD-Ds and its composite with glucose oxidase (GOx) have been utilized as efficient peroxidase mimics and for the selective detection of glucose in aqueous medium as well as on paper strips.

The contents of each chapter included in the thesis are discussed as follows:

1. Introduction

This chapter discusses the role of membraneless compartments in various biological processes inside the natural cell. It also gives a brief overview of the development of various self-assembled nanostructures

with a major focus on micelles and membraneless coacervates. Subsequently, the properties and role of synthetic organic and hybrid coacervates as artificial protocells, nanoreactors, delivery agents, etc., have been discussed in detail. In addition, the role of nanoparticles (NPs) and polyelectrolytes on the formulation and optoelectronic properties of NP-embedded hybrid coacervates has been discussed. Finally, a brief discussion about environmental remediation, photocatalysis, and enzyme catalysis has been provided.

2. Materials, sample preparation, experimental techniques

This chapter includes the details of all the chemicals and instrumentation utilized for the work done in this thesis. It also discusses the complete synthetic procedures of QDs, CDs, and gold nanoparticles (Au NPs), along with the different NP-embedded coacervates such as ATP-, CD-, and QD-coacervates. This chapter also covers the sample preparation, experimental procedures, and techniques used during the entire thesis work.

3. Metal-free photocatalysis at charged aqueous interfaces: boosting the photocatalytic oxidative coupling of arylamines to azoaromatics under ambient conditions

This chapter illustrates the tremendous potential of CAI toward boosting the efficacy of an important class photocatalytic organic transformation. In this work, the photophysical properties of a negatively charged photocatalyst, Eosin Y (EY) have been studied at the CAI of anionic, cationic, and neutral micelles of sodium dodecyl sulfate (SDS), CTAB, and Triton X-100 (TX-100), respectively. An effective interaction has been observed in the case of negatively charged EY and positively charged micelles of CTAB, with a 2.4-fold enhancement in the emission of EY at and at the critical micellar concentration of CTAB. In contrast, no such enhancement has been observed in the case of SDS and TX-100. Moreover, an increase in the fluorescence lifetime of EY from 1.17 ns in water to 2.74 ns in CTAB micellar medium has been observed, which signifies its association at the CAI of CTAB micelles. Herein, we have

utilized the EY@CTAB composite for the photocatalytic oxidative coupling of arylamines to azoaromatics in the aqueous medium under ambient conditions.
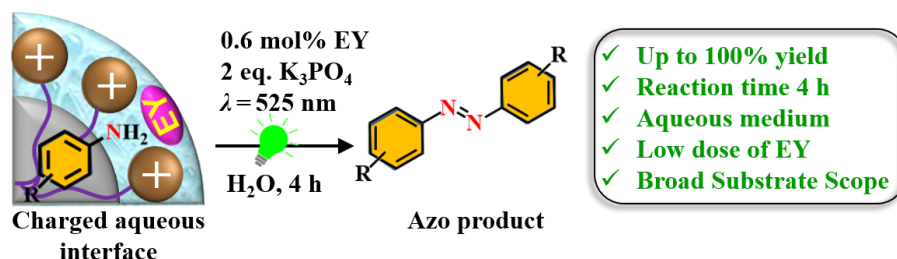
Scheme 1. Schematic representation of the photocatalytic oxidative coupling of arylamines to azoaromatics at the charged aqueous interface of micelles.

The present approach showed a broad substrate scope with excellent yields (up to 100%), fast kinetics (4 h), and 100% selectivity under ambient air atmosphere in the aqueous medium without any unwanted byproducts (Scheme 1). The current approach is easily scalable with about 0.11 (90%) and 0.47 g (80%) isolated yield for 1 mmol and 5 mmol *p*-anisidine, respectively, under standard reaction conditions. Herein, the hydrophobic region of CTAB micelles not only helps to solubilize the arylamines in its cavity but also aligns them in such a way as to allow an effective photoexcited electron transfer (PET) from arylamines to EY, present at the CAI of CTAB micelles. Moreover, the CAI not only acts as an efficient host for an ultrafast non-diffusive PET, but also modulates the redox potentials of arylamines and EY in a favorable manner. The present methodology may find wide-ranging implications in various chemical transformations.

4. Quantum dot-based hybrid coacervate droplets for ultrasensitive detection of Hg^{2+}

Designing effective optically active nanostructures for the simultaneous detection and removal of harmful environmental contaminants has found great importance in recent times. In this chapter, the formation of QD-embedded hybrid coacervate droplets (QD-Ds) has been discussed.

The QD-Ds are formed by simple mixing of negatively charged CdTe QDs (85 nM) and positively charged polymer PDADMAC (32.5 μM) in the aqueous medium under constant stirring. Here, the electrostatic attractions between anionic QDs and cationic PDADMAC allow them to undergo liquid-liquid phase separation to form highly luminescent QD-Ds. This approach has also been utilized to form green (G-Ds) and red (R-Ds) emissive coacervate droplets by using appropriate QDs. Subsequently, the optoelectronic properties of these droplets have been utilized for the detection of Hg^{2+} (Scheme 2).
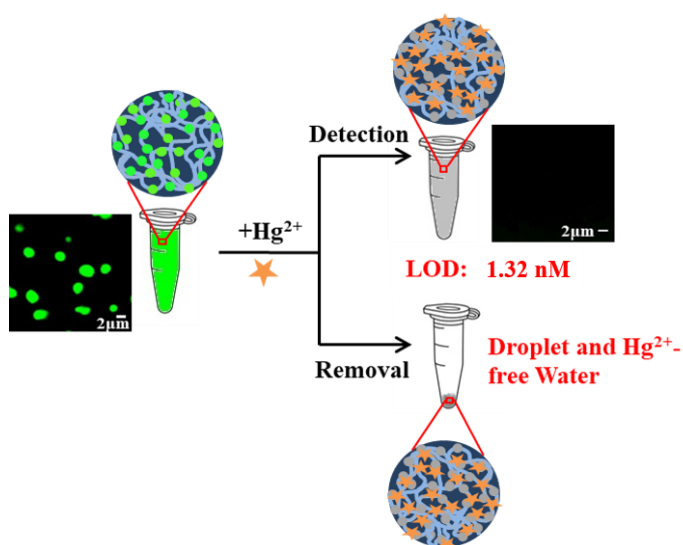
Scheme 2. Schematic representation of the ultrasensitive detection and efficient removal of Hg^{2+} with QD-embedded hybrid coacervates.

Selective quenching of G-Ds and R-Ds has been observed in the presence of Hg^{2+} with a limit of detection of 1.32 and 1.45 nM in G-Ds in Milli-Q and tap water, respectively. The mechanistic studies highlighted the role of free MSA-ligands present over the surface of QDs embedded inside the coacervates for the effective trapping of Hg^{2+} inside the droplets. The presence of Hg^{2+} inside G-Ds has been further confirmed using elemental mapping. Moreover, the decrease in the PL lifetime of G-Ds upon the addition of Hg^{2+} signifies a photoexcited electron transfer from QDs to Hg^{2+}, which is responsible for its selective detection. Finally, the membraneless architecture and sequestration ability of G-Ds has been utilized for the efficient removal of Hg^{2+} from

the contaminated water via a simple centrifugation method. Notably, the G-Ds sequestered even trace amounts of Hg^{2+} from the solution with over 98% removal efficiency. The present study provides fundamental insights and highlights the role of optically active hybrid coacervates for the detection and remediation of environmental contaminants.

5. NP-embedded hybrid nanoreactors for visible light photocatalysis and dye degradation

Designing of artificial photocatalytic nanoreactors with multiple catalytic centers inside their architecture without unwanted agglomeration and accessibility barriers for reactants finds tremendous importance in carrying out complex chemical transformations. In this chapter, we have studied the efficacy of QD-Ds and CD-embedded hybrid coacervates (CD-Ds) as a new class of photocatalytic nanoreactor to carry out the visible-light-driven one electron photo redox conversion of ferricyanide to ferrocyanide and photocatalytic degradation of RhB and MB as model environmental pollutants (Scheme 3). Notably, the bare QDs and CDs failed to catalyze the photoredox conversion of ferricyanide to ferrocyanide due to the electrostatic repulsion between negatively charged CDs/QDs and ferricyanide. In contrast, the membraneless architecture of the QD- and CD-Ds provides an ideal microenvironment to drive this incompatible reaction in the confined space by regulating the surface charge density and effective concentrations of ferricyanide inside the droplets. Interestingly, QD-Ds showed better photocatalytic efficacy for the conversion of ferricyanide to ferrocyanide than CD-Ds under blue light illumination. Notably, while QD-Ds showed a reaction rate constant of $3.5 \times 10^{-2} \, min^{-1}$ and a conversion yield of ~80% for ferricyanide conversion, the CD-Ds exhibited a lower rate constant of $3.0 \times 10^{-2} \, min^{-1}$ and a conversion yield of 60% under similar reaction conditions. The above results clearly highlight that the change in the embedded NPs inside these droplets can alter their photocatalytic properties, thus making them highly useful for a wide range of applications. Importantly, both QD- and CD-Ds

exhibited excellent recyclability without any compromise in reaction kinetics and conversion yield.
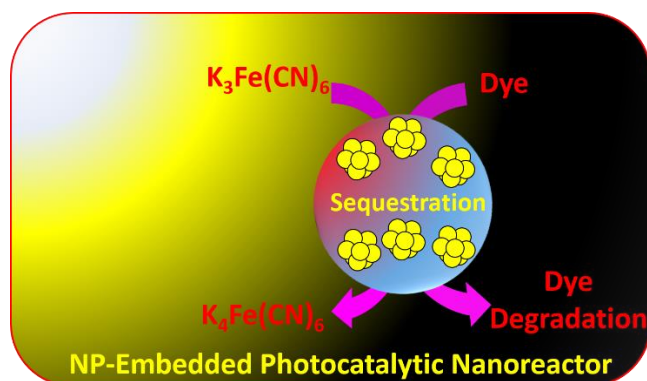
Scheme 3. Schematic representation of NP-embedded coacervates as photocatalytic nanoreactors for the photocatalytic conversion of ferricyanide to ferrocyanide and dye degradation.

Subsequently, the QD-Ds have been utilized for the photocatalytic degradation of model organic pollutants like RhB and MB. The bare QDs showed a photocatalytic degradation of 43 and 33% for RhB and MB, respectively in the presence of H_2O_2 in 180 min. In contrast, a significant enhancement in the degradation efficiency has been observed for RhB-and MB-loaded QD-Ds under the same experimental conditions, with 96 and 84% photodegradation of RhB and MB, respectively. Notably, the significant enhancement in the photocatalytic degradation of RhB and MB in the presence of QD-Ds in comparison to the aqueous QDs can be attributed to the confinement as well as increased local concentrations of RhB and MB near the surface of embedded QDs inside the QD-Ds. Altogether, the membraneless structure of these droplets with multiple NPs (catalytic sites) embedded inside their architecture makes them an ideal candidate for photocatalytic nanoreactors.

6. Coacervate-based plexcitonic assembly toward peroxidase-like activity and ultrasensitive glucose sensing

In this chapter, the QD-Ds have been utilized as a confined compartment for the in situ synthesis of small-size Au NPs without additional reducing and capping agents. Control experiments revealed that the free surface carboxylic acid groups of embedded QDs simultaneously act as reducing and stabilizing agents for Au NPs. The in situ synthesized Au NPs inside QD-Ds (Au@QD-Ds) have been found to be stable for over 28 days without any agglomeration. Furthermore, Au@QD-Ds exhibited high stability over a broad range of pH and temperatures. Notably, the Au@QD-Ds exhibited superior peroxidase-like activity compared to bulk aqueous Au NPs and Au@QDs under similar experimental conditions. The observed peroxidase-like activity followed the classical Michaelis−Menten model inside the Au@QD-Ds via the fast electron-transfer pathway.
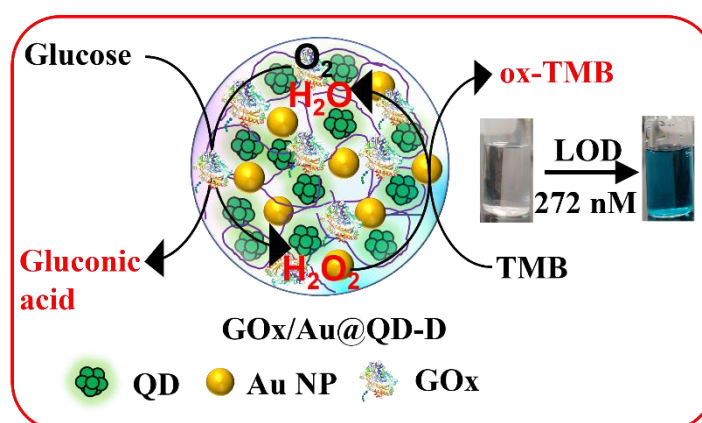
Scheme 4. Schematic representation of the peroxidase-like activity of Au@QD-Ds and its composite with glucose oxidase as an effective bioplatform for the detection of glucose.

The enhanced peroxidase-like activity has been explained by considering confinement, mass action, and the ligand-free surface of embedded Au NPs. The present plexcitonic nanocomposites exhibit excellent recyclability over several consecutive cycles without any compromise in their catalytic activity. Finally, a cascade reaction with glucose oxidase (GOx)-loaded Au@QD-Ds has been utilized for colorimetric detection of glucose with a limit of detection of 272 nM in solution as well as on filter paper (Scheme 4). The present work

highlights a facile and robust methodology for the fabrication of optically active functional hybrid plexcitonic assemblies, which may find importance in various fields, including bioanalytical chemistry and optoelectronics.

7. Conclusions

The conclusions of the thesis can be described as follows:

1) The POC of arylamines at CAIs of micelles highlights the tremendous potential of CAIs toward boosting the efficacy of a wide range of important organic transformations. Furthermore, the CAIs can not act as a medium to carry out the organic transformation but can also modulate the redox potentials of reactants and photocatalysts in a favorable manner.

2) The membraneless architecture of optically active QD-Ds not only makes them an efficient sensor for the detection of harmful contaminants such as Hg^{2+} but can also help in the efficient removal of pollutants from contaminated water.

3) This study highlights the tremendous potential of NP-embedded coacervates as efficient photocatalytic nanoreactors. These nanoreactors can even drive incompatible reactions to completion. Furthermore, the photocatalytic efficacy of these nanoreactors can be easily tuned by changing the embedded NPs as per the requirements of the chemical transformation

4) This study highlights the importance of hybrid coacervates as an efficient and stable scaffold for the ligand and reducing agent-free synthesis of nanoparticles. It provides a highly efficient platform for detecting glucose both in aqueous solution and on paper strips. Furthermore, this work presents a unique methodology for designing optically active functional hybrid plexcitonic assemblies.

8. References

1) Stroberg W., Schnell S. (2018), Do cellular condensates accelerate biochemical reactions? lessons from microdroplet chemistry, Biophys. J., 115, 3−8. (DOI:10.1016/j.bpj.2018.05.023)

2) Tu Y., Peng F., Adawy A., Men Y., Abdelmohsen L. K., Wilson D. A. (2016), Mimicking the cell: bio-inspired functions of supramolecular assemblies, Chem. Rev., 116, 2023– 2078. (DOI:10.1021/acs.chemrev.5b00344)

3) Perumal S., Atchudan R., Lee W. (2022), A review of polymeric micelles and their applications, Polymers, 14, 2510. (DOI:10.3390/polym14122510)

4) Williams D. S., Koga S., Hak C. R. C., Majrekar A., Patil A. J., Perriman A. W., Mann S. (2012), Polymer/nucleotide droplets as bio-inspired functional micro-compartments, Soft Matter, 8, 6004. (DOI:10.1039/c2sm25184a)

5) Banani S. F., Lee H. O., Hyman A. A., Rosen M. K. (2017), Biomolecular condensates: organizers of cellular biochemistry, Nat. Rev. Mol. Cell Biol., 18, 285–298. (DOI:10.1038/nrm.2017.7)

6) Vaishnav J. K., Mukherjee T. K. (2019), Highly photostable and two-photon active quantum dot–polymer multicolor hybrid coacervate droplets, Langmuir, 35, 11764–11773. (DOI:10.1021/acs.langmuir.9b01783)

7) Koga S., Williams D. S., Perriman A. W., Mann S. (2011), Peptide–nucleotide microdroplets as a step towards a membrane-free protocell model, Nat. Chem., 3, 720–724. (DOI:10.1038/nchem.1110)

List of Publications

❖ **Publications included in this Thesis:**

1) **<u>Singh S.,</u>** Vaishnav J. K., Mukherjee T. K. (2020), Quantum dot-based hybrid coacervate nanodroplets for ultrasensitive detection of Hg^{2+}, ACS Appl. Nano Mater., 3, 3604−3612. (DOI:10.1021/acsanm.0c00317)

2) Saini# B., **<u>Singh</u>**# **<u>S.,</u>** Mukherjee T. K. (2021), Nanocatalysis under nanoconfinement: a metal-free hybrid coacervate nanodroplet as a catalytic nanoreactor for efficient redox and photocatalytic reactions, ACS Appl. Mater. Interfaces, 13, 51117−51131. (DOI:10.1021/acsami.1c17106) (#: Equal contribution)

3) **<u>Singh S.,</u>** Rao C., Nandi C. K., Mukherjee T. K. (2022), Quantum dot-embedded hybrid photocatalytic nanoreactors for visible light photocatalysis and dye degradation, ACS Appl. Nano Mater., 5, 7427−7439. (DOI:10.1021/acsanm.2c01446)

4) **<u>Singh S.,</u>** Mukherjee T. K. (2023), Coacervate-based plexcitonic assembly toward peroxidase-like activity and ultrasensitive glucose sensing, ACS Appl. Mater. Interfaces, 15, 25524–25535. (DOI:10.1021/acsami.3c02863)

5) **<u>Singh# S.,</u>** Agarwal# V., Sarma T. K., Mukherjee T. K. (2023), Metal-free photocatalysis at charged aqueous interfaces: boosting the photocatalytic oxidative coupling of arylamines to azoaromatics under ambient conditions, Green Chem., 23, 9109–9114. (DOI:10.1039/D3GC03150K) (#: Equal contribution)

❖ **Publications apart from this Thesis:**

6) Patel C. K., **Singh S.,** Saini B., Mukherjee T. K. (2022), Macromolecular crowding-induced unusual liquid-liquid phase separation of human serum albumin via soft protein-protein interactions, J. Phys. Chem. Lett., 13, 3636–3644. (DOI: 10.1021/acs.jpclett.2c00307)

7) **Singh S.,** Mukherjee T. K. (2024), Photosensitizer-free singlet oxygen generation via charge transfer transition involving molecular O_2 toward highly efficient oxidative coupling of arylamines to azoaromatics, Chem. Sci., 15, 13949–13957. (DOI: 10.1039/D4SC04115A)

Table of Contents

Chapter 2: Materials, Sample Preparation, and Experimental Techniques

Chapter 3: Metal-Free Photocatalysis at Charged Aqueous Interfaces: Boosting the Photocatalytic Oxidative Coupling of Arylamines to Azoaromatics under Ambient Conditions

Chapter 4: Quantum Dot-Based Hybrid Coacervates for Ultrasensitive Detection of Hg^{2+}

Chapter 5: NP-Embedded Hybrid Coacervates as Efficient Nanoreactors for Visible Light Photocatalysis and Dye Degradation

Chapter 6: Coacervate-Based Plexcitonic Assembly toward Peroxidase-like Activity and Ultrasensitive Glucose Sensing

Chapter 7: Conclusions and Future Scope

Appendix A

List of Schemes

List of Figures

mixture at 15 min and 60 min time intervals under green LED irradiation in the presence of 10 mM p-anisidine, 40 mM CTAB, 0.6 mol% EY, and 2 equiv. K_3PO_4. (C) Daylight photographs of peroxide test strips for (a) blank strips without any measurement, (b) before the photocatalytic experiment, and (c) after 4 h of reaction (EY@CTAB + p-anisidine + K_3PO_4) under standard reaction conditions. The red arrow indicates the desired color change of the strip.

light. PL spectra of (D) G-Ds and (E) R-Ds in the presence of various interfering metal ions. (F) Selectivity and anti-interference capability of G-Ds towards Hg^{2+} detection in the presence of different metal ions (2.0 equiv).

sequestration process. (D) Quantitative estimation of sequestration efficiency of Hg^{2+} from the standard calibration curve. The inset shows the PL calibration plot for the G-Ds and Hg^{2+} system.

in aqueous solution (upper panel) and paper strip (lower panel) for TMB oxidation on varying the glucose concentration (0–500 µM). (E) Selective response of Au@QD-D toward different sugars. The data represent the mean ± SEM for three (n = 3) independent experiments. Statistical significance was assessed by a two-tailed, unpaired Student's t-test with the three-asterisk symbol (***) representing a P value of < 0.001.

List of Tables

Acronyms

QD	Quantum dot
CD	Carbon dot
QD-Ds	QD-embedded coacervate droplets
CD-Ds	CD-embedded coacervate droplets
G-Ds	Green droplets
R-Ds	Red droplets
PDADMAC	Poly(diallyldimethylammonium
PL	chloride)
	Photoluminescence
UV	Ultraviolet
Vis	Visible
AFM	Atomic force microscopy
FTIR	Fourier transform infrared
PXRD	Powder X-ray diffraction
TEM	Transmission electron microscopy
HR-TEM	High-resolution transmission electron microscopy
QY	Quantum yield
OD	Optical density
NaOH	Sodium hydroxide
FESEM	Field-emission scanning electron Microscopy
CLSM	Confocal laser scanning microscopy
NaCl	Sodium chloride
DIC	Differential Interference Contrast
FITC	Fluorescein isothiocyanate
NPs	Nanoparticles

Au NPs	Gold nanoparticles
ATP	Adenosine triphosphate
NMR	Nuclear magnetic resonance
ESI-MS	Electrospray ionization-mass spectrometry
LC-MS	Liquid chromatography-mass spectrometry
HR-MS	High resolution-mass spectrometry
$CDCl_3$	Deuterated chloroform
MeOH	Methanol
CTAB	Cetyltrimethylammonium bromide
TX-100	Triton X-100
CMC	Critical micelle concentration
SDS	Sodium dodecyl sulfate
TCSPC	Time-correlated single-photon counting
IRF	Instrument response function
PBS	Phosphate buffer saline
EE	Encapsulation efficiency
XPS	X-ray photoelectron spectroscopy
MSA	Mercaptosuccinic acid
N_2	Nitrogen
$NaBH_4$	Sodium borohydride
GC-MS	Gas chromatography-mass spectrometry
DMSO-d^6	Deuterated dimethyl sulfoxide
Rh6G	Rhodamine 6G
GOx	Glucose oxidase
HRP	Horseradish peroxidase
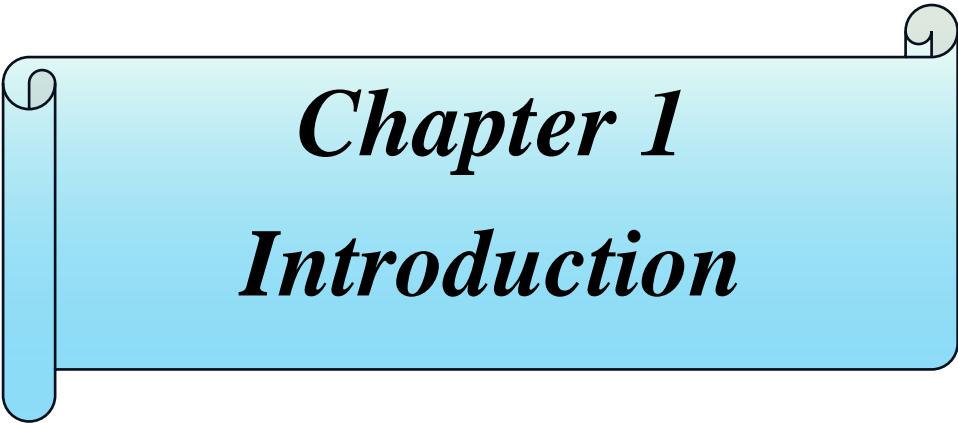
OPD	o-Phenylenediamine
TMB	3,3′,5,5′-Tetramethylbenzidine
H_2O_2	Hydrogen peroxide
O_2	Oxygen
s.e.m.	Standard error of mean
LOD	Limit of detection
RBITC	Rhodamine B isothiocyanate
LLPS	Liquid-liquid phase separation
LCST	Lower critical solution temperature
UCST	Upper critical solution temperature
MB	methylene blue
ABTS	2,2'-azino-bis(3-ethylbenzothiazoline-6-sulfonic acid)
HOMO	Highest occupied molecular orbital
LUMO	Lowest unoccupied molecular orbital
CB	Conduction band
VB	Valence band

Nomenclature

nm	Nanometer
cm	Centimeter
η	Refractive index
θ	Diffraction angle
d	Interplanar spacing
ζ	Zeta
mV	Millivolt
pH	The negative logarithm of hydronium-ion concentration
h	Hour
mg	Milligram
mL	Milliliter
μM	Micromolar
pKa	Dissociation constant of an acid in the ground state
m	Millimolar
M	
rpm	Rotation per minute
min	Minute
K	Partition coefficient
μg	Microgram
μM	Micromolar
I	Intensity
ns	Nanosecond
τ	Excited-state lifetime
Tm	Transition temperature
°C	Degree Celsius

K	Kelvin
A	Absorbance
eV	Electron Volt
nM	Nanomolar
C	Concentration
k_{app}	Apparent rate constant
k	Reaction rate constant
M	Molar
t	Time
T	Temperature
ΔG	Gibbs free energy of activation
ΔH	Enthalpy of activation
ΔS	Entropy of activation
k_B	Boltzmann's constant
h	Planck's constant
E_a	Activation energy
A	Pre-exponential factor
KJ	Kilojoule
mol	Mole
ppm	Parts per million
ppb	Parts per billion
δ	Chemical shift
λ	Wavelength
RT	Room temperature
s	Second
μm	Micrometer
pM	Picomolar
ε	Molar absorption coefficient

V_0	Initial velocity
[S]	Molar concentration of substrate
k_{cat}	Catalytic rate constant
K_m	Michaelis-Menton constant
V_{max}	Maximum velocity
P	Probability
NS	Not significant
λ_{em}	Emission wavelength
λ_{max}	Absorption wavelength
ps	Picosecond
SD	Standard deviation
μL	Microliter
ng	Nanogram
g	Gram

Chapter 1
Introduction

1.1. Preface

Over the years, nature has inspired numerous scientific advancements, and one such advancement is the development of self-assembled structures that mimic the physiological properties of natural membrane-bound and membraneless compartments. Self-assembly is often described as the spontaneous arrangement of different monomeric units into well-defined structures. Nature utilizes self-assembly to form numerous complex and functional biological structures, such as the formation of DNA, chromatin, cell membranes, and the folding of proteins into complex three-dimensional structures *[1]*. Cells, also known as the fundamental unit of any living entity, consist of various complex assemblies such as protein aggregates, molecular machines, lipid membranes, folded proteins, structured nucleic acids, etc. which helps in its efficient functioning *[2]*. Notably, replication, metabolism, compartmentalization, and adaptation are the essential characteristics of a cellular system *[3–4]*.
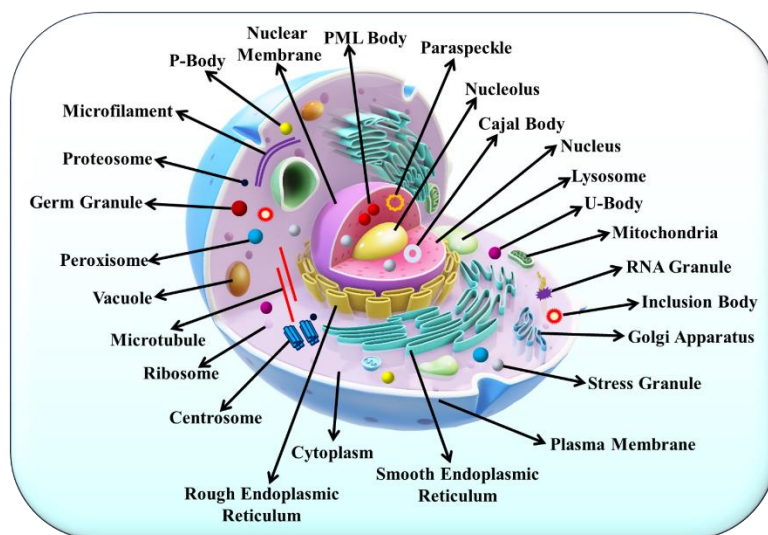
Scheme 1.1. Structure of eukaryotic cell with various membraneless and membrane-bound organelles.

Among them, compartmentalization is an elementary property of the eukaryotic cells which comprises of various membraneless and membrane-bound organelles (Scheme 1.1). They utilize

compartmentalization to carry out a wide range of biochemical reactions in a highly regulated and efficient manner *[5–18]*. For example, membrane-bound organelles like lysosomes and mitochondria are responsible for the destruction of macromolecules *[5]* and ATP production *[6]*, respectively. In contrast, the membraneless organelles like centrosomes *[7]*, Cajal bodies *[8]*, nucleoli *[9]*, P bodies, and stress granules *[10, 11]* are widely linked to congenital immunity *[12]*, regulation of RNA processing and transportation *[13, 14]*, intracellular environmental sensing *[15]*, the events of neurodegenerative diseases *[16]*, DNA repairing *[17]*, and neurotransmitter reservoir *[18]*. However, unlike membrane-bound organelles, cells carry out most of the biochemical transformations in membraneless organelles in the nucleus and cytoplasm. Recent studies show that the organelles inside the cells behave similarly to the liquid-like droplets under the crowding effect of cytoplasm *[3, 10, 19–26]*. Furthermore, the droplets in the cells exhibit liquid-like properties such as surface wetting, dripping, and fusion, emphasizing their liquid-like behavior *[19, 27]*. Interestingly, the efficient spatiotemporal positioning of the biomolecules inside these membraneless and membrane-bound organelles results in the coherent working of several cascade reactions such as intracellular digestion, osmotic control, removal of ROS, CO_2 sequestration, and energy production inside the cell *[8, 22–26, 28]*.

Inspired from these naturally occurring and highly efficient organelles, researchers have utilized self-assembly to design and fabricate a wide range of dynamic artificial self-assembled nanostructures (Scheme 1.2). Self-assembly occurs via noncovalent interactions such as π-π stacking, van der Waals forces, hydrogen bonding, electrostatic, and/or hydrophobic interactions between the monomeric units *[1, 29, 30]*. Although noncovalent interactions are moderately weak, multivalent interactions between several monomeric units can lead to highly stable dynamic structures. Furthermore, it is possible to generate different shapes and sizes of self-assembled

3

nanostructures simply by optimizing pH, temperature, concentrations, and intermolecular forces between the molecular units.
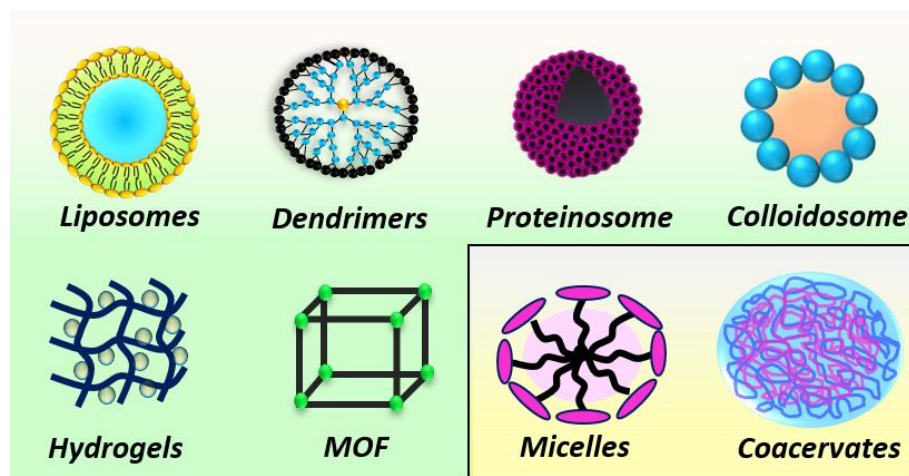
Scheme 1.2. Schematic illustration of the well-explored self-assembled nanostructures.

The unique structural and surface properties of self-assembled nanostructures such as confined architecture, tunable size, etc., make them an exemplary medium to understand and replicate the naturally occurring self-assembly processes. Previously, researchers have used various strategies to create a wide range of three-dimensional self-assembled nanostructures to mimic the natural properties of cells and their functional responses. Some of these self-assembled nanostructures are discussed below.
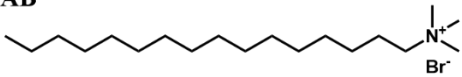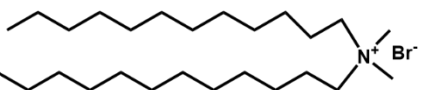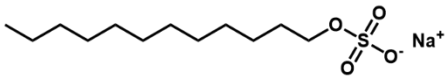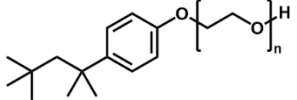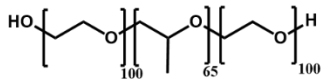
1.2. Different types of three-dimensional self-assembled nanostructures

1.2.1. Micelles

Micelles are the simplest type of self-assembled nanostructures formed via self-assembly of amphiphilic molecules in the aqueous medium. Notably, the surfactant molecules, having polar head groups and nonpolar hydrocarbon chains, form spherical micelles in the aqueous medium at and beyond a specific concentration known as critical micellar concentration (CMC) *[31]*. Micelles are self-assembled structures of amphiphilic molecules such as surfactants, polymers,

copolymers, etc., with a hydrophobic core and a hydrophilic shell *[31]*. The hydrophobic core of micelles is surrounded by a Stern layer containing polar head groups with $(1-\alpha)N$ counter ions, where α is the degree of ionization, and N is the number of surfactant molecules in the micelles. The Stern layer is accompanied by the Gouy-Chapman layer, which contains the remaining αN counter ions *[32]*.

Table 1.1. Structure, CMC values, and surface charge of some well-known micelles.

S. No.	Surfactant	CMC (mM)	Surface Charge
1.	CTAB	0.9	positive
2.	DDAB	0.8	positive
3.	SDS	8.0	negative
4.	TX-100	0.24	non-ionic
5.	Pluronic F-127	0.003	non-ionic

The shape, size, and surface charge of micelles can be tuned by substituting the monomeric surfactants or by varying their concentrations. Some of the examples of ionic and non-ionic surfactants are discussed in Table 1.1 *[31–33]*. Although micelles are primarily spherical with a size range of 3 to 5 nm, other shapes of micelles such as bilayers, cylinders, and ellipsoids are also known *[33]*. The size and shape of a micelle further depend on the orientation of the surfactant molecules, the concentration of surfactants, and the temperature, pH, and ionic strength of the solution *[33]*. The hydrophilic shell of micelles makes them highly dispersible in water, while the hydrophilic core of micelles possesses a high affinity for

various organic molecules and can easily encapsulate them in its hydrophobic core. The encapsulation of organic molecules inside the core of micelles increases their solubility, which makes them highly sought after for various applications such as catalysis *[34–36]*, environmental remediation *[37–39]*, and biomedical applications *[40–42]*. For example, Zhao and coworkers used the Pluoronic F-127, a nonionic biocompatible surfactant, to encapsulate a NIR-absorbing squaraine dye (D1) inside its micellar architecture and utilized it as an excellent contrast agent for fluorescence and photoacoustic bimodal imaging *[43]*. Similarly, Wang and coworkers developed glutathione (GSH)-responsive poly(ethylene glycol)-b-polycarbonate-b-poly-(ethylene glycol) triblock copolymer micellar nanoparticles. Subsequently, they utilized them to carry hydrophobic anticancer drugs such as doxorubicin for a stimuli-responsive controlled drug release *[44]*.

Previously, it has been observed that the micellar medium can regulate the bimolecular electron transfer (ET) dynamics via its interfacial properties *[45, 46]*. For instance, Pal and coworkers studied the photoinduced bimolecular ET dynamics between N,N-dimethylaniline (DMAN) and 7-aminocoumarin derivatives in different micellar mediums *[46]*. Here, they observed very fast decay time constant (τ) of less than ~10 ps for the coumarins in the presence of DMAN in all the micellar media. Recently, the utilization of water as a primary reaction medium for sustainable organic transformations has emerged as an appealing approach. However, the low solubility of organic substrates in the aqueous medium hampers this strategy. To circumvent this problem, micellar catalysis has emerged as an efficient solution where the amphiphilic molecules alter the bulk aqueous medium's solvation properties and promote the desired chemical transformation under milder conditions *[47]*. The unique interfacial properties of micelles have been instrumental in developing a wide range of green and sustainable catalytic strategies *[47-49]*.

The hydrophilic nature and confined architecture of micelles have been utilized in tandem to carry out various organic transformations that were otherwise incompatible in the aqueous solution. For instance, Handa and coworkers utilized PS-750M, proline-based amphiphile micelles for the in-situ synthesis of ultrasmall Pd nanoparticles and subsequently used them for the α-arylation reaction of nitriles in aqueous medium *[50]*. In a similar study, Darensbourg and coworkers utilized an amphiphilic metallosurfactant to form uniform spherical micelles with the catalytic Pd center located in the hydrophobic pocket of the micelle. The metallosurfactant-based micelles were found to catalyze carbon-carbon coupling reactions effectively at very low catalyst concentrations *[51]*. In the present thesis, we have studied the role of the charge aqueous interface of micelles on the photophysical properties of Eosin Y (EY), an organic dye and well-known photocatalyst. The EY@CTAB composite was utilized to carry out the photocatalytic oxidative coupling of arylamines in the aqueous medium under ambient conditions.

1.2.2. Liposomes

Liposomes are spherical vesicles formed by the self-assembly of *diacyl-chain phospholipids [52]*. They are the first described synthetic analog for biomimetic systems, formulated by techniques such as thin-film hydration, solvent injection, electro-formation, high-pressure extrusion, reverse-phase evaporation, and microfluidics *[52, 53]*. Monolayer vesicles such as small unilamellar vesicles (SUVs; < 100 nm), large unilamellar vesicles (LUVs; 100 nm-1 μm), and giant unilamellar vesicles (GUVs; > 1 μm) along with multilayered vesicles (MLVs) have been used to understand the organization, functions, and dynamics of lipid membrane with specific peptide chains *[54]*. The size and morphology of GUVs were similar to natural cells and were used to study the properties of cell membranes. For instance, Nuñez and coworkers fabricated phospholipid-based GUVs and then encapsulated them with cyprosins, a proteolytic enzyme *[55]*. Here,

they have observed accelerated cheese production, enhanced flavor intensity, and shortened ripening time. Similarly, Lee and coworkers designed a protocellular system or biomimetic vesicle that regulates two ATP-dependent reactions, carbon fixation and actin polymerization [56]. Furthermore, distinct and efficient cell-like bioreactors with modified lipid composition have been created and utilized for selective permeability of nutrients [57], intracellular signaling cascade [58], intercellular communication [59], translation of chemical messages or sensing [60], and evolutionary mechanisms [61].

1.2.3. Polymersomes

Polymersomes are artificial vesicles made from amphiphilic synthetic block copolymers with a size ranging from 50 nm to 5 μm or more [62]. They possess a robust structure and resemble cell-membrane-like properties [62, 63]. Compared to liposomes, polymersomes formed from amphiphilic block copolymers show lower leakage, higher stability, lower mobility, controlled membrane permeability, and excellent chemical versatility, which makes them a good candidate for the construction of biomimetic systems [64, 65]. For instance, Chang and coworkers demonstrated that semipermeable membranes of polymersomes could not only pass small molecules such as nutrients, metabolites, etc. [66] and can also encapsulate cells, microorganisms, enzymes, hormones, short peptides, hemoglobin, adsorbents, and bioactive substances [66–72]. Similarly, Sun and coworkers fabricated an alginate-polylysine-alginate membrane as a protocell model, evidencing the prolonged xenograft survival rate [73]. Kataoka and coworkers designed injectable enzyme-loaded polymersomes as nanoreactors for activating prodrugs at the tumor site that can be utilized for enzyme/prodrug therapies (EPT) and enzyme-replacement therapies [74]. Furthermore, hybrid vesicles or advanced vesicles fabricated from lipid and copolymers such as poly(dimethylsiloxane)-graft-poly(ethylene oxide) (PDMS-g-PEO), polyethylene glycol (PEG), polycaprolactone (PCL), and polylactide (PLA) have been designed by adjusting the lipid/polymer ratio, showing their

applicability toward surface mechanisms, drug delivery, encapsulation, and selective permeability *[75, 76]*.

1.2.4. Dendrimers

Dendrimers are stable, homogenous, monodispersed uni- or multilamellar vesicles self-assembled in water from amphiphilic Janus dendrimers (AJDs). They exhibit the ability to self-assemble into chemically versatile uniform structures such as vesicles, micelles, tubular, and cubosomes. Furthermore, they can also incorporate transmembrane channels, making them an alternate model to polymersomes and liposomes *[77]*. Dendrimers have been utilized in chemical catalysis *[78]*, drug delivery carriers *[79]*, targeting delivery *[80]*, solubility enhancement *[81]*, and therapeutic agents *[82]*. For example, Tanenbaum and coworkers designed a unique type of nanoreactors through the adsorption of different copolymers onto the laccase enzyme in an aqueous medium and displayed amended catalytic performances under green chemistry conditions *[83]*. Ornelas and coworkers constructed triazolylferrocenyl dendrimers in water containing nontraditional green fluorescence (NTIL) for nanotheranostic devices *[84]*.

1.2.5. Colloidosomes

Colloidosomes are interiorly hollow elastic shells and are formed by self-assembly of colloid particles at the interface of liquid/liquid biphasic systems which can be inorganic, organic, or both *[85–87]*. The high chemical versatility and good physiochemical properties of colloidosomes exemplify their importance as a microreactor for catalysis, photoreactions, oscillation reactions, and theranostic applications *[85, 86, 88]*. For example, Lin and coworkers designed a hybrid catalytic reactor from hemoglobin-modified silica nanoparticles which demonstrated good biocatalytic stability, enhanced cascade reaction rates, and good functional response toward biological computing *[89]*. Also, Liang and coworkers fabricated dual-enzyme colloidosome reactors (DECRs) with silica nanoparticles and

encapsulated water-soluble glucose oxidase (GOx) inside the colloidosomes *[90]*. The fabricated microreactor showed high performance of biphasic cascade reactions of N-heteroaromatic compounds without any decrease in yield even after four cycles. Similarly, Mann and coworkers utilized catalase, lipase, or alkaline phosphatase-loaded colloidosomes to understand the dynamics of the protocellular community for artificial phagocytosis response *[91]*. Furthermore, Meng and coworkers prepared lipase-encapsulated hollow colloidosomes by green methodology and demonstrated a good encapsulation rate, better biocompatibility, enhanced catalytic rate, and excellent reusability over ten catalytic cycles *[92]*. Therefore, it has been found that colloidosomes provide adequate enzyme active sites at the organic phase-water interface, which arises due to the high surface area of the nanoparticles present over the structure. However, their complex synthetic procedure and harsh crosslinked enzyme immobilization process limit their applicability *[93]*.

1.2.6. Protienosomes

Proteinosomes are permeable, biocompatible, and bifunctional compartments consisting of monolayers of conjugated protein-polymer building blocks and enclosed by hydrophilic lumen *[94, 95]*. Protein-based versatile protocells exhibit high encapsulation efficiency, selective membrane permeability, multi-compartmentalization, and cytoskeleton-like matrix formation. For example, Mann and coworkers developed the first proteinosomes formed by bovine serum albumin-poly(N-isopropylacrylamide) (BSA-NH$_2$/PNIPAM) at the oil/water interface. They demonstrated its properties toward selective permeability, encapsulation, targeted delivery, stimuli-responsiveness, and gene-directed protein synthesis *[95]*. Similarly, Zhao and coworkers fabricated proteinosomes by using electrostatic interaction between negatively-charged BSA-PNIPAM and positively charged enzymes, lysozymes, and trypsin and further highlighted the importance of structural and functional integrity of enzymes *[96]*. Moreover, different types of enzyme-polymers nanoconjugates have

been fabricated and utilized for multi-step membrane-mediated cascade reactions *[97]*, and spatiotemporal release of different components *[98, 99]*.

1.2.7. Metal-organic frameworks

Metal-organic frameworks (MOFs) are self-assembled structures consisting of metal clusters coordinated to the organic linkers to generate one-, two- or three-dimensional structures. MOFs have a potentially porous architecture where their sub-units align in a repeating pattern at a constant ratio *[100]*. Their ultrahigh porosity and enormous surface area make them highly important in a wide range of applications in clean energy, high-capacity absorbents, catalysis, biomedical imaging, thin-film devices, and environmental remediation *[100–105]*. For example, Jiang and coworkers utilized the Pt nanocrystals integrated porphyrinic MOFs, PCN-224(M) for the selective photo-oxidation of aromatic alcohols to aldehydes via synergistic effect of $^1O_2$ and photothermal effect *[106]*. Similarly, Jiang and coworkers synthesized an unusual out-of-plane porphyrin-based MOF and highlighted the role of the location of metal ions in metalloporphyrins in boosting photocatalytic activity for hydrogen production *[107]*. In another study, Li and coworkers developed unique MOF-on-MOF nanofabrics by self-assembling MIL-101(Cr) and UiO-66-NH_2 crystals on polyacrylonitrile (PAN) nanofabrics *[108]*. They exhibited highly synergistic effects between the MOF composites for detoxifying blistering and nerve agent simulants. Although these studies highlight the unique advantages of MOFs, they also have some shortcomings. Notably, synthesizing and purifying MOFs is often tedious and requires sophisticated instruments. They usually lack water stability as water molecules can attack the coordination bonds between organic ligands and metal centers. Furthermore, their poor processability, brittleness, and insolubility restrict their practical applications in the aqueous medium.

1.2.8 Coacervates

Coacervates are dense liquid-like droplets self-assembled via liquid-liquid phase separation (LLPS)/coacervation in the aqueous medium *[109,110]*. LLPS is a spontaneous phenomenon in the aqueous mixtures of polymers, polyelectrolytes, proteins, RNA, and/or polypeptides, which results in the formation of membraneless liquid-like droplets via multivalent intermolecular interactions *[109–114]*. Notably, LLPS separates the colloidal solution into colloid-poor and colloid-rich phases. The colloid-rich phase bearing a more extensive colloidal component content is known as a coacervate droplet, which remains in equilibrium with the dilute phase, and both are present in a single medium. Coacervates exhibit a sponge-like structure, also known as the sponge phase, eccentric phase, or L3 phase *[115]*. The term coacervate originates from two Latin words, "co" (jointly) and "acerv" (a mound), and was named by Kruyt and Bungenberg de Jong in 1929 while examining the coacervation process in the gum Arabic and gelatin *[116]*.

1.2.8.1 Types of coacervation

The coacervation process is mainly divided into simple and complex coacervation (Scheme 1.3).
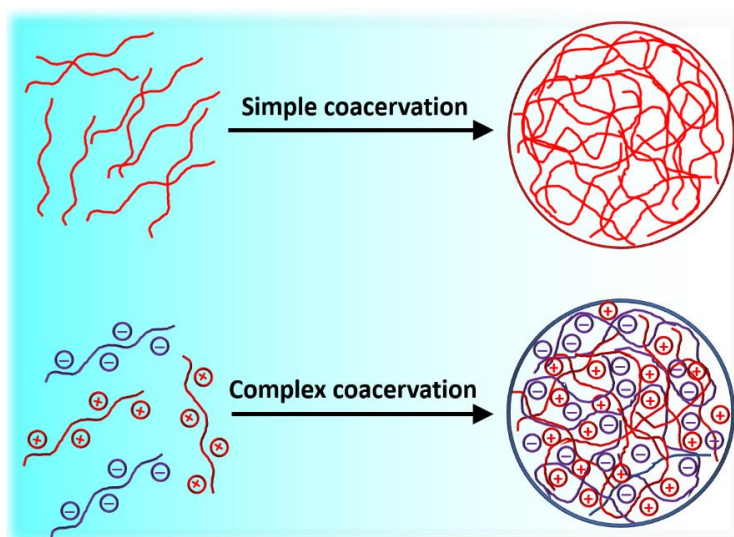
Scheme 1.3. Schematic representation of different types of coacervation.

Simple coacervation is also known as self-coacervation, where only one type of biomolecule, along with additives such as salt, etc., are responsible for the formation of coacervates. In contrast, in complex coacervation, a mixture of different polymers, polyelectrolytes, proteins, RNA, and/or polypeptides undergo LLPS via multivalent intermolecular interactions to form liquid-like coacervates *[117]*. These intermolecular interactions can be electrostatic, π–π, cation–π, hydrogen bonding, and/or hydrophobic interactions *[118–120]*. Two main reasons propel the formation of coacervates: the release of counterions that lead to an increase in entropy and the electrostatic interactions that direct the decrease in enthalpy *[121]*. Complex coacervation is mainly driven by the increase in the translational entropy of the system upon the release of small ions or solvent molecules bound to the polyelectrolytes *[122]*. Notably, the the membraneless architecture of coacervates makes them highly efficient towards bio compartmentalization strategy as they can dynamically exchange materials with intracellular cytosol, sequester various macromolecules, and preserve structural integrity *[123, 124]*. The structural advantages of coacervates have expanded their scope of formation from polysaccharides and proteins to synthetic polymers *[125]*, surfactants *[126]*, nanoparticles *[127]*, polynucleotides *[110, 128, 129]*, and other self-assembled structures *[130–132]*. Altogether, over the years a wide variety of functional coacervates have been developed and utilized for various applications such as food science *[133]*, additives *[134]*, emulsifiers *[134]*, personal care products *[135]*, drug carriers *[128, 136]*, viscosity modifiers *[137]*, cellular biology *[138]*, sensing *[139]*, nano/bioreactors *[125, 139]*, and adhesives *[141]*.

1.2.8.2 Factors affecting coacervation

The coacervation process utilizes weak noncovalent interactions for the formation of coacervates, and once these interactions are broken or disturbed, the coacervates tend to disassemble or precipitate out.

Therefore, factors such as stochiometric ratio, pH, temperature, ionic strength, and aging strongly affect coacervation *[118, 119, 142–145]*.

1.2.8.2.1. Effect of stoichiometric ratio

The stoichiometric ratio defines the relative ratio of different constituents present in the solution. In the complex coacervation process, the stoichiometric ratio of the positive and negative charges of the polyelectrolyte mixture, also known as the charge stoichiometric ratio, is the most crucial parameter that affects the formation of coacervates and also dictates their morphology (Scheme 1.4) *[118]*.

Stochiometric ratio of macroions

Homogeneous binary solution — Clear solution — First turbid point — Precipitate — Second turbid point — Clear solution
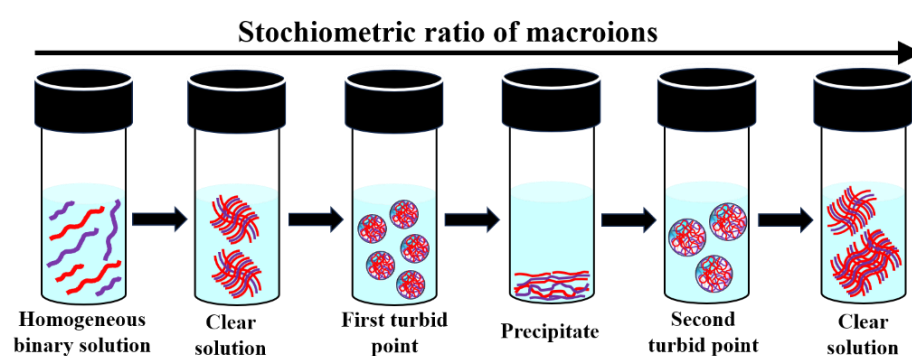
Scheme 1.4. Schematic illustration showing the effect of stochiometric ratio of macroions for coacervation.

The electroneutrality between the positive and negative charges, which occurs in a very narrow range of stochiometric compositions, is critical for the coacervation. Notably, this narrow range can be expanded by adding different concentrations of appropriate salts *[120]*.

1.2.8.2.2. Effect of pH

The pH of the solution plays a critical role in coacervation. Alteration in pH can tune the degree of ionization of typically small molecule ions or weak polyelectrolytes, which further affects the electrostatic interactions between molecules and hence this property varies as a function of pH (Scheme 1.5). The pH response of a singly charged acidic group can be defined by the negative logarithm of the acid dissociation constant or pK_a value. When the pH of the solution becomes equal to the pK_a value, half of the molecules will be

protonated and half will be charged. The number of charged groups will increase upon increasing the pH value above pK_a for the acidic groups like carboxylates. Similarly, for the basic groups like amines, the number of charged groups will increase upon a decrease in the pH value below pK_a. A similar approach can also be applicable for the base dissociation constant or pK_b. In the case of complex macromolecules isoelectric point or pI is the best parameter to define the electroneutrality of multiple charged protein. When the pH of the solution is above or below the pI, a protein bears a net negative or positive charge, respectively.

$$pH < pK_a$$
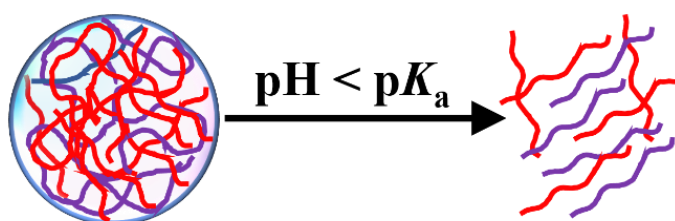
Scheme 1.5. Schematic illustration showing the effect of pH on coacervation.

For instance, Mann and coworkers fabricated pH-responsive coacervate droplets using poly(diallyldimethylammonium)chloride and dipeptide *N*-fluorenyl-9-methoxy-carbonyl-*D*-alanine-*D*-alanine and found that upon decreasing the pH of the medium, coacervate droplets converted into supramolecular hydrogel *[146]*. Similarly, Xiao and coworkers examined the pH-dependent morphological changes of *O*-carboxymethyl chitosan and gum Arabic droplets *[147]*. They observed that upon an increase in the pH of the solution, the network structure became more regular and showed smaller pore sizes *[147]*. Bohidar and coworkers explored the phase behavior of gelatin A/pectin binary mixture *[148]*. Here, they observed that at pH<*p*I, electrostatic interactions were found to be dominant, whereas at pH>*p*I, no such interactions were found. Recently, Mukherjee and coworkers fabricated QD-embedded coacervates via the LLPS between MSA-capped CdTe QDs and PDADMAC *[149]*. They observed that these coacervates were highly pH-responsive and upon a decrease in the pH

of the solution below the pK_a of MSA (~ 4.5) these droplets disassemble. Notably, the droplets showed excellent stability above the pK_a value of MSA in the range of 5–11.

1.2.8.2.3. Effect of ionic strength

The stability of coacervates is strongly influenced by the ionic strength of the medium (Scheme 1.6). The presence of low salt concentration in the system can facilitate the formation of coacervates by modulating the extent of electrostatic attraction between the polyelectrolytes and allowing extrinsic charge compensation to trigger molecular rearrangement. However, the high salt concentration inhibits the coacervate formation and disfavors the entropic release of bound counterions. Notably, the critical salt concentration is the concentration of optimum salt at which the LLPS is diminished. However, this concentration is influenced by the valency of the metal ion used. For instance, divalent salts such as $CaCl_2$, Na_2SO_4 etc., have lower critical salt concentration than the monovalent salt NaCl. A significant decrease in critical salt concentration is observed for divalent cations like Ca^{2+} compared to divalent anions like SO_4^{2-} *[120, 150, 151]*. These differences in critical salt concentration may be attributed to the differences in the hardness of constituent ions and the chaotropic or kosmotropic Hofmeister behavior of ions.
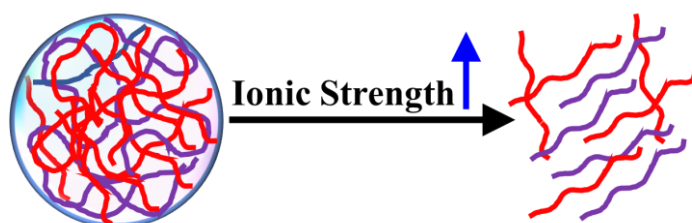
Scheme 1.6. Schematic illustration showing the effect of ionic strength on coacervation.

For instance, Tirrell and coworkers utilized a poly(acrylic acid/poly(allylamine) (PAA/PAH) system to explore the effect of ionic strength on the coacervation process *[143]*. Here, at low concentrations of PAA and PAH in the presence of 100 mM NaCl, no coacervate

formation is observed. However, at higher concentrations precipitation occurred. Subsequently, a limited amount of precipitate and coacervate regions were obtained at 400 mM NaCl. While increasing the NaCl concentration upto 1500 mM, coacervation is observed without precipitation.

1.2.8.2.4. Effect of temperature

The influence of temperature on the coacervation process can be described by a number of pathways (Scheme 1.7). The increased electrostatic dissociation and increased hydrophobic interactions are closely associated with temperature, which is affected by changing the degree of ionization *[134]*. The strong effect of temperature on the coacervate formation depends on the nature of individual molecules, not the self-assembly process (Scheme 1.7).
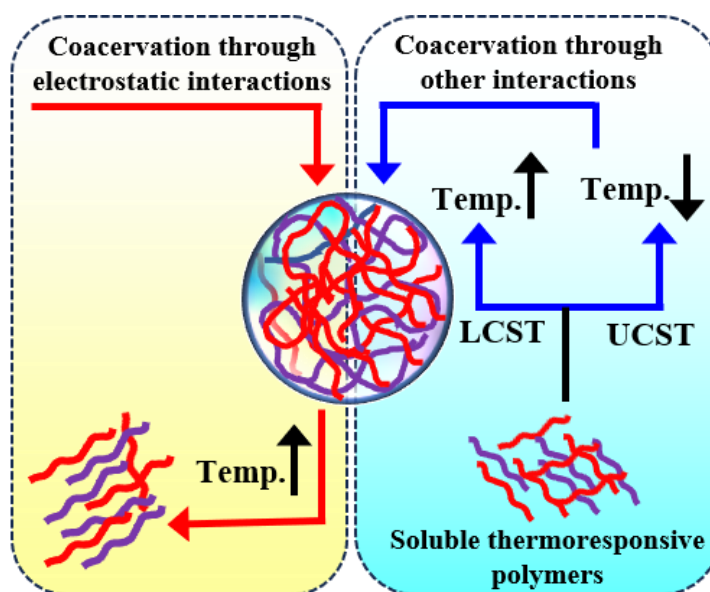
Scheme 1.7. Schematic illustration showing the effect of temperature on coacervation.

The electrostatic interaction between polyelectrolytes decreases with increasing temperature. On the other hand, the thermoresponsive polymers can either show a lower critical solution temperature (LCST) or an upper critical solution temperature (UCST). In the LCST region, a polymer is entirely soluble at lower temperatures and phase separation occurs upon heating, which is generally driven by entropic

factors. However, in the UCST region, the polymer is completely soluble at higher temperatures, and phase separation occurs upon cooling, where the interaction between polymer-polymer and solvent-solvent is dominant.

For instance, Geest and coworkers reported thermoresponsive polymer formed from poly(*N*-(2-hydroxypropyl) methacrylamide-glycolamide) (poly(HPMA-GA)) *[152]*. This polymer showed coacervation at lower temperatures due to the dominating hydrogen bonding and hydrophobic interactions, and upon increasing the temperature, coacervation stops due to the decreasing hydrogen bonding. Similarly, Yui and coworkers designed a pH- and temperature-responsive coacervate system based on LCST-type polymer *β*-cyclodextrin-threaded polyrotaxane and encapsulated model proteins such as albumin protein (BSA), lysozyme, and galactosidases *[153]*. Here, they observed temperature-induced coacervate formation. While decreasing the pH from physiological condition to pH 5, the polymer readily degrades and thence releases ~80% proteins without any loss in activity after 24 h. Subsequently, Keating and coworkers fabricated thermoresponsive polyU/polyamine coacervate droplets. They found that polyU forms soluble complexes with polyamines at low temperatures due to intramolecular secondary structure and base-stacking interactions. In contrast, the secondary structure gets broken upon heating and converted into a random coil conformation that favors coacervation *[154]*.

1.2.8.2.5. Effect of aging

The liquid-like properties of coacervates make them metastable and undergo a coalescence phenomenon over time *[155]*. The smaller coacervates fuse to form larger coacervates or turn into a bulk/macroscopic coacervate phase over time (Scheme 1.8).

Time
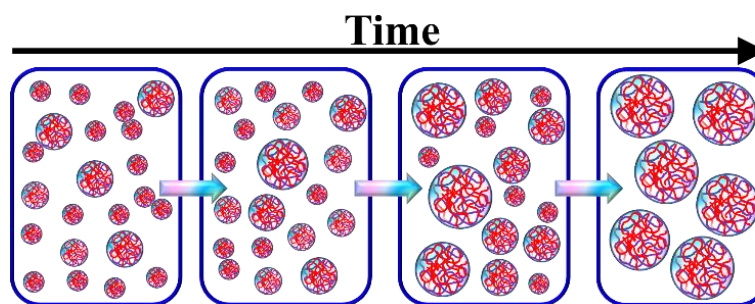
Scheme 1.8. Schematic illustration showing the effect of aging on coacervation.

The coalescence phenomenon changes the dynamics of the coacervate phase and can even lead to the precipitation of coacervates. Moreover, the coacervation between oppositely charged polyelectrolytes can even form hydrogel over an extended incubation period *[146]*. Notably, the coalescence phenomenon can be accelerated by centrifugation at high rotation per minute *[156]*.

1.2.8.3. Type of membraneless coacervates

Coacervates can be mainly classified into biomolecular coacervates, organic coacervates, and hybrid coacervates. In the present thesis, we have primarily focused on synthetic organic and hybrid coacervates.

1.2.8.3.1. Organic coacervates

The LLPS of organic macroions, including polyelectrolytes, biopolymers, amphiphilic polymers, surfactants, and dendrimers, form synthetic coacervates via noncovalent interactions in aqueous medium (Scheme 1.9). Organic coacervates have gained massive attention due to their membraneless architecture and role in artificial protocell research *[109, 110, 157–162]*. Previously, Mann and coworkers reported a new variety of membraneless protocells formed from low-molecular-weight mononucleotides and simple cationic peptides *[109, 110]*. They observed that these molecules spontaneously undergo LLPS to form stable microdroplets in a wide range of temperatures and salt concentrations. Moreover, these coacervates selectively sequester foreign materials such as nanoparticles, porphyrins, enzymes, etc., and have been utilized toward efficient oxidase-like activity, light-

harvesting molecules, and enhanced rates of glucose phosphorylation, respectively *[109, 110]*.
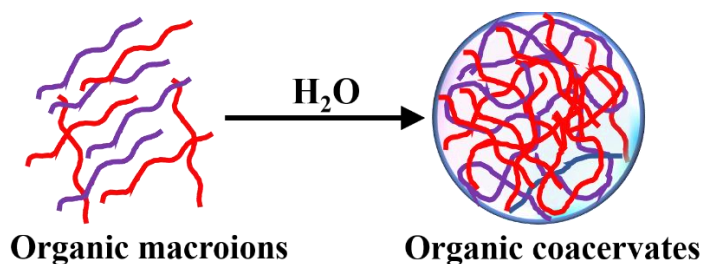
Scheme 1.9. Schematic illustration of the formation of organic coacervates.

Berret and coworkers observed complexation between the positively charged polymer poly(diallyldimethylammonium) (PDADMAC) and a negatively charged polymer sodium polyacrylate (PANa) via a two-step process *[163]*. They further demonstrated that the formation of coacervates generally follows a two-step behavior in thermodynamic titration which is a kinetically controlled process that starts only after the polyelectrolyte complex formation. Mello and coworkers reported the formation of coacervate droplets from PDADMAC with either carboxymethyl-dextran or adenosine triphosphate (ATP) by using a microfluidic flow-focusing system *[164]*. Notably, the coacervate droplets formed using a microfluidic system are in a narrow size range with improved stability compared to the conventional vortex dispersion technique *[164, 165]*.

In another work, Chapel and coworkers reported a comparative structural difference between the phase separation in PDADMAC/PANa and PDADMAC/PSSNa systems *[166]*. They observed that the systems undergoing weak interactions, like in the case of PDADMAC/PANa, undergo liquid-liquid phase separation, resulting in coacervate formation. In contrast, systems with highly electrostatic interactions, like PDADMAC/PSSNa, tend to form solid aggregates via liquid-to-solid phase transition. Similarly, Bian and coworkers reported the formation of polyethyleneimine/thioctic acid (PEI/TA) coacervates and utilized the hydrophobic aggregation of TA

molecules and strong electrostatic interaction between PEI and TA for the in situ conversion of PEI/TA coacervates into a hydrogel without any external stimuli *[167]*. Furthermore, they utilized this robust bulk adhesion and enhanced matrix cohesion for water repulsion and wound healing. Similar works have been carried out to study the formation of coacervate hydrogels and utilized for various applications *[168–170]*.

Previously, it has been observed that the concentration of various ions, salts, and also the valency of polyions affects the formation of coacervates. For instance, Schlenoff and coworkers demonstrated the unique role of concentration and position of co-ions and counterions in the formation of PDADMAC and poly(styrene sulfonate) coacervate droplets *[171]*. Tirrell and coworkers utilized the ternary coacervates system of poly(allylamine)hydrochloride (PAH) or branched poly(ethyleneimine) (PEI) with poly(acrylic acid) (PAA) and poly(*N*,*N*-dimethylaminoethyl methacrylate) (PDMAEMA) to demonstrate the increase in salt resistance of ternary coacervates compared to the binary coacervates of PAA/PDMAEMA *[172]*. Keating and coworkers studied the role of lower, more prebiotically relevant multivalency of adenosine mono-, di-, and triphosphate nucleotides on the functional performance of coacervates as membraneless compartments. *[173]*. They observed that the coacervates formed from the shorter polyions can accumulate RNA, generate distinct pH microenvironments, and preserve duplexes more effectively than those formed by the longer polyions.

While a wide range of coacervates are studied using polyelectrolytes and polynucleotides, the complex coacervation between polymers, polynucleotides, and surfactants has also been explored extensively *[174–178]*. For example, Moulik and coworkers utilized an amphiphilic surfactant sodium N-Dodecanoylsarcosinate (SDDS) and polycationic hydroxyethyl cellulose to study the formation of coacervates *[174]*. Furthermore, they explored the nature of interactions between different species and subsequently examined the concentration-dependent phase transition from complexation to

aggregation and finally to coacervation *[174]*. In a similar study, Miyake and coworkers studied the electrostatic interaction-driven coacervation between oppositely charged anionic surfactants and cationic polymers to explain the role of molecular structures and concentration on the coacervation process in shampoos and body wash *[176]*. Douliez and coworkers explored the possibility of complex coacervation between cationic surfactants like cetylpyridinium chloride (CPCl) or cetyltrimethylammonium bromide (CTAB) with decanoic acid in the pH range of 4.0 to 8.0 in the presence of different salts *[178]*. They further explored the properties of these coacervates for the encapsulation of biomolecules such as DNA, enzymes, organic dyes, and polysaccharides.

Although synthetic organic coacervates have many advantages over other self-assembled structures, the absence of any optically active unit embedded inside their architecture limits their applicability as sensors for detecting pollutants, bioimaging agents, catalysis, photocatalysis, etc. To overcome these limitations, a new class of hybrid coacervates with enhanced optoelectronic properties has emerged recently.

1.2.8.3.2. Hybrid coacervates

The synthetic hybrid coacervates are formed via the simple mixing of oppositely charged organic polyelectrolytes and inorganic nanoparticles (NPs) such as metal clusters, polyoxometalate, quantum dots, carbon dots, etc., in the aqueous medium (Scheme 1.10). The electrostatic attraction between the oppositely charged inorganic and organic counterparts, as well as the entropy change from the release of counterions and water of solvation near polyelectrolytes and nanoparticles, are identified as the primary force driving the formation of synthetic coacervates *[179–181]*. Previously, researchers have extensively studied the interactions of oppositely charged NPs with polymers or polyelectrolytes and recorded some unique observations *[182]*.
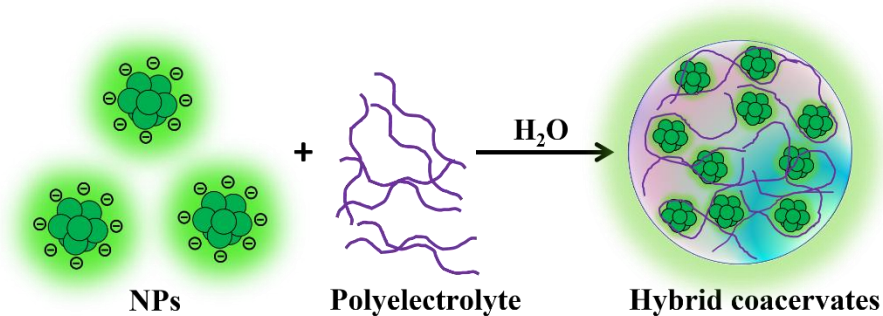
Scheme 1.10. Schematic illustration of the formation of hybrid coacervates via LLPS of inorganic NPs and organic polyelectrolytes.

Earlier, Berret and coworkers studied the interactions between cationic-neutral block copolymers and highly charged anionic cerium oxide (CeO_2) nanoparticles *[183]*. They observed core-shell aggregates of around 100 nm, and the cryo-TEM showed an accumulation of nanoparticles inside the core, possibly through the complexation of the polyelectrolyte blocks by the surface charges. Similarly, Zhu and coworkers demonstrated the complex coacervation between inorganic polyoxometalate (POM) polyanions and net neutral zwitterionic poly(sulfobetaine methacrylate) (PSBMA) in LiCl aqueous solutions *[184]*. Furthermore, they demonstrated that hybrid macroion coacervation is a facile approach to integrate the unique functions and enhance the material properties of different materials into functional nanocomposites for applications in various fields such as catalysis, nano-medicines, drug delivery, etc. In another study, Zhu and coworkers reported that high-density inorganic polyoxometalate (POM) shows a faster phase-separation rate in the presence of zwitterionic polyampholytes to form hybrid coacervates *[185]*. They further utilized their high loading capacity for methylene blue (MB) to effectively remove MB from contaminated water *[185]*. Although these earlier reports demonstrated interactions between oppositely charged polyelectrolytes and NPs, they failed to discuss the inherent properties of coacervates such as membraneless architecture and their ability to sequester a wide range of foreign materials such as

biomolecules, proteins, dyes, etc. Furthermore, these reports lacked any in-depth morphological characterizations for these coacervates.

Recently, Mukherjee and coworkers demonstrated the formation of a new class of organic-inorganic hybrid coacervates by utilizing stoichiometric amounts of anionic CdTe quantum dots (QDs) and cationic PDADMAC [49]. These hybrid coacervates were found to be perfectly spherical droplets with intrinsic green/red emission observed from their interior due to the entanglement of emissive CdTe QDs inside their architecture. Furthermore, they were found to be colloidally stable over a broad range of composition, pH, time, and ionic strength. These hybrid coacervates not only retain the intrinsic properties of organic coacervates but also possess the material properties of CdTe QDs. The droplets were found to be two-photon active, and their membraneless architecture was utilized to sequester a wide range of biomolecules such as HSA, BSA, FITC, Nile blue, and Rh6G. In their subsequent study, Mukherjee and coworkers utilized the negatively charged carbon dots (CDs) and positively charged PDADMAC to form biocompatible CDs-embedded hybrid coacervates and made use of these coacervates for theranostic applications [180]. In the present thesis, we have explored the optoelectronic properties and the role of different NP-embedded hybrid coacervates for various applications such as environmental remediation Hg^{2+}, photocatalytic conversions, and dye degradation. Herein, we have also developed a new type of hybrid plexcitonic coacervates and explored them as a new class of nanozymes for their enhanced peroxidase-like activity. The integrated bio-platform of plexcitonic coacervates with glucose-oxidase (GOx) has also been utilized for the detection of glucose.

The synthetic architecture of hybrid coacervates mainly includes charged nanoparticles like QDs, CDs, etc., and organic polyelectrolytes such as PDADMAC, poly-l-lysine, etc. A brief discussion about the constituents of hybrid coacervates used in the present thesis work are discussed below,

1.2.8.3.2.1. Quantum dots (QDs)

Over the last few decades, QDs have garnered significant attention due to their unique optoelectronic properties *[186]*. The term "quantum" in quantum dot describes the confinement of excitons or the electron-hole pair of QDs in all three spatial dimensions *[187]*. The average distance between an electron and the hole is known as the exciton Bohr radius. When the size of the QDs is less than its exciton Bohr radius, the energy bands become discrete due to the quantum confinement effect *[188]*. QDs exhibit size-dependent properties, such as a simple increase in the reaction time; one can easily tune the size and optoelectronic properties of QDs. Notably, as the size of the QDs increases, a bathochromic shift is observed in their absorption and emission spectrum. They exhibit broad excitation spectra, narrow emission, high PL QY, and better stability against photobleaching compared to organic dyes *[189]*. Among all others, CdX QDs (X= Te and Se) have attracted significant attention due to their tunable and stable PL properties in the visible-NIR region *[190–193]*.

CdTe QDs are well-explored semiconductor material among II–VI groups, with a narrow band gap (~1.5 eV) and a large exciton Bohr radius of 7.3 nm, making them widely applicable in a wide range of fields *[194]*. They are crystalline and emit in the broad electromagnetic spectrum range of 450 to 700 nm with excellent quantum yield (QY) of 20–85% *[194, 195]*. Furthermore, they can be synthesized in both aqueous and organic mediums simply by tuning the surface functionization and ligand engineering. The commonly used ligands for the aqueous synthesis of CdTe QDs are thiol-containing compounds such as mercaptosuccinic acid (MSA), thioglycolic acid (TGA), 3-mercaptopropionic acid (MPA), glutathione (GSH) and cysteine (CYS) *[196, 197]*. In this thesis, we have studied the optoelectronic properties of MSA-capped CdTe QDs using various spectroscopic and microscopic techniques. We have also investigated the self-assembly of anionic CdTe QDs with a cationic polymer, PDADMAC for the formation of QD-embedded coacervates (QD-Ds)

and studied their role in environmental remediation and photocatalytic transformations.

1.2.8.3.2.2. Carbon dots (CDs)

CDs are the optically active members of the carbon family with sizes ranging from 2-10 nm. They are mainly synthesized through bottom-up approaches, such as hydrothermal and microwave methods *[198]*. They are primarily amorphous with an aromatic sp^2 hybridized carbon core and aliphatic carbon atoms *[199, 200]*. They exhibit strong absorption peaks in the UV region and are highly stable towards photobleaching. With their remarkable optoelectronic properties, tunable fluorescence, small size, excellent water solubility, cost-effectiveness, biocompatible nature, and easy-to-tune surface functionalization, they have been proven helpful in a diverse range of applications such as drug delivery *[201–203]*, bioimaging *[204–206]*, biosensing *[207, 208]*, optoelectronics *[209, 210]*, photovoltaics *[211]*, catalysis *[212, 213]*, and anticounterfeiting *[214]*. Furthermore, their non-toxic nature makes them an excellent probe for live cell imaging. In this thesis, we have synthesized negatively charged CDs from citric acid and ethylene diamine via a simple hydrothermal method and utilized them for the fabrication of CD-embedded coacervate (CD-Ds). We have studied the photophysical properties of CDs and CD-Ds using various spectroscopic and microscopic techniques and further utilized them to study the photocatalytic conversion of ferricyanide to ferrocyanide.

1.2.8.3.2.3. Gold NPs (Au NPs)
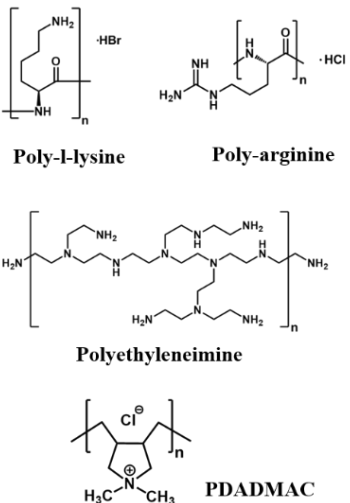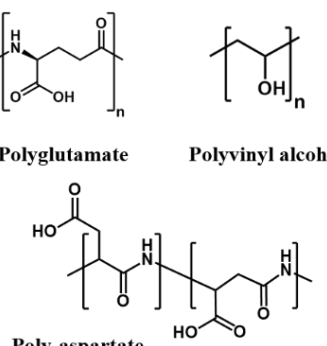
Au NPs are metal NPs with wine-red to brown color depending upon their size *[215]*. The remarkable physical and optical properties of Au NPs are attributed to their small size and the large surface-to-volume ratio *[216]*. In fact, the properties of Au NPs can be controlled by changing their size and shape. One of the unique size-dependent optical properties displayed by Au NPs is localized surface plasmon resonance (LSPR). Plasmons are the unsaturated/free electrons present

at the surface of metal NPs such as Au NPs, Ag NPs, Cu NPs, etc. Notably, these surface plasmons interact with the electromagnetic field of the incident light. This results in coherent localized oscillation of the electron density with a resonant frequency that depends upon the size and shape of NPs as well as the dielectric of metal and surrounding medium [217]. The LSPR band of metal NPs can be tuned from visible to near-infrared regions by varying the size of the NPs; this makes them highly suitable for a wide range of applications such as catalysis, biomedical, sensing, etc. For example, Aptamer-conjugated Au NPs have been used to detect lymphoma cells with very high sensitivity [218]. Au NPs have also been utilized for drug delivery and gene regulation [219].

Previously, the optoelectronic properties of Au NPs and their composites have been utilized for various catalytic, photocatalytic, and enzymatic transformations [220-224]. Jain and coworkers studied the role of electrostatics over the surface of Au NPs toward the reduction of various charged substrates. Notably, modulation of the surface charge of Au NPs via ligand engineering was found to be an effective way to regulate their catalytic activity for various transformations [221]. Chen and co-workers observed that bare Au NPs possess enhanced peroxidase-like activity compared to that of ligand-capped Au NPs and further utilized it for ultrasensitive detection of Ce^{3+} [222]. The ligand-free surface of Au NPs was found to be responsible for effective redox recycling of electrons from Ce^{3+} resulting in enhanced peroxidase-like activity. In a similar study, Yang and co-workers fabricated a zero-dimensional/two-dimensional bimetallic nanocomposite of Au/Pd using galvanic displacement for enhanced peroxidase-mimic catalysis by utilizing the increased surface area and modified electronic structure of palladium nanosheets [223]. In the present thesis, we have fabricated a new class of hybrid plexcitonic assembly via the in situ synthesis of Au NPs inside QD-Ds and studied their peroxidase-like activity.

1.2.8.3.2.4. Polyelectrolytes

Polyelectrolytes are macromolecules with repeated units that can dissociate in ionizing solvents (e.g., water), yielding a highly charged polymeric chain with either positively (polycation) or negatively (polyanion) charged units. Previously, various polyelectrolytes *[225]* with varied charges, such as poly(diallyldimethylammonium chloride) (PDADMAC), poly(sodium styrene sulfonate) (PSS), polyacrylic acid (PAA), polyethyleneimine (PEI), poly-l-lysine (PLys), etc. have been utilized for simple as well as complex coacervation (Scheme 1.11). One of the most common polyelectrolytes utilized to form coacervates is PDADMAC. It is a water-soluble cationic polymer with quaternary ammonium groups on the rings of the polymer backbone. The positive charge on PDADMAC remains unchanged, irrespective of the pH of the solution, which makes it highly useful for self-assembly processes. The complexation between PDADMAC and different oppositely charged polyelectrolytes is well explored in the literature *[119, 154, 226, 227]*.

Scheme 1.11. List of some cationic and anionic polyelectrolytes.

In this thesis, we have investigated the spontaneous formation of complex coacervates in the binary mixture of QDs/CDs with

PDADMAC in the aqueous medium and utilized them for various applications.

1.2.8.4. Applications of coacervates

Coacervates are well known for hosting various chemical reactions inside their membraneless architecture. Their excellent sequestering ability towards various biomolecules, enzymes, proteins, and other essential materials makes them highly useful in many scientific fields and industries. They have been utilized extensively as drug carriers *[228, 229]*, additives *[230]*, wastewater treatment *[231, 232]*, emulsifiers *[233, 234]*, cosmetics *[235]*, viscosity modifiers *[236]*, storage agents *[237]*, food formulations *[238, 239]*, adhesives *[240, 241]*, and scaffolds for synthesizing nanomaterials *[242]*. Some of the recent utilization of coacervates for various applications are listed below (Scheme 1.12).
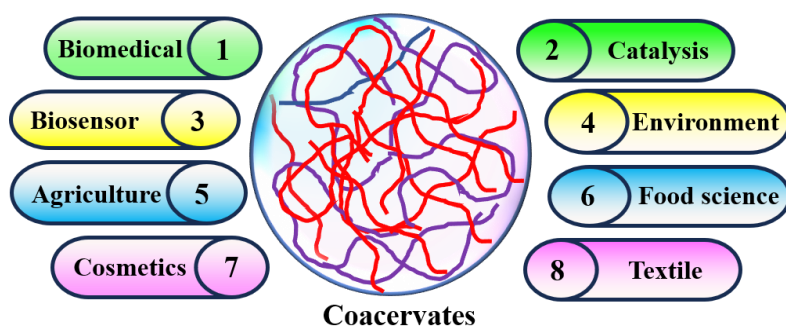
Scheme 1.12. Applications of membraneless coacervates.

Previously, the membraneless architecture and high sequestration efficiency of coacervates have been utilized to extract and separate various compounds from aqueous systems *[185, 243–245]*. For instance, Wang and coworkers utilized cationic gemini surfactant hexamethylene-1,6-bis (dodecyl dimethylammonium bromide) and polyacrylamide (HPAM, 10% hydrolyzed) at neutral conditions to form complex coacervates *[243]*. Preferable adsorption toward negatively charged methyl orange was observed compared to the positively charged methylene blue, with an extraction efficacy of >95% due to various synergistic interactions. Gradzielski and coworkers highlighted the role of pH-sensitive chitosan/surfactant

coacervates toward the efficient removal and subsequent recovery of dye contaminants from aqueous solution *[244]*. In a similar study, Zacharia and coworkers utilized three different sets of complex coacervates and compared their sequestration efficiency for MB *[245]*. The complex coacervates from polyethylene imine/poly(4-styrenesulfonic acid) showed the highest extraction efficiency (>80%) compared to other coacervate systems. These results highlighted the importance of introducing strong π-π interactions inside the coacervates along with electrostatic and hydrophobic interactions to improve the extraction efficacy of targeted compounds from the solution mixture.

The membraneless architecture of coacervates has also been extensively utilized as stimuli-responsive delivery systems for the controlled release of various drugs and biomolecules. Notably, encapsulating biomolecules, such as drugs, enzymes, proteins, etc., inside the scaffold of coacervates increases their solubility in water, improves shelf-life, and protects them from external denaturants *[109, 246–248]*. For instance, Kim and coworkers formulated biocompatible coacervates with Heparin and positively charged poly(ethylene argininylaspartatediglyceride) (PEAD), which shows good bioactivity and acts as an efficient carrier for growth factor (GF) with high loading efficiency (>90%) *[249]*. They show a sustained release with an increased half-life and a decreased administration of dose frequency. The heparin/PEAD coacervates and composites such as hydrogels have been extensively utilized to deliver GF for wound healing, bone regeneration, heart repair, etc *[249]*. Notably, a large number of studies have been undertaken to develop stimuli-responsive coacervates for the delivery of essential biomolecules, proteins, enzymes, and drugs such as insulin, ibuprofen, etc. *[250–253]*.

Perriman and coworkers reported a new approach to delivering biomolecular payloads like proteins, oligonucleotides, and molecular dyes to specific positions of stem cell membranes with high spatial precision using ATP/PDADMAC coacervates *[254]*. In another study, they designed biocompatible and biodegradable amylose-based

coacervate microvectors, which interacted spontaneously with the plasma membrane of human mesenchymal stem cells to release the sequestered payloads *[255]*. Bian and coworkers designed the nanoparticle-based hybrid coacervates via hydrogen bonding-driven self-assembly *[256]*. The coacervates were found to be an excellent drug delivery vehicle and bioadhesive. They further depicted sustained drug release in the rat acute colitis model compared with the oral administration of the same amount of drug in solution form. Lehr and coworkers synthesized starch nanoparticles through a coacervation process and utilized it for the pulmonary delivery of proteins such as insulin, IgG1, RNAse, etc. *[257]*. In recent work, Mann and coworkers designed light-responsive coacervates from double-stranded DNA and *trans*-azobenzene trimethyl ammonium bromide *[258]*. They demonstrated the disassembly and assembly of these coacervates via trans/cis photoisomerization of azobenzene upon UV and blue light irradiation. Notably, a faster trans-to-cis isomerization was observed at high temperatures.

Coacervate-based systems have also been utilized in the food industry. Microencapsulation of food systems has various benefits, including masking disagreeable odors or tastes, extending shelf life, preserving delicate agents in harsh environments, and easy handling and transportation *[259–261]*. Recently, coacervate-based systems have proven to be suitable for microencapsulating hydrophobic substances. Vanillin, a major flavor component of dairy products, has a volatile nature and a short shelf life, which makes its transport and storage very complicated. Recently, Rafe and coworkers first generated an inclusion complex of β-cyclodextrin with vanillin and subsequently encapsulated this inclusion complex using rice bran protein and flaxseed gum coacervates *[259]*. This strategy substantially decreased the degradation rate of vanillin, with the initial amount of vanillin staying at 75% after 30 days at room temperature. In another interesting study, Fávaro-Trindade and coworkers demonstrated the microencapsulation of aspartame using double emulsion followed by the complex coacervation of gum Arabic and gelatin to improve its

heat resistance *[260]*. Ponce-Alquicira and coworkers studied the microencapsulation of an antimicrobial peptide, nisin, and antioxidant from avocado peel extract inside the coacervates of collagen formed with pectin/alginate *[261]*.

In the present thesis, we have utilized the NP-embedded coacervates for environmental remediation, photocatalytic transformations, and enzyme catalysis. We have also studied the role of the charged aqueous interface of micelles in the photocatalytic conversion of arylamines to azoaromatics.

1.3. Environmental remediation

Environmental remediation is the monitoring and cleanup of hazardous contaminants via detection, removal, treatment, or containment of various pollutants from the biosphere, such as land, water, and air. The increasing environmental pollution has disrupted the balance of the biosphere, and the highly polluted air and water bodies make it unsuitable for sustaining marine and terrestrial life in the long run *[262]*. The present condition makes the facile detection and efficient removal of environmental contaminants of primary importance for a clean and healthier environment. Previously, researchers have extensively utilized various metallic, inorganic, polymeric, and carbon-based materials for the remediation of various hazardous pollutants such as pesticides, pharmaceuticals, dyes, halogenated herbicides, chlorinated and volatile organic compounds *[263–267]*. Optically active nanoreactors have garnered immense interest in the past few decades because of their unique microenvironment and robust structure. Their ability to accommodate multiple catalytic sites in a confined volume has made them highly effective for the detection, removal, and degradation of a wide range of pollutants *[268–278]*. However, most of the earlier reported systems often lack in-built optically active (OA) centers for harvesting visible light, and the externally incorporated OA materials, such as NPs often undergo unwanted agglomeration inside these nanoreactors, which hinders their efficiency and reusability. Hence, accommodating multiple OA sites inside the confined architecture of nanoreactors remains a crucial

challenge. To overcome this challenge, we have developed a new type of intrinsically optically active nanoreactors by integrating optically active NPs inside the polymer matrix via a simple process of complex coacervation. The NP-embedded complex coacervates exhibit a membraneless architecture and have been utilized for the efficient detection and removal of Hg^{2+}, a well-known hazardous heavy metal. These hybrid coacervates were also used for the photocatalytic degradation of model pollutant dyes, rhodamine b (RhB) and methylene blue (MB).

1.4. Photocatalysis

Photocatalysis was first mentioned in 1911 by Dr. Alexander Eibner, a German chemist *[279]*, who integrated the concept of his research on the irradiation of zinc oxide for the bleaching of Prussian blue, a dark blue pigment. In simple terms, photocatalysis is carrying out a chemical reaction in the presence of a catalyst activated by light, where the excited state of the catalyst interacts with the substrates, converts them into products via appropriate intermediates, and regenerates itself after each catalytic cycle *[280]*. Photocatalysis can be classified into two main categories: heterogeneous and homogeneous photocatalysis. In heterogeneous photocatalysis, the catalyst is in a different phase from that of the reactants. In contrast, the reactants and the catalysts exist in the same phase in homogeneous photocatalysis. Another type of photocatalysis is plasmonic antenna-reactor photocatalysis, where the catalyst is combined with an antenna that increases the ability of the catalyst to absorb light, thereby increasing its efficiency *[281]*.

Over the last few decades, photocatalysis has become an efficient tool for synthesizing industrially essential compounds, combating pollution, averting energy crises, medical treatment, etc., *[47–51, 212, 213, 263–267]*. However, constant advancement in the field of photocatalysis is vital for a better and sustainable future. In this context, efficient visible light harvesting for generating charge carriers and their fruitful utilization for chemical transformations is essential *[220, 221, 224, 282]*. Toward that end, photocatalytic nanoreactors with multiple catalytic units embedded inside their architecture hold

great promise for the efficient utilization of visible light toward chemical and enzymatic transformations. Notably, the confinement of catalysts and substrates inside a small volume of nanoreactor alters their chemical reactivity, which results in enhanced reaction kinetics and better conversion yields *[283]*. For instance, Fang and co-workers utilized the porous structure of an anionic coordination cage for photocatalytic degradation of methylene blue in the presence of a ruthenium complex *[283]* The sequential encapsulation of both a dye and catalyst inside the confined structure of the coordination cage overcomes the charge repulsion between the positively charged catalyst and methylene blue, which in turn significantly enhance their interactions, thus enhancing its photocatalytic activity. Similarly, Kim and coworkers demonstrated efficient photocatalytic hydrogenation of olefins at the confined interfaces of MOFs and COFs using platinum NPs *[277]*. In the present thesis, we have utilized the NP-embedded coacervates as photocatalytic nanoreactors to carry out the visible-light-driven photoredox conversion of ferricyanide to ferrocyanide and photocatalytic degradation of RhB and MB.

We have also utilized the CAI of CTAB micelle to host Eosin Y (EY), a well-known organic dye molecule, and modulate its photocatalytic efficacy towards the photo-oxidative coupling of arylamines to azoaromatics in aqueous medium. EY has many industrial applications such as pH indicator, staining agent in cells, and dye pigment *[284–286]*. EY exhibits excellent photophysical properties, which has led to its comprehensive utilization as a photoredox catalyst in organic synthesis for a wide range of organic transformations *[284, 285]*. EY is comparatively cheaper, easy to handle, less toxic, and even outperforms some commercially available inorganic and organometallic catalysts in some aspects *[287–289]*.

Azo compounds are an essential class of organic molecules that have a wide range of applications in molecular switches *[290]*, optical storage *[291, 292]*, and other industrial applications *[293]*. Previously, researchers have developed several strategies for the synthesis of azo compounds, and among them, the diazotization of primary aromatic

amines in the presence of sodium nitrite and hydrochloric acid is the traditional pathway that generates unstable diazonium intermediates, unwanted waste and requires careful handling *[294]*. Recently, various catalysts have been utilized for the synthesis of azo compounds from nitroarenes and aromatic amines by both thermal and photocatalytic approaches *[295–303]*. However, most of these earlier works require high temperatures, expensive catalysts, and organic solvents. Moreover, they suffer from poor selectivity, slow kinetics, and moderate to low yields. To overcome this challenge, we utilized the charge aqueous interface of CTAB micelles to host a cost-effective organic photocatalyst EY and utilized the EY@CTAB assembly to carry out the photocatalytic oxidative coupling (POC) of arylamines to azoaromatics in aqueous medium under ambient conditions.

1.5. Enzyme catalysis

Enzymes are biomolecules/proteins that act as catalysts to accelerate the reaction rate of a biochemical reaction by lowering the activation energy. Nature utilizes enzymes to drive and boost a variety of biochemical reactions inside the intracellular environments via spatiotemporal regulation. Almost all the metabolic processes in the Cell utilize enzyme catalysis to occur at rates fast enough to sustain life *[304]*.
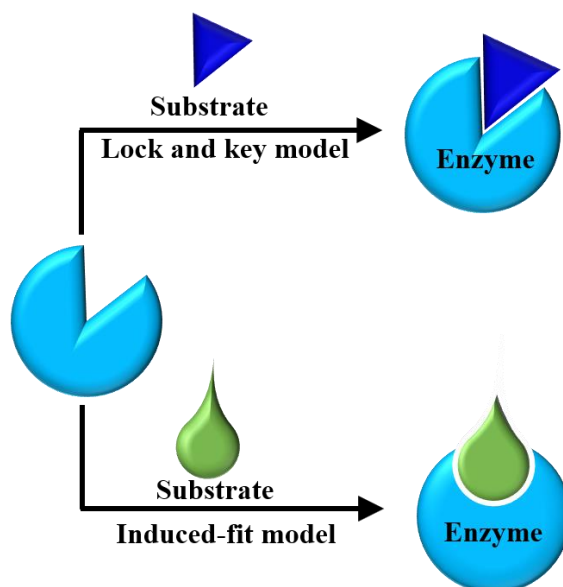
Scheme 1.13. Schematic illustration of different models of substrate-enzyme binding.

35

Like all other catalysts, enzymes do not affect the equilibrium constant nor get consumed during the reaction. The enzyme-substrate interactions can be classified into two main categories: (1) Lock and key model and (2) Induced fit model *[305]* (Scheme 1.13). The lock and key model was given by Emil Fisher in 1898, which stated that the active site of an enzyme can only be occupied by a substrate with a fixed composition and shape that binds perfectly to the active site. Here, the enzyme's active site is highly specific to the surface of the substrate. However, the induced fit model proposes that the shape of the active site within enzymes is malleable and can be induced to fit the substrate through the conformational changes in the active site to make it suitable for a better fit for substrate binding.

The tremendous potential of enzymes as catalysts has been recognized in organic synthesis in both basic sciences and industrial applications *[306−308]*. However, due to the fragile nature of these biocatalysts, immobilized enzymes often suffer from various issues, such as long-term stability, thermal and chemical stability, and recyclability. The extensive role of naturally occurring enzymes, even in our day-to-day life, has attracted much attention toward developing artificial nanozymes with comparable or better enzymatic activity with improved stability. Nanozymes are artificially synthesized nanomaterials that possess inherent enzyme-like activities *[309]*. Artificial nanozymes are much more efficient than naturally occurring enzymes as they possess tuneable enzyme-like activity, are cost-effective, more stable even in harsh environmental conditions, and can be easily mass-produced. These advantages have prompted extensive investigations of different nanomaterials towards their intrinsic enzyme-like activities, such as oxidase *[310]*, peroxidase *[311]*, superoxide dismutase *[312]*, and catalase *[313]*. Nanozymes with inherent peroxidase-like activity have especially been of great interest due to their wide range of clinical and bioanalytical chemistry applications. These nanozymes carry out the oxidation of various colorimetric substrates such as 3,3′,5,5′-tetramethylbenzidine (TMB),

o-phenylenediamine (OPD), dopamine, and 2,2-azino-bis-(3-ethylbenzothiazoline-6-sulfonic acid) (ABTS) in the presence of H_2O_2 either via Fenton-like mechanism or fast electron transfer pathway. The colorimetric assays of these nanozymes make them highly applicable for fabricating various simple, rapid, cost-effective immunoassays and biosensors.

Till date, different nanomaterials of transition metal oxides and chalcogenides (Fe_3O_4, MoS_2, CeO_2, CuO, FeS_2, etc.), noble metals (Ag, Au, Pt, Pd), carbon nanomaterials, and metal-organic frameworks (MOFs) have been found to possess intrinsic peroxidase-like activity [314–325]. However, previously known peroxidase mimics show much lower selectivity and catalytic activity than horseradish peroxidase (HRP). Although, metal oxide NPs and carbon nanomaterials are cheaper, they possess comparatively mild peroxidase-like activity. In contrast, noble metal NPs are found to have better or comparable peroxidase-like activity than HRP but are comparatively much more expensive. Recently, researchers have tried multiple methods and exploited different properties of nanomaterials to design a wide range of nanozymes with enhanced enzyme-mimicking activity [314–324]. For instance, Cai and coworkers fabricated a zero-dimension/two-dimension bimetallic nanocomposite using galvanic displacement for enhanced peroxidase-mimic catalysis by utilizing the increased surface area and modified electronic structure of palladium nanosheets [223]. Previously, many reports have discussed the role of confinement of catalysts and substrates on the catalytic efficacy for various chemical transformations [325]. In this thesis, we have designed a new type of nanozyme by utilizing the QD-Ds as a scaffold for the fabrication of a new class of coacervate-based plexcitonic assembly (Au@QD-Ds) and used it to study its intrinsic peroxidase-like activity. Plexcitonic assembly is the integration of excitons of CdTe QDs and plasmons of Au NPs inside the confined architecture of hybrid coacervates. We have also utilized the naturally occurring enzyme glucose oxidase (GOx) to design the GOx-loaded Au@QD-Ds and utilized them for the rapid and selective colorimetric detection of

37

glucose in the aqueous medium and paper strip. Glucose oxidase (GOx) is an oxidoreductase enzyme comprising 605 amino acid residues that catalyze the glucose oxidation to gluconic acid and hydrogen peroxide (H_2O_2). Among all the sugars, GOx is only specific towards glucose oxidation and is regarded as an ideal enzyme because of its fast mode of action, high specificity, and stability [326].

1.6. Organizations of the thesis

The work presented in the thesis aims to explore the physicochemical properties of optically active self-assembled structures for environmental remediation and catalytic applications.

Chapter 1 discusses the role of membraneless compartments in the various biological processes inside the natural cell. A brief overview of the different types of three-dimensional self-assembled structures/ artificial cells designed to mimic natural cells and their formulations and applications have been discussed. Subsequently, the evolution of liquid-liquid phase-separated membraneless coacervates and their evolution as a prominent biomimetic system, along with their features, types, and applications, have been discussed in detail. Finally, environmental remediation, photocatalysis, and enzyme catalysis have been discussed briefly.

Chapter 2 includes the details of all the chemicals used. It also discusses the complete synthetic procedures of QDs and CDs along with the different NP-embedded coacervates such as ATP-, CD-, and QD-coacervates. This chapter also covers the sample preparation, experimental procedures, and techniques used during the entire thesis work.

Chapter 3 explores the effect of the charged aqueous interface of micelles on the photophysical properties of Eosin Y and the subsequent utilization of EY@CTAB composite for the photocatalytic oxidative coupling of arylamines to azoaromatics in the aqueous medium have been explored.

Chapter 4 investigates the role of green and red emissive QD-embedded coacervates towards ultrasensitive detection and efficient removal of Hg^{2+} from contaminated water.

Chapter 5 investigates the role of membraneless architecture and confined environment of the NP-embedded coacervates for the photoredox conversion of ferricyanide to ferrocyanide and the subsequent utilization of QD-embedded coacervates for the photocatalytic degradation of model pollutants, RhB and MB.

Chapter 6 highlights the utilization of QD-embedded coacervates as a scaffold for in situ synthesis of small-size Au NPs to create a new type of plexcitonic coacervates (Au@QD-Ds). The work further demonstrates the peroxidase-like activity of Au@QD-Ds and its subsequent use for glucose detection.

Chapter 7 highlights the conclusion of the work done in the entire thesis and its scope for future applications.

1.7. References

1. Mendes A. C., Baran E. T., Reis R. L., Azevedo H. S. (2013) Self-assembly in nature: using the principles of nature to create complex nanobiomaterials, Wiley Interdiscip. Rev. Nanomedicine Nanobiotechnology, 5, 582−612 (DOI:10.1002/wnan.1238)

2. Rajapaksha R. D. A. A. (2019). Self-assembling smart materials for biomaterials applications, Polymer Nanocomposite-Based Smart Materials, 121-147. (DOI:10.1016/B978-0-08-103013-4.00007-8)

3. Rasmussen S., Chen L., Nilsson M., Abe S. (2003), Bridging nonliving and living matter, Artificial Life, 9, 269–316. (DOI:10.1162/106454603322392479)

4. Tu Y., Peng F., Adawy A., Men Y., Abdelmohsen L. K. E. A., Wilson D. A. (2016), Mimicking the cell: bio-inspired functions of supramolecular assemblies, Chem. Rev., 116, 2023–2078. (DOI:10.1021/acs.chemrev.5b00344)

5. Luzio J. P., Pryor P. R., Bright N. A. (2007), Lysosomes: fusion and function, Nat. Rev. Mol. Cell Biol., 8, 622–632. (DOI:10.1038/nrm2217)

6. Friedman J. R., Nunnari J. (2014), Mitochondrial form and function, Nature, 505, 335–343. (DOI:10.1038/nature12985)

7. Mahen R., Venkitaraman A. R. (2012), Pattern formation in centrosome assembly, Curr. Opin. Cell Biol., 24, 14–23. (DOI:10.1016/j.ceb.2011.12.012)

8. Dubey N. C., Tripathi B. P. (2021), Nature inspired multienzyme immobilization: Strategies and concepts, ACS Appl. Bio Mater., 4, 1077–1114. (DOI:10.1021/acsabm.0c01293)

9. Brangwynne C. P., Mitchison T. J., Hyman A. A. (2011), Active liquid-like behavior of nucleoli determines their size and shape in Xenopus laevis oocytes, Proc. Natl. Acad. Sci. U.S.A., 108, 4334–4339. (DOI:10.1073/pnas.1017150108)

10. Molliex A., Temirov J., Lee J., Coughlin M., Kanagaraj A. P., Kim H. J., Mittag T., Talor J. P. (2015), Phase separation by low complexity domains promotes stress granule assembly and drives pathological fibrillization, Cell, 163, 123–133. (DOI:10.1016/j.cell.2015.09.015)

11. Hennig S., Kong G., Mannen T., Sadowska A., Kobelke S., Blythe A., et al. (2015), Prion-like domains in RNA binding proteins are essential for building subnuclear paraspeckles, J. Cell Biol., 210, 529–539. (DOI:10.1083/jcb.201504117)

12. Du M., Chen Z. J. (2018), DNA-induced liquid phase condensation of cGAS activates innate immune signaling, Science, 361, 704–709. (DOI:10.1126/science.aat1022)

13. Boija A., Klein I. A., Sabari B. R., Dall'Agnese A., Coffey E. L., Zamudio AV., et al. (2018), Transcription factors activate genes through the phase-separation capacity of their activation domains, Cell, 175, 1842-1855.e16. (DOI:10.1016/j.cell.2018.10.042)

14. Sabari B. R., Dall'Agnese A., Boija A., Klein I. A., Coffey E. L., Shrinivas K., et al. (2018), Coactivator condensation at super-enhancers links phase separation and gene control, Science, 361, eaar3958. (DOI:10.1126/science.aar3958)

15. Franzmann T. M., Jahnel M., Pozniakovsky A., Mahamid J., Holehouse A. S., Nüske E., Richter D., Baumeister W., Grill S. W., Pappu R. V., Hyman A. A., Alberti S. (2018), Phase separation of a

yeast prion protein promotes cellular fitness, Science, 359, eaao5654. (DOI:10.1126/science.aao5654)

16. Zbinden A., Pérez-Berlanga M., De Rossi P., Polymenidou M. (2020), Phase separation and neurodegenerative diseases: A disturbance in the force, Dev. Cell, 55, 45–68. (DOI:10.1016/j.devcel.2020.09.014)

17. Kilic S., Lezaja A., Gatti M., Bianco E., Michelena J., Imhof R., Altmeyer M. (2019), Phase separation of 53 BP 1 determines liquid-like behavior of DNA repair compartments, EMBO J., 38, e101379. (DOI:10.15252/embj.2018101379)

18. Milovanovic D., Wu Y., Bian X., De Camilli P. (2018), A liquid phase of synapsin and lipid vesicles, Science, 361, 604–607. (DOI:10.1126/science.aat5671)

19. Brangwynne C. P., Eckmann C. R., Courson D. S., Rybarska A., Hoege C., Gharakhani J., Jülicher F., Hyman A. A. (2009), Germline P granules are liquid droplets that localize by controlled dissolution/condensation, Science, 324, 1729–1732. (DOI:10.1126/science.1172046)

20. Agapakis C. M., Boyle P. M., Silver P. A. (2012), natural strategies for the spatial optimization of metabolism in synthetic biology, Nat. Chem. Biol., 8, 527–535. (DOI:10.1038/nchembio.975)

21. Alberti S., Hyman A. A. (2016), Are aberrant phase transitions a driver of cellular aging?, BioEssays, 38, 959–968. (DOI:10.1002/bies.201600042)

22. Gear A. R. L. (1970), Inner- and outer-membrane enzymes of mitochondria during liver regeneration, Biochem. J., 120, 577–587. (DOI:10.1042/bj1200577)

23. Igamberdiev A. U., Kleczkowski L. A. (2015), Optimization of ATP synthase function in mitochondria and chloroplasts via the adenylate kinase equilibrium, Front. Plant Sci., 6 (DOI:10.3389/fpls.2015.00010)

24. Che H., van Hest J. C. M. (2019), Adaptive polymersome nanoreactors, ChemNanoMat., 5, 1092–1109. (DOI:10.1002/cnma.201900245)

25. Kerfeld C. A., Aussignargues C., Zarzycki J., Cai F., Sutter M. (2018), Bacterial microcompartments, Nat. Rev. Microbiol., 16, 277–290. (DOI:10.1038/nrmicro.2018.10)

26. Mason A. F., Yewdall N. A., Welzen P. L. W., Shao J., van Stevendaal M., van Hest J. C. M., et al. (2019), Mimicking cellular compartmentalization in a hierarchical protocell through spontaneous spatial organization, ACS Cent. Sci., 5, 1360–1365. (DOI:10.1021/acscentsci.9b00345)

27. Hyman A. A., Weber C. A., Jülicher F. (2014), Liquid-liquid phase separation in biology, Annu. Rev. Cell Dev. Biol., 30, 39–58. (DOI:10.1146/annurev-cellbio-100913-013325)

28. Alberti S. (2017), The wisdom of crowds: regulating cell function through condensed states of living matter, J. Cell Sc., 17, 2789-2796. (DOI:10.1242/jcs.200295)

29. Grzybowski B. A., Wilmer C. E., Kim J., Browne K. P., Bishop K. J. (2009), Self-assembly: from crystals to cells, Soft Matter, 5, 1110–1128. (DOI:10.1039/b819321p)

30. Wang Y., Rencus-Lazar S., Zhou H., Yin Y., Jiang X., Cai K., Gazit E., Ji W. (2024), Bioinspired amino acid based materials in bionanotechnology: from minimalistic building blocks and assembly mechanism to applications, ACS Nano, 18, 1936-0851. (DOI: 10.1021/acsnano.3c08183)

31. Perumal S., Atchudan R., Lee W. (2022), A review of polymeric micelles and their applications, Polymers, 14, 2510. (DOI:10.3390/polym14122510)

32. Us'yarov O.G. (2007), The electrical double layer of micelles in ionic surfactant solutions in the presence of a background electrolyte: 1. diluted micellar solutions of sodium dodecyl sulfate, Colloid J, 69, 95–102. (DOI:10.1134/S1061933X07010139)

33. Torchilin V. P. (2001), Structure and design of polymeric surfactant-based drug delivery systems, J. Control Release, 73, 137–172. (DOI:10.1016/S0168-3659(01)00299-1)

34. Virdi J. K., Dusunge A., Handa S. (2024), Aqueous micelles as solvent, ligand, and reaction promoter in catalysis, JACS Au, 4, 301–317. (DOI:10.1021/jacsau.3c00605)

35. Borrego E., Caballero A., Pérez P. J. (2022), Micellar catalysis as a tool for C-H bond functionalization toward C-C bond formation, Organometallics, 41, 3084–3098. (DOI: 10.1021/acs.organomet.2c00309)

36. Ballmann M., Ruer P. C., Hofnagel O., Hiller W., Krause N. (2022), Recyclable polyethylene glycol ubiquinol succinate-bound N-heterocyclic carbene–gold(I) complexes: sustainable micellar catalysis in water, ACS Sustain. Chem. Eng., 10, 7288–7298. (DOI:10.1021/acssuschemeng.2c00713)

37. Shah A., Shahzad S., Munir A., Nadagouda M. N., Khan G. S., Shams D. F., Dionysiou D. D., Rana U. A. (2016), Micelles as soil and water decontamination agents, Chem. Reviews, 116, 6042–6074. (DOI:10.1021/acs.chemrev.6b00132)

38. Kim H.-J., Lee H.-I. (2018), Polymeric micelles based on light-responsive block copolymers for the phototunable detection of mercury(II) ions modulated by morphological changes, ACS Appl. Mater. Interfaces 10, 34634–34639. (DOI:10.1021/acsami.8b12441)

39. Huang W.; Smarsly E.; Han J.; Bender M., Seehafer, K., Wacker I., Schröder R. R., Bunz U. H. F. (2017), Truxene-based hyperbranched conjugated polymers: fluorescent micelles detect explosives in water, ACS Appl. Mater. Interfaces, 9, 3068–3074. (DOI:10.1021/acsami.6b12419)

40. Ishii S., Kaneko J., Nagasaki Y. (2015), Dual stimuli-responsive redox-active injectable gel by polyion complex based flower micelles for biomedical applications, Macromolecules, 48, 3088–3094. (DOI:10.1021/acs.macromol.5b00305)

41. Li, P. Y.; Sun, M. M.; Xu, Z. K.; Liu, X. Y.; Zhao, W. G.; Gao, W. P. (2018), Site-selective in situ growth-induced self-assembly of protein-polymer conjugates into pH-responsive micelles for tumor microenvironment triggered fluorescence imaging,

Biomacromolecules, 19, 4472–4479. (DOI:10.1021/acs.biomac.8b01368)

42. Finnegan J. R., He X., Street S. T. G., Garcia-Hernandez J. D., Hayward D. W., Harniman R. L., Richardson R. M., Whittell G. R., Manners I. (2018), Extending the scope of "living" crystallization-driven self-assembly: well-defined 1D micelles and block comicelles from crystallizable polycarbonate block copolymers, J. Am. Chem. Soc., 140, 17127–17140. (DOI:10.1021/jacs.8b09861)

43. Sreejith S., Joseph J., Lin M., Menon N. V., Borah P., Ng H. J., Loong Y. X., Kang Y., Yu S. W.-K., Zhao Y. (2015), Near-infrared squaraine dye encapsulated micelles for in vivo fluorescence and photoacoustic bimodal imaging, ACS Nano, 9, 5695–5704. (DOI:10.1021/acsnano.5b02172)

44. Xu Z., Liu S., Kang Y., Wang M. (2015), Glutathione-responsive polymeric micelles formed by a biodegradable amphiphilic triblock copolymer for anticancer drug delivery and controlled release, ACS Biomater. Sci. Eng., 1, 585–592. (DOI:10.1021/acsbiomaterials.5b00119)

45. Tavernier H. L., Laine F. Fayer M. D. (2001), Photoinduced intermolecular electron transfer in micelles: dielectric and structural properties of micelle headgroup regions, J. Phys. Chem. A, 105, 8944–8957. (DOI:10.1021/jp0106597)

46. Kumbhakar M., Singh P. K., Nath S., Bhasikuttan A. C., Pal H. (2008), Ultrafast bimolecular electron transfer dynamics in micellar media, J. Phys. Chem. B, 112, 6646–6652. (DOI:10.1021/jp800752d)

47. Ansari T. N., Xu G., Preston A., Gao P. (2024), Recent highlights in micellar catalysis: an industrial outlook, Org. Process Res. Dev. 2024, 28, 4, 816–830. (DOI:10.1021/acs.oprd.3c00453)

48. Isley N. A., Linstadt R. T. H., Kelly S. M., Gallou F., Lipshutz B. H. (2015), Nucleophilic aromatic substitution reactions in water enabled by micellar catalysis, Org. Lett. 17, 4734–4737. (DOI:10.1021/acs.orglett.5b02240)

49. Lee N. R., Moghadam F. A., Braga F. C., Lippincott D. J., Zhu B., Gallou F., Lipshutz B. H. (2020), Sustainable palladium-catalyzed tsuji-trost reactions enabled by aqueous micellar catalysis, Org. Lett. 22, 4949–4954. (DOI:10.1021/acs.orglett.0c01329)

50. Bihani M., Ansari T. N., Finck L., Bora P. P., Jasinski J. B., Pavuluri B., Leahy D. K., Handa S. (2020), Scalable α-arylation of nitriles in aqueous micelles using ultrasmall Pd nanoparticles: surprising formation of carbanions in water, ACS Catal., 10, 6816–6821. (DOI:10.1021/acscatal.0c01196)

51. Sengoden M., Bhat G. A., Rutledge R. J., Rashid S., Dar A. A., Darensbourg D. J. (2023), Micellar catalysis: polymer bound palladium catalyst for carbon-carbon coupling reactions in water, Proc. Natl. Acad. Sci. U.S.A., 120, e2312907120. (DOI:10.1073/pnas.2312907120

52. Šturm L., Poklar Ulrih N. (2021), Basic methods for preparation of liposomes and studying their interactions with different compounds, with the emphasis on polyphenols, Int. J. Mol. Sci., 22, 6547. (DOI:10.3390/ijms22126547)

53. Bangham A. D., Horne R. W. (1964), Negative staining of phospholipids and their structural modification by surface-active agents as observed in the electron microscope, J. Mol. Biol., 8, 660-IN10. (DOI:10.1016/S0022-2836(64)80115-7)

54. Jelinek R., Kolusheva S. (2005), Membrane interactions of host-defense peptides studied in model systems, CPPS, 6, 103–114. (DOI:10.2174/1389203053027511)

55. Picon A., Serrano C., Gaya P., Medina M., Nuñez M. (1996), The effect of liposome-encapsulated cyprosins on manchego cheese ripening, J. Dairy Sci., 79, 1699–1705. (DOI:10.3168/jds.S0022-0302(96)76535-9)

56. Lee K. Y., Park S-J., Lee K. A., Kim S-H., Kim H., Meroz Y., et al. (2018), Photosynthetic artificial organelles sustain and control ATP-dependent reactions in a protocellular system, Nat. Biotechnol., 36, 530–535. (DOI:10.1038/nbt.4140)

57. Noireaux V., Libchaber A. (2004), A vesicle bioreactor as a step toward an artificial cell assembly, Proc. Natl. Acad. Sci. U.S.A., 101, 17669–17674. (DOI:10.1073/pnas.0408236101)

58. Elani Y., Law R. V., Ces O. (2014), Vesicle-based artificial cells as chemical microreactors with spatially segregated reaction pathways, Nat. Commun., 5, 5305. (DOI:10.1038/ncomms6305)

59. Gardner P. M., Winzer K., Davis B. G. (2009), Sugar synthesis in a protocellular model leads to a cell signaling response in bacteria, Nat. Chem., 1, 377–383. (DOI:10.1038/nchem.296)

60. Lentini R., Santero S. P., Chizzolini F., Cecchi D., Fontana J., Marchioretto M., et al. (2014), Integrating artificial with natural cells to translate chemical messages that direct E. coli behaviour, Nat. Commun., 5, 4012. (DOI:10.1038/ncomms5012)

61. Adamala K., Szostak JW. (2013), Competition between model protocells driven by an encapsulated catalyst, Nat. Chem., 5, 495–501. (DOI:10.1038/nchem.1650)

62. Discher, B. M., Won, Y., Ege, D. S., Lee, M., Bates, F. S., Discher, D. E., & Hammer, D. A. (1999), Polymersomes: Tough vesicles made from diblock copolymers, Science, 284, 1143–1146. (DOI:10.1126/science.284.5417.1143)

63. Meierhenrich U. J., Filippi J-J., Meinert C., Vierling P., Dworkin J. P. (2010), On the origin of primitive cells: From nutrient intake to elongation of encapsulated nucleotides, Angew. Chem. Int. Ed., 49, 3738–3750. (DOI:10.1002/anie.200905465)

64. Lu Y., Allegri G., Huskens J. (2022), Vesicle-based artificial cells: materials, construction methods and applications, Mater. Horiz., 9, 892–907. (DOI:10.1039/D1MH01431E)

65. Green J. J., Elisseeff J. H. (2016), Mimicking biological functionality with polymers for biomedical applications, Nature, 540, 386–394. (DOI:10.1038/nature21005)

66. Chang T. M. S. (1964), Semipermeable microcapsules, Science, 146, 524–525. (DOI:10.1126/science.146.3643.524)

67. Chang T. M. S. (2005), Therapeutic applications of polymeric artificial cells, Nat. Rev. Drug Discov., 4, 221–235. (DOI:10.1038/nrd1659)

68. Liu Z. C., Swi Chang T. M. (2010), Artificial cell microencapsulated stem cells in regenerative medicine, tissue engineering and cell therapy, Chapter: In Pedraz JL, Orive G (eds), Therapeutic applications of cell microencapsulation, New York, NY Springer New York, pp.68–79. (DOI:10.1007/978-1-4419-5786-3_7)

69. Orive G., Hernández R. M., Gascón A. R., Calafiore R., Chang T. M. S., Vos P. D., et al. (2003), Cell encapsulation: Promise and progress, Nat. Med., 9, 104–107. (DOI:10.1038/nm0103-104)

70. Chang T. M. S. (1969), Removal of endogenous and exogenous toxins by a microencapsulated absorbent, Can. J. Physiol. Pharmacol., 47, 1043–1045. (DOI:10.1139/y69-170)

71. Chang T. M. S. (1971), The in vivo Effects of semipermeable microcapsules containing L-Asparaginase on 6C3HED lymphosarcoma, Nature, 229, 117–118. (DOI:10.1038/229117a0)

72. Chang T. M. S. (2004), Artificial cells for cell and organ replacements, Artif. Organs, 28, 265–270. (DOI:10.1111/j.1525-1594.2004.47343.x)

73. O'Shea G. M., Sun A. M. (1986), Encapsulation of rat islets of Langerhans prolongs xenograft survival in diabetic mice, Diabetes, 35, 943–946. (DOI:10.2337/diab.35.8.943)

74. Anraku Y., Kishimura A., Kamiya M., Tanaka S., Nomoto T., Toh K., et al. (2016), Systemically injectable enzyme-loaded polyion complex vesicles as in vivo nanoreactors functioning in tumors, Angew. Chem., 128, 570–575. (DOI:10.1002/ange.201508339)

75. Chemin M., Brun P-M., Lecommandoux S., Sandre O., Le Meins J-F. (2012), Hybrid polymer/lipid vesicles: fine control of the lipid and polymer distribution in the binary membrane, Soft Matter, 8, 2867. (DOI:10.1039/c2sm07188f)

76. Khan S., McCabe J., Hill K., Beales P. A. (2020), Biodegradable hybrid block copolymer–lipid vesicles as potential drug delivery

systems, J. Colloid Interface Sci., 562, 418–428. (DOI:10.1016/j.jcis.2019.11.101)

77. Percec V., Wilson D. A., Leowanawat P., Wilson C. J., Hughes A. D., Kaucher M. S., et al. (2010), Self-Assembly of Janus dendrimers into uniform dendrimersomes and other complex architectures, Science, 328, 1009–1014. (DOI:10.1126/science.1185547)

78. Wu L., Li B-L., Huang Y-Y., Zhou H-F., He Y-M., Fan Q-H. (2006), Phosphine dendrimer-stabilized palladium nanoparticles, a highly active and recyclable catalyst for the Suzuki−Miyaura Reaction and Hydrogenation, Org. Lett., 8, 3605–3608. (DOI:10.1021/ol0614424)

79. Patri A. K., Majoros I. J., Baker J. R. (2002), Dendritic polymer macromolecular carriers for drug delivery, Curr. Opin. Chem. Biol., 6, 466–471. (DOI:10.1016/S1367-5931(02)00347-2)

80. Patri A., Kukowskalatallo J., Bakerjr J. (2005), Targeted drug delivery with dendrimers: Comparison of the release kinetics of covalently conjugated drug and non-covalent drug inclusion complex, Adv. Drug Deliv. Rev., 57, 2203–2214. (DOI:10.1016/j.addr.2005.09.014)

81. Gupta U., Agashe H. B., Asthana A., Jain N. K. (2006), Dendrimers: Novel polymeric nanoarchitectures for solubility enhancement, Biomacromolecules, 7, 649–658. (DOI:10.1021/bm050802s)

82. Gajbhiye V., Palanirajan V. K., Tekade R. K., Jain N. K. (2010), Dendrimers as therapeutic agents: a systematic review, J. Pharm. Pharmacol., 61, 989–1003. (DOI:10.1211/jpp.61.08.0002)

83. Gitsov I., Hamzik J., Ryan J., Simonyan A., Nakas J. P., Omori S., et al. (2008), Enzymatic nanoreactors for environmentally benign biotransformations. 1. Formation and catalytic activity of supramolecular complexes of laccase and linear−dendritic block copolymers, Biomacromolecules, 9, 804–811. (DOI:10.1021/bm701081m)

84. Perli G., Wang Q., Braga C. B., Bertuzzi D. L., Fontana L. A., Soares MCP., et al. (2021), Self-Assembly of a triazolylferrocenyl dendrimer in water yields nontraditional intrinsic green fluorescent vesosomes for Nanotheranostic Applications, J. Am. Chem. Soc., 143, 12948–12954. (DOI:10.1021/jacs.1c05551)

85. Li M., Green D. C., Anderson J. L. R., Binks B. P., Mann S. (2011), In vitro gene expression and enzyme catalysis in bio-inorganic protocells, Chem. Sci., 2, 1739. (DOI:10.1039/c1sc00183c)

86. Dinsmore A. D., Hsu M. F., Nikolaides M. G., Marquez M., Bausch A. R., Weitz D. A. (2002), Colloidosomes: selectively permeable capsules composed of colloidal particles, Science, 298, 1006–1009. (DOI:10.1126/science.1074868)

87. Wang C., Liu H., Gao Q., Liu X., Tong Z. (2007), Facile fabrication of hybrid colloidosomes with alginate gel cores and shells of porous $CaCO_3$ microparticles, ChemPhysChem, 8, 1157–1160. (DOI:10.1002/cphc.200700147)

88. Li S., Moosa B. A., Croissant J. G., Khashab N. M. (2015), Electrostatic assembly/disassembly of nanoscaled colloidosomes for light-triggered cargo release, Angew. Chem. Int. Ed., 54, 6804–6808. (DOI:10.1002/anie.201501615)

89. Pan Y., Qiu W., Li Q., Zhu S., Lin C., Zeng W., et al. (2019), Assembling two-phase enzymatic cascade pathways in pickering emulsion, ChemCatChem, 11, 1878–1883. (DOI:10.1002/cctc.201900098)

90. Liu Z., Wang B., Jin S., Wang Z., Wang L., Liang S. (2018), Bioinspired dual-enzyme colloidosome reactors for high-performance biphasic catalysis, ACS Appl. Mater. Interfaces, 10, 41504–41511. (DOI:10.1021/acsami.8b14321)

91. Rodríguez-Arco L., Kumar B. V. V. S. P., Li M., Patil A. J., Mann S. (2019), Modulation of higher-order behaviour in model protocell communities by artificial phagocytosis, Angew. Chem. Int. Ed., 58, 6333–6337. (DOI:10.1002/anie.201901469)

92. Sun M., Yin W., Chen J., Wang W., Guo T., Meng T. (2021), Hollow colloidosomes with an enzyme confined in a porous shell

as Pickering interfacial biocatalysts for efficient bioconversions, Green Chem., 23, 740–744. (DOI:10.1039/D0GC02999H)

93. Li M., Harbron R. L., Weaver J. V. M., Binks B. P., Mann S. (2013), Electrostatically gated membrane permeability in inorganic protocells, Nat. Chem., 5, 529–536. (DOI:10.1038/nchem.1644)

94. Huang X., Patil A. J., Li M., Mann S. (2014), Design and construction of higher-order structure and function in proteinosome-based protocells, J. Am. Chem. Soc., 136, 9225–9234. (DOI:10.1021/ja504213m)

95. Huang X., Li M., Green D. C., Williams D. S., Patil A. J., Mann S. (2013), Interfacial assembly of protein–polymer nano-conjugates into stimulus-responsive biomimetic protocells, Nat. Commun., 4, 2239. (DOI:10.1038/ncomms3239)

96. Cai Y., Yu Q., Zhao H. (2020), Electrostatic assisted fabrication and dissociation of multi-component proteinosomes, J. Colloid Interface Sci., 576, 90–98. (DOI:10.1016/j.jcis.2020.05.013)

97. Huang X., Li M., Mann S. (2014), Membrane-mediated cascade reactions by enzyme–polymer proteinosomes, Chem. Commun., 50, 6278–6280. (DOI:10.1039/C4CC02256D)

98. Liu X., Zhou P., Huang Y., Li M., Huang X., Mann S. (2016), Hierarchical proteinosomes for programmed release of multiple components, Angew. Chem. Int. Ed., 55, 7095–7100. (DOI:10.1002/anie.201601427)

99. Liu L., Su D., Liu X., Wang L., Zhan J., Xie H., et al. (2017), Construction of biological hybrid microcapsules with defined permeability towards programmed release of biomacromolecules, Chem. Commun., 53, 11678–11681. (DOI:10.1039/C7CC06243E)

100. Freund R., Zaremba O., Arnauts G., Ameloot R., Skorupskii G., Dinca M., Bavykina A., Gascon J., Ejsmont A., Goscianska J., Kalmutzki M., Lachelt U., Ploetz E., Diercks C. S., Wuttke S. (2021), The current status of MOF and COF applications, Angew. Chem., Int. Ed., 60, 23975–24001. (DOI:10.1002/anie.202106259MOF2)

101. Shalini S. S., Balamurugan R., Velmathi S., Bose A. C. (2022), Systematic investigation on the electrochemical performance of pristine silver metal-organic framework as the efficient electrode material for supercapacitor application, Energy Fuels, 36, 7104–7114. (DOI: 10.1021/acs.energyfuels.2c01034)

102. Guo J., Yang L., Gao Z., Zhao C., Mei Y., Song Y. Y. (2020), Insight of MOF environment-dependent enzyme activity via MOFs-in-nanochannels configuration, ACS Catalysis, 10, 5949–5958. (DOI:10.1021/acscatal.0c00591)

103. Yang J., Yang Y., (2020), Metal-organic frameworks for biomedical applications, Small, 16, e1906846, (DOI:10.1002/smll.201906846)

104. Ghosh S., Rana A., Biswas S. (2024), Metal-organic framework-based fluorescent sensors for the detection of pharmaceutically active compounds, Chem. Mater., 36, 99–131. (DOI: 10.1021/acs.chemmater.3c02459)

105. Peng, X.; Wu, X.; Zhang, M.; Yuan, H. (2023), Metal-organic framework coated devices for gas sensing, ACS Sens., 8, 2471–2492. (DOI:10.1021/acssensors.3c00362)

106. Chen Y.-Z., Wang Z. U., Wang H., Lu J., Yu S.-H., Jiang H.-L. (2017), Singlet oxygen-engaged selective photo-oxidation over Pt nanocrystals/porphyrinic MOF: the roles of photothermal effect and Pt electronic state, J. Am. Chem. Soc., 139, 2035–2044. (DOI:10.1021/jacs.6b12074)

107. Leng F., Liu H., Ding M., Lin Q. P., Jiang H. L. (2018), Boosting photocatalytic hydrogen production of porphyrinic MOFs: the metal location in metalloporphyrin matters, ACS Catal., 8, 4583–4590. (DOI:10.1021/acscatal.8b00764)

108. Xu R., Wu T., Jiao X., Chen D., Li C. (2023), Self-assembled MOF-on-MOF nanofabrics for synergistic detoxification of chemical warfare agent simulants, ACS Appl. Mater. Interfaces, 15, 30360–30371. (DOI:10.1021/acsami.3c06032)

109. Williams D. S., Koga S., Hak C. R. C., Majrekar A., Patil A. J., Perriman A. W., Mann S. (2012), Polymer/nucleotide droplets as

bio-inspired functional micro-compartments, Soft Matter, 8, 6004. (DOI:10.1039/c2sm25184a)

110. Koga S., Williams D. S., Perriman A. W., Mann S. (2011), Peptide–nucleotide microdroplets as a step towards a membrane-free protocell model, Nat. Chem., 3, 720–724. (DOI:10.1038/nchem.1110)

111. Mastiani M., Firoozi N., Petrozzi N. et al. (2019), Polymer-salt aqueous two-phase system (ATPS) micro-droplets for cell encapsulation, Sci Rep 9, 15561. (DOI:10.1038/s41598-019-51958-4)

112. Dignon G. L., Best R. B., Mittal J. (2020), Biomolecular phase separation: from molecular driving forces to macroscopic properties, Annu. Rev. Phys. Chem., 71, 53–75. (DOI:10.1146/annurev-physchem-071819-113553)

113. Priftis D., Leon L., Song Z., Perry S. L., Margossian K. O., Tropnikova A., Cheng J., Tirrell M. (2015), Self-assembly of α-helical polypeptides driven by complex coacervation, Angew. Chem., Int. Ed., 54, 11128–11132. (DOI:10.1002/anie.201504861)

114. Abbas M., Lipiński W. P., Nakashima K. K., Huck W. T. S., Spruijt E. (2021), A short peptide synthon for liquid–liquid phase separation, Nat. Chem., 13, 1046–1054. (DOI:10.1038/s41557-021-00788-x)

115. Menger F. M., Peresypkin A. V., Caran K. L., Apkarian R. P. (2000), A sponge morphology in an elementary coacervate, Langmuir, 16, 9113–9116. (DOI:10.1021/la0010626)

116. Booij H. L., Bungenberg de Jong H. G. (1956), Colloid systems, Chapter: In biocolloids and their Interactions. Vienna Springer Vienna, pp.8–14. (DOI:10.1007/978-3-7091-5456-4_2)

117. Veis A. (2011), A review of the early development of the thermodynamics of the complex coacervation phase separation, Adv. Colloid Interface Sci., 167, 2–11. (DOI:10.1016/j.cis.2011.01.007)

118. Zhou L., Shi H., Li Z., He C. (2020), Recent Advances in complex coacervation design from macromolecular assemblies and

emerging applications, Macromol. Rapid Commun., 41, 2000149. (DOI:10.1002/marc.202000149)

119.   Gucht J van der., Spruijt E., Lemmers M., Cohen Stuart M. A. (2011), Polyelectrolyte complexes: bulk phases and colloidal systems, J. Colloid Interface Sci., 361, 407–422. (DOI:10.1016/j.jcis.2011.05.080)

120.   Perry S., Li Y., Priftis D., Leon L., Tirrell M. (2014), The effect of salt on the complex coacervation of vinyl polyelectrolytes, Polymers, 6, 1756–1772. (DOI:10.3390/polym6061756)

121.   van Stevendaal M. H. M. E., Vasiukas L., Yewdall N. A., Mason A. F., van Hest J. C. M. (2021), Engineering of biocompatible coacervate-based synthetic cells, ACS Appl. Mater. Interfaces, 13, 7879–7889. (DOI:10.1021/acsami.0c19052)

122.   Rathee V. S., Sidky H., Sikora B. J., Whitmer J. K. (2018), Role of associative charging in the entropy–energy balance of polyelectrolyte complexes, J. Am. Chem. Soc., 140, 15319–15328. (DOI:10.1021/jacs.8b08649)

123.   Orti F., Navarro A. M., Rabinovich A., Wodak S. J., Marino-Buslje C. (2021), Insight into membraneless organelles and their associated proteins: Drivers, clients and regulators, Comput. Struct. Biotechnol. J., 19, 3964–3977. (DOI:10.1016/j.csbj.2021.06.042)

124.   Crowe C. D., Keating C. D. (2018), Liquid–liquid phase separation in artificial cells, Interface Focus, 8, 20180032. (DOI:10.1098/rsfs.2018.0032)

125.   Kawamura A., Harada A., Kono K., Kataoka K. (2007), Self-assembled nano-bioreactor from block ionomers with elevated and stabilized enzymatic function, Bioconjug. Chem., 18, 1555–1559. (DOI:10.1021/bc070029t)

126.   Voets I. K., de Keizer A., Cohen Stuart M. A. (2009), Complex coacervate core micelles, Adv. Colloid Interface Sci., 147–148, 300–318. (DOI:10.1016/j.cis.2008.09.012)

127.   Pawar N., Bohidar H. B. (2011), Anisotropic domain growth and complex coacervation in nanoclay-polyelectrolyte solutions,

Adv. Colloid Interface Sci., 167, 12–23. (DOI:10.1016/j.cis.2011.06.007)

128. Frankel E. A., Bevilacqua P. C., Keating C. D. (2016), Polyamine/nucleotide coacervates provide strong compartmentalization of Mg^{2+}, nucleotides, and RNA, Langmuir, 32, 2041–2049. (DOI:10.1021/acs.langmuir.5b04462)

129. Spoelstra W. K., Sluis EO. V. D., Dogterom M., Reese L. (2020), Nonspherical coacervate shapes in an enzyme-driven active system, Langmuir, 36, 1956–1964. (DOI:10.1021/acs.langmuir.9b02719)

130. Krogstad D. V., Lynd N. A., Choi S-H., Spruell J. M., Hawker C. J., Kramer E. J., et al. (2013), Effects of polymer and salt concentration on the structure and properties of triblock copolymer coacervate hydrogels, Macromolecules, 46, 1512–1518. (DOI:10.1021/ma302299r)

131. Hunt J. N., Feldman K. E., Lynd N. A., Deek J., Campos L. M., Spruell J. M., et al. (2011), Tunable, high modulus hydrogels driven by ionic coacervation, Adv. Mater., 23, 2327–2331. (DOI:10.1002/adma.201004230)

132. Kim B., Lam C. N., Olsen B. D. (2012), Nanopatterned protein films directed by ionic complexation with water-soluble diblock copolymers, Macromolecules, 45, 4572–4580. (DOI:10.1021/ma2024914)

133. Schmitt C., Turgeon S. L. (2011), Protein/polysaccharide complexes and coacervates in food systems, Adv. Colloid Interface Sci., 167, 63–70. (DOI:10.1016/j.cis.2010.10.001)

134. Moulik S. P., Rakshit A. K., Pan A., Naskar B. (2022), An overview of coacervates: The special disperse state of amphiphilic and polymeric materials in solution, Colloids Interfaces, 6, 45. (DOI:10.3390/colloids6030045)

135. Pir Cakmak F., Grigas A. T., Keating C. D. (2019), Lipid vesicle-coated complex coacervates, Langmuir, 35, 7830–7840. (DOI:10.1021/acs.langmuir.9b00213)

136. Chen W. C. W., Lee B. G., Park D. W., Kim K., Chu H., Kim K., et al. (2015), Controlled dual delivery of fibroblast growth factor-2 and Interleukin-10 by heparin-based coacervate synergistically enhances ischemic heart repair, Biomater., 72, 138–151. (DOI:10.1016/j.biomaterials.2015.08.050)

137. Hwang D. S., Zeng H., Srivastava A., Krogstad D. V., Tirrell M., Israelachvili J. N., et al. (2010), Viscosity and interfacial properties in a mussel-inspired adhesive coacervate, Soft Matter, 6, 3232. (DOI:10.1039/c002632h)

138. Fromm S. A., Kamenz J., Nöldeke E. R., Neu A., Zocher G., Sprangers R. (2014), In vitro reconstitution of a cellular phase-transition process that involves the mRNA decapping machinery, Angew. Chem. Int. Ed., 53, 7354–7359. (DOI:10.1002/anie.201402885)

139. Singh S., Vaishnav J. K., Mukherjee T. K. (2020), Quantum dot-based hybrid coacervate nanodroplets for ultrasensitive detection of Hg^{2+}, ACS Appl. Nano Mater., 3, 3604–3612. (DOI:10.1021/acsanm.0c00317)

140. Schoonen L., van Hest J. C. M. (2016), Compartmentalization approaches in soft matter science: From nanoreactor development to organelle mimics, Adv. Mater., 28, 1109–1128. (DOI:10.1002/adma.201502389)

141. Ivinova O. N., Izumrudov V. A., Muronetz V. I., Galaev I. Yu., Mattiasson B. (2003), Influence of complexing polyanions on the thermostability of basic proteins, Macromol. Biosci., 3, 210–215. (DOI:10.1002/mabi.200390024)

142. Priftis D., Tirrell M. (2012), Phase behaviour and complex coacervation of aqueous polypeptide solutions, Soft Matter, 8, 9396–9405. (DOI:10.1039/C2SM25604E)

143. Chollakup R., Smitthipong W., Eisenbach C. D., Tirrell M. (2010), Phase behavior and coacervation of aqueous poly(acrylic acid)−poly(allylamine) solutions, Macromolecules, 43, 2518–2528. (DOI:10.1021/ma902144k)

144. Liu Y., Winter H. H., Perry S. L. (2017), Linear viscoelasticity of complex coacervates, Adv. Colloid Interface Sci., 239, 46–60. (DOI:10.1016/j.cis.2016.08.010)

145. Ali S., Bleuel M., Prabhu V. M. (2019), Lower critical solution temperature in polyelectrolyte complex coacervates, ACS Macro Lett., 8, 289–293. (DOI:10.1021/acsmacrolett.8b00952)

146. Nichols M. K., Kumar R. K., Bassindale P. G., Tian L., Barnes A. C., Drinkwater B. W., et al. (2018), Fabrication of micropatterned dipeptide hydrogels by acoustic trapping of stimulus-responsive coacervate droplets, Small, 14, 1800739. (DOI:10.1002/smll.201800739)

147. Huang G-Q., Han X-N., Xiao J-X. (2017), Glutaraldehyde-crosslinked O-carboxymethyl chitosan–gum arabic coacervates: characteristics versus complexation acidity, J. Dispers. Sci. Technol., 38, 1607–1612. (DOI:10.1080/01932691.2016.1265454)

148. Joshi N., Rawat K., Bohidar H. B. (2018), pH and ionic strength induced complex coacervation of pectin and gelatin A, Food Hydrocoll., 74, 132–138. (DOI:10.1016/j.foodhyd.2017.08.011)

149. Vaishnav J. K., Mukherjee T. K. (2019), Highly photostable and two-photon active quantum dot–polymer multicolor hybrid coacervate droplets, Langmuir, 35, 11764–11773. (DOI:10.1021/acs.langmuir.9b01783)

150. Fares H. M., Ghoussoub Y. E., Delgado J. D., Fu J., Urban V. S., Schlenoff J. B. (2018), Scattering neutrons along the polyelectrolyte complex/coacervate continuum, Macromolecules, 51, 4945–4955. (DOI:10.1021/acs.macromol.8b00699)

151. Priftis D., Laugel N., Tirrell M. (2012), Thermodynamic characterization of polypeptide complex coacervation, Langmuir, 28, 15947–15957. (DOI:10.1021/la302729r)

152. Zhang Z., Li H., Kasmi S., Van Herck S., Deswarte K., Lambrecht BN., et al. (2019), A synthetic, transiently thermoresponsive homopolymer with UCST behaviour within a

physiologically relevant window, Angew. Chem. Int. Ed., 58, 7866–7872. (DOI:10.1002/anie.201900224)

153. Nishida K., Tamura A., Yui N. (2018), pH-Responsive coacervate droplets formed from acid-labile methylated polyrotaxanes as an injectable protein carrier, Biomacromolecules, 19, 2238–2247. (DOI:10.1021/acs.biomac.8b00301)

154. Aumiller W. M., Pir Cakmak F., Davis B. W., Keating C. D. (2016), RNA-based coacervates as a model for membraneless organelles: formation, properties, and interfacial liposome assembly, Langmuir, 32, 10042–10053. (DOI:10.1021/acs.langmuir.6b02499)

155. Douliez J., Perro A., Béven L. (2019), Stabilization of all-in-water emulsions to form capsules as artificial cells, ChemBioChem, 20, 2546–2552. (DOI:10.1002/cbic.201900196)

156. Chollakup R., Beck J. B., Dirnberger K., Tirrell M., Eisenbach C. D. (2013), Polyelectrolyte molecular weight and salt effects on the phase behavior and coacervation of aqueous solutions of poly(acrylic acid) sodium salt and poly(allylamine) hydrochloride, Macromolecules, 46, 2376–2390. (DOI:10.1021/ma202172q)

157. Lu T., Javed S., Bonfio C., Spruijt E. (2023), Interfacing Coacervates with Membranes: From Artificial Organelles and Hybrid Protocells to Intracellular Delivery, Small, 7, 2300294 (DOI:10.1002/smtd.202300294)

158. Slootbeek A. D., van Haren M. H. I., Smokers I. B. A., Spruijt E. (2022), Growth, replication and division enable evolution of coacervate protocells, Chem. Commun., 58, 11183–11200, (DOI:10.1039/D2CC03541C)

159. Qi, C., Ma, X., Zeng, Q., Huang Z., Zhang S., Deng X., Kong T., Liu Z. (2024), Multicompartmental coacervate-based protocell by spontaneous droplet evaporation, Nat. Commun., 15, 1107. (DOI:10.1038/s41467-024-45411-y)

160. Nakashima K. K., van Haren, M. H. I., André, A. A. M. Robu I., Spruijt E. (2021), Active coacervate droplets are protocells that

grow and resist Ostwald ripening, Nat. Commun., 12, 3819. (DOI:10.1038/s41467-021-24111-x)

161. Jiang L., Zeng Y., Li H., Lin Z., Liu H., Richardson J. J., Gao Z., Wu D., Liu L., Caruso F., Zhou J. (2023), Peptide-based coacervate protocells with cytoprotective metal-phenolic network membranes, J. Am. Chem. Soc., 145, 24108–24115. (DOI:10.1021/jacs.3c07748)

162. Chen Y., Yuan M., Zhang Y., Liu S., Yang X., Wang K., Liu J. (2020), Construction of coacervate-in-coacervate multi-compartment protocells for spatial organization of enzymatic reactions, Chem. Sci., 11, 8617–8625. (DOI:10.1039/D0SC03849K)

163. Vitorazi L., Ould-Moussa N., Sekar S., Fresnais J., Loh W., Chapel J-P., et al. (2014), Evidence of a two-step process and pathway dependency in the thermodynamics of poly(diallyldimethylammonium chloride)/poly(sodium acrylate) complexation, Soft Matter, 10, 9496–9505. (DOI:10.1039/C4SM01461H)

164. van Swaay D., Tang T-YD., Mann S., de Mello A. (2015), Microfluidic formation of membrane-free aqueous coacervate droplets in water, Angew. Chem. Int. Ed., 54, 8398–8401. (DOI:10.1002/anie.201502886)

165. Deng N., Huck W. T. S. (2017). Microfluidic formation of monodisperse coacervate organelles in liposomes, Angewandte Chemie International Edition, 56, 9736-9740. (DOI:10.1002/anie.201703145)

166. Li H., Fauquignon M., Haddou M., Schatz C., Chapel J-P. (2021), Interfacial behavior of solid- and liquid-like polyelectrolyte complexes as a function of charge stoichiometry, Polymers, 13, 3848. (DOI:10.3390/polym13213848)

167. Peng X., Li Y., Li T., Li Y., Deng Y., Xie X., Wang Y., Li G., Bian L. (2022), Coacervate-derived hydrogel with effective water repulsion and robust underwater bioadhesion promotes wound

healing, Advanced. Science, 9, 2203890. (DOI: 10.1002/advs.202203890)

168.   Wu B., Lewis R. W., Li G., Gao Y., Fan B., Klemm B., Huang J., Wang J., Cohen Stuart M. A., Eelkema R. (2023), Chemical signal regulated injectable coacervate hydrogels, Chem. Sci., 14, 1512–1523. (DOI:10.1039/D2SC06935K)

169.   Narayanan A., Menefee J. R., Liu Q., Dhinojwala A., Joy A. (2020), Lower critical solution temperature-driven self-coacervation of nonionic polyester underwater adhesives, ACS Nano, 14, 8359–8367. (DOI:10.1021/acsnano.0c02396)

170.   Krishna Kumar R., Harniman R. L., Patil AJ., Mann S. (2016), Self-transformation and structural reconfiguration in coacervate-based protocells, Chem. Sci., 7, 5879–5887. (DOI:10.1039/C6SC00205F)

171.   Yang M., Digby Z. A., Schlenoff J. B. (2020), Precision doping of polyelectrolyte complexes: Insight on the role of ions, Macromolecules, 53, 5465–5474. (DOI:10.1021/acs.macromol.0c00965)

172.   Priftis D., Xia X., Margossian K. O., Perry S. L., Leon L., Qin J., et al. (2014), Ternary, tunable polyelectrolyte complex fluids driven by complex coacervation, Macromolecules, 47, 3076–3085. (DOI:10.1021/ma500245j)

173.   Cakmak F. P., Choi S., Meyer M.O., Bevilacqua P. C., Keating C. D. (2020), Prebiotically-relevant low polyion multivalency can improve functionality of membraneless compartments, Nat. Commun., 11, 5949. (DOI:10.1038/s41467-020-19775-w)

174.   Dan A., Ghosh S., Moulik S. P. (2009), Physiochemistry of the interaction between inulin and alkyltrimethylammonium bromides in aqueous medium and the formed coacervates, J. Phys. Chem. B, 113, 8505–8513. (DOI:10.1021/jp902641d)

175.   Kizilay E., Dinsmore A. D., Hoagland D. A., Sun L., Dubin P. L. (2013), Evolution of hierarchical structures in polyelectrolyte–micelle coacervates, Soft Matter, 9, 7320. (DOI:10.1039/c3sm50591j)

176. Kakizawa Y., Miyake M. (2019), Creation of new functions by combination of surfactant and polymer - complex coacervation with oppositely charged polymer and surfactant for shampoo and body wash, J. Oleo Sci., 68, 525–539. (DOI:10.5650/jos.ess19081)

177. Keshavarzi B., Schwarzenberger K., Huang M., Javadi A., Eckert K. (2019), Formation of structured membranes by coacervation of xanthan gum with C_nTAB surfactants, Langmuir, 35, 13624–13635. (DOI:10.1021/acs.langmuir.9b02220)

178. Douliez J-P., Martin N., Gaillard C., Beneyton T., Baret J-C., Mann S., et al. (2017), Catanionic coacervate droplets as a surfactant-based membrane-free protocell model, Angew. Chem. Int. Ed., 56, 13689–13693. (DOI:10.1002/anie.201707139)

179. Jing B., Qiu J., Zhu Y. (2017), Organic–inorganic macroion coacervate complexation, Soft Matter, 13, 4881–4889. (DOI:10.1039/C7SM00955K)

180. Saini B., Singh R. R., Nayak D., Mukherjee T. K. (2020), Biocompatible pH-responsive luminescent coacervate nanodroplets from carbon dots and poly(diallyldimethylammonium chloride) toward theranostic applications, ACS Appl. Nano Mater., 3, 5826–5837. (DOI:10.1021/acsanm.0c00995)

181. Sing C. E., Perry S. L. (2020), Recent progress in the science of complex coacervation, Soft Matter, 16, 2885–2914, (DOI:10.1039/D0SM00001A)

182. Spalla O. (2002), Nanoparticle interactions with polymers and polyelectrolytes, Curr. Opin. Colloid Interface Sci., 7, 179−185. (DOI:10.1016/S1359-0294(02)00045-6)

183. Qi L., Chapel J-P., Castaing J-C., Fresnais J., Berret J-F. (2008), Organic versus hybrid coacervate complexes: co-assembly and adsorption properties, Soft Matter, 4, 577. (DOI:10.1039/b716178f)

184. Jing B., Qiu J., Zhu Y. (2017), Organic–inorganic macroion coacervate complexation, Soft Matter, 13, 4881–4889. (DOI:10.1039/C7SM00955K)

185. Valley B., Jing B., Ferreira M., Zhu Y. (2019), Rapid and efficient coacervate extraction of cationic industrial dyes from

wastewater, ACS Appl. Mater. Interfaces, 11, 7472–7478. (DOI:10.1021/acsami.8b21674)

186.   Chang J., Waclawik E. R. (2014), Colloidal semiconductor nanocrystals: controlled synthesis and surface chemistry in organic media, RSC Adv., 4, 23505–23527. (DOI: 10.1039/C4RA02684E)

187.   Reed M. A., Randall J. N., Aggarwal R. J., Matyi R. J., Moore T. M., Wetsel A. E. (1988), Observation of discrete electronic states in a zero-dimensional semiconductor nanostructure, Phys. Rev. Lett., 60, 535–537. (DOI: 10.1103/PhysRevLett.60.535)

188.   Alivisatos A. P. (1996), Semiconductor clusters, nanocrystals, and quantum dots, Science, 271, 933–937. (DOI: 10.1126/science.271.5251.933)

189.   Ng S. M., Koneswaran M., Narayanaswamy R. (2016), A review on fluorescent inorganic nanoparticles for optical sensing applications, RSC Adv., 6, 21624–21661. (DOI: 10.1039/C5RA24987B)

190.   Zeng Y., Kelley D. F. (2015), Two-photon photochemistry of CdSe quantum dots, ACS Nano, 9, 10471–10481. (DOI:10.1021/acsnano.5b04710)

191.   Wang X., Qu L., Zhang J., Peng X., Xiao M. (2003), Surface-related emission in highly luminescent CdSe quantum dots, Nano Lett., 3, 1103–1106, (DOI:10.1021/nl0342491)

192.   Wuister S. F., Swart I., van Driel F., Hickey S. G., de Mello Donegá C. (2003), Highly luminescent water-soluble CdTe quantum dots, Nano Lett., 3, 503–507. (DOI:10.1021/nl034054t)

193.   Sun W.-T., Yu Y., Pan H.-Y., Gao X.-F., Chen Q., Peng L.-M. (2008), CdS quantum dots sensitized TiO_2 nanotube-array photoelectrodes, J. Am. Chem. Soc., 130, 1124–1125. (DOI:10.1021/ja0777741)

194.   Yong K.-T., Law W.-C., Roy I., Jing Z., Huang H., Swihart M. T., Prasad P. N. (2011), Aqueous phase synthesis of CdTe quantum dots for biophotonics, J. Biophotonics, 4, 9–20. (DOI: 10.1002/jbio.201000080)

195. Ma Y., Zhang Y., Yu W. W. (2019), Near infrared emitting quantum dots: synthesis, luminescence properties and applications, J. Mater. Chem. C, 7, 13662–13679. (DOI: 10.1039/C9TC04065J)

196. Resch-Genger U., Grabolle M., Cavaliere-Jaricot S., Nitschke R., Nann T. (2008), Quantum dots versus organic dyes as fluorescent labels, Nat. Methods, 5, 763–775. (DOI: 10.1038/nmeth.1248)

197. Rogach A. L., Franzl T., Klar T. A., Feldmann J., Gaponik N., Lesnyak V., Shavel A., Eychmüller A., Rakovich Y. P., Donegan J. F. (2007), Aqueous synthesis of thiol-capped CdTe nanocrystals: state-of-the-art, J. Phys. Chem. C, 111, 14628–14637. (DOI: 10.1021/jp072463y)

198. Ozyurt D., Kobaisi M. A., Hocking R. K., Fox B. (2023), Properties, synthesis, and applications of carbon dots: a review, Carbon Trends, 12, 100276. (DOI:10.1016/j.cartre.2023.100276)

199. Bhattacharya A., Chatterjee S., Prajapati R., Mukherjee T. K. (2015), Size-dependent penetration of carbon dots inside the ferritin nanocages: evidence for the quantum confinement effect in carbon dots, Phys. Chem. Chem. Phys., 17, 12833–12840. (DOI:10.1039/C5CP00543D)

200. Bhattacharya A., Chatterjee S., Khorwal V., Mukherjee T. K. (2016), Luminescence turn-on/off sensing of biological iron by carbon dots in transferrin, Phys. Chem. Chem. Phys., 18, 5148–5158. (DOI:10.1039/C5CP05890B)

201. Su W., Wu H., Xu H., Zhang Y., Li Y., Li X., Fan L. (2020), Carbon dots: a booming material for biomedical applications, Mater. Chem. Front., 4, 821–836. (DOI: 10.1039/C9QM00658C)

202. Ding H., Du F., Liu P., Chen Z., Shen J. (2015), DNA–carbon dots function as fluorescent vehicles for drug delivery, ACS Appl. Mater. Interfaces, 7, 6889–6897. (DOI:10.1021/acsami.5b00628)

203. Qi J., Zhang R., Liu X. M., Liu Y., Zhang Q. M., Cheng H. Y., Li R., Wang L., Wu X. P., Li B. (2023), Carbon dots as advanced drug-delivery nanoplatforms for antiinflammatory, antibacterial,

and anticancer applications: a review, ACS Appl. Nano Mater., 6, 9071– 9084. (DOI:10.1021/acsanm.3c01207)

204. Karakoçak B. B., Liang J., Kavadiya S., Berezin M. Y., Biswas P., Ravi N. (2018), Optimizing the synthesis of red-emissive nitrogen-doped carbon dots for use in bioimaging, ACS Appl. Nano Mater., 1, 3682–3692. (DOI:10.1021/acsanm.8b00799)

205. Du J., Xu N., Fan J., Sun W., Peng X. (2019), Carbon dots for in vivo bioimaging and theranostics, Small, 15, 1805087. (DOI:10.1002/smll.201805087)

206. Yue L., Li H., Sun Q., Zhang J., Luo X., Wu F., Zhu X. (2020), Red-emissive ruthenium-containing carbon dots for bioimaging and photodynamic cancer therapy, ACS Appl. Nano Mater., 3, 869–876. (DOI:10.1021/acsanm.9b02394)

207. Ji C., Zhou Y., Leblanc R. M., Peng Z. (2020), Recent developments of carbon dots in biosensing: a review, ACS Sens., 5, 2724–2741. (DOI: 10.1021/acssensors.0c01556)

208. Chakraborty D., Sarkar S., Das P. K. (2018), Blood dots: hemoglobin-derived carbon dots as hydrogen peroxide sensors and pro-drug activators, ACS Sustainable Chem. Eng., 6, 4661–4670. (DOI:10.1021/acssuschemeng.7b03691)

209. Madonia A., Minervini G., Terracina A., Pramanik A., Martorana, V., Sciortino A., Carbonaro C. M., Olla C., Sibillano T., Giannini C., Fanizza E., Curri M. L., Panniello A., Messina F., Striccoli M. (2023), Dye-derived red-emitting carbon dots for lasing and solid-state lighting, ACS Nano, 17, 21274–21286. (DOI:10.1021/acsnano.3c05566)

210. Behera R., Sau A., Mishra L., Bera K., Mallik S., Nayak A., Basu S., Sarangi M. K. (2019), Redox modifications of carbon dots shape their optoelectronics, J. Phys. Chem. C, 123, 27937–27944. (DOI:10.1021/acs.jpcc.9b08289)

211. Li X., Yan L., Ding C., Song H., Yang Y., Ma, C. Q. (2023), Carbon dots in perovskite solar cells: properties, applications, and perspectives, Energy Fuels, 37, 876–901, (DOI:10.1021/acs.energyfuels.2c03362)

212. Hutton G. A. M., Reuillard B., Martindale B. C. M., Caputo C. A., Lockwood C. W. J., Butt J. N., Reisner E. (2016), Carbon dots as versatile photosensitizers for solar-driven catalysis with redox enzymes, J. Am. Chem. Soc., 138, 16722–16730. (DOI:10.1021/jacs.6b10146)

213. Cailotto S., Mazzaro R., Enrichi F., Vomiero A., Selva M., Cattaruzza E., Cristofori D., Amadio E., Perosa A. (2018), Design of carbon dots for metal-free photoredox catalysis, ACS Appl. Mater. Interfaces, 10, 40560–40567. (DOI:10.1021/acsami.8b14188)

214. Dong Y., Zhao H., Wang S., Cheng Q., Liu S., Li Y. (2022), Multimode anticounterfeiting labels based on a flexible and water-resistant $NaGdF_4Yb^{3+},Er^{3+}$@Carbon dots chiral fluorescent cellulose film, ACS Appl. Mater. Interfaces, 14, 40313–40321. (DOI:10.1021/acsami.2c09971)

215. Mody V. V., Siwale R., Singh A., Mody H. R. (2010), Introduction to metallic nanoparticles, J. Pharm. Bioallied Sci., 2, 282-289. (DOI: 10.4103/0975-7406.72127)

216. González A. L., Reyes-Esqueda J. A., Noguez C. (2008), Optical properties of elongated noble metal nanoparticles, J. Phys. Chem. C, 112, 7356–7362. (DOI: 10.1021/jp800432q)

217. Fong K. E., Yung L.-Y. L. (2013), Localized surface plasmon resonance: a unique property of plasmonic nanoparticles for nucleic acid detection, Nanoscale, 5, 12043–12071. (DOI: 10.1039/C3NR02257A)

218. Gedi V., Kim Y.-P. (2014), Detection and characterization of cancer cells and pathogenic bacteria using aptamer-based nano-conjugates, Sensors, 14, 18302–18327. (DOI: 10.3390/s141018302)

219. Chinen A. B., Guan C. M., Ferrer J. R., Barnaby S. N., Merkel T. J., Mirkin C. A. (2015), Nanoparticle probes for the detection of cancer biomarkers, cells, and tissues by fluorescence, Chem. Rev., 115, 10530–10574. (DOI: 10.1021/acs.chemrev.5b00321)

220. Kim Y., Smith J. G., Jain P. K. (2018), Harvesting multiple

electron-hole pairs generated through plasmonic excitation of Au nanoparticles, Nat. Chem., 10, 763–769. (DOI:10.1038/s41557-018-0054-3)

221.   Roy S., Rao A., Devatha G., Pillai P. P. (2017), Revealing the role of electrostatics in gold-nanoparticle-catalyzed reduction of charged substrates, ACS Catal., 7, 7141–7145. (DOI:10.1021/acscatal.7b02292)

222.   Deng H. H., Luo B. Y., He S. Bin, Chen R. T., Lin Z., Peng H. P., Xia X. H., Chen W. (2019), Redox recycling-triggered peroxidase-like activity enhancement of bare gold nanoparticles for ultrasensitive colorimetric detection of rare-earth Ce^{3+} ion, Anal. Chem., 91, 4039–4046. (DOI:10.1021/acs.analchem.8b05552)

223.   Cai S., Fu Z., Xiao W., Xiong Y., Wang C., Yang R. (2020), Zero-dimensional/two-dimensional Au_xPd_{100-x} nanocomposites with enhanced nanozyme catalysis for sensitive glucose detection, ACS Appl. Mater. Interfaces, 12, 11616–11624. (DOI:10.1021/acsami.9b21621)

224.   Kim Y., Torres D., Jain P. K. (2016), Activation energies of plasmonic catalysts, Nano Lett., 16, 3399–3407. (DOI:10.1021/acs.nanolett.6b01373)

225.   Zhou L., Shi H., Li Z., He, C. (2020), Recent advances in complex coacervation design from macromolecular assemblies and emerging applications, Macromol. Rapid Commun., 41, e2000149. (DOI:10.1002/marc.202000149)

226.   Mukherjee P., Padhan S. K., Dash S., Patel S., Mishra B. K. (2011), Clouding behaviour in surfactant systems, Adv. Colloid Interface Sci., 162, 59–79. (DOI:10.1016/j.cis.2010.12.005)

227.   Lu T., Spruijt E. (2020), Multiphase complex coacervate droplets, J. Am. Chem. Soc., 142, 2905–2914, (DOI:10.1021/jacs.9b1146)

228.   Wang J., Abbas M., Huang Y., Li Y. (2023), Redox-responsive peptide-based complex coacervates as delivery vehicles with controlled release of proteinous drugs, Commun. Chem., 6, 243. (DOI:10.1038/s42004-023-01044-8)

229. Ban E., Kim A. (2022), Coacervates: recent developments as nanostructure delivery platforms for therapeutic biomolecules, Int. J. Pharm., 624, 122058. (DOI: 10.1016/j.ijpharm.2022.122058)

230. Moschakis T., Biliaderis C. G. (2017), Biopolymer-based coacervates: structures, functionality and applications in food products, Curr. Opin. Colloid Interface Sci., 28, 96–109. (DOI: 10.1016/j.cocis.2017.03.006)

231. Ballesteros-Gómez A., Caballero-Casero N., García-Fonseca S., Lunar L., Rubio S. (2019), Multifunctional vesicular coacervates as engineered supramolecular solvents for wastewater treatment, Chemosphere, 223, 569–576. (DOI:10.1016/j.chemosphere.2019.02.089)

232. Liu B., Zhao W., Shen Y., Fan Y., Wang Y. (2021), Trimeric cationic surfactant coacervation as a versatile approach for removing organic pollutants, Langmuir, 37, 5993–6001. (DOI:10.1021/acs.langmuir.1c00557)

233. Liu X., Xue F., Adhikari B. (2023), Hemp protein isolate-polysaccharide complex coacervates and their application as emulsifiers in oil-in-water emulsions, Food Hydrocoll., 137, 108352. (DOI: j.foodhyd.2022.108352)

234. Xiong W., Deng Q., Li J., Li B., Zhong Q. (2020), Ovalbumin-carboxymethylcellulose complex coacervates stabilized high internal phase emulsions: comparison of the effects of pH and polysaccharide charge density, Food Hydrocoll., 98, 105282. (DOI: 10.1016/j.foodhyd.2019.105282)

235. Hiwatari Y., Yoshida K., Akutsu T., Yabu M., Iwai S. (2004), Polyelectrolyte-micelle coacervation: effect of coacervate on the properties of shampoo, Int. J. Cosmet., 26, 316–316. (DOI:10.1111/j.1467-2494.2004.00242_3.x)

236. Liu Y., Winter H. H., Perry S. L. (2016), Linear viscoelasticity of complex coacervates, Adv. Colloid Interface Sci., 239, 46–60. (DOI:10.1016/j.cis.2016.08.010)

237. Napiórkowska A., Kurek M. (2021), Coacervation as a novel method of microencapsulation of essential oils—a review, Molecules, 27, 5142. (DOI:10.3390/molecules27165142)

238. Yuan Y., Kong Z.-Y., Sun Y.-E., Zeng Q.-Z., Yang X.-Q. (2017), Complex coacervation of soy protein with chitosan: constructing antioxidant microcapsule for algal oil delivery, LWT, 75, 171–179. (DOI:10.1016/j.lwt.2016.08.045)

239. Alexandre J. D. B., Barroso T. L. C. T., Oliveira M. D. A., Mendes F. R. D. S., Costa J. M. C. D., Moreira R. D. A., Furtado R. F. (2019), Cross-linked coacervates of cashew gum and gelatin in the encapsulation of pequi oil, Cienc. Rural, 49, e20190079. (DOI:10.1590/0103-8478cr20190079)

240. Vahdati M., Cedano-Serrano F. J., Creton C., Hourdet D. (2020), Coacervate-based underwater adhesives in physiological conditions, ACS Appl. Polym. Mater., 2, 3397–3410. (DOI:10.1021/acsapm.0c00479)

241. Peng Q., Chen J., Zeng Z., Wang T., Xiang L., Peng X., Liu J., Zeng H. (2020), Adhesive coacervates driven by hydrogen-bonding interaction, Small, 16, e2004132. (DOI: 10.1002/smll.202004132)

242. Patra S., Basak P., Tibarewala D.N. (2016), Synthesis of gelatin nano/submicron particles by binary nonsolvent aided coacervation (BNAC) method, Mater. Sci. Eng. C, 59, 310–318. (DOI:10.1016/j.msec.2015.10.011)

243. Zhao W., Fan Y., Wang H., Wang Y. (2017), Coacervate of polyacrylamide and cationic gemini surfactant for the extraction of methyl orange from aqueous solution, Langmuir, 33, 6846–6856. (DOI:10.1021/acs.langmuir.7b01421)

244. Chiappisi L., Simon M., Gradzielski M. (2015), Toward bioderived intelligent nanocarriers for controlled pollutant recovery and pH-sensitive binding, ACS Appl. Mater. Interfaces, 7, 6139–6145. (DOI:10.1021/am508846r)

245. Zhao M., Zacharia N. S. (2016), Sequestration of methylene blue into polyelectrolyte complex coacervates, Macromol. Rapid Commun., 37, 1249–1255. (DOI:10.1002/marc.201600244)

246.   Keating C. D. (2012), Aqueous phase separation as a possible route to compartmentalization of biological molecules, Acc. Chem. Res., 45, 2114–2124. (DOI:10.1021/ar200294y)

247.   Martin N., Li M., Mann S. (2016), Selective uptake and refolding of globular proteins in coacervate microdroplets, Langmuir, 32, 5881–5889. (DOI:10.1021/acs.langmuir.6b01271)

248.   Timilsena Y. P., Akanbi T. O., Khalid N., Adhikari B., Barrow C. J. (2019), Complex coacervation: principles, mechanisms and applications in microencapsulation, Int. J. Biol. Macromol., 121, 1276–1286. (DOI:10.1016/j.ijbiomac.2018.10.144)

249.   Park U., Lee M. S., Jeon J., Lee S., Hwang M. P., Wang Y., Yang H. S., Kim K. (2019), Coacervate-mediated exogenous growth factor delivery for scarless skin regeneration, Acta Biomater., 90, 179–191. (DOI:10.1016/j.actbio.2019.03.052)

250.   Guo H., Song S., Dai T., Sun K., Zhou G., Li M., Mann S., Dou H. (2020), Near-infrared fluorescent and magnetic resonance dual-imaging coacervate nanoprobes for trypsin mapping and targeted payload delivery of malignant tumors, ACS Appl. Mater. Interfaces, 12, 17302–17313. (DOI:10.1021/acsami.0c03433)

251.   Sun Y., Lau S. Y., Lim Z. W., Chang S. C., Ghadessy F., Partridge A., Miserez A. (2022), Phase-separating peptides for direct cytosolic delivery and redox-activated release of macromolecular therapeutics, Nat. Chem., 14, 274–283. (DOI:10.1038/s41557-021-00854-4)

252.   Lim Z. W., Ping Y., Miserez A. (2018), Glucose-responsive peptide coacervates with high encapsulation efficiency for controlled release of insulin, Bioconj. Chem., 29, 2176–2180. (DOI:10.1021/acs.bioconjchem.8b00369)

253.   de Silva U. K., Brown J. L., Lapitsky Y. (2018), Poly(allylamine)/tripolyphosphate coacervates enable high loading and multiple-month release of weakly amphiphilic anionic drugs: an in vitro study with ibuprofen, RSC Adv., 8, 19409–19419. (DOI:10.1039/C8RA02588F)

254. Armstrong J. P. K., Olof S. N., Jakimowicz M. D., Hollander A. P., Mann S., Davis S. A., et al. (2015), Cell paintballing using optically targeted coacervate microdroplets, Chem. Sci., 6, 6106–6111. (DOI:10.1039/C5SC02266E)

255. Xiao W., Jakimowicz M. D., Zampetakis I., Neely S., Scarpa F., Davis S. A., et al. (2020), Biopolymeric coacervate microvectors for the delivery of functional proteins to cells, Adv. Biosys., 4, 2000101. (DOI:10.1002/adbi.202000101)

256. Zhao P., Xia X., Xu X., Leung K. K. C., Rai A., Deng Y., et al. (2021), Nanoparticle-assembled bioadhesive coacervate coating with prolonged gastrointestinal retention for inflammatory bowel disease therapy, Nat. Commun., 12, 7162. (DOI:10.1038/s41467-021-27463-6)

257. Barthold S., Kletting S., Taffner J., de Souza Carvalho-Wodarz C., Lepeltier E., Loretz B., Lehr C.-M. (2016), Preparation of nanosized coacervates of positive and negative starch derivatives intended for pulmonary delivery of proteins, J. Mater. Chem. B, 4, 2377–2386. (DOI:10.1039/C6TB00178E)

258. Martin N., Tian L., Spencer D., Coutable-Pennarun A., Anderson JLR., Mann S. (2019), Photoswitchable phase separation and oligonucleotide trafficking in DNA coacervate microdroplets, Angew. Chem. Int. Ed., 58, 14594–14598. (DOI:10.1002/anie.201909228)

259. Hasanvand E., Rafe A. (2019), Development of vanillin/β-cyclodexterin inclusion microcapsules using flax seed gum-rice bran protein complex coacervates, Int. J. Biol. Macromol., 131, 60–66. (DOI:10.1016/j.ijbiomac.2019.03.066)

260. Rocha-Selmi G. A., Bozza F. T., Thomazini M., Bolini H. M., Fávaro-Trindade C. S. (2013), Microencapsulation of aspartame by double emulsion followed by complex coacervation to provide protection and prolong sweetness, Food Chem., 139, 72-78. (DOI:10.1016/j.foodchem.2013.01.114)

261. Calderón-Oliver M., Pedroza-Islas R., Escalona-Buendía H. B., Pedraza-Chaverri J., Ponce-Alquicira E. (2016), Comparative study

of the microencapsulation by complex coacervation of nisin in combination with an avocado antioxidant extract, Food Hydrocoll., 62, 49–57. (DOI:10.1016/j.foodhyd.2016.07.028)

262.   Bayabil H. K., Teshome F. T., Li Y. C. (2022), Emerging contaminants in soil and water, Front. Environ. Sci., 10, 873499. (DOI:10.3389/fenvs.2022.873499)

263.   Ojea-Jiménez I., López X., Arbiol J., Puntes V. (2012), Citrate-coated gold nanoparticles as smart scavengers for mercury(II) removal from polluted waters, ACS Nano, 6, 2253–2260. (DOI:10.1021/nn204313a)

264.   Shah K.J., Imae, T. (2016), Selective gas capture ability of gas-adsorbent-incorporated cellulose nanofiber films, Biomacromolecules, 17, 1653–1661. (DOI: 10.1021/acs.biomac.6b00065)

265.   Liu X., Zhou Y., Zhang J., Tang L., Luo L., Zeng G. (2017), Iron containing metal–organic frameworks: structure, synthesis, and applications in environmental remediation, ACS Appl. Mater. Interfaces, 9, 20255–20275. (DOI:10.1021/acsami.7b02563)

266.   Saini D., Aggarwal R., Sonker A. K., Sonkar S. K. (2021), Photodegradation of azo dyes in sunlight promoted by nitrogen−sulfur−phosphorus codoped carbon dots, ACS Appl. Nano Mater., 4, 9303−9312. (DOI: 10.1021/acsanm.1c01810)

267.   Yen C. W., Mahmoud M. A., El-Sayed M. A. (2009), Photocatalysis in gold nanocage nanoreactors, J. Phys. Chem. A, 113, 4340–4345. (DOI:10.1021/jp811014u)

268.   Shaban M., Ashraf A. M., Abukhadra M. R. (2018), TiO_2 nanoribbons/carbon nanotubes composite with enhanced photocatalytic activity; fabrication, characterization, and application, Sci. Rep. 2018, 8, 1–17. (DOI:10.1038/s41598-018-19172-w)

269.   Zou Y., Xiao K., Qin Q., Shi J. W., Heil T., Markushyna Y., Jiang L., Antonietti M., Savateev A. (2021), Enhanced organic photocatalysis in confined flow through a carbon nitride nanotube

membrane with conversions in the millisecond regime, ACS Nano, 15, 6551–6561. (DOI: 10.1021/acsnano.0c09661)

270. Sousa-Castillo A., Couceiro J. R., Tomás-Gamasa M., Mariño-López, A., López F., Baaziz W., Ersen O., Comesaña-Hermo M., Mascareñas J. L., Correa-Duarte M. A. (2020), Remote activation of hollow nanoreactors for heterogeneous photocatalysis in biorelevant media, Nano Lett., 20, 7068–7076. (DOI: 10.1021/acs.nanolett.0c02180)

271. Yu Z., Lu X., Sun L., Xiong J., Ye L., Li X., Zhang R., Ji N. (2021), Metal-loaded hollow carbon nanostructures as nanoreactors: microenvironment effects and prospects for biomass hydrogenation applications, ACS Sustain. Chem. Eng., 9, 2990–3010. (DOI:10.1021/acssuschemeng.0c08422)

272. Li A., Zhu W., Li C., Wang T., Gong J. (2019), Rational design of yolk-shell nanostructures for photocatalysis, Chem. Soc. Rev., 48, 1874–1907. (DOI:10.1039/C8CS00711J)

273. Chen Y. A., Wang Y. T., Moon, H. S., Yong K., Hsu Y. J. (2021), Yolk-shell nanostructures: synthesis, photocatalysis and interfacial charge dynamics, RSC Adv., 11, 12288–12305. (DOI: 10.1039/D1RA00803J)

274. Li H., Yang Y., He C., Zeng L., Duan C. (2019), Mixed-ligand metal-organic framework for two-photon responsive photocatalytic C-N and C-C coupling reactions, ACS Catal., 9, 422–430. (DOI: 10.1021/acscatal.8b03537)

275. Chen L. W., Hao Y. C., Guo Y., Zhang Q., Li J., Gao W. Y., Ren L., Su X., Hu L., Zhang N., Li S., Feng X., Gu L., Zhang Y. W., Yin A. X., Wan, B. (2021), Metal-organic framework membranes encapsulating gold nanoparticles for direct plasmonic photocatalytic nitrogen fixation, J. Am. Chem. Soc., 143, 5727–5736. (DOI: 10.1021/jacs.0c13342)

276. Wang H., Wang H., Wang Z., Tang L., Zeng G., Xu P., Chen M., Xiong T., Zhou C., Li X., Huang D., Zhu Y., Wang Z., Tang J. (2020), Covalent organic framework photocatalysts: structures and

applications, Chem. Soc. Rev., 49, 4135–4165. (DOI:10.1039/D0CS00278J)

277. Sun D., Kim D. P. (2020), Hydrophobic MOFs@metal nanoparticles@COFs for interfacially confined photocatalysis with high efficiency, ACS Appl. Mater. Interfaces 2020, 12, 20589–20595. (DOI:10.1021/acsami.0c04537)

278. Jiao J., Tan C., Li Z., Liu Y., Han X., Cui Y. (2018), Design and assembly of chiral coordination cages for asymmetric sequential reactions, J. Am. Chem. Soc. 2018, 140, 2251–2259. (DOI:10.1021/jacs.7b11679)

279. Eibner A. J. C.-Z. (1911), Action of light on pigments I. Chem-Ztg, 35, 753–755.

280. Zhu S., Wang D. (2017), Photocatalysis: basic principles, diverse forms of implementations and emerging scientific opportunities, Adv. Energy Mater., 7, 1700841 (DOI: 10.1002/aenm.201700841)

281. Yuan L., Zhou J. Y., Zhang M., Wen X. L., Martirez J. M. P., Robatjazi H., Zhou L. A., Carter E. A., Nordlander P., Halas N. J. (2022), Plasmonic photocatalysis with chemically and spatially specific antenna-dual reactor complexes, ACS Nano, 16, 17365–17375. (DOI:10.1021/acsnano.2c08191)

282. Prier C. K., Rankic D. A., MacMillan D. W. C. (2013), Visible light photoredox catalysis with transition metal complexes: applications in organic synthesis, Chem. Rev., 113, 5322–5363. (DOI:10.1021/cr300503r)

283. Fang Y., Xiao Z., Kirchon A., Li J., Jin F., Togo T., Zhang L., Zhu C., Zhou H. C. (2019), Bimolecular proximity of a ruthenium complex and methylene blue within an anionic porous coordination cage for enhancing photocatalytic activity, Chem. Sci., 10, 3529–3534. (DOI:10.1039/C8SC05315D)

284. Wang Z. S., Sayama K., Sugihara H. (2005), Efficient eosin Y dye-sensitized solar cell containing Br^-/Br^{3-} electrolyte, J. Phys. Chem. B, 109, 22449– 22455. (DOI:10.1021/jp053260h)

285. Haria D. P., König B. (2014), Synthetic applications of eosin Y in photoredox catalysis, Chem. Commun., 50, 6688 (DOI:10.1039/C4CC00751D)

286. Diercxsens N. (2017), Eosin Y, Encyclopedia of Reagents for Organic Synthesis, Chichester, UK: John Wiley & Sons, Ltd, 1–3. (DOI:10.1002/047084289x.rn02033)

287. Ravelli D., Fagnoni M., Albini A. (2013), Photoorganocatalysis. what for?, Chem. Soc. Rev., 42, 97–113. (DOI:10.1039/C2CS35250H)

288. Nicewicz D. A., Nguyen T. M. (2014), Recent applications of organic dyes as photoredox catalysts in organic synthesis, ACS Catal., 4, 355–360. (DOI:10.1021/cs400956a)

289. Cantillo D., de Frutos O., Rincon J. A., Mateos C., Kappe, C. O. (2014), Continuous flow alpha-trifluoromethylation of Ketones by metal-free visible light photoredox catalysis, Org. Lett., 16, 896–899. (DOI:10.1021/ol403650y)

290. Murakami H., Kawabuchi A., Kotoo K., Kunitake M., Nakashima N. (1997), A light-driven molecular shuttle based on a rotaxane, J. Am. Chem. Soc., 119, 7605–7606. (DOI: 10.1021/ja971438a)

291. De Boni L., Piovesan E., Misoguti L., Zílio S. C., Mendonca C. R. (2007), Two-photon absorption dependence on the temperature for azoaromatic compounds: effect of molecular conformation, J. Phys. Chem. A, 111, 6222–6224. (DOI: 10.1021/jp0716684)

292. dos Santos D. S. Jr., Bassi A., Rodrigues, J. J. Jr., Misoguti L., Oliveira O. N. Jr., Mendonca C. R. (2003), Light-induced storage in layer-by-layer films of chitosan and an azo dye, Biomacromolecules, 4, 1502–1505. (DOI:10.1021/bm025754f)

293. Bafana A., Devi S. S., Chakrabarti T. (2011), Azo dyes: past, present and the future, Environ. Rev., 19, 350–371. (DOI: 10.1139/a11-018)

294. Merino E. (2011), Synthesis of azobenzenes: the coloured pieces of molecular materials, Chem. Soc. Rev., 40, 3835–3853. (DOI: 10.1039/C0CS00183J)

295. Saha A., Payra S., Selvaratnam B., Bhattacharya S., Pal S., Koodali R. T., Banerjee S. (2018), Hierarchical mesoporous RuO_2/Cu_2O nanoparticle-catalyzed oxidative homo/hetero azo-coupling of anilines, ACS Sustainable Chem. Eng., 6, 11345–11352. (DOI:10.1021/acssuschemeng.8b01179)

296. Zou Y., Zhang M., Cao F., Li J., Zhang S., Qu Y. (2021), Single crystal MnOOH nanotubes for selective oxidative coupling of anilines to aromatic azo compounds, J. Mater. Chem. A 2021, 9, 19692–19697. (DOI:10.1039/D1TA04415J)

297. Han S., Cheng Y., Liu S., Tao C., Wang A., Wei W., Yu H., Wei Y. (2021), Selective oxidation of anilines to azobenzenes and azoxybenzenes by a molecular Mo oxide catalyst, Angew. Chem., Int. Ed., 60, 6382–6385. (DOI:10.1002/anie.202013940)

298. Qin J., Long Y., Sun F., Zhou P.-P., Wang W. D., Luo N., Ma J. (2022), $Zr(OH)_4$-catalyzed controllable selective oxidation of anilines to azoxybenzenes, azobenzenes and nitrosobenzenes, Angew. Chem., Int. Ed., 61, e202112907. (DOI:10.1002/anie.202112907)

299. Zhu H., Ke X., Yang X., Sarina S., Liu H. (2010), Reduction of nitroaromatic compounds on supported gold nanoparticles by visible and ultraviolet light, Angew. Chem., Int. Ed., 49, 9657–9661. (DOI:10.1002/anie.201003908)

300. Guo X., Hao C., Jin G., Zhu H.-Y., Guo X.-Y. (2014), Copper nanoparticles on graphene support: an efficient photocatalyst for coupling of nitroaromatics in visible light, Angew. Chem., Int. Ed. 53, 1973–1977. (DOI:10.1002/anie.201309482)

301. Mondal B., Mukherjee P. S. (2018), Cage encapsulated gold nanoparticles as heterogeneous photocatalyst for facile and selective reduction of nitroarenes to azo compounds, J. Am. Chem. Soc., 140, 12592–12601. (DOI:10.1021/jacs.8b07767)

302. Dai Y., Li C., Shen Y., Lim T., Xu J., Li Y., Nie-mantsverdriet H., Besenbacher F., Lock N., Su R. (2018), Light-tuned selective photosynthesis of azo- and azoxy-aromatics using graphitic C_3N_4, Nat. Commun., 9, 60. (DOI:10.1038/s41467-017-02527-8)

303. Sitter J. D., Vannucci A. K. (2021), Photocatalytic oxidative coupling of arylamines for the synthesis of azoaromatics and the role of O_2 in the mechanism, J. Am. Chem. Soc., 143, 2938–2943. (DOI:10.1021/jacs.0c13101)

304. Agarwal P. K. (2006), Enzymes: an integrated view of structure, dynamics and function, Microb. Cell Factories, 5, 2. (DOI:10.1186/1475-2859-5-2)

305. Espinosa-Cantú A., Cruz-Bonilla E., Noda-Garcia L., DeLuna A. (2020), Multiple forms of multifunctional proteins in health and disease, Front. Cell Dev. Biol., 8, 451. (DOI:10.3389/fcell.2020.00451)

306. Knowles J. R. (1991), Enzyme catalysis: not different, just better, Nature, 350, 121–124. (DOI:10.1038/350121a0)

307. Callender R., Dyer R. B. (2015), The dynamical nature of enzymatic catalysis. Acc. Chem. Res., 48, 407–413. (DOI:10.1021/ar5002928)

308. Hauer B. (2020), Embracing nature's catalysts: a viewpoint on the future of biocatalysis, ACS Catal., 10, 8418–8427. (DOI:10.1021/acscatal.0c01708)

309. Huang Y., Ren J., Qu X. (2019), Nanozymes: classification, catalytic mechanisms, activity regulation, and applications, Chem. Rev., 119, 4357– 4412. (DOI:10.1021/acs.chemrev.8b00672)

310. Qiu N., Liu Y., Guo R. (2020), Electrodeposition-assisted rapid preparation of Pt nanocluster/3D graphene hybrid nanozymes with outstanding multiple oxidase-like activity for distinguishing colorimetric determination of dihydroxybenzene isomers, ACS Appl. Mater. Interfaces, 12, 15553–15561. (DOI: 10.1021/acsami.9b23546)

311. Kim M. S., Cho S., Joo S. H., Lee J., Kwak S. K., Kim M. Il, Lee J. (2019), N- and B-codoped graphene: a strong candidate to replace natural peroxidase in sensitive and selective bioassays, ACS Nano, 13, 4312–4321. (DOI:10.1021/acsnano.8b09519)

312. Wu G., Berka V., Derry P. J., Mendoza K., Kakadiaris E., Roy T., Kent T. A., Tour J. M., Tsai A. L. (2019), Critical comparison of

the superoxide dismutase-like activity of carbon antioxidant nanozymes by direct superoxide consumption kinetic measurements, ACS Nano, 13, 11203–11213. (DOI:10.1021/acsnano.9b04229)

313.   Hu M., Korschelt K., Daniel P., Landfester K., Tremel W., Bannwarth M. B. (2017), Fibrous nanozyme dressings with catalase-like activity for H_2O_2 reduction to promote wound healing, ACS Appl. Mater. Interfaces, 9, 38024–38031. (DOI:10.1021/acsami.7b12212)

314.   Gao L., Zhuang J., Nie L., Zhang J., Zhang Y., Gu N., Wang T., Feng J., Yang D., Perrett S., Yan X. (2007), Intrinsic peroxidase-like activity of ferromagnetic nanoparticles, Nat. Nanotechnol., 2, 577–583. (DOI:10.1038/nnano.2007.260)

315.   Zhao H., Dong Y., Jiang P., Wang G., Zhang J. (2015), Highly dispersed CeO_2 on TiO_2 nanotube: a synergistic nanocomposite with superior peroxidase-like activity, ACS Appl. Mater. Interfaces, 7, 6451–6461. (DOI:10.1021/acsami.5b00023)

316.   Nagvenkar A. P., Gedanken A. (2016), $Cu_{0.89}Zn_{0.11}O$, a new peroxidase-mimicking nanozyme with high sensitivity for glucose and antioxidant detection, ACS Appl. Mater. Interfaces, 8, 22301–22308. (DOI:10.1021/acsami.6b05354)

317.   Ding W., Liu H., Zhao W., Wang J., Zhang L., Yao Y., Yao C., Song C. (2020), A hybrid of FeS_2 nanoparticles encapsulated by two-dimensional carbon sheets as excellent nanozymes for colorimetric glucose detection, ACS Appl. Bio Mater., 3, 5905–5912. (DOI:10.1021/acsabm.0c00605)

318.   Ali S. R., De M. (2021), Thiolated ligand-functionalized MoS_2 nanosheets for peroxidase-like activities, ACS Appl. Nano Mater., 4, 12682–12689. (DOI:10.1021/acsanm.1c03242)

319.   Chen H., Yuan C., Yang X., Cheng X., Elzatahry A. A., Alghamdi A., Su J., He X., Deng Y. (2020), Hollow mesoporous carbon nanospheres loaded with Pt nanoparticles for colorimetric detection of ascorbic acid and glucose, ACS Appl. Nano Mater., 3, 4586–4598. (DOI:10.1021/acsanm.0c00638)

320. Zhang P., Sun D., Cho A., Weon S., Lee S., Lee J., Han J. W., Kim D. P., Choi W. (2019), Modified carbon nitride nanozyme as bifunctional glucose oxidase-peroxidase for metal-free bioinspired cascade photocatalysis, Nat. Commun., 10, 1–14. (DOI:10.1038/s41467-019-08731-y)

321. Fan Y., Zhang W., Liu Y., Zeng Z., Quan X., Zhao H. (2019), Three-dimensional branched crystal carbon nitride with enhanced intrinsic peroxidase-like activity: a hypersensitive platform for colorimetric detection, ACS Appl. Mater. Interfaces, 11, 17467–17474. (DOI:10.1021/acsami.9b04320)

322. Zheng H. Q., Liu C. Y., Zeng X. Y., Chen J., Lü J., Lin R. G., Cao R., Lin Z. J., Su J. W. (2018), MOF-808: a metal-organic framework with intrinsic peroxidase-like catalytic activity at neutral pH for colorimetric biosensing, Inorg. Chem., 57, 9096–9104. (DOI:10.1021/acs.inorgchem.8b01097)

323. Xu W., Jiao L., Yan H., Wu Y., Chen L., Gu W., Du D., Lin Y., Zhu C. (2019), Glucose oxidase-integrated metal-organic framework hybrids as biomimetic cascade nanozymes for ultrasensitive glucose biosensing, ACS Appl. Mater. Interfaces, 11, 22096–22101. (DOI:10.1021/acsami.9b03004)

324. Yang Y., Gong Y., Li X., Li M., Wei Q., Zhou B., Zhang J. (2022), Alkaline-stable peroxidase mimics based on biological metal-organic frameworks for recyclable scavenging of hydrogen peroxide and detecting glucose in apple fruits, ACS Sustain. Chem. Eng., 10, 10685–10698. (DOI:10.1021/acssuschemeng.2c03184)

325. Mouarrawis V., Plessius R., Ivar J., Reek J. N. (2018), Confinement effects in catalysis using well-defined materials and cages, Front. Chem., 6, 419863. (DOI:10.3389/fchem.2018.00623)

326. Bauer J. A., Zámocká M., Majtán J., Bauerová-Hlinková V. (2022), Glucose oxidase, an enzyme "Ferrari": Its structure, function, production and properties in the light of various industrial and biotechnological applications, Biomolecules, 12, 472. (DOI:10.3390/biom12030472)

Chapter 2

Materials, Sample Preparation, and Experimental Techniques

2.1. Introduction

This chapter contains a detailed description of all the chemicals utilized during the thesis work. Complete synthetic procedures of QDs, CDs, and Au NPs, along with the different types of coacervates, such as QD-, CD-, and ATP-coacervates, have been discussed here. This chapter also covers the detailed sample preparation, experimental procedures, techniques, and instruments involved during the entire work of the thesis.

2.2. Chemicals

Cadmium chloride ($CdCl_2$), sodium tellurite (Na_2TeO_3), sodium chloride (NaCl), cetyltrimethylammonium bromide (CTAB), sodium dodecyl sulfate (SDS), TritonX-100 (TX-100), potassium phosphate (K_3PO_4), rhodamine B isothiocyanate (RBITC), sucrose, lactose, glucose, mannose, maltose, ethylenediamine (99.5%), potassium ferricyanide ($K_3[Fe(CN)_6]$), chloroform-d ($CDCl_3$), ethylacetate, potassium bromide (KBr), rhodamine 6G (Rh6G), hydrochloric acid (HCl), tris(hydroxymethyl)aminomethane, glucose oxidase (GOx), adenosine triphosphate (ATP), 2,6-Di-tert-butyl-4-methylphenol (BHT), mercaptosuccinic acid (MSA), sodium hydroxide (NaOH), potassium chloride (KCl), rhodamine B (RhB), trisodium citrate dihydrate, methylene blue (MB), hellmanex III, poly(diallyldimethylammonium chloride) (PDADMAC, MW = 100000−200000), and the Pur-A-Lyzert dialysis kit (molecular weight cutoff 3.5 kDa) were purchased from Sigma-Aldrich. Sodium borohydride, *p*-anisidine, Eosin yellow (Eosin Y/EY), 1,4-diazabicyclo[2.2.2]octane (DABCO), potassium hydroxide (KOH), *p*-bromoaniline, 3,4-dimethylaniline, aniline, and phosphotungstic acid (PTA) were procured from SRL. H_2O_2 test strips (MQuant test peroxide) were purchased from Supelco, Sigma-Aldrich. Potassium dichromate ($K_2Cr_2O_7$) was purchased from Finar Chemicals Limited. 2,2'-Azinobis(3-ethylbenothiazoline-6-sulfonic acid]-diammonium salt

(ABTS), *p*-chloroaniline, 5,5-dimethyl-1-pyrroline N-oxide (DMPO), and *p*-toluidine were procured from TCI.

Lead nitrate (Pb(NO$_3$)$_2$), nickel nitrate hexahydrate (Ni(NO$_3$)$_2$·6H$_2$O), zinc chloride (ZnCl$_2$), iron sulfate heptahydrate (FeSO$_4$.7H$_2$O), *o*-phenylenediamine (OPD), iron chloride anhydrous (FeCl$_3$), ethanol (EtOH), citric acid monohydrate (99.5%), methanol (MeOH), silver nitrate (AgNO$_3$), benzoquinone (BQ), ethylenediaminetetraacetic acid (EDTA), sodium dihydrogen phosphate monohydrate (NaH$_2$PO$_4$.H$_2$O), dimethyl sulfoxide, acetic acid (CH$_3$COOH), sodium acetate trihydrate (CH$_3$COONa.3H$_2$O), sodium bicarbonate (NaHCO$_3$), sodium carbonate anhydrous (Na$_2$CO$_3$), and disodium hydrogen phosphate heptahydrate (Na$_2$HPO$_4$.7H$_2$O) terephthalic acid (TA), chromium nitrate nonahydrate (Cr(NO$_3$)$_3$), ethyl acetate, and mercury chloride (HgCl$_2$) were purchased from Merck (India). 3,3',5,5'-Tetramethylbenidine (TMB), *p*-nitroaniline, *p*-phenylenediamine (PPD), *o*-phenylenediamine (OPD), *p*-nitroaniline, and hydrogen peroxide (H$_2$O$_2$) were procured from Loba Chemie (India). 3,5-dimethoxyaniline, 5,6,7,8-tetrahydro-2-naphthylamine, and *o*-methoxyaniline hydrochloride were procured from BLD Pharmatech, India. Milli-Q water was obtained from a Millipore water purifier system (Milli-Q integral).

2.3. Synthetic procedures

2.3.1. Synthesis of MSA-capped CdTe QDs

MSA-capped CdTe QDs were synthesized using an earlier reported method *[1, 2]*. Briefly, 0.04 M CdCl$_2$ in 4 mL was diluted to 50 mL in a one-necked flask and then Na$_2$TeO$_3$ (0.01 M, 1 mL), trisodium citrate dihydrate (100 mg), mercaptosuccinic acid (50 mg), and NaBH$_4$ (100 mg) were added with continuous stirring at room temperature. When the color of the mixture changed to green, the flask was attached to a condenser and refluxed under open-air conditions for 0.5 and 5.0 h to obtain green and red QDs, respectively. The reaction mixtures were

purified using dialysis (molecular weight cutoff 3.5 kDa) against Milli-Q water for 24 h to remove excess free MSA ligands and unreacted starting materials. The purified dispersions of CdTe QD were kept at 4°C for further use. The stock concentration of QD was calculated using earlier reported literature [1, 2].
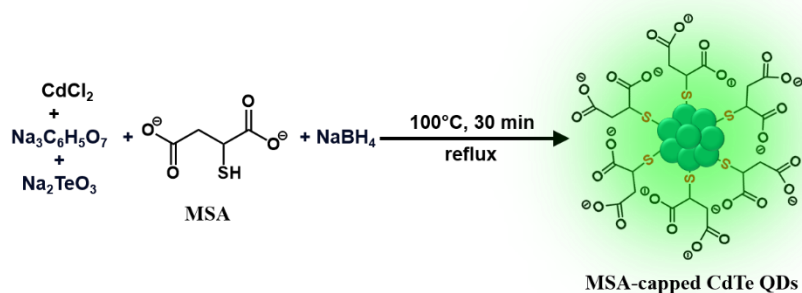
Scheme 2.1. Synthesis of MSA-capped CdTe QDs.

2.3.2. Synthesis of blue emissive CDs

Colloidal CDs were synthesized according to the earlier reported hydrothermal method [3, 4]. In a typical synthesis, 1.015 g of citric acid was dissolved in 10 mL of Milli-Q water by ultrasonication for 5 min. Thereafter, 335 μL of ethylenediamine was added to it and further sonicated for 5 min. The solution was transferred to a 25 mL Teflon-padded autoclave and heated at 200 °C for 5 h (Scheme 2.2). Subsequently, the reactor was cooled down to room temperature naturally, and the solution was dialyzed by using a Pur-A-Lyzer dialysis kit (molecular weight cutoff 3.5 kDa) to remove excess free reactants from the reaction mixture.
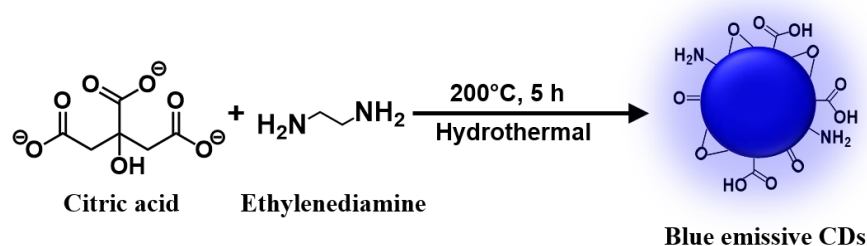
Scheme 2.2. Synthesis of blue emissive CDs.

2.3.3. Synthesis of citrate-capped Au NPs

Briefly, 486 μL of 1% (w/v) HAuCl$_4$ was added in 45 mL water kept in an ice bath with constant stirring. Subsequently, 1 mL of 1% (w/v) Na$_3$C$_6$H$_5$O$_7$ was added to the above mixture after 1 min (Scheme 2.3). Next, 500 μL of 0.075% (w/v) NaBH$_4$ was added to the above mixture and was stirred for 5 min. The as-prepared Au NPs were kept at 4 °C for further use.
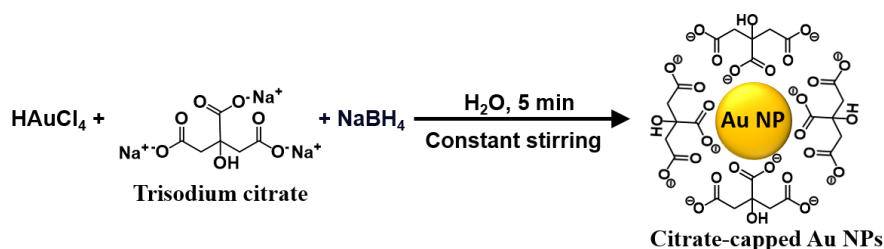
Scheme 2.3. Synthesis of citrate-capped Au NPs.

2.3.4. Formulation of QD-embedded coacervate droplets (QD-Ds)

All the samples were prepared in aqueous solution (pH 7) at room temperature. QD-embedded coacervates (QD-Ds) were fabricated by simple mixing of 65 μM of PDADMAC and 170 nM of QDs in Milli-Q water. The aqueous binary mixture was further equilibrated for 4 h at constant stirring before performing any experiments.

2.3.5. Formulation of Au@QD-Ds.

Au NPs incorporated hybrid droplets were fabricated using QD-Ds as a template as well as a reducing agent. First, QD-Ds were fabricated via simple mixing of PDADMAC (65 μM) and QDs (170 nM) in aqueous solution and equilibrated for 4 h. Next, to the as-prepared QD-Ds, 300 μM HAuCl$_4$ was added with constant stirring. A spontaneous color change from colorless to wine-red color was observed, indicating the in situ formation of Au NPs inside these QD-Ds.

2.3.6. Formulation of CD-embedded coacervates droplets (CD-Ds)

CD-embedded coacervates were fabricated at room temperature by equilibrating the aqueous binary mixture of 0.06 mg/mL CDs and 32 μM PDADMAC at pH 10 for 12 h *[4]*. The pH was controlled with 0.1 M NaOH. The equilibrated coacervate dispersion was purified from

free CDs and PDADMAC by centrifugation (10000 rpm, 30 min). Finally, the purified droplets were further redispersed by pH 10 aqueous medium.

2.3.7. Formulation of ATP coacervate droplets (ATP-Ds)

Similarly, ATP coacervates were fabricated by mixing 50 μM PDADMAC and 16.5 μM ATP in the aqueous solution (pH 7) at room temperature. The aqueous binary mixture was further equilibrated for ~1 h at constant stirring *[5]*. The coacervated phase was obtained by centrifugation at 8000 rpm for 15 min and further redispersed by Milli-Q water.

2.4. Sample preparations and experimental procedures

2.4.1. Calculation of PL quantum yield

The relative PL QY of CdTe QDs was calculated w.r.t rhodamine 6G ($\phi = 0.95$) as a reference in aqueous medium from the equation:

$$\phi_{QD} = \phi_R \left(\frac{I_{QD}}{I_R}\right) \left(\frac{\eta_{QD}^2}{\eta_R^2}\right) \left(\frac{OD_R}{OD_{QD}}\right) \tag{1}$$

Where η, I, ϕ, stand for the refractive index of solvent, integrated PL intensity, and PL QY, respectively. Here, OD corresponds to the absorption value at the excitation wavelength, whereas the subscript "QD" corresponds to the QD sample, and "R" corresponds to the reference sample.

2.4.2. Preparation of Buffer Solutions

The buffer solutions of different pH (2, 5, 6, 7.4, 9, and 11) were prepared using Milli-Q water. The strength of all the buffers were kept constant at 10 mM. Citric acid-disodium phosphate buffer (pH = 2), acetate buffer (pH = 5), phosphate buffer (pH = 6 and 7.4), tris buffer (pH = 9), and carbonate-bicarbonate buffer (pH = 11) were utilized during the course of the study.

2.4.3. Limit of detection (LOD) of Hg^{2+} and glucose

The Limit of detection (LOD) for Hg^{2+} and glucose was calculated by using the following equation;

$$LOD = 3\left(\frac{SD}{K_{SV}}\right)$$

Where SD is the standard deviation of blank QD-Ds and Au@QD-Ds solution over five different measurements and K_{sv} is the Stern–Volmer constant obtained from linear PL quenching and absorbance plot during the concentration-dependent detection of Hg^{2+} and glucose.

2.4.4. Partitioning of solutes (ferricyanide, RhB, and MB) in coacervate droplets

In brief, we first prepared an aqueous stock solution of 30 mM Fe^{3+}. Next, 250 μM of Fe^{3+} was added individually to CD-Ds, ATP-Ds, and QD-Ds solution. This mixture was then equilibrated at room temperature for ~1 h. Finally, the mixture was centrifuged at 16,000 rpm for 20 min to obtain the Fe^{3+}-loaded droplets. The effective concentration of encapsulated Fe^{3+} in the coacervate phase and free Fe^{3+} in the supernatant was calculated using UV-vis spectroscopy.

Similarly, 5 μM of RhB and MB were added individually to the QD-embedded coacervates. This mixture was then equilibrated at room temperature for ~1 h. Finally, the mixture was centrifuged at 16,000 rpm for 20 min to obtain the RhB and MB-loaded droplets.

The equilibrium partition coefficient (K) was calculated using the equation:

$$K = \frac{[\text{Substrate}]_{\text{Coacervates}}}{[\text{Substrate}]_{\text{Supernatant}}} \qquad (2)$$

2.4.5. Photocatalytic reduction of ferricyanide to ferrocyanide

All the photocatalytic reduction experiments were carried out in a 3.5 mL quartz cuvette under the irradiation of two blue or green LEDs (6W each) and the cuvette was placed at a distance of 14 cm from the LEDs at both sides. All the experiments were performed in aqueous medium pH 7, and the temperature of the reaction mixture was established with the help of a constant temperature water bath. Every single experiment was performed in the presence of 0.66 M EtOH unless stated

otherwise. In a typical experiment, 170 nM QD-Ds or 0.06 mg/mL CD-Ds (3 mL), EtOH (0.66 M), and Fe^{3+} (230 μM) were mixed in a 3.5 ml quartz cuvette and purged with N_2 for 10 min. The reaction mixture was then further incubated for 15-20 min to equilibrate at a particular temperature under dark conditions before light irradiation. Photoreduction of ferricyanide was observed by monitoring the absorbance of the reaction mixture using the fast scan mode at 5 min intervals for 40 min using a varian UV−vis spectrophotometer.

2.4.6. Photocatalytic degradation of RhB and MB

All the photocatalytic dye degradation experiments were carried out in a 3.5 mL quartz cuvette under the irradiation of three blue LEDs (6W each) and the cuvette was placed at a distance of 10 cm from the LEDs. All the experiments were performed in aqueous medium pH ~7 at room temperature. In a typical experiment, 170 nM QD-Ds were incubated with 5 μM of RhB and MB in a 3.5 ml quartz cuvette to fabricate the RhB and MB-loaded droplets. Next, 80 mM H_2O_2 was added to the dye-loaded droplets and incubated for 30 min under dark prior to light irradiation in the photocatalytic chamber. Photocatalytic degradation of RhB and MB was observed by monitoring the absorbance of the reaction mixture at 554 nm and 654 nm, respectively, using a varian UV−vis spectrophotometer.

2.4.7. Glucose sensing in the solution phase

The colorimetric detection of glucose in the solution phase was checked using GOx/Au@QD-D composite by varying the glucose concentrations in the range of 0–500 μM. Initially, 250 nM GOx and 600 μM TMB were mixed with Au@QD-Ds and equilibrated for 12 h at room temperature to get TMB and GOx loaded Au@QD-Ds (GOx/Au@QD-D). Subsequently, O_2 gas was purged in the reaction mixture for 15 min. Finally, glucose solution was added to the mixture and the colorimetric changes of TMB to ox-TMB were observed using UV-vis spectroscopy.

2.4.8. Glucose sensing on Whatman filter paper

TMB and GOx loaded GOx/Au@QD-Ds were fabricated by mixing TMB and GOx to Au@QD-D solution and equilibrating it for 12 h at room temperature. The above mixture was then deposited on Whatman filter paper and dried at 37 °C. Subsequently, the GOx/Au@QD-D-loaded filter papers were soaked in O_2-purged solutions of glucose (0–500 µM) and daylight photographs were taken.

2.4.9. Interactions of EY with different surfactants

The interactions of negatively charged EY were studied with different surfactants like CTAB (positively charged), SDS (negatively charged), and TX-100 (neutral). Initially, 2 µM EY was added to the different concentrations of CTAB (0–10 mM) and the solution was incubated for 10 min before taking any measurements. Subsequently, the absorption spectra of the above mixtures were recorded. Similarly, the emission spectra of the EY@CTAB mixtures were recorded by exciting the samples at $\lambda_{ex} = 510$ nm, and the emission was recorded in the range of 520–700 nm.

2.4.10. Photocatalytic synthesis of azo compounds

Initially, 40 mM CTAB micellar solution was prepared by dissolving an appropriate amount of CTAB in 5 mL Milli-Q water. Subsequently, 0.6 mol% Eosin Y was added to the above solution and equilibrated for 5 minutes. Next, 0.05 mmol amine substrate and 2 equiv. K_3PO_4 were added to the above solution. The reaction mixture was then irradiated for 4 h with green LED ($\lambda = 525$ nm) inside a homemade photocatalytic reactor equipped with a portable fan under ambient conditions. The reaction mixture was extracted with diethyl ether after completion and washed several times with water and then dried using anhydrous sodium sulfate. The solvent was evaporated using a rotary evaporator and then the residue obtained was purified using a silica gel column and the obtained product was air-dried overnight for NMR analysis.

2.4.11. Construction of corrected spectra

87

The corrected spectra have been constructed by following a reported procedure to subtract the effect of QD- and CD-droplets in rate constant calculation [6, 7].

$$\text{Spectrum}_{\text{corrected}} = \text{Spectrum}_{\text{sample}} - (\text{peak absorbance}_{\text{sample}}/\text{peak absorbance}_{\text{coacervates}}) \times \text{Spectrum}_{\text{coacervates}} \qquad (3)$$

Peak absorbance$_{\text{sample}}$ is the difference between the absorbance at λ_{max} NP-Ds and at 800 nm in sample spectra. Peak absorbance NP-Ds is the difference between the absorbance at λ_{max} droplets and at 800 nm for only NP-Ds (without ferricyanide) with the same catalyst concentration as in the reaction mixture.

2.4.12. Determination of rate constant

The rate constant for the photocatalytic reduction of ferricyanide to ferrocyanide and photocatalytic degradation of RhB and MB was monitored by following the constant decline in the absorption value of ferricyanide at 420 nm, RhB at 554 nm, and MB at 664 nm. The photoconversion (C) vs. time (t) plot was fitted according to the first-order kinetics

$$C_t = C_0(1 - e^{-kt}) \qquad (4)$$

Taking $\log_e$ on both sides and rearranging,

$$-\ln\left(\frac{C_t}{C_0}\right) = kt \qquad (5)$$

where C_0 is the concentration of ferricyanide, RhB, and MB at initial time t=0, C_t is the concentration of ferricyanide, RhB, and MB at any time t during the photocatalytic reduction, and k is the rate constant. This approach involved the calculation of rate constant from first-order rate equation $-\ln(C_t/C_0)$ vs time as reported previously.

2.4.13. Calculation of conversion yield (%) and degradation (%)

The conversion yield for the photocatalytic reduction of ferricyanide was obtained by observing the decrease in the absorbance of

ferricyanide from its corrected spectra at 420 nm after ~ 40 min of constant irradiation.

Similarly, the percentage degradation of RhB and MB was obtained by observing the decrease in the absorbance of RhB and MB at 554 and 654 nm, respectively, under constant blue light irradiation.

$$\text{Conversion yield} = \left(\frac{C_0 - C_t}{C_0}\right) \times 100 \qquad (6)$$

where C_0 is the concentration of ferricyanide, RhB, and MB at initial time t=0 and C_t is the concentration of ferricyanide, RhB, and MB left at any time (t) during the reaction.

2.4.14. Temperature-dependent photocatalytic conversion of ferricyanide to ferrocyanide

Temperature-dependent photocatalytic reduction of ferricyanide was carried out under blue light irradiation with constant stirring. A constant-temperature water bath was utilized to maintain the temperature during the reaction. The photocatalytic kinetic study was done at four different temperatures i.e., 292, 298, 303, and 313 K. To verify the involvement of thermal effect in photocatalytic reduction of ferricyanide, a control experiment was carried out at 313 K in the absence of light. During the photoreduction of ferricyanide, the reaction was carefully observed by monitoring the absorbance of the solution in a fast scan mode at 10 min intervals for 40 min.

2.4.15. Calculation of thermodynamic parameters

The relationship between the reaction temperature (T) and rate constant (k) is given by Eyring equation;

$$\ln\left(\frac{k}{T}\right) = \frac{-\Delta H}{R}\left(\frac{1}{T}\right) + \ln\frac{k_B}{h} + \frac{\Delta S}{R} \qquad (7)$$

where h is Planck's constant, k_B is Boltzmann's constant, k is the reaction rate constant, ΔH is the enthalpy of activation, ΔG is the Gibbs free energy of activation, and ΔS is the entropy of activation. The activation enthalpy, ΔH was obtained from the plot of $\ln(k/T)$ versus

(1/T) by using its slope $-\Delta H/R$, where R is 8.31451 J K^{-1} mol^{-1} and the unit of ΔH is J mol^{-1}. The entropy of activation, ΔS was estimated from the intercept of the plot $\ln(k/T)$ vs $(1/T)$ using the thermodynamic equation;

$$\Delta S = \left(intercept - ln\left(\tfrac{k_B}{h}\right)\right) \times R \tag{8}$$

and Gibbs free energy of activation, ΔG was estimated using the thermodynamic equation;

$$\Delta G = \Delta H - T\Delta S \tag{9}$$

$$k = Ae^{\left(-Ea/RT\right)} \tag{10}$$

The above Arrhenius equation (10) was utilized to calculate activation energy (E_a) and pre-exponential factor (A).

2.4.16. Evaluation of peroxidase-like activity and kinetic parameters

The peroxidase-like activity of Au@QD-D was estimated using different chromogenic substrates like TMB, ABTS, and OPD in the presence of H_2O_2 in pH 5 acetate buffer. Typically, 500 μM TMB, ABTS, or OPD was added to Au@QD-D (40 nM) and incubated for 1 h to get substrate-loaded Au@QD-D. Next, 1 mM H_2O_2 was added to the above solution, and UV-vis spectroscopy was utilized to study the peroxidase-like activity of Au@QD-D.

The kinetic experiments were carried out at fixed TMB concentration (500 μM) by varying the H_2O_2 concentration (0–1200 μM) in pH 5 acetate buffer. Similarly, H_2O_2 was kept constant (1 mM) while varying the TMB concentration (0–1000 μM). All the absorbance measurements were recorded at 652 nm corresponding to the formation of ox-TMB. The initial rates of the reactions were plotted against substrate concentrations by considering the molar extinction coefficient of ox-TMB at 652 nm as 39000 M^{-1}cm^{-1}.[36] The obtained kinetic data were fitted to Michaelis-Menten and double reciprocal Lineweaver-Burk plot to obtain the Michaelis-Menten constant, K_m

and the maximum initial velocity V_{max}. The kinetic parameters were evaluated using the equation,

$$\frac{1}{V_0} = \frac{K_m}{V_{max}[S]} + \frac{1}{V_{max}} \qquad (11)$$

2.4.17. Temperature- and pH-dependent study of Au@QD-Ds

The temperature-dependent peroxidase-like activity of Au@QD-D was studied in the range of 5–65 °C by using a constant temperature water bath. Similarly, the pH-dependent peroxidase-like activity of Au@QD-D was studied in the pH range of 2–11. The morphology, shape, and structure of Au@QD-Ds at different temperatures and pH was confirmed using CLSM.

2.4.18. Preparation of Au@QD-D modified electrode

The glassy carbon electrode (GCE) was cleaned using alumina slurry on a clean microcloth pad to get a clear glossy surface. The cleaned GCE was further sonicated in methanol and water. A concentrated solution of Au@QD-D was obtained by centrifuging the Au@QD-D solution at 12000 rpm. The obtained precipitate was redispersed in 100 µL water and sonicated to get well dispersed homogeneous solution of Au@QD-D. Subsequently, 10 µL of concentrated Au@QD-D was drop casted over the clean GCE and dried at 40 °C. Similar, process was repeated 2–3 times to get a homogeneous layer of Au@QD-D over the GCE. The cyclic voltammetry (CV) measurements were carried out on a CHI620D electrochemical analyser by using clean bare GCE and Au@QD-D modified GCE as working electrodes, platinum wire as counter electrode and pseudo Ag|AgCl as reference electrode. During the whole study 10 mM pH 5 acetate buffer was utilized as electrolyte.

2.4.19. Sequestration of GOx and estimation of encapsulation efficiency (EE%)

The stock solution of GOx (4 mg/mL) was prepared in pH 7.4 phosphate buffer. Next, 250 nM GOx was added to Au@QD-D and QD-D solution, respectively. The above mixtures were then equilibrated for 12 h at room temperature. Subsequently, the

equilibrated mixtures were centrifuged at 16000 rpm for 10 min to collect the GOx-loaded Au@QD-Ds and GOx-loaded QD-Ds. Finally, the encapsulation efficiency of GOx inside the Au@QD-Ds and QD-Ds was estimated through UV-vis spectroscopy by using the following equation:

$$EE\ (\%) = \left(\frac{W_t}{W_i}\right) \times 100\% \qquad (12)$$

Here, W_t is the amount of GOx loaded inside Au@QD-Ds or QD-Ds, while W_i is the amount of GOx added initially.

2.4.20. Fluorescent labeling of GOx

GOx was fluorescently labeled with RBITC, according to an earlier reported literature *[8]*. In brief, 25 pM of GOx was mixed with RBITC in a molar ratio of 10:1 ([Dye]:[Enzyme]). The dye-enzyme mixture was then incubated for 4 h at room temperature followed by 6 h at 4 °C at constant stirring (500 rpm). Subsequently, the free dye in the solution mixture was removed using dialysis (molecular weight cut-off 3.5 kDa) against 10 mM PBS for 12 h at 4 °C.

2.4.21. Fluorescence quenching experiments

Fluorescence quenching experiments were carried out with the EY@CTAB micellar system. Typically, 2 µM EY solution was added to a 1 mM CTAB solution at room temperature. Subsequently, different substrates were added to the above micellar solution by varying their concentrations. The above mixture was then equilibrated for 5 min before recording the fluorescence spectra. The solutions were excited at 510 nm. For the quenching experiments in the presence of a base, 0.2 mM K_3PO_4 was added to the solution before the addition of substrates. Quenching rate constants were calculated from the SV constant by considering a fluorescence lifetime of 2.74 ns for EY@CTAB using the following equation:

$$K_{SV} = k_q \times \tau \qquad (13)$$

2.4.22. H₂O₂ detection

The H_2O_2 detection experiment was carried out under the standard optimized reaction conditions. Briefly, in 5 ml CTAB solution (40 mM), 0.6 mol% EY was added and incubated for 5 min. Subsequently, 0.05 mmol *p*-anisidine and 2 equiv. K_3PO_4 were added to the above solution and irradiated under green light for 4 h. Finally, 10-20 μl of the reaction mixture was dropped over the H_2O_2 test strips (MQuant test peroxide) to check the presence of H_2O_2.

2.4.23 Calculation of excited-state reduction potential

The excited-state reduction potential of EY@CTAB ($E_{1/2}(PC^*/PC^{\bullet-})$) was estimated using earlier reported literature *[9]*.

$$E^*_{red} = E_{red} + E_{0,0} \tag{14}$$

Briefly, we first estimated the zero-zero transition energy ($E_{0,0}$) for EY@CTAB using UV-vis and fluorescence spectroscopy. Notably, the intersection point at 533 nm of the absorption and emission spectrum of EY@CTAB corresponds to $E_{0,0}$. The $E_{0,0}$ was converted to electrode potential using the following equation,

$$E = \frac{hc}{\lambda} \tag{15}$$

The $E_{0,0}$ for the EY@CTAB was estimated to be 2.33 V, while the ground state reduction potential of EY@CTAB was found to be 1.03 V using CV measurements. Subsequently, utilizing equation 2, the excited state reduction potential of EY@CTAB was estimated to be 1.33 V.
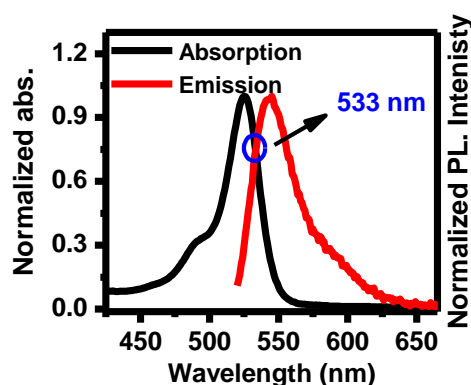
Figure 2.1. Normalized UV-vis and emission spectrum of EY@CTAB to estimate the zero-zero transition energy ($E_{0,0}$).

2.4.24. Scalability experiments

The scalability for the present reaction was estimated by increasing the substrate (*p*-anisidine) concentration from 0.05 mmol to 1 mmol under 1 green LED (44 W) irradiation at standard reaction conditions. Next, to further scale up the reaction to 5 mmol substrate concentration 4 green LEDs (44 W) were utilized to carry out the reaction under the standard conditions.

2.4.25. Radical trapping experiments

Briefly, in 5 ml CTAB solution (40 mM), 0.6 mol% EY was added and incubated for 5 min. Subsequently, 0.05 mmol *p*-anisidine and 2 equiv. K_3PO_4 were added to the above solution and irradiated under green light. After 5 mins of irradiation, 1 equiv. 2,6-Di-tert-butyl-4-methylphenol (BHT) was added to the above reaction mixture to trap the radical. Subsequently, the above mixture was irradiated with a green light for 4 h. The solution obtained was utilized for the HR-MS and GC-MS analysis.

2.4.26. Recyclability experiments

For the recycling experiment during the thesis work, the different fabricated NP-embedded coacervates were examined for five consecutive cycles toward their respective reactions.

2.4.26.1. QD-and CD-Ds for photocatalytic reduction of Fe^{3+} to Fe^{2+}

To check the recyclability of these QD- and CD-Ds during the photocatalytic reduction of ferricyanide to ferrocyanide, we utilized the assembly and subsequent disassembly of the droplets at different pH. For the first cycle, QD- or CD-Ds were first loaded with 230 μM ferricyanide along with 0.66 M EtOH. The reaction mixture was then purged with N_2 for 10 min. Subsequently, the reaction mixture was photoirradiated for 40 min under blue LED. After the first reaction cycle, these droplets were first disassembled by decreasing the pH of the reaction mixture by using 10% HCl solution to ~4.5. The obtained

mixture was then dialyzed for 2-3 h at constant stirring to separate all the unreacted reactants and products from the solution. After 3 h, a clear solution was obtained from the dialysis bag, and the droplets were reassembled by increasing the pH of this solution to ~7 by using 1 M NaOH solution. The solution obtained was then equilibrated for 3-4 h at 25 °C before repeating the same procedure for subsequent cycles. In each cycle, the droplets were first loaded with 230 μM ferricyanide and 0.66 M EtOH and then purged with N_2 before photoirradiation with blue LED. The conversion yield (%) and k_{app} were estimated in each cycle by following the same protocol as used for the first step.

2.4.26.2. QD-Ds for photocatalytic degradation of RhB and MB

Similarly, to check the reusability of our QD-Ds during the photocatalytic degradation of RhB and MB, we utilized solvent extraction to extract any smaller organic molecules formed during the degradation cycle from the QD-Ds. In brief, after the first degradation cycle, the reaction mixture was subjected to solvent extraction using ethyl acetate. After the extraction, the ethyl acetate phase was discarded and the water phase containing the QD-Ds was taken. The same process was repeated 2-3 times to remove any undegraded dye or degraded products present inside the QD-Ds in the water phase. The purified water phase containing the QD-Ds was utilized as it is for the next cycle. Similarly, the same procedure was followed to recycle the QD-Ds during the subsequent cycles.

2.4.26.3. Au@QD-Ds for peroxidase-like activity

To check the recyclability of Au@QD-D towards peroxidase-like activity, the fabricated Au@QD-Ds were examined for five consecutive cycles. The whole study was carried out in pH 5 acetate buffer. For the first cycle, 600 μM TMB was added to Au@QD-D solution and equilibrated for 1 h to get TMB-loaded Au@QD-D. Subsequently, 800 μM H_2O_2 was added to the above solution and absorbance at 652 nm (ox-TMB) was observed using UV-vis

spectroscopy. After the first catalytic cycle, the reaction mixture was centrifuged at 12000 rpm to separate Au@QD-Ds from the solution. The separated Au@QD-Ds were further washed with water to remove any TMB/ox-TMB present inside the droplets. The washed Au@QD-Ds were then utilized for the second catalytic cycle. Subsequently, a similar procedure was followed to carry out the successive catalytic cycles.

2.5. Instrumentation

2.5.1. Ultraviolet-visible (UV-vis) spectroscopy

UV-vis spectroscopy accounts for transitions from the ground state to the excited state by absorption of appropriate radiations of the electromagnetic spectrum. Absorption spectra were obtained using a Varian UV-vis spectrophotometer (Cary 100 Bio) and a Perkin Elmer UV/vis/NIR spectrophotometer (Perkin-Elmer Lambda 750). The spectral measurements were carried out in a 1×1 cm^2 quartz cuvette.

It works on the principle of Beer-Lambert law,

$$A = log\frac{I_0}{I} = \varepsilon c l \qquad (16)$$

Where A is absorption, I_0 is the intensity of incident light, I is the intensity of transmitted light, ε is the molar extinction coefficient, c is the molar concentration of the sample, and l is the optical path length of the sample cell.

2.5.2. Photoluminescence (PL) spectroscopy

The PL emission spectra were obtained using Fluoromax-4 spectrofluorometer (HORIBA Jobin Yvon). The spectral measurements were carried out in a 1×1 cm^2 quartz cuvette.

2.5.3. Time-correlated single-photon-counting technique (TCSPC)

The PL lifetime decays were obtained from a picosecond time-correlated single photon counting (TCSPC) spectrometer of HORIBA

Jobin Yvon (Fluorocube-01-NL model). A 445 nm picosecond diode laser was utilized to excite the samples. All the decay traces were collected using a photomultiplier tube (TBX-07C) and were then analyzed with a IBH DAS 6.0 software using previously reported literature *[10, 11]*.

2.5.4. Atomic force microscopy (AFM)

AFM images were captured on a cleaned glass coverslip and mica surface in a noncontact mode using a scanning probe AIST-NT microscope (model SmartSPM-1000). The samples were deposited on the coverslip by spin-coating at 750 rpm for 3 minutes.

2.5.5. Confocal laser scanning microscopy (CLSM)

Confocal laser scanning microscopy (CLSM) was carried out on an inverted confocal microscope (Olympus, model no. FV1200MPE, IX-83). Samples were excited with a diode laser source of 405, 488, and 559 nm through an oil immersion objective (100×1.4 NA) with suitable dichroic mirrors and emission filters (blue channel: 410-480 nm, green channel: 490-570 nm and red channel: 570-670 nm) along the optical path. A 20 μL aliquot of the sample solution was drop-casted onto cleaned glass slides and dried overnight before imaging.

2.5.6. Field-emission scanning electron microscopy (FESEM)

The FESEM images were captured using a Supra 55 Zeiss field-emission scanning electron microscope. For FESEM measurements, samples were drop-casted on a cleaned glass slide and overnight in a desiccator. The dried samples were initially coated with gold prior to use. EDX analysis was performed using a Supra 55 Zeiss field emission scanning electron microscope.

2.5.7. X-ray photoelectron spectroscopy (XPS)

XPS measurements were performed using an Al Kα surface analysis ESCA+ omicron nanotechnology-based X-ray photoelectron

spectrophotometer. The chamber pressure during the XPS measurements was 1×10^{-8} Torr.

2.5.8. Transmission electron microscopy (TEM)

TEM measurements were performed on a 200 kV UHR FEG-TEM (JEOL, Model JEM 2100F) and a 300 kV UHR FEG-TEM, FEI Tecnai G2, F30 field-emission scanning electron microscope fitted with a Lab6 source. The CTAB micellar solution was prepared in pH 7.4 aqueous solution. The sample was dropcasted over a carbon-coated copper TEM grid and was negatively stained using one drop of 1% (w/v) PTA. Finally, the excess staining agent was removed by washing it with Milli-Q water, and the sample was dried at room temperature under an IR lamp. A similar procedure was followed for the TEM imaging of QD-Ds and Au@QD-Ds without any staining with PTA.

2.5.9. Zeta-potential (ζ) measurements

All the samples for ζ-potential experiments were prepared in Milli-Q water filtered through a 0.22 μm syringe filter. The ζ-potential measurements were performed on a particle analyzer (model-Litesizer 500 and Nanoplus-3).

2.5.10. Fourier transform infrared spectroscopy (FTIR)

FTIR was used to confirm the surface functionalization of different nanoparticles. All spectra were recorded with the help of a KBr pellet using a Bruker spectrometer (Tensor-27) in the range of 800 to 4000 cm^{-1}.

2.5.11. Powder X-ray diffraction (PXRD)

PXRD pattern was recorded on a Rigaku SmartLab, an automated multipurpose X-ray diffractometer with a Cu Kα source (the wavelength of X-rays was 0.154 nm).

2.5.12. Cyclic voltammetry (CV)

The Glassy Carbon electrode (GCE) was cleaned using alumina slurry on a clean microcloth pad to get a clear glossy surface. The cleaned GCE was further sonicated in methanol and water. For the CV measurements, all the solutions of EY (12 µM), CTAB (12 mM), EY@CTAB mixture, and different substrates (10 mM) were prepared in pH 7.4 phosphate buffer. The CV measurements were carried out on a CHI1103C electrochemical analyzer by using clean bare GCE as working electrodes, platinum wire as a counter electrode, and pseudo Ag|AgCl as a reference electrode. The CV measurements were carried out at a scan rate of 100 mV/s. To convert the redox potentials from vs Ag/AgCl to vs SCE, a factor of -0.045 V was added to the redox potentials obtained from CV measurements. During the whole study, 10 mM pH 7.4 phosphate buffer was utilized as an electrolyte.

2.5.13. Electron paramagnetic resonance (EPR)

EPR spectra were recorded on a Bruker EMX MicroX spectrometer to confirm the presence of reactive oxygen species (ROS). Briefly, a reaction was set up under standard conditions with 10 mM *p*-anisidine as the substrate. Initially, the reaction was performed for 5 minutes under green light irradiation. Subsequently, 20 mM 5,5-dimethyl-1-pyrroline N-oxide was added to the reaction mixture to trap the superoxide radical. The reaction was carried out, and 500 µL aliquots were taken from the reaction mixture at 15 min and 60 min. The aliquots were then transferred to a quartz EPR tube and analyzed at 150 K.

2.5.14. Liquid chromatography- and high-resolution mass spectrometry (LC- and HR-MS)

LC-MS and HRMS spectra were recorded using an electrospray ionization (ESI) quadrupole time-of-flight liquid chromatography-mass spectrometer (Bruker Daltonik) in MeOH as the solvent by positive-ion mode ESI.

2.5.15. Gas chromatography-mass spectrometry (GC-MS)

Gas chromatography-mass spectrometry (GC-MS) spectra were recorded using a Shimadzu GC-MS, QP2010 mass spectrometer with a 30 m long Rxi-5Sil MS separation column with a 0.25 mm diameter and 0.25 µM thickness. The column oven temperature was set at 40 °C for 5 min, followed by a 20 °C/min ramp to 280 °C and held for 8 min.

2.5.16. Nuclear magnetic resonance (NMR)

AVANCE NEO Ascend 500 Bruker BioSpin, a 500 MHz spectrometer, was used to record ^{1}H and ^{13}C nuclear magnetic resonance (NMR) spectra. NMR data was recorded using either $CDCl_3$ or DMSO-D^6 as the solvent. Data for ^{1}H NMR spectra are reported as chemical shift (δ ppm), multiplicity (s = singlet, d = doublet, t = triplet, m = multiplet), coupling constant (J Hz) and integration, whereas assignment data for ^{13}C NMR spectra are reported as chemical shift.

2.5.17. Fluorescence up-conversion experiment

Ultrafast fluorescence decays were obtained using fluorescence up-conversion, widely known as femtosecond optical gating (FOG) with a FOG100 spectrometer from CDP corporation, Russia as discussed in earlier literature reports.[12] Briefly 800 nm, 100 fs pulses from a mode-locked Ti:sapphire oscillator (Tsunami, Spectra Physics), with 80 MHz repetition rate, pumped by a 4.2 W Millennia (Spectra Physics) DPSS laser, were focused on a nonlinear crystal (NC1, 0.5 mm b-BBO, y = 251, f = 901) to generate second harmonic 400 nm excitation light, which was used to excite the solutions of EY@CTAB and EY@CTAB in the presence of *p*-anisidine in a rotating cell with a 1 mm pathlength. Residual 800 nm light (gate) was focused, along with fluorescence from the sample, on another nonlinear crystal (NC2, 0.5 mm BBO, y = 381, f = 901), to generate an up-converted signal. This was dispersed by a double grating monochromator and detected by a photomultiplier tube at different path differences between the gate and fluorescence signal, to generate transient fluorescence. The decays were recorded at magic angle

polarization with respect to the excitation pulse and were fitted with iterative reconvolution using an Igor Pro routine *[12]*.

2.5.18 Ultracentrifugation

Ultracentrifugation experiments were carried out using a Remi PR-24 ultracentrifuge at room temperature.

2.6. References

1. Vaishnav J. K., Mukherjee T. K. (2018), Long-range resonance coupling-induced surface energy transfer from CdTe quantum dot to plasmonic nanoparticle, J. Phys. Chem. C, 122, 28324−28336. (DOI:10.1021/acs.jpcc.8b08757)

2. Vaishnav J. K., Mukherjee T. K. (2019), Surfactant-induced self-assembly of CdTe quantum dots into multicolor luminescent hybrid vesicles, Langmuir, 35, 6409−6420. (DOI:10.1021/acs.langmuir.9b00357)

3. Bhattacharya A., Chatterjee S., Khorwal V., Mukherjee T. K. (2016), Luminescence turn-on/off sensing of biological iron by carbon dots in transferrin, Phys. Chem. Chem. Phys., 18, 5148–5158. (DOI:10.1039/C5CP05890B)

4. Saini B., Singh R. R., Nayak D., Mukherjee T. K. (2020), Biocompatible pH-responsive luminescent coacervate nanodroplets from carbon Dots and poly(diallyldimethylammonium chloride) toward theranostic applications, ACS Appl. Nano Mater., 3, 5826–5837. (DOI:10.1021/acsanm.0c00995)

5. Williams D. S., Koga S., Hak C. R. C., Majrekar A., Patil A. J., Perriman A. W., Mann S. (2012), Polymer/nucleotide droplets as bio-inspired functional micro-compartments, Soft Matter, 8, 6004. (DOI:10.1039/c2sm25184a)

6. Kim Y., Smith J. G., Jain P. K. (2018), Harvesting multiple electron-hole pairs generated through plasmonic excitation of Au nanoparticles, Nat. Chem., 10, 763−769. (DOI: 10.1038/s41557-018-0054-3)

7. Kim Y., Torres D., Jain P. K. (2016), Activation energies of plasmonic catalysts, Nano Lett., 16, 3399−3407. (DOI:10.1021/acs.nanolett.6b01373)

8. Ray S., Singh N., Kumar R., Patel K., Pandey S., Datta D., et al. (2020), α-Synuclein aggregation nucleates through liquid–liquid phase separation, Nat. Chem., 12, 705–716. (DOI:10.1038/s41557-020-0465-9)

9. Speckmeier E., Fischer T. G., Zeitler K. A (2018), Toolbox approach to construct broadly applicable metal-free catalysts for photoredox chemistry: deliberate tuning of redox potentials and importance of halogens in donor-acceptor cyanoarenes, J. Am. Chem. Soc., 140, 15353–15365. (DOI:10.1021/jacs.8b08933)

10. Prajapati R., Chatterjee S., Kannaujiya K. K., Mukherjee T. K. (2016), Effect of compartmentalization of donor and acceptor on the ultrafast resonance energy transfer from dapi to silver nanoclusters, Nanoscale, 8, 13006−13016. (DOI:10.1039/C6NR01792D)

11. Prajapati R., Bhattacharya A., Mukherjee T. K. (2016), Resonant excitation energy transfer from carbon dots to different sized silver nanoparticles, Phys. Chem. Chem. Phys., 18, 28911− 28918. (DOI:10.1039/C6CP05451J)

12. Banerjee S., Maddala B. G., Ali F., Datta A. (2019), Enhancement of the band edge emission of CdSe nano-tetrapods by suppression of surface trapping, Phys. Chem. Chem. Phys., 21, 9512–9519. (DOI:10.1039/C9CP00198K)

Chapter 3

Metal-Free Photocatalysis at Charged Aqueous Interfaces: Boosting the Photocatalytic Oxidative Coupling of Arylamines to Azoaromatics under Ambient Conditions

3.1. Introduction

Developing an efficient protocol for the synthesis of important organic compounds in an aqueous medium under ambient conditions is highly desirable from a green and sustainable chemistry point of view. The facile synthesis of azoaromatics under ambient conditions has recently gained immense attention due to their tremendous potential in optical storage *[1, 2]*, molecular switches *[3]*, and industrial applications *[4]*. Over the years, several methodologies have been developed for the synthesis of substituted azoaromatics, and among these, diazotization in the presence of stoichiometric amounts of nitrile salts is the traditional method, which produces unstable diazonium intermediates and unwanted waste *[5]*. Metal nanoparticle-catalyzed synthesis of azo compounds has also been reported from anilines and nitroaromatics *[6–16]*. However, most of these methods suffer from slow kinetics, poor selectivity, high temperature, and/or an inert atmosphere. On the other hand, photocatalytic reductive coupling *[17–20]* of nitrobenzenes in the presence of various photocatalysts (PCs) suffers from poor product selectivity due to the simultaneous generation of azoxyaromatics or nitrosobenzene and the requirement of an inert atmosphere, which limit their large-scale practical applicability. In contrast, photocatalytic oxidative coupling (POC) in the presence of sustainable O_2 as an oxidant has been widely utilized for a vast range of chemical reactions *[21–23]*.

Recently, the POC of arylamines was achieved with high selectivity and moderate to good yields using an Ir-based photocatalyst (Scheme 3.1A) *[24]*. However, this methodology suffers from slow reaction kinetics, moderate yields, high catalyst dose, and limited substrate scope. Moreover, all the earlier reports have utilized organic solvents to carry out the synthesis of azo compounds, which prompts us to design an

efficient and green catalytic route for the synthesis of azo compounds in aqueous medium with high selectivity and yields under ambient atmosphere. In this context, we formulated a highly efficient POC methodology for the synthesis of azo compounds at the charged aqueous interfaces (CAIs) of micelles under an ambient atmosphere, utilizing a common and low-cost organic photocatalyst, Eosin Y (EY) and K_3PO_4 as the base (Scheme 3.1B).

(A) Previous work

5 mol% Ir
3 eq. K_3PO_4
$\lambda = 450$ nm

Acetonitrile
24 h

❑ **Moderate to good yields**
❑ **Reaction time 24 h**
❑ **Acetonitrile medium**
❑ **High dose of Ir**

(B) Present work

0.6 mol% EY
2 eq. K_3PO_4
$\lambda = 525$ nm

H_2O, 4 h

✓ **Up to 100% yield**
✓ **Reaction time 4 h**
✓ **Aqueous medium**
✓ **Low dose of EY**
✓ **Broad Substrate Scope**
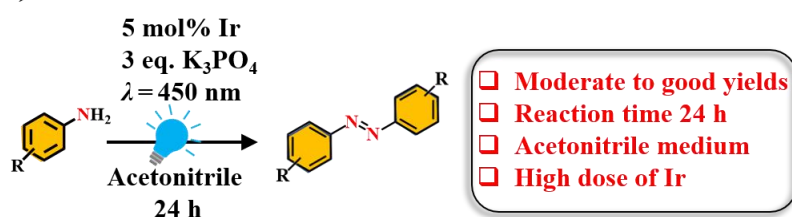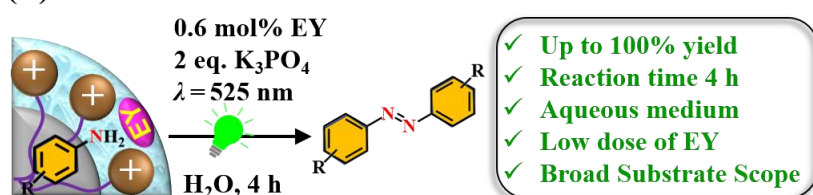
Scheme 3.1. Previous and present synthetic approaches for the POC of arylamines.

3.2. Results and discussion

The CAIs can dramatically modulate many chemical and photochemical reactions that are otherwise inefficient in the bulk medium *[25–31]*. Apart from confinement, CAIs provide unique electric fields that align probe dipoles with respect to the interface and facilitate product selectivity. Among these interfaces, CAIs of micelles provide a unique microenvironment to solubilize both hydrophilic and hydrophobic probes at distinct locations in the micellar scaffold, which brings the PC and substrates in close proximity, which is particularly important for bimolecular reactions.

Our methodology is primarily based on the specific association of a substrate and a photocatalyst with the micellar assembly. To probe

these interactions, we initially studied the photophysical behavior of EY in the presence of cetyltrimethylammonium bromide (CTAB), sodium dodecyl sulfate (SDS), and Triton X-100 (TX-100).

The absorption peak of EY in water at 516 nm exhibits a bathochromic shift of 9 and 16 nm in the presence of CTAB and TX-100 micelles, respectively (Figure 3.1A), indicating micellar association.
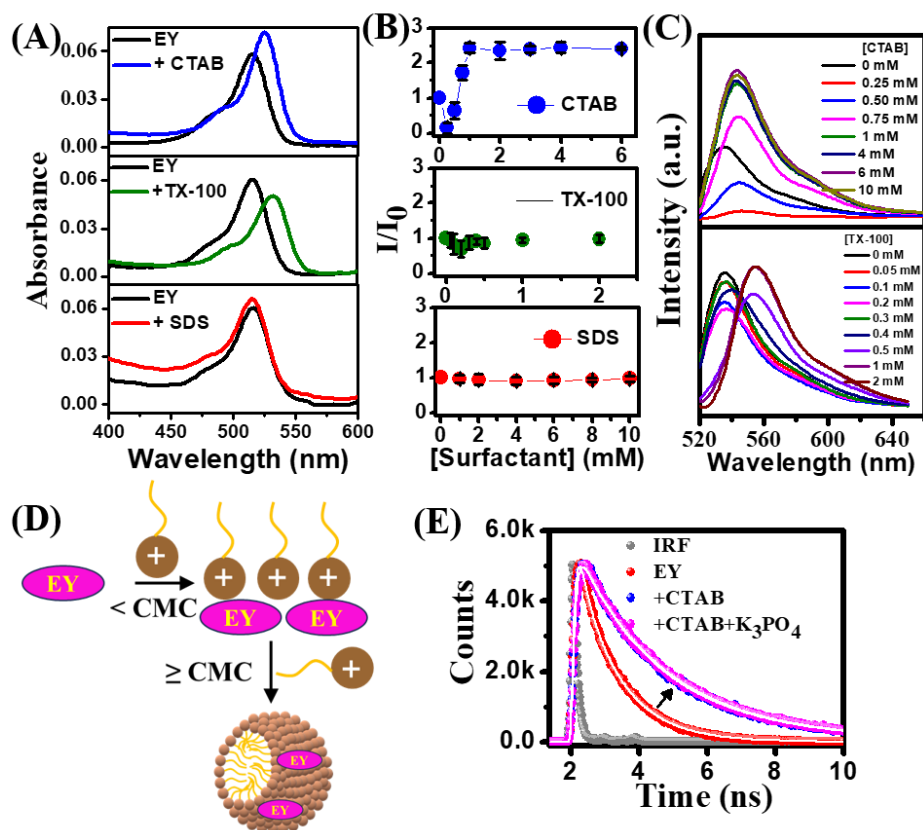
Figure 3.1. Changes in the (A) absorption spectra and (B) fluorescence intensity ratios of EY in the presence of different surfactants. The data represent mean $\pm$ SEM for three (n = 3) independent experiments. (C) Changes in the fluorescence spectra of EY in the presence of different concentrations of CTAB and TX-100. (D) Schematic showing the interaction of EY with CTAB surfactants. (E) Fluorescence decay curves of EY in the absence and presence of CTAB and K_3PO_4.

On the other hand, EY exhibits fluorescence quenching in the presence of premicellar concentrations of CTAB and TX-100 (Figure 3.1B & C). However, EY shows enhanced fluorescence (2.4-fold) only

in the presence of CTAB at and near (0.75–1.0 mM) the critical micellar concentration (CMC). No such spectral changes have been observed in the presence of SDS (Figure 3.1A and B), signifying the lack of any interaction. These findings suggest a higher binding affinity of EY towards CTAB (EY@CTAB) than that towards TX-100 (EY@TX-100). This is expected as EY bears two negative charges at pH 7 *[32]* and interacts electrostatically with the positively charged CTAB. At the premicellar concentration of CTAB, EY undergoes CTAB-induced aggregation due to the ion-pair formation; however, these aggregates subsequently dissociate at or near the CMC of CTAB due to the entrapment of EY at the micellar Stern layer (Figure 3.1D) *[33, 34]*.

Table 3.2. Fluorescence lifetime decay parameters of EY, estimated in the presence of CTAB and K_3PO_4 from TCSPC measurements.

S. No.	Sample	τ_1 (ns)	a_1	$<\tau>$(ns)	χ^2
1.	EY	1.17	1	1.17	1.04
2.	CTAB + EY	2.74	1	2.74	1.14
3.	CTAB + EY + K_3PO_4	2.76	1	2.76	1.16

This argument gains further support from the enhanced fluorescence lifetime of EY from 1.17 ns in water to 2.74 ns upon micellization of CTAB (Figure 3.1E and Table 3.2), signifying the micellar association. As the present POC reaction occurs in the presence of a base, we checked the stabilities of the micellar composites of EY in the presence of K_3PO_4. Although EY@CTAB is found to be stable in the presence of K_3PO_4, EY@TX-100 suffers disassembly (Figure 3.2).

Therefore, we utilized the EY@CTAB composite for our subsequent studies. Here, it is important to note that K_3PO_4 neither interferes with the specific association of EY with CTAB nor interacts
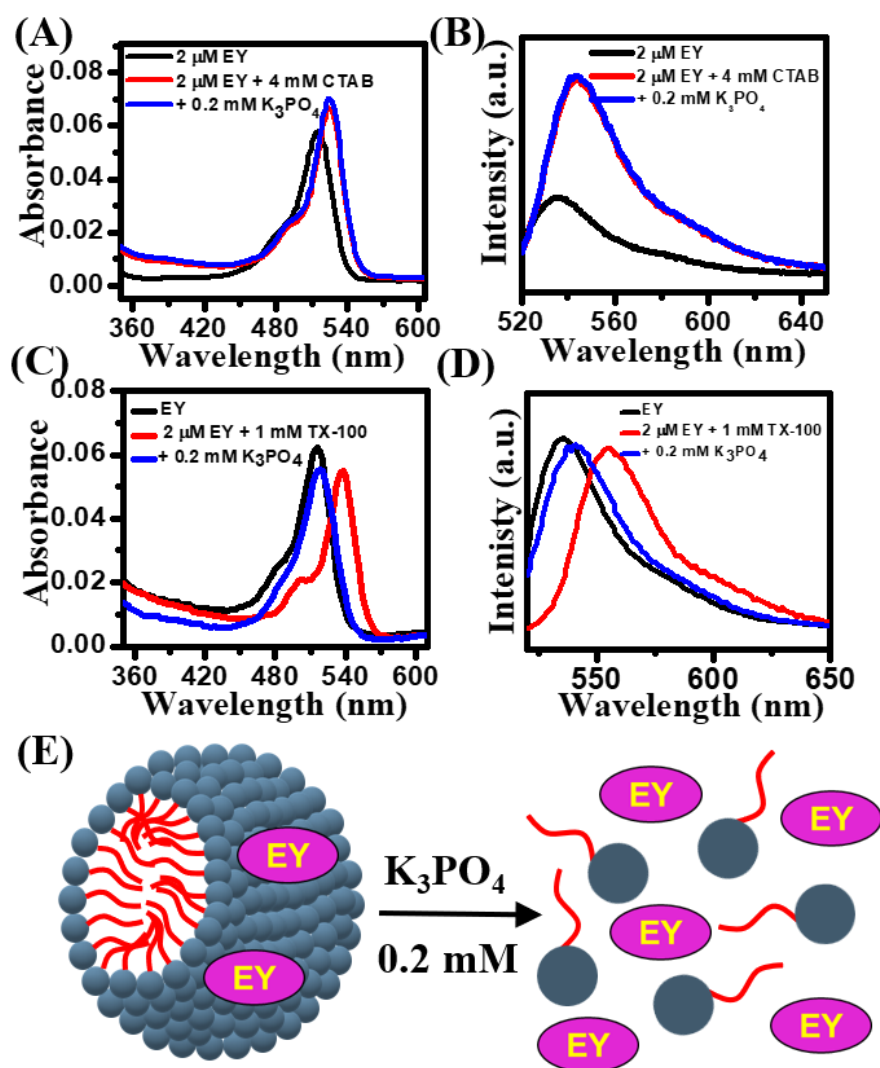
Figure 3.2. Changes in the (A) absorption and (B) emission spectra of EY@CTAB in the presence of 0.2 mM K_3PO_4. Changes in the (C) absorption and (D) emission spectra of EY@TX-100 in the presence of 0.2 mM K_3PO_4. (E) Schematic representation of the disassembly of TX-100 micelles after the addition of 0.2 mM K_3PO_4.

directly with the excited state of EY@CTAB, as revealed from the unperturbed fluorescence lifetime (Figure 3.1E and Table 3.2). Moreover, it is well documented in the literature that arylamines prefer to solubilize at the less polar hydrocarbon/aqueous interface of the micellar Stern layer compared to the aqueous bulk medium *[35, 36]*. Therefore, both the substrate and PC remain solubilized inside the micellar scaffold.

Table 3.3. Optimization of reaction conditions
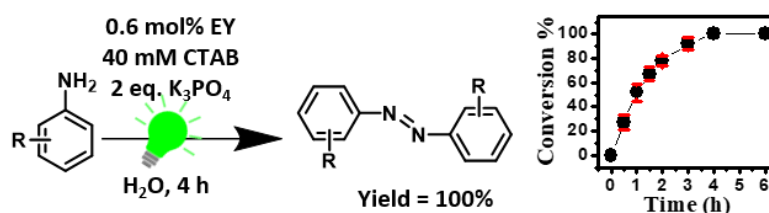
Deviation from Standard Conditions	Yield [%][a]
Standard[b]	100
no light	0
no Eosin Y	0
no CTAB	22
30 mM CTAB	65
0.3 mol% EY	68
no K_3PO_4	0
1 equiv. of K_3PO_4	89
2 equiv. KOH	98
2 equiv. DABCO	93
N_2 atmosphere	0

[a]Yields are determined from GC-MS. [b]Standard conditions: 10 mM *p*-anisidine, 40 mM CTAB, 0.6 mol% Eosin Y, 2 equiv. K_3PO_4, 5 mL H_2O, under ambient air atmosphere with green LED (λ = 525 nm, 44 W) illumination for 4 h. The data points in the conversion versus time plot represent mean ± SEM for three (n = 3) independent experiments.

The optimized reaction conditions for the conversion of *p*-anisidine to 1,2-bis(4-methoxyphenyl)diazene are tabulated in Table 3.3. The reaction was triggered by a green light (λ = 525 nm) under an ambient air atmosphere, and within 4 h we observed 100% conversion to the desired azo product in the presence of 0.6 mol% EY, 2 equiv. K_3PO_4, and 40 mM CTAB as determined from GC-MS measurements (Table 3.3). CTAB forms spherical micelles at an optimized concentration of 40 mM, as revealed from HR-TEM measurements (Figure 3.3).
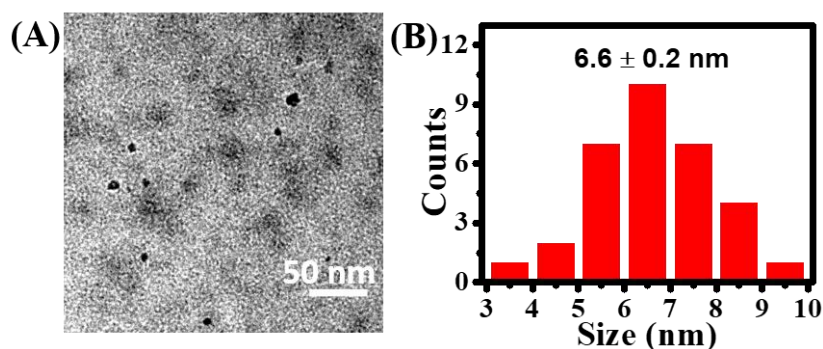
Figure 3.3. (A) HRTEM image of CTAB micelles at a CTAB concentration of 40 mM, and (B) the size distribution histogram.

The remarkable enhancement in the efficacy of the reaction, even with an appreciably lower (8.3-fold) dose of EY compared to the previous report *[24]* occurs only in the presence of CTAB micelles, suggesting the critical role of the micellar environment on the feasibility of this reaction in water. The reaction is also feasible with blue light as reported previously *[24]*; however, it requires 6 h for 100% conversion under standard conditions (Figure 3.4A).
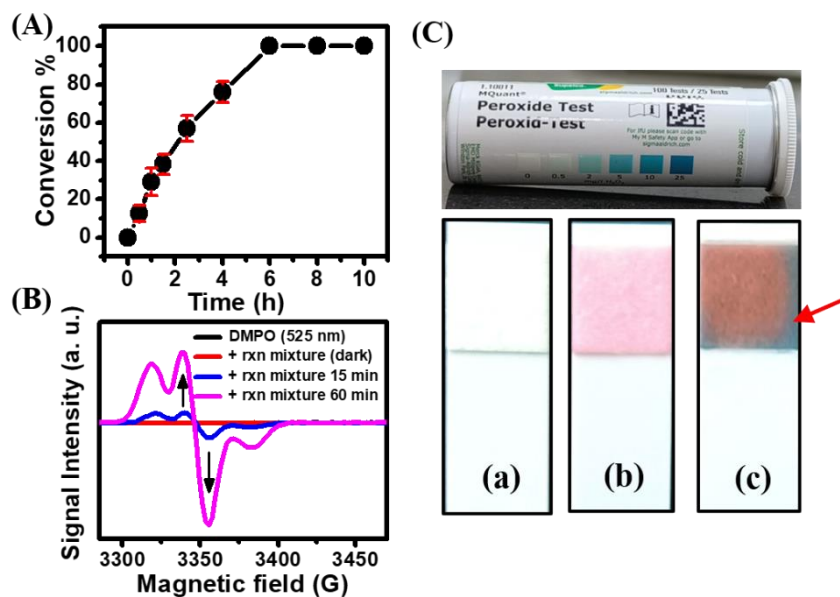
Figure 3.4. (A) The kinetic plot of conversion% for the POC of *p*-anisidine to 1,2-bis(4-methoxyphenyl)diazene as a function of reaction time under blue light irradiation for 10 h at standard reaction conditions. The data represent mean ± SEM for three (n = 2) independent experiments. (B) Changes in the EPR spectra of DMPO

(20 mM) in the absence and presence of reaction mixture at 15 min and 60 min time intervals under green LED irradiation in the presence of 10 mM p-anisidine, 40 mM CTAB, 0.6 mol% EY, and 2 equiv. K_3PO_4. (C) Daylight photographs of peroxide test strips for (a) blank strips without any measurement, (b) before the photocatalytic experiment, and (c) after 4 h of reaction (EY@CTAB + p-anisidine + K_3PO_4) under standard reaction conditions. The red arrow indicates the desired color change of the strip.

Table 3.3 shows that the reaction is feasible only in the presence of a base, as proton abstraction is a critical step for the POC of amine substrates [24]. Both inorganic (K_3PO_4 and KOH) and organic (DABCO) bases are effective; however, the conversion yields are slightly less with DABCO. Importantly, no conversion has been observed under an N_2 atmosphere, signifying the critical role of atmospheric O_2 in the reaction mechanism.

The absence of any oxygenated side products, such as azoxy-, nitroso-, or nitro-compounds, indicates that O_2 does not react directly with the amine substrates. Previously, it has been shown that O_2 can act as a sacrificial electron acceptor for the regeneration cycle of the photocatalyst via the generation of superoxide radical anion in the POC reactions and transforms to hydrogen peroxide (H_2O_2) [24]. To authenticate the formation of superoxide radical anion in the reaction mixture, we performed electron paramagnetic resonance (EPR) spectroscopy in the presence of 5,5-dimethyl- 1-pyrroline N-oxide (DMPO) as a spin trap probe [37]. The characteristic peaks observed in the EPR spectrum indicate the formation of DMPO-trapped superoxide radicals in the reaction mixture under standard reaction conditions (Figure 3.4B) [38]. Notably, the EPR signal intensity increases gradually as a function of reaction time, suggesting a progressive increase in the concentration of superoxide radicals during the course of the reaction. Control experiments were performed with H_2O_2 sensing strips to detect the formation of H_2O_2 in the reaction mixture (Figure 3.4C). The distinct color change of the strip observed

before and after the light irradiation indicates the formation of H_2O_2 in the reaction mixture via the reduction of aerial O_2. Therefore, atmospheric O_2 acts as a sacrificial oxidant and is involved in the regeneration of the PC via the formation of H_2O_2 as a byproduct.
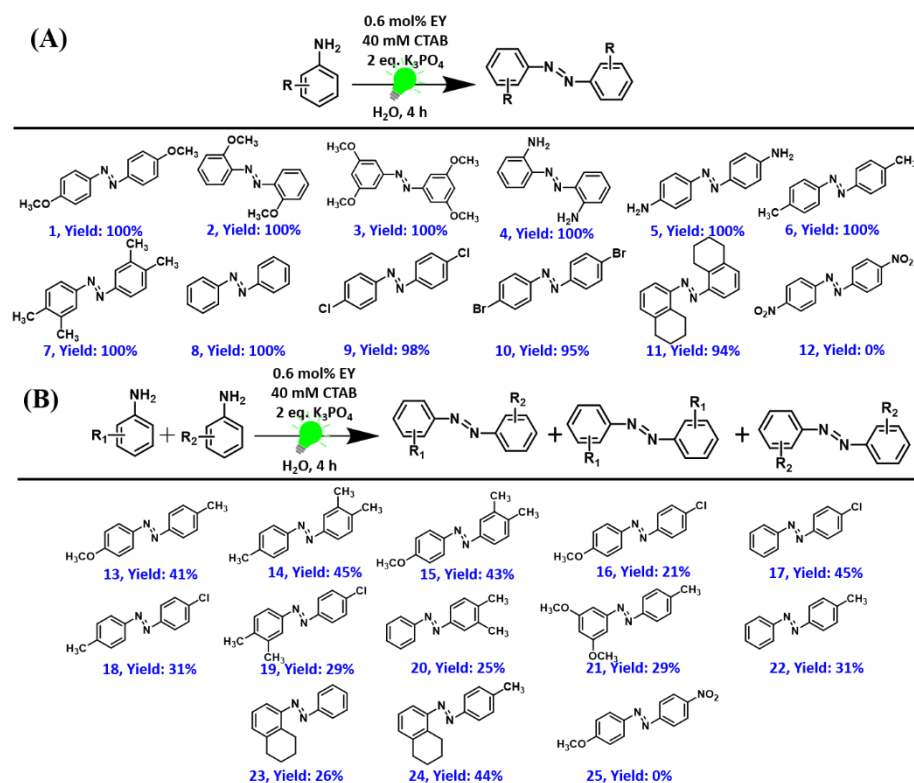
Scheme 3.2. Substrate scope for the photocatalytic oxidative coupling of arylamines for the synthesis of substituted azo compounds under standard reaction conditions. (A) Homo-coupling, and (B) hetero-coupling of arylamines.

The present methodology shows a broad substrate scope, including electron-rich and -deficient amine centers (Scheme 3.2A). Products were isolated and characterized using GC-MS and NMR measurements (Appendix A). Importantly, arylamines with electron-rich amine centers show 100% conversion within 4 h of the reaction (1–7, Scheme 3.2A), which is remarkable compared to the previously reported 64% conversion after 24 h of the reaction in bulk acetonitrile *[24]*. Similarly, 100% conversion has also been observed with aniline as the substrate under standard conditions (8, Scheme 3.2A). However, *p*-chloroaniline and *p*-bromoaniline show a conversion yield of 98%

and 95%, respectively (9 and 10, Scheme 3.2A), possibly due to the electron-deficient amine centers. The present approach also shows excellent yield (94%) of the azo product with fused ring amine, namely 5,6,7,8-tetrahydronaphthalen-1-amine (11, Scheme 3.2A). On the other hand, *p*-nitroaniline shows no product formation, possibly due to its highly electron-deficient amine center. Moreover, both homo- and hetero-coupled azo compounds have been observed from a mixture of different arylamines under standard reaction conditions, except for *p*-nitroaniline (Scheme 3.2B & Appendix A).
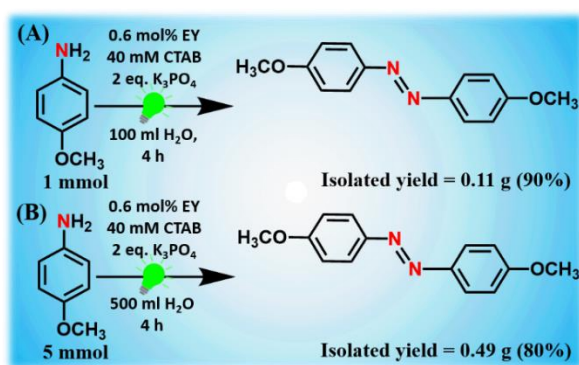
Figure 3.5. Schematic representation of scalability experiment for the photocatalytic oxidative coupling of p-anisidine to its corresponding azo compound.

Our present synthetic approach can be easily scalable. To show the scalability of our present approach, we performed two sets of scaled-up reactions with 1 and 5 mmol *p*-anisidine in 100 and 500 ml of water, respectively with 40 mM CTAB, 0.6 mol% EY, and 2 equiv. of K$_3$PO$_4$ (Figure 3.5). The isolated yields of 0.11 (90%) and 0.49 g (80%) of 1,2-bis(4-methoxyphenyl)diazene have been obtained with 1 and 5 mmol of *p*-anisidine in 100 and 500 ml of water under standard reaction conditions, using one and four green LEDs, respectively. The observed trend in the reactivity of arylamines indicates the possible role of photoinduced electron transfer (PET) from the amine centers of arylamines to the excited state (ES) of PC at the micellar surface.

To know the feasibility of PET, we mapped the oxidation potentials of arylamines with the ES reduction potential of EY@CTAB

(Figure 3.6). The oxidation potentials of a few representative amine substrates and ES reduction potential of EY (EY*/EY⁻•) were measured in 12 mM CTAB solutions using cyclic voltammetry (CV) (Figure 3.6G).
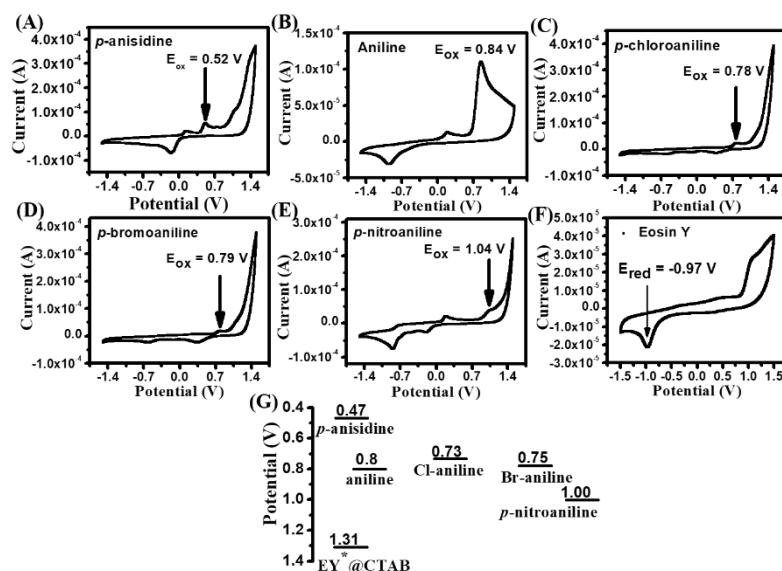
Figure 3.6. Cyclic voltammogram of arylamines (2 mM) and EY in 12 mM CTAB solution carried out at a scan rate of 100 mV/s versus Ag/AgCl electrode. (A) *p*-anisidine, (B) aniline, (C) *p*-chloroaniline, (D) *p*-bromoaniline, (E) *p*-nitroaniline, and (F) Eosin Y. (G) Mapping of the redox potentials of arylamines and EY*@CTAB.

Notably, the ES reduction potential of EY is significantly higher than that reported in bulk acetonitrile solution *[24]*. The mapped redox potentials indicate that the oxidation of arylamines by EY* is thermodynamically feasible at the micellar surface irrespective of the substituents. Fluorescence quenching experiments were performed to further validate the PET phenomenon. The fluorescence intensity of EY@CTAB at 545 nm decreases gradually upon the addition of increasing concentrations of *p*-anisidine (Figure 3.7A). A linear Stern–Volmer (SV) plot with a quenching rate constant (k_q) of 6.3×10^{12} M^{-1} s^{-1} suggests a non-diffusive bimolecular quenching process (Figure 3.7B) *[39, 40]*. The quenching parameters for other arylamines are tabulated in Figure 3.7C. Notably, the lack of fluorescence quenching

with *p*-nitroaniline suggests a lack of any electron transfer to EY*@CTAB (Figure 3.7B).
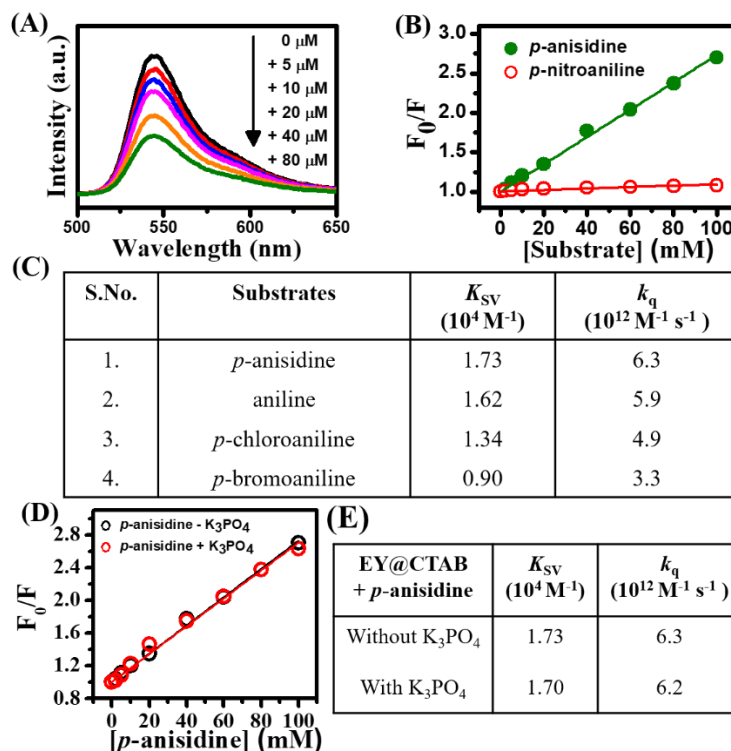
Figure 3.7. (A) Fluorescence quenching of EY@CTAB with the gradual addition of different concentrations of *p*-anisidine. (B) SV plots with *p*-anisidine and *p*-nitroaniline. (C) Fluorescence quenching parameters of EY@CTAB in the presence of different substrates. (D) Steady-state Stern−Volmer plot of EY@CTAB upon addition of different concentrations of *p*-anisidine in the absence and presence of 0.2 mM K_3PO_4, and (E) their quenching parameters (K_{SV} and k_q).

It is noteworthy to mention that the presence of K_3PO_4 has no noticeable effect on the SV plots and quenching rate constant (Figure 3.7D & E), signifying that PET precedes the proton abstraction step by base. Fluorescence lifetime measurements were carried out to validate the PET mechanism. The fluorescence lifetime of EY@CTAB decreases from 2.74 to 1.96 ns in the presence of 100 µM *p*-anisidine (Figure 3.8A & B). Although PET at the micellar surface is instantaneous in nature and occurs in a few picoseconds *[41–44]* the marked decrease in the fluorescence lifetime of EY@CTAB authenticates the excited state quenching by *p*-anisidine. Fluorescence

up-conversion measurements reveal an ultrafast PET with a time constant of 0.3 ps in the presence of *p*-anisidine (Figure 3.8C).
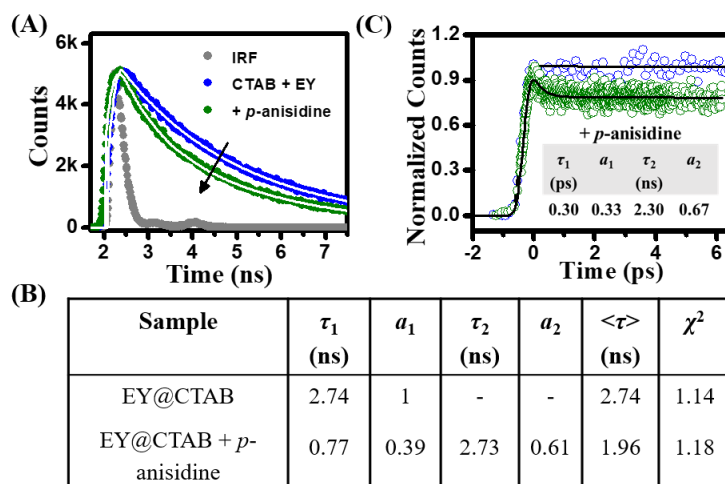
Figure 3.8. Lifetime decays and its parameters for EY@CTAB in the absence and presence of *p*-anisidine using (A, B) TCSPC and (C) fluorescence up-conversion techniques.

Radical trap experiments were carried out to validate the formation of amine radicals via the PET mechanism *[45]*. The reaction mixture was irradiated with green light for 5 min under standard conditions with *p*-anisidine as the substrate. Subsequently, 1 equivalent of 2,6-di-tert-buty-4-methylphenol (BHT) was added to the reaction mixture to trap the radicals (Scheme 3.3). The mixture was further irradiated with green light for 4 h. The products were analyzed using HR-MS and GC-MS measurements. A characteristic HR-MS peak for *p*-anisidine-BHT adducts appears at a molecular weight of 342.2399 g mol^{-1} (Figure 3.9).
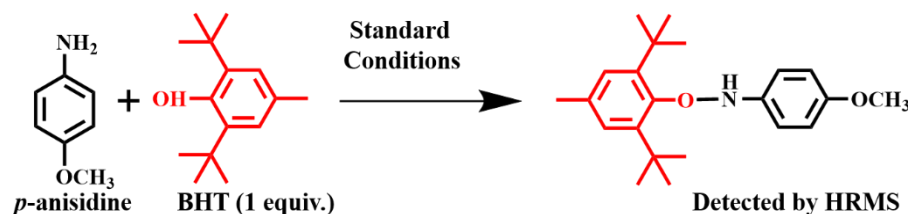
Scheme 3.3. Radical trap experiment of *p*-anisidine with 1 equiv. of BHT.
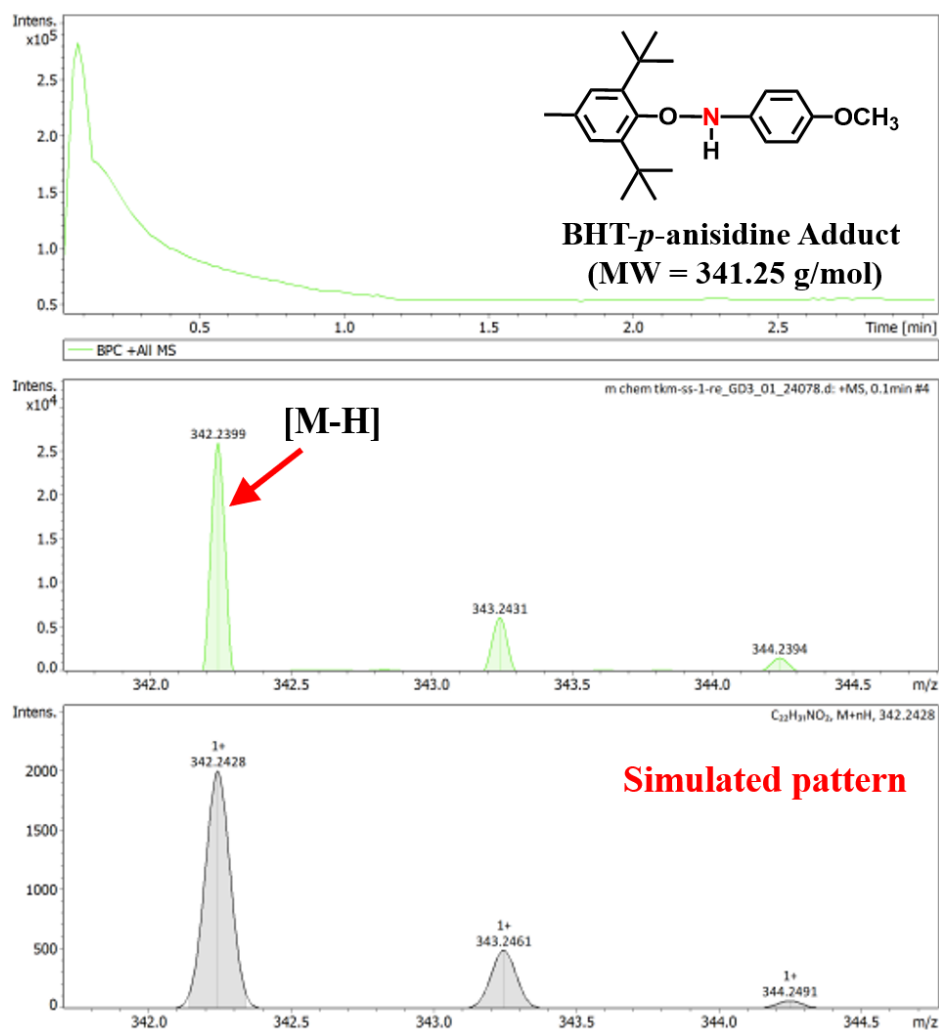
Figure 3.9. HR-MS spectra of BHT-*p*-anisidine adduct obtained after radical scavenger experiment.

Moreover, the presence of BHT results in negligible conversion ($\sim$5.0%) to the desired azo product even after 4 h of irradiation. These observations authenticate the formation of amine radicals during the POC of *p*-anisidine at the micellar surface. Finally, the formation of hydrazobenzene intermediate was confirmed using LC-MS measurements. Using *p*-anisidine as the substrate, we observed a characteristic peak at a m/z value of 244.1319 for 1,2-bis(4-methoxyphenyl)hydrazine in the LC-MS, which matches well with the simulated pattern (Figure 3.10).
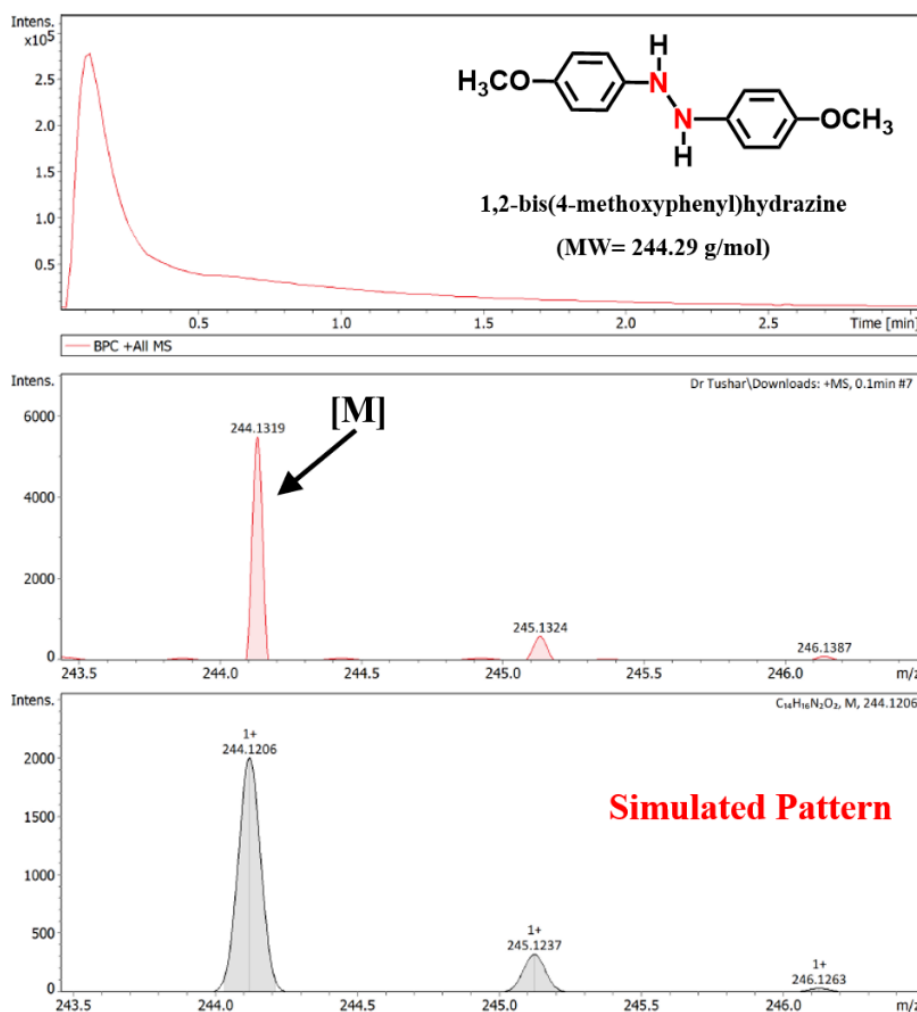
Figure 3.10. LC-MS spectra of intermediate 1,2-bis(4-methoxyphenyl)hydrazine (hydrazobenzene) obtained during the photo-oxidative coupling to *p*-anisidine to its corresponding azo compound.

Based on our findings, we propose a possible mechanistic pathway for the POC of arylamines at the micellar surface (Scheme 3.4). The overall coupling reaction proceeds via the generation of 4 electrons and 4 protons as proposed previously *[24]*. Initially, ultrafast PET from arylamines to the photoexcited EY@CTAB generates amine radicals at the micellar surface. After proton abstraction by a base, these radicals undergo coupling reactions to form a hydrazobenzene intermediate, which is subsequently converted to the desired azo products after another round of photocatalytic cycle with the generation of 2 equivalent of H_2O_2 as the byproduct. To the best of our

knowledge, this is the first report on the selective and sustainable synthesis of azo compounds in the aqueous medium under an ambient atmosphere without any unwanted toxic byproducts *[8, 10–16, 18–20, 24]*.
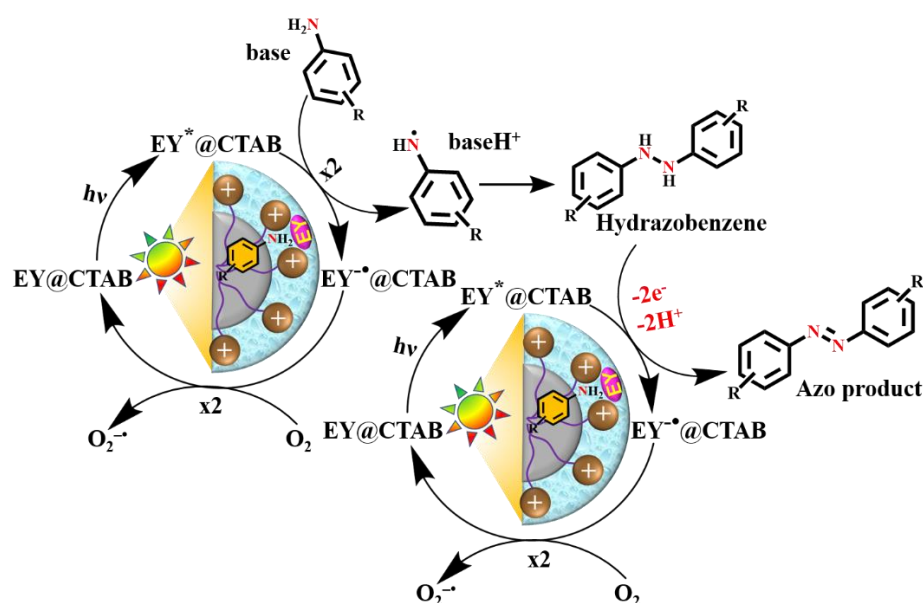
Scheme 3.4. Schematic representation of the plausible reaction mechanism for the POC of arylamines at the CAI of micelles.

3.3. Conclusions

In summary, we demonstrated the tremendous potential of CAI of micelles for boosting the POC of arylamines in aqueous medium. Our approach showed broad substrate scope with excellent yields (up to 100%), fast kinetics (4 h), and 100% selectivity under ambient air atmosphere in aqueous medium without any unwanted byproducts. The CAI not only acts as an efficient host for an ultrafast non-diffusive PET, but also modulates the redox potentials in a favorable manner. The present methodology may find wide-ranging implications in the chemical and pharmaceutical industries.

3.4. References

1. De Boni L., Piovesan E., Misoguti L., Zílio S. C., Mendonca C. R. (2007), Two-photon absorption dependence on the temperature for azoaromatic compounds: effect of molecular conformation, J. Phys. Chem. A, 111, 6222–6224. (DOI: 10.1021/jp0716684)

2. Dos Santos D. S., Bassi A., Rodrigues J. J., Misoguti L., Oliveira O. N., Mendonca C. R. (2003), Light-induced storage in layer-by-layer films of chitosan and an azo dye, Biomacromolecules, 4, 1502–1505. (DOI: 10.1021/bm025754f)

3. Murakami H., Kawabuchi A., Kotoo K., Kunitake M., Nakashima N. (1997), A light-driven molecular shuttle based on a rotaxane, J. Am. Chem. Soc., 119, 7605–7606. (DOI: 10.1021/ja971438a)

4. Bafana A., Devi S. S., Chakrabarti T. (2011), Azo dyes: past, present and the future, Environ. Rev., 19, 350–371. (DOI: 10.1139/a11-018)

5. Merino E. (2011), Synthesis of azobenzenes: the coloured pieces of molecular materials, Chem. Soc. Rev., 40, 3835–3853. (DOI: 10.1039/C0CS00183J)

6. Corma A., Concepción P., Serna P. A (2007), Different reaction pathway for the reduction of aromatic nitro compounds on gold catalysts, Angew. Chem. Int. Ed., 46, 7266–7269. (DOI: 10.1002/ange.200700823)

7. Grirrane A., Corma A., García H. (2008), Gold-catalyzed synthesis of aromatic azo compounds from anilines and nitroaromatics, Science, 322, 1661–1664. (DOI: 10.1126/science.11664)

8. Zhang C., Jiao N. (2010), Copper-catalyzed aerobic oxidative dehydrogenative coupling of anilines leading to aromatic azo compounds using dioxygen as an oxidant, Angew. Chem. Int. Ed., 49, 6174–6177. (DOI:10.1002/ange.201001651)

9. Grirrane A., Corma A., Garcia H. (2010), Preparation of symmetric and asymmetric aromatic azo compounds from aromatic amines or

nitro compounds using supported gold catalysts, Nat. Protoc., 5, 429–438. (DOI: 10.1038/nprot.2009.242)

10. Cai S., Rong H., Yu X., Liu X., Wang D., He W., Li Y. (2013), Room temperature activation of oxygen by monodispersed metal nanoparticles: oxidative dehydrogenative coupling of anilines for azobenzene syntheses, ACS Catal., 3, 478–486. (DOI: 10.1021/cs300707y)

11. Dutta B., Biswas S., Sharma V., Savage N. O., Alpay S. P., Suib S. L. (2016), Mesoporous manganese oxide catalyzed aerobic oxidative coupling of anilines to aromatic azo compounds, Angew. Chem. Int. Ed., 55, 2171–2175. (DOI: 10.1002/ange.201508223)

12. Wang M., Ma J., Yu M., Zhang Z., Wang F. (2016), Oxidative coupling of anilines to azobenzenes using heterogeneous manganese oxide catalysts, Catal. Sci. Technol., 6, 1940–1945. (DOI: 10.1039/C5CY01015B)

13. Saha A., Payra S., Selvaratnam B., Bhattacharya S., Pal S., Koodali R. T., Banerjee S. (2018), Hierarchical mesoporous RuO_2/Cu_2O nanoparticle-catalyzed oxidative homo/hetero azo-coupling of anilines, ACS Sustainable Chem. Eng., 6, 11345–11352. (DOI: 10.1021/acssuschemeng.8b01179)

14. Zou Y., Zhan M., Cao F., Li J., Zhang S., Qu Y. (2021), Single crystal MnOOH nanotubes for selective oxidative coupling of anilines to aromatic azo compounds, J. Mater. Chem. A, 9, 19692–19697. (DOI: 10.1039/D1TA04415J)

15. Han S., Cheng Y., Liu S., Tao C., Wang A., Wei W., Yu H., Wei Y. (2021), Selective oxidation of anilines to azobenzenes and azoxybenzenes by a molecular Mo oxide catalyst, Angew. Chem. Int. Ed., 60, 6382–6385. (DOI: 10.1002/anie.202013940)

16. Qin J., Long Y., Sun F., Zhou P.-P., Wang W. D., Luo N., Ma J. (2022), $Zr(OH)_4$-catalyzed controllable selective oxidation of anilines to azoxybenzenes, azobenzenes and nitrosobenzenes, Angew. Chem. Int. Ed., 61, e202112907. (DOI: 10.1002/ange.202112907)

17. Zhu H., Ke X., Yang X., Sarina S., Liu H. (2010), Reduction of nitroaromatic compounds on supported gold nanoparticles by visible and ultraviolet light, Angew. Chem. Int. Ed., 49, 9657–9661. (DOI: 10.1002/anie.201003908)

18. Guo X., Hao C., Jin G., Zhu H.-Y., Guo X.-Y. (2014), Copper nanoparticles on graphene support: an efficient photocatalyst for coupling of nitroaromatics in visible light, Angew. Chem. Int. Ed., 53, 1973–1977. (DOI: 10.1002/anie.201309482)

19. Mondal B., Mukherjee P. S. (2018), Cage encapsulated gold nanoparticles as heterogeneous photocatalyst for facile and selective reduction of nitroarenes to azo compounds, J. Am. Chem. Soc., 140, 12592–12601. (DOI: 10.1021/jacs.0c08029)

20. Dai Y., Li C., Shen Y., Lim T., Xu J., Li Y., Niemantsverdriet H., Besenbacher F., Lock N., Su R. (2018), Light-tuned selective photosynthesis of azo- and azoxy-aromatics using graphitic C_3N_4, Nat. Commun., 9, 60. (DOI: 10.1038/s41467-017-02527-8)

21. Niederer K. A., Gilmartin P. H., Kozlowski M. C. (2020), Oxidative photocatalytic homo- and cross-coupling of phenols: nonenzymatic, catalytic method for coupling tyrosine, ACS Catal., 10, 14615–14623.ss (DOI: 10.1021/acscatal.0c04515)

22. Song S., Song H., Li L., Wang S., Chu W., Peng K., Meng X., Wang Q., Deng B., Liu Q., et al. (2021), A selective Au-ZnO/TiO_2 hybrid photocatalyst for oxidative coupling of methane to ethane with dioxygen, Nat. Catal., 4, 1032–1042. (DOI: 10.1038/s41929-021-00708-9)

23. Qi M.-Y., Conte M., Anpo M., Tang Z.-R., Xu Y.-J. (2021), Cooperative coupling of oxidative organic synthesis and hydrogen production over semiconductor-based photocatalysts, Chem. Rev., 121, 13051–13085. (DOI: 10.1021/acs.chemrev.1c00197)

24. Sitter J. D., Vannucci A. K. (2021), Photocatalytic oxidative coupling of arylamines for the synthesis of azoaromatics and the role of O_2 in the mechanism, J. Am. Chem. Soc., 143, 2938–2943. (DOI: 10.1021/jacs.0c13101)

25. Ruiz-Lopez M. F., Francisco J. S., Martins-Costa M. T. C., Anglada J. M. (2020), Molecular reactions at aqueous interfaces, Nat. Rev. Chem., 4, 459–475. (DOI: 10.1038/s41570-020-0203-2)

26. Bhattacharya A., Mukherjee T. K. (2017), Synergistic enhancement of electron-accepting and -donating ability of nonconjugated polymer nanodot in micellar environment, Langmuir, 33, 14718–14727. (DOI: 10.1021/acs.langmuir.7b04030)

27. Banerjee S., Zare R. N. (2015), Syntheses of isoquinoline and substituted quinolines in charged microdroplets, Angew. Chem. Int. Ed., 54, 14795–14799. (DOI: 10.1002/ange.201507805)

28. Saini B., Singh S., Mukherjee T. K. (2021), Nanocatalysis under nanoconfinement: a metal-free hybrid coacervate nanodroplet as a catalytic nanoreactor for efficient redox and photocatalytic reactions, ACS Appl. Mater. Interfaces, 13, 51117–51131. (DOI: 10.1021/acsami.1c17106)

29. Fallah-Araghi A., Meguellati K., Baret J.-C., Harrak A. E., Mangeat T., Karplus M., Ladame S., Marques C. M., Griffiths A. D. (2014), Enhanced chemical synthesis at soft interfaces: a universal reaction-adsorption mechanism in microcompartments. Phys. Rev. Lett., 112, 028301. (DOI: 10.1103/PhysRevLett.112.028301)

30. Müller T., Badu-Tawiah A., Cooks R. G. (2012). Accelerated carbon–carbon bond-forming reactions in preparative electrospray, Angew. Chem. Int. Ed., 51, 11832–11835. (DOI: 10.1002/anie.201206632)

31. Lee J. K., Samanta D., Nam H. G., Zare R. N. (2019), Micrometer-sized water droplets induce spontaneous reduction, J. Am. Chem. Soc., 141, 10585–10589. (DOI: 10.1021/jacs.9b03227)

32. Majek M., Filace F., Von Wangelin A. J. (2014), On the mechanism of photocatalytic reactions with eosin Y, Beilstein J. Org. Chem., 10, 981–989. (DOI: 10.3762/bjoc.10.97)

33. Saini B., Singh R., Mukhopadhyay S., Mukherjee T. K. (2021), Specific loading and in vitro controlled release of a Ru-based hydrophobically encapsulated model anticancer drug inside

nanoassemblies toward stimuli-responsive drug delivery, ACS Appl. Nano Mater., 4, 2037–2051. (DOI: 10.1021/acsanm.0c03356)

34. Chatterjee S., Mukherjee T. K. (2013), Size-dependent differential interaction of allylamine-capped silicon quantum dots with surfactant assemblies studied using photoluminescence spectroscopy and imaging technique, J. Phys. Chem. C, 117, 10799–10808. (DOI: 10.1021/jp402408d)

35. Eriksson J. C., Gillberg G. (1966), NMR-studies of the solubilisation of aromatic compounds in cetyltrimethylammonium bromide solution II, Acta Chem. Scand., 20, 2019–2027. (DOI: 0.1016/B978-1-4832-2873-0.50016-5)

36. Weidemaier K., Tavernier H. L., Fayer M. D. (1997), Photoinduced electron transfer on the surfaces of micelles, J. Phys. Chem. B, 101, 9352–9361. (DOI: 10.1021/jp972245c)

37. Hayyan M., Hashim M. A., AlNashef I. M. (2016), Superoxide ion: generation and chemical implications, Chem. Rev., 116, 3029–3085. (DOI:10.1021/acs.chemrev.5b00407)

38. Usselman R. J., Hill I., Singel D. J., Martino C. F. (2014), Spin biochemistry modulates reactive oxygen species (ROS) production by radio frequency magnetic fields, PLoS One, 9, e93065. (DOI: 10.1371/journal.pone.0093065)

39. Shirota H., Pal H., Tominaga K., Yoshihara K. (1998), Substituent effect and deuterium isotope effect of ultrafast intermolecular electron transfer: coumarin in electron-donating solvent, J. Phys. Chem. A, 102, 3089–3102. (DOI: 10.1021/jp973376g)

40. Venkatesan M., Mandal H., Bheerappagari R., Bangal P. R. (2019), Bimolecular photoinduced electron transfer between 7-methylbenzo[a]pyrene and aromatic amine donors in stationary and static regimes, J. Photochem. Photobiol. A, 376, 212–223. (DOI: 10.1016/j.jphotochem.2019.03.012)

41. Mukherjee T. K., Mishra P. P., Datta A. (2005), Photoinduced electron transfer from chlorin p_6 to methyl viologen in aqueous

micelles, Chem. Phys. Lett., 407, 119–123. (DOI: 10.1016/j.cplett.2005.03.055)

42. Ghosh S., Mondal S. K., Sahu K., Bhattacharyya K. (2007), Ultrafast photoinduced electron transfer from dimethylaniline to coumarin dyes in sodium dodecyl sulfate and triton X-100 micelles, J. Chem. Phys., 126, 204708. (DOI: 10.1063/1.2733667)

43. Kumbhakar M., Singh P. K., Nath S., Bhasikuttan A. C., Pal H. (2008), Ultrafast bimolecular electron transfer dynamics in micellar media, J. Phys. Chem. B, 112, 6646–6652. (DOI: 10.1021/jp800752d)

44. Mukherjee P., Das A., Sengupta A., Sen P. (2017), Bimolecular photoinduced electron transfer in static quenching regime: illustration of marcus inversion in micelle, J. Phys. Chem. B, 121, 1610–1622. (DOI: 10.1021/acs.jpcb.6b11206)

45. Zhu Y., Huang K., Pan J., Qiu X., Luo X., Qin Q., Wei J., Wen X., Zhang L., Jiao N. (2018), Silver-catalyzed remote Csp^3-H functionalization of aliphatic alcohols, Nat. Commun., 9, 2625. (DOI: 10.1038/s41467-018-05014-w)

Chapter 4

Quantum Dot-Based Hybrid Coacervates for Ultrasensitive Detection of Hg^{2+}

4.1. Introduction

In recent years, due to increasing pollution, facile detection and efficient removal of environmental contaminants have been of primary importance for a clean and healthy environment. Among various environmental contaminations, heavy metal ions, particularly mercuric ion (Hg^{2+}) in water, is one of the most toxic and hazardous contaminants for human health due to its strong affinity towards various biomacromolecules, which can cause a wide variety of diseases in the brain, liver, and kidney *[1−4]*. Furthermore, aqueous Hg^{2+} ions can also react with various microorganisms to yield highly toxic and stable methylmercury and dimethylmercury *[5, 6]*. To avoid this Hg poisoning, the U.S. Environmental Protection Agency (EPA) has kept the maximum contamination level of Hg in drinking water as low as 10 nM (2 ppb) *[7]*. Therefore, rapid detection and efficient removal of this toxic contaminant in drinking water is of significant importance for a healthy environment.

Over the years, numerous analytical methods have been developed for the detection of Hg^{2+} ions in the aqueous medium. These methods are mainly based on colorimetric *[8, 9]*, fluorescence *[10–12]*, phosphorescence *[13]*, resonance scattering *[14]*, surface-enhanced Raman scattering *[15]*, atomic absorption spectroscopy *[16]*, and electrochemical techniques *[17]*. Among these, particular attention has been dedicated to developing colorimetric and fluorescence-based sensors due to their rapid and highly sensitive response as well as for their noninvasive nature *[8–12]*. Previously, researchers have explored different dye-based methods for the facile detection of Hg^{2+} *[18–20]*. Moreover, various functionalized NPs such as carbon nanoparticles *[21, 22]*, surfactant-stabilized- Au NPs *[23]*, ligand-stabilized Ag NPs *[24]*, oligonucleotide-functionalized Au NP hybrids *[25, 26]*, and nucleic acid-functionalized CdSe/ZnS QDs *[11]* have been fabricated for selective and ultrasensitive detection of Hg^{2+}. In addition, composite thin films consisting of Ag NPs and Au nanoclusters have also been designed for the detection of Hg^{2+} *[27, 28]*. While most of

these earlier reported sensors are susceptible to Hg^{2+} detection, these simple molecule or nanoparticle-based systems lack removal capability from contaminated water, which is equally essential to avoid Hg poisoning. Integration of these two functionalities in a single system is challenging and requires a complex designing strategy. In recent times, different nanocomposite-based complex systems, such as MOFs *[29, 30]*, COFs *[31, 32]*, POPs *[33]*, hydrogels *[34]*, mesoporous nanosphere *[35]*, gold composites *[36]*, and microgels *[37]* have been fabricated for better sensitivity, selectivity, and removal capability towards Hg^{2+}. However, while these earlier studies provide significant insight into the sensing and removal mechanism of Hg^{2+} along with improved sensitivity and selectivity, the fabrication and subsequent purification of these nanocomposites are often complex and tedious. Moreover, most of the earlier reported materials can either exhibit sensing or removal capability, except for a few hybrid nanostructure materials *[30, 36]*. Therefore, the facile fabrication of multifunctional hybrid materials with rapid and ultrasensitive responses towards Hg^{2+} and efficient removal capability is highly desirable.

In this study, we fabricated a unique class of membrane-free luminescent hybrid coacervate droplets via simple one-step mixing of oppositely charged MSA-capped CdTe quantum dots (QDs) and poly(diallyldimethylammonium chloride) (PDADMAC) polyelectrolytes in water (Scheme 4.1) and utilized them for ultrasensitive detection and efficient removal of aqueous Hg^{2+}. The tailorability of our strategy was illustrated using two different-sized QDs, namely green luminescent QDs (QDs[523]) and red luminescent QDs (QDs[666]). To the best of our knowledge, the performance of QD-embedded coacervates towards Hg^{2+} remediation was either comparative or better among most of the earlier reported hybrid nanocomposites in terms of fast uptake kinetics, ultrasensitive detection, and high sequestration efficiency.
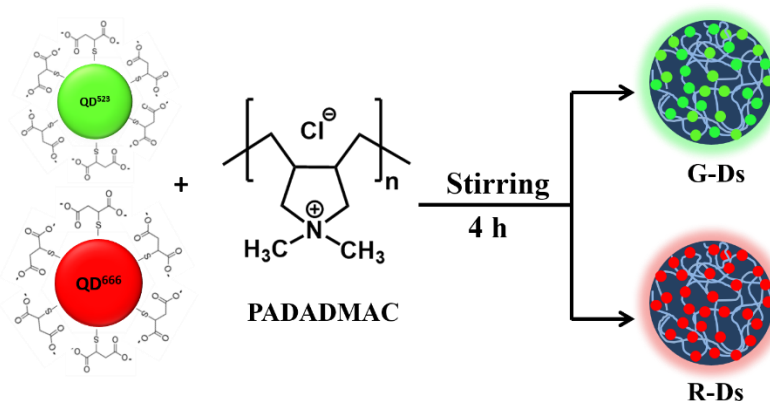
Scheme 4.1. Illustration of QD droplet formation via QD–PDADMAC nanocomposite formation

4.2 Results and Discussion

4.2.1 Characterization of QDs and hybrid droplets

Two different-sized MSA-capped CdTe QDs were synthesized and characterized using various spectroscopic and microscopic techniques *[38, 39]*. The synthesized QDs exhibit excitonic peak positions at 482 and 614 nm, while the corresponding PL peaks appear at 523 (QD^{523}) and 666 nm (QD^{666}), respectively (Figure 4.1A). The estimated PL QYs of QD^{523} and QD^{666} are 0.27 and 0.57, respectively. The size distributions and mean sizes of these QDs were estimated from AFM height profiles. Figure 4.1B shows the AFM images of QD^{523} and QD^{666}. AFM images reveal the presence of well-dispersed spherical QDs. The estimated mean sizes of QD^{523} and QD^{666} are 2.3 and 3.1 nm, respectively (Figure 4.1B). The covalent attachment of MSA ligands on the surface of QDs has been established by FTIR spectroscopy *[38, 39]*. The estimated ξ potentials for QD^{523} and QD^{666} are -25.4 ± 1.1 and -11.1 ± 0.4 mV, respectively. The powder XRD pattern of QD^{523} reveals peaks at 2θ values of 24.8, 41.4, and 47.3º, corresponding to the (111), (220), and (311) crystalline planes, respectively (Figure 4.1C) *[38]*. Taken together, these findings confirm the Synthesis of colloidally stable MSA-capped CdTe QDs.

The coacervate droplet formation has been initiated by mixing negatively charged MSA-capped QDs (85 nM) with PDADMAC (32.5

μM) in Milli-Q water. This binary mixture was equilibrated for different time intervals with stirring at room temperature. Notably, it has been observed that the mean size of these droplets changes as a function of equilibration time in the initial phases and saturates beyond 4 h of equilibration (Figure 4.1D). Therefore, all the binary mixtures of QDs and PDADMAC were equilibrated for 4 h at room temperature before any measurements to get well-dispersed stable spherical droplets. The SEM image of this equilibrated binary mixture shows the formation of well-dispersed spherical coacervates in the size range between 50-1500 nm with a mean size of 430 ± 20 nm (Figure 4.1E).
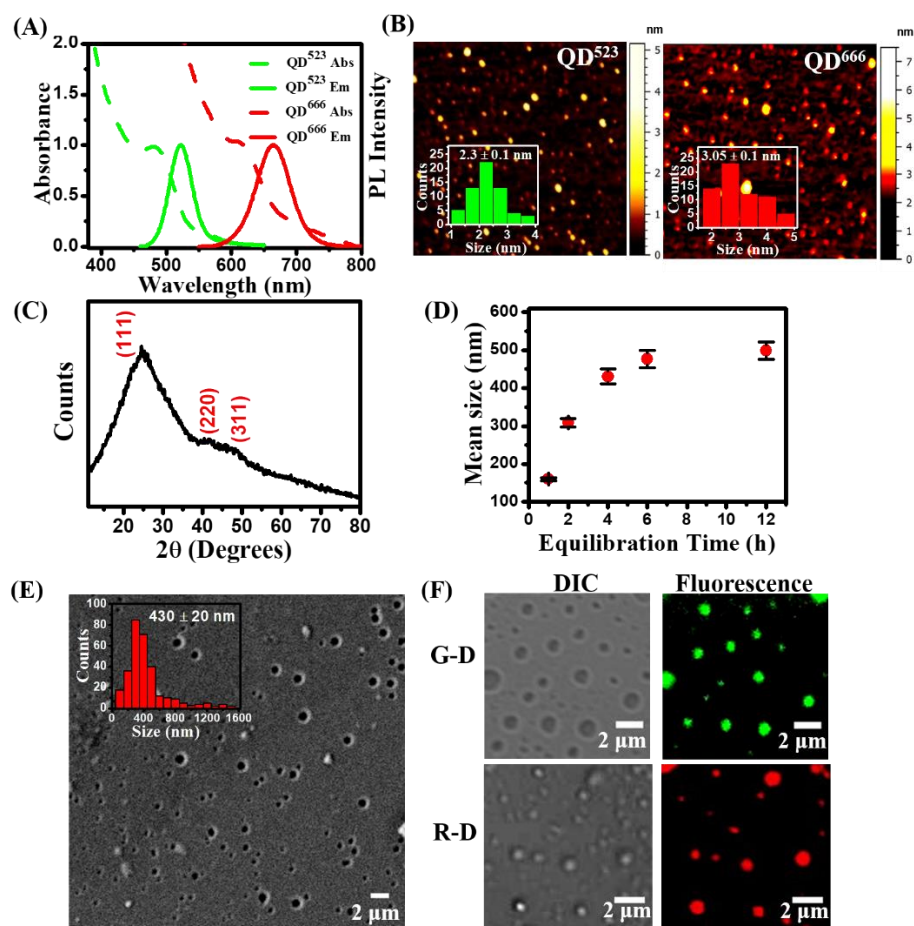
Figure 4.1. (A) Electronic absorption and emission spectra ($\lambda_{ex} = 450$ nm) of QD^{523} and QD^{666}. (B) AFM images of MSA-capped QD^{523} and QD^{666}. The inset shows the size distribution histogram of QD^{523} and QD^{666}. (C) Powder XRD pattern of MSA-capped CdTe QD^{523}. (D) Changes in the mean size of droplets as a function of equilibration

time. (E) FESEM image of G-Ds. The inset shows the size distribution histogram. (F) Confocal microscopy images (DIC and fluorescence) of G-Ds and R-Ds.

The estimated ξ potential of these droplets is +8.1 mV *[38]*. Notably, no droplet formation has been observed in the absence of either QDs or PDADMAC, indicating the essential role of both the constituents in the droplet formation. Moreover, the presence of QDs makes these coacervates inherently luminescent. Figure 4.1F shows the CLSM images of coacervate droplets prepared from QD[523] (G-Ds) and QD[666] (R-Ds). The differential interference contrast (DIC) images of G-Ds and R-Ds reveal the formation of uniform spherical droplets similar to that has been observed in SEM measurements. More importantly, the images in the fluorescence channels reveal distinct green and red luminescence, which originates exclusively from the interior of G-Ds and R-Ds, respectively. These findings unambiguously indicate the presence of self-assembled QDs inside these coacervates. The colloidal stability of these hybrid droplets has been recently explored by our group in a wide range of compositions, pH, and ionic strength of the solution *[38]*. While these droplets are quite stable in neutral to basic pH (>7), they disassembled in lower acidic pH (<5). Similar disassembly has also been observed in the presence of a high ionic strength medium (>100 mM NaCl). Moreover, it has been shown that the luminescence of these individual droplets is quite stable relative to those of individual QDs *[38]*. In the present study, we have utilized the unique inherent PL properties of these droplets towards ultrasensitive detection and removal of toxic Hg^{2+} ions from contaminated water.

Figure 4.2A shows the changes in the PL spectra of G-Ds in the presence of different concentrations of Hg^{2+} ions. It is evident that the PL intensity of G-Ds quenches by 1.5 and 3.1 fold in the presence of 2 and 5 μM Hg^{2+} ions, respectively. Notably, the spectral shape and PL peak position remain unaltered in the presence of Hg^{2+}, indicating the absence of any aggregation of G-Ds in the presence of 5 μM Hg^{2+}. The

inset shows the photographs of G-Ds aqueous suspensions in the absence and presence of Hg^{2+} upon UV light (λ_{ex}= 365 nm) illumination. The visual disappearance of distinct green luminescence of G-D is clearly evident in the presence of 5 μM Hg^{2+}. The kinetic experiment in the presence of 1 μM Hg^{2+} ions reveals that the PL intensity of G-Ds saturates at 15 min of equilibration (Figure 4.2B), which is comparatively less than most of the earlier reported nanocomposite materials *[11, 15, 24, 26, 30, 34, 35, 37]*. Here it is important to mention that the saturation time for the PL intensity of G-D in the presence of Hg^{2+} depends strongly on the concentrations of Hg^{2+} present in the solution and may vary from 5 to 15 min in the concentration range of 5 to 1 μM Hg^{2+}, respectively.
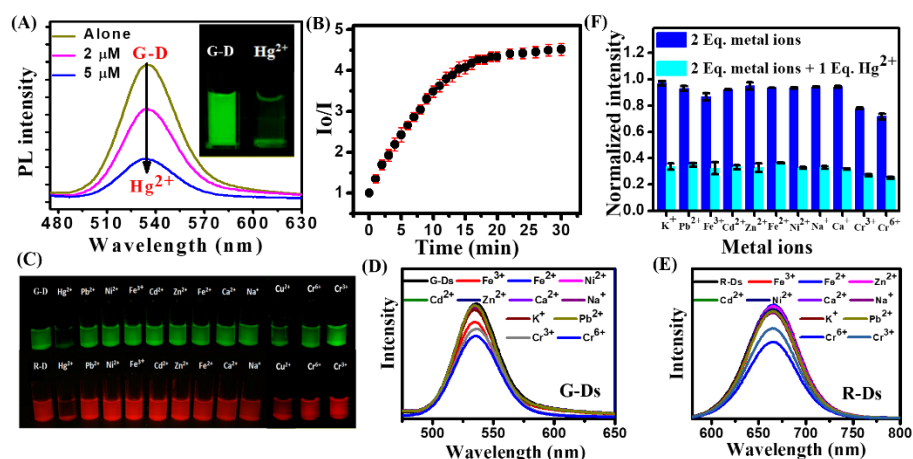
Figure 4.2. (A) Changes in the PL spectra of G-Ds in the presence of 2 and 5 μM of Hg^{2+}. The inset shows the photograph of G-Ds solutions in the absence and presence of 5 μM Hg^{2+} upon UV illumination. (B) Changes in the PL intensity of G-Ds in the presence of 1 μM Hg^{2+} as a function of equilibration time. (C) Photograph showing the PL of G-Ds and R-Ds solutions in the absence and presence of various metal ions (5 μM) under UV light. PL spectra of (D) G-Ds and (E) R-Ds in the presence of various interfering metal ions**.** (F) Selectivity and anti-interference capability of G-Ds towards Hg^{2+} detection in the presence of different metal ions (2.0 equiv).

Notably, the PL of G-Ds and R-Ds remains almost unaltered in the presence of other metal ions (5 μM) such as Pb^{2+}, Ni^{2+}, Fe^{2+}, Cr^{3+},

Cr^{6+}, Cd^{2+}, Zn^{2+}, Ca^{2+}, Fe^{3+}, Na^{+}, and K^{+} suggesting selective interactions with Hg^{2+} (Figure 4.2C–E). It is evident from Figure 4.2C that other metal ions do not alter the visible green and red luminescence of G-Ds and R-Ds, respectively. Similarly, the PL spectra of both G-Ds and R-Ds remain almost unaltered in the presence of these interfering metal ions (Figure 4.2D & 4.2E). These observations clearly indicate that the changes in PL signals of these hybrid droplets are selective towards Hg^{2+}. To explore the anti-interference ability of these droplets towards Hg^{2+} detection in the presence of excess interference ions, we have performed competition experiments in the presence of 2.0 equiv of other interference metal ions and 1.0 equiv of Hg^{2+} ions. Figure 4.2F display the selectivity and the anti-interference ability of these hybrid droplets towards Hg^{2+} detection. It is evident that irrespective of the nature of interference metal ions, hybrid droplets show similar responses towards Hg^{2+}.
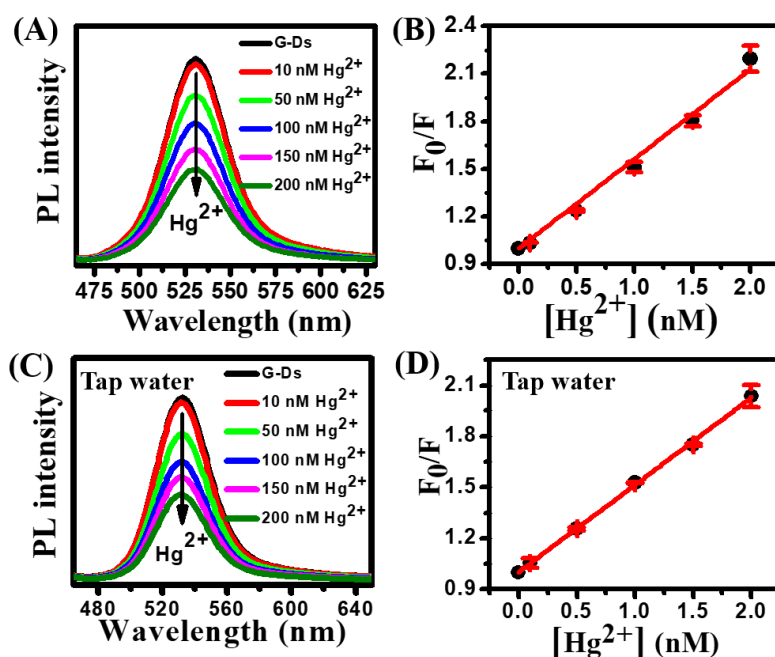
Figure 4.3. (A), (C) Changes in PL spectra of G-Ds upon addition of different concentrations (0−200 nM) of Hg^{2+} at 450 nm excitation in Milli-Q and Tap water, respectively. (B), (D) Steady-state Stern–Volmer plots of G-Ds in Milli-Q and Tap water, respectively.

Table 4.1. Comparison of LOD of various recently reported Hg^{2+} sensors.

S. No.	Sensor	LOD	Ref.
1.	Lanthanide MOF	220 nM	40
2.	NH2-MIL-53(Al) MOF	150 nM	30
3.	Ruthenium complexes	99.7 nM	9
4.	Polytriazine nanospheres (NOP-28)	59.8 nM	41
5.	Porous organic polymer	18.4 nM	33
6.	TFPPy-CHYD COF	17 nM	42
7.	Luminescent MOF-263	16.5 nM	29
8.	$g\text{-}C^3N_4$ nanosheets	12 nM	43
9.	CdS-DNA nanocomposite	8.6 nM (30°C) 4.3 nM (50°C)	44
10.	Tween 20 stabilized AuNPs	5 nM	23
11.	N-doped carbon dots	6.8 nM	21
12.	Au ND−PNIPAM hybrid microgel	1.7 nM	37
13.	Tryptophan-dithiocarbamate-based polymeric probe	1.5 nM	45
14.	DNA-derived polymeric sensor	0.65 nM	46
15.	G-Ds	1.32 nM	Present Study

Next, we have estimated the LOD of these droplets towards Hg^{2+} sensing. Figure 4.3A displays the changes in the PL spectra of G-Ds in the presence of different concentrations (10-200 nM) of Hg^{2+} ions. The PL intensity decreases gradually with an increase in the concentrations of Hg^{2+} ions. The Stern-Volmer (SV) plot reveals linear behavior ($R^2 = 0.9990$) with a SV constant of 5.63×10^6 M^{-1} (Figure 4.3B). Notably, the estimated SV constant is an order of magnitude higher than most of the previously reported nanocomposite systems

[30, 33] and indicates a high binding affinity of Hg^{2+} towards these droplets. The LOD at a signal-to-noise ratio of 3 is calculated using the estimated SV constant. The estimated LOD of Hg^{2+} for G-Ds is 1.32 nM (0.26 ppb), which is superior to most of the previously reported materials (Table 4.1). Here it is important to mention that the equilibration time for the fabrication of G-Ds slightly influences the estimated LOD of Hg^{2+} (Table 4.2). However, beyond 4 h of equilibration, the LOD remains almost constant.

Table 4.2. Changes in the mean size of droplets and LOD of Hg^{2+} sensing as a function of equilibration time.

Equilibration Time	Mean Size	LOD
1 h	160 ± 4 nm	1.87 nM
2 h	309 ± 11 nm	1.72 nM
4 h	430 ± 20 nm	1.32 nM
6 h	477 ± 24 nm	1.27 nM
12 h	499 ± 23 nm	1.25 nM

This observation can be explained by considering the formation of well-dispersed stable droplets at and beyond 4 h of equilibration. Nevertheless, the estimated LOD of the present system is lower than the maximum permittable limit (10 nM) of Hg^{2+} in drinking water and hence can be utilized to detect trace amounts of Hg^{2+} contamination in real water samples. Next, we have explored the response and sensitivity of our system towards Hg^{2+}-spiked tap water. It is evident from Figure 4.3C that the PL intensity of G-Ds decreases gradually with increases in the concentrations of Hg^{2+} in tap water in the range of 10-200 nM. The estimated LOD of G-Ds towards Hg^{2+}-spiked tap water is 1.45 nM (0.29 ppb), which is close to that estimated for Milli-Q water (Figure 4.3D). The similar sensitivity in Milli-Q and tap water further substantiates that the PL response of these droplets is highly

selective towards Hg^{2+}. Therefore, our findings clearly reveal the potential of these hybrid droplets towards highly selective and ultrasensitive detection of Hg^{2+} in water.

4.2.2. Mechanism of Hg^{2+} sensing

In order to explore the luminescence behaviors of individual G-D and R-D in the presence of Hg^{2+}, we have performed confocal imaging.
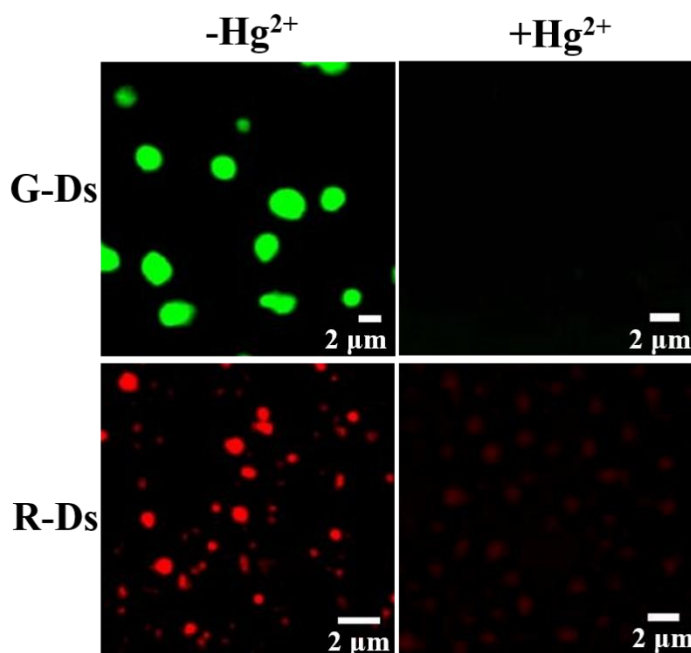
Figure 4.4. Confocal fluorescence images of G-D and R-D in the absence and presence of 5 μM Hg^{2+}.

Figure 4.4 displays the confocal images of G-D and R-D in the absence and presence of 5 μM Hg^{2+} ions. Distinct green and red luminescent spherical droplets are observed in the absence of Hg^{2+} (Figure 4.4, left panel). Interestingly, the luminescence of individual G-D and R-D disappears completely in the presence of 5 μM Hg^{2+} (Figure 4.4, right panel). These observations suggest that Hg^{2+} ions interact with individual droplets and quench their inherent PL.

To establish the presence of Hg^{2+} ions inside individual droplets, we have performed EDX and elemental mapping in the presence of Hg^{2+} ions. The aqueous suspension of G-D was mixed with

5 µM of Hg^{2+} and equilibrated for 15 min at room temperature. The excess Hg^{2+} ions if any were separated out from the mixture by centrifugation (10,000 rpm for 10 min).
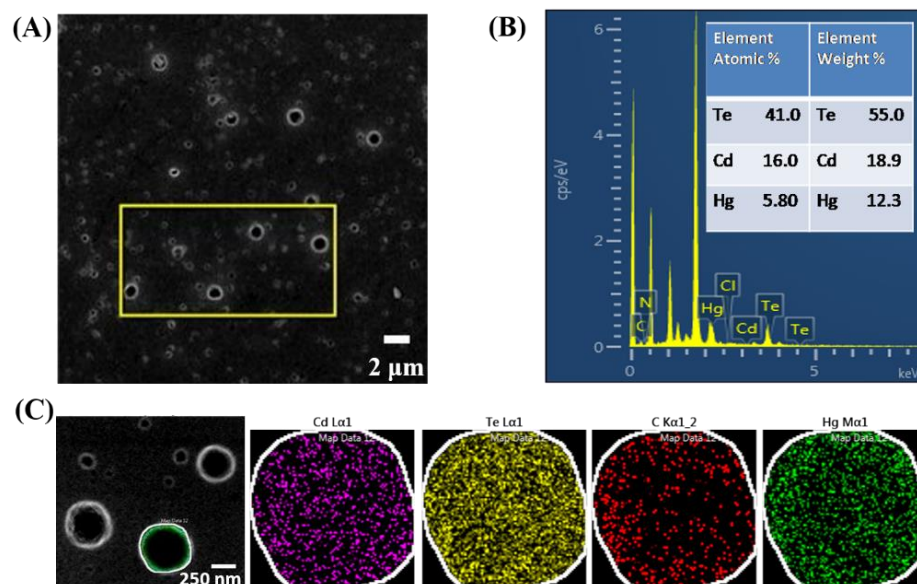
Figure 4.5. (A) FESEM image of G-Ds in the presence of 5 µM Hg^{2+}. (B) EDX spectrum of G-Ds in the presence of Hg^{2+}. The inset shows the atomic and weight % of different elements. (C) Corresponding elemental mappings of the Cd, Te, C, and Hg^{2+} in G-D.

The SEM image of G-Ds-Hg^{2+} composites reveals well-dispersed spherical droplets (Figure 4.5A), similar to those observed earlier in the absence of Hg^{2+}. This observation suggests that Hg^{2+} ions neither induce aggregation nor alter the shape of G-Ds. Furthermore, the EDX spectrum shows the presence of all the essential elements of G-D along with Hg (Figure 4.5B), which unambiguously confirms the presence of Hg^{2+} inside the porous structure of G-D. Figure 4.5C displays the results of the corresponding EDX elemental mapping of an individual G-D-Hg^{2+} composite for Cd, Te, C, and Hg. The uniform distribution of Hg inside the droplet is clearly evident and substantiates the fact that Hg^{2+} ions specifically bind with G-Ds. Taken together, these findings suggest that Hg^{2+} ions specifically associate with droplets and quench their inherent PL. As mentioned earlier, the intrinsic PL of these hybrid droplets arises due to the presence of QDs,

and it is expected that the bound Hg^{2+} ions directly interact with QDs and modulate their PL properties inside the droplet. In order to understand the mechanism of interaction between self-assembled QDs inside the droplets and Hg^{2+} ions, we have performed time-resolved PL lifetime and FTIR measurements of QDs and hybrid droplets in the absence and presence of Hg^{2+} ions.

Figure 4.6 displays the PL decay traces (λ_{ex} = 445 nm; λ_{em} = 523 nm) of QDs and G-Ds in the absence and presence of 5 µM Hg^{2+}. The PL decay curve of QDs fits satisfactorily with a three-exponential decay function (Figure 4.6A). This three exponential decay kinetics is to the radiative recombination at band edge, deep trap, and shallow trap states of QDs. Similar three exponential decay kinetics have been reported earlier for ligand-capped CdTe QDs. MSA-capped CdTe QDs show three lifetime components of 4.38 (16%), 0.30 (23%), and 23.13 ns (61%) with an average lifetime of 14.90 ns (Table 4.3). While the 4.38 ns component arises due to the exciton recombination at the band edge of CdTe QDs, the 0.30 and 23.13 ns components can be assigned due to the recombination at deep and shallow trap states, respectively *[47]*. Interestingly, the PL decay curve of QD gets steeper upon the formation of G-Ds (Figure 4.6A). The PL lifetime of QD in G-Ds shortens to 0.50 ns with lifetime components of 1.30 (5%), 0.03 (90%), and 7.07 ns (5%) (Table 4.3). The observed PL lifetime quenching of QD upon G-Ds formation arises mainly due to exciton-exciton annihilation between closely associated QDs inside the droplets.

Notably, the PL lifetime of QD in G-Ds decreases further in the presence of 5 µM Hg^{2+}, indicating dynamic PL quenching. The PL decay curve of G-Ds in the presence of 5 µM Hg^{2+} overlaps exactly with the IRF and hence we could not able to extract the decay parameters. Nevertheless, the significant lifetime quenching of G-Ds upon the addition of Hg^{2+} clearly suggests the involvement of ultrafast photoinduced excited state processes, such as electron or energy
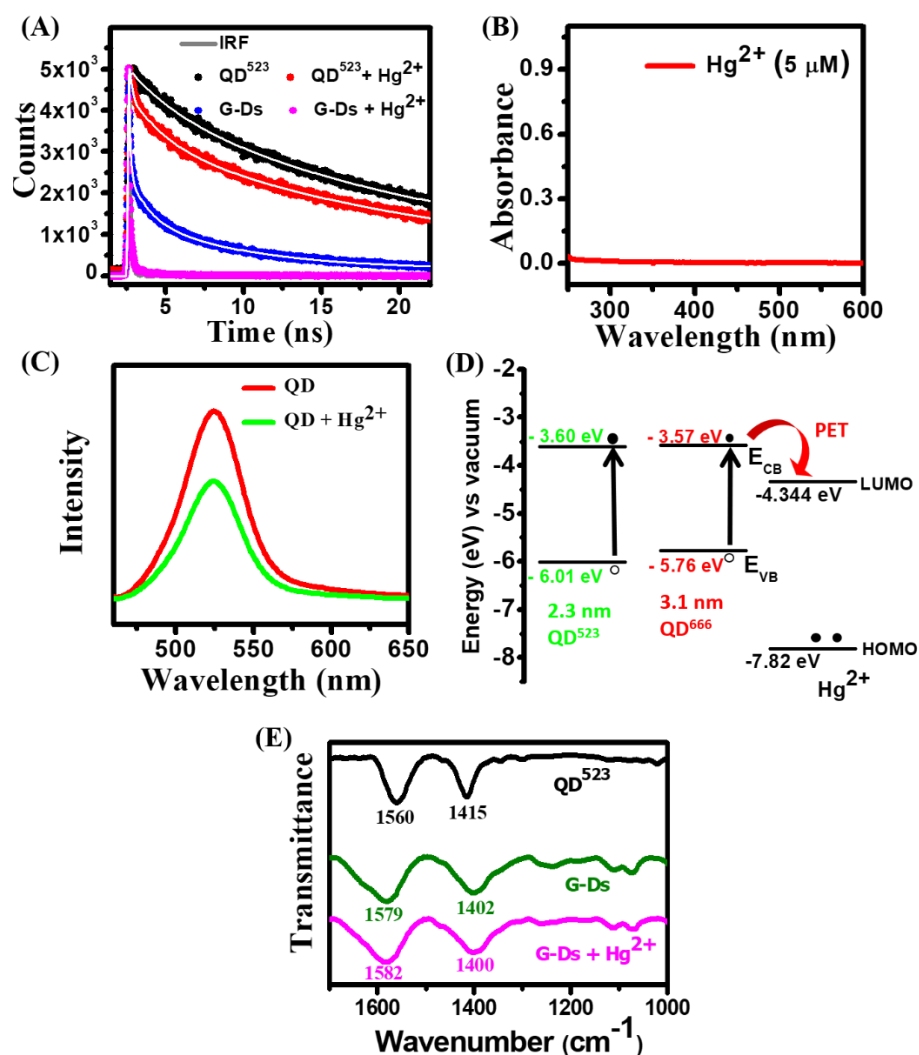
Figure 4.6. (A) PL decay traces (λ_{ex} = 445 nm; λ_{em} = 523 nm) of QD^{523} and G-Ds in the absence and presence of 5 µM Hg^{2+}. (B) Absorbance spectrum Hg^{2+}. (C) PL spectra of QDs in the absence and presence of 5 µM Hg^{2+}. (D) Band alignment of VB and CB of QD^{523} and QD^{666} with the HOMO and LUMO of Hg^{2+}. (E) FTIR spectra of CdTe QD^{523} and G-Ds with and without 5 µM Hg^{2+}.

transfer, behind the observed PL quenching. Notably, aqueous Hg^{2+} ions don't have any absorption or emission in the visible wavelength region (400-700 nm) (Figure 4.6B). As a consequence, the involvement of excitation energy transfer between self-assembled QDs in droplets and Hg^{2+} ions can be ruled out due to the absence of any spectral overlap. Therefore, photoinduced electron transfer (PET) from

photoexcited QDs to Hg^{2+} ions inside the droplets is the most probable mechanism behind the observed PL quenching.

Table 4.3. The PL lifetime decay parameters of QD^{523} and G-Ds in the absence and presence of 5 μM Hg^{2+}.

Sample	τ_1 (ns)	a_1	T_2 (ns)	a_2	τ_3 (ns)	a_3	$<\tau>$ (ns)	χ^2
QD	4.38	0.16	0.30	0.23	23.13	0.61	14.9	1.03
QD + Hg^{2+}	3.34	0.15	0.17	0.54	22.8	0.38	9.20	1.08
G-Ds	1.30	0.05	0.03	0.90	7.07	0.05	0.50	1.10

Here, it is important to note that the PL intensity and lifetime of bare MSA-capped QDs decrease noticeably upon the addition of 5 μM of Hg^{2+} (Figure 4.6A & 4.6C). However, the extent of this PL quenching is significantly lower than that observed inside the droplets. This can be explained by considering the significant confinement of QDs and encapsulated Hg^{2+} ions inside the porous microcompartment of droplets. The involvement of similar PET processes for Hg^{2+} sensing has been reported in the literature for various sensors [11, 20-22, 33, 35]. For instance, Freeman *et al.* demonstrated PET from photoexcited nucleic acid-functionalized CdSe/ZnS QDs to Hg^{2+}-thymine complex at the surface [11]. Similarly, PET processes from photoexcited CNPs to surface-conjugated Hg^{2+} ions have been demonstrated [21, 22]. Zhu *et al.* proposed a static electron transfer PL quenching mechanism for the sensing of Hg^{2+} by cerium phosphonate nanostructured spheres [35]. Here, it is important to comment on the selective PL quenching of G-Ds in the presence of Hg^{2+}. To address this selective PL quenching of QDs in the presence of Hg^{2+} via PET process, we have aligned the band positions of the conduction band (CB) and valence band (VB) of QDs with the HOMO and LUMO of Hg^{2+} (Figure 4.6D). The band positions of QDs and HOMO-LUMO positions of Hg^{2+} are taken from literature reports [48, 49]. Band alignment reveals that the LUMO of Hg^{2+} falls in the band gap region

of both the QDs, which facilitates the ultrafast PET between photoexcited QD and Hg^{2+} (Figure 4.6D). We believe that the observed selectivity arises mainly due to the variation of the position of LUMO of other interfering metal ions outside the band gap region of both the QDs. Notably, this feature makes our present system unique, as by simple variation of the nature and/or size of QDs, it is possible to selectively detect a range of toxic metal ions.

Next, we performed FTIR measurements to understand the nature of interactions between various groups of G-Ds and Hg^{2+} ions. Notably, the estimated ζ potentials of MSA-capped CdTe QDs and G-Ds are – 25.4 and +8.1 mV, respectively. Earlier, we have shown that these positively charged droplets can spontaneously sequester various foreign molecules irrespective of their charges as a consequence of both hydrophobic and electrostatic interactions [38]. To explore the local interactions of negatively charged carboxylate groups of MSA ligands at the surface of QDs inside the droplets with encapsulated Hg^{2+} ions, we have recorded the changes in carboxylate stretching frequencies in the absence and presence of Hg^{2+}. Figure 4.6E shows the changes in FTIR spectra in the carboxylate stretching frequency region (1000-1700 cm^{-1}) of CdTe QDs and G-Ds in the absence and presence of Hg^{2+}. MSA-capped QDs show two distinct peaks at 1560 and 1415 cm^{-1} due to the asymmetric and symmetric stretching of carboxylate ions, respectively. Interestingly, both these peaks broaden significantly upon the formation of G-Ds. Moreover, the asymmetric and symmetric stretching peaks of carboxylate groups in G-Ds shifted at 1579 and 1402 cm^{-1}, respectively. These spectral changes clearly reveal the interaction of carboxylate groups of MSA ligands with PDADMAC. The difference (Δ) between these two peaks is estimated to be 177 cm^{-1} for G-Ds. This Δ value signify the coordination of carboxylate groups with PDADMAC in a bridging bidentate manner [24]. Moreover, the Δ value between asymmetric and symmetric stretching frequencies increases further in the presence of Hg^{2+} and shows a value of 182 cm^{-1}. Earlier, Sumesh et al. observed similar

changes in the FTIR spectrum of mercaptosuccinic acid (MSA)-capped Ag NPs in the presence of Hg^{2+} *[24]*. They have observed both bridging bidentate and monodentate modes of interactions between carboxylate groups of MSA and Hg^{2+}. Taken together, our FTIR study reveals interactions of negatively charged carboxylate groups of MSA ligands on the surface of QDs with positively charged PDADMAC and Hg^{2+} ions in solution.

4.2.3. Sequestration of Hg^{2+} from contaminated water using G-Ds

Our findings clearly reveal sequestration of Hg^{2+} ions by G-Ds and subsequent PL quenching due to the ultrafast PET from photoexcited QD to Hg^{2+} inside the droplet. To know the Hg^{2+} sequestration capability of G-Ds from contaminated water, the separation efficiency has been estimated using simple centrifugation method in the absence and presence of other heavy metal ions such as Pb^{2+}, Cd^{2+}, Cr^{3+}, Fe^{2+}, and Fe^{3+}. Figure 4.7A shows the schematic illustration of the separation process. Initially, droplets were prepared in Milli-Q water using 85 nM QD and 32.5 µM PDADMAC and equilibrated for 4 h at room temperature. Subsequently, appropriate amount of Hg^{2+} ions were added into the equilibrated G-Ds solution to make the final concentration of 1 µM. The mixture was further equilibrated for 15 min and subsequently centrifuged at 10,000 rpm for 20 min. The resultant supernatant was further mixed with 85 nM QD and 32.5 µM PDADMAC to regenerate G-Ds. Finally, the relative PL intensity of initial G-Ds and regenerated G-Ds from the supernatant was compared to estimate the trace amount of Hg^{2+} remaining in the supernatant using a PL calibration plot. It is evident that the aqueous suspension of G-Ds shows distinct green luminescence (Figure 4.7B & C).

The addition of 1 µM Hg^{2+} results in significant PL quenching as has been observed earlier. Upon centrifugation, the supernatant shows no PL, suggesting the absence of any G-Ds in the supernatant (Figure 4.7B & C). This observation reveals that simple centrifugation can efficiently remove these droplets from aqueous suspension.
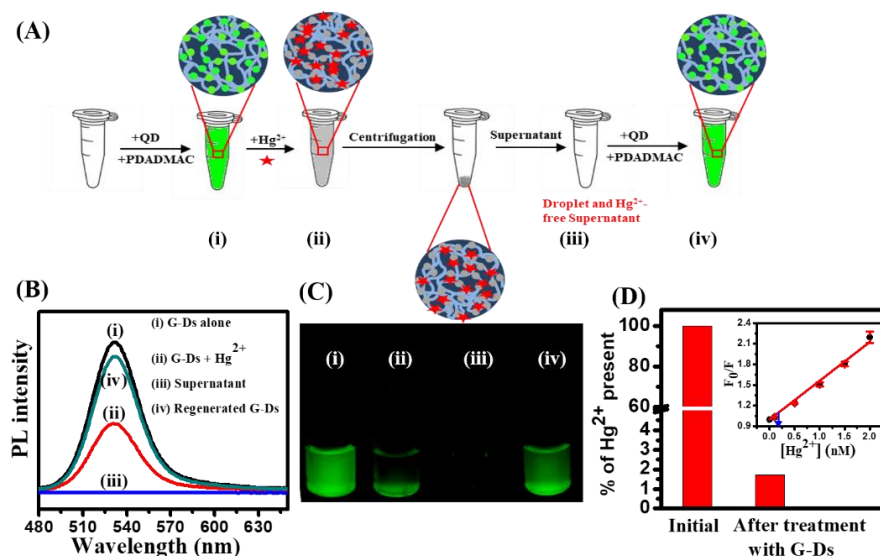
Figure 4.7. (A) Schematic illustration of Hg^{2+} sequestration from contaminated water using G-Ds via centrifugation process. (B) PL spectra of (i) initial G-Ds, (ii) G-Ds + 1 μM Hg^{2+}, (iii) supernatant, (iv) regenerated G-Ds in the supernatant. (C) Corresponding UV light photograph of solutions at different stages of Hg^{2+} sequestration process. (D) Quantitative estimation of sequestration efficiency of Hg^{2+} from the standard calibration curve. The inset shows the PL calibration plot for the G-Ds and Hg^{2+} system.

In order to know whether all the added Hg^{2+} ions removed with the G-Ds from the supernatant or not, we have regenerated G-Ds in supernatant with exactly same concentrations of QDs and PDADMAC that have been used earlier. Interestingly, the PL intensity of regenerated G-Ds in supernatant approaches very close to the initial PL intensity of G-Ds (Figure 4.7B). Moreover, intense green PL reappears in the regenerated G-Ds in supernatant upon UV illumination (Figure 4.7C). These observations suggest that most of the added Hg^{2+} ions are removed from the supernatant with G-Ds. The remaining amount of Hg^{2+} in supernatant has been estimated from the standard PL calibration curve and the sequestration efficiency of the present droplets is calculated to be 98.3% (Figure 4.7D). However, it has been observed that in the presence of the same concentration of other heavy metal ions, such as Pb^{2+}, Cd^{2+}, Cr^{3+}, Fe^{2+}, and Fe^{3+} the sequestration

efficiency of Hg^{2+} becomes 93.3%. These findings not only reveal the ultrasensitive and rapid response of our present hybrid droplets towards Hg^{2+} sensing but also illustrate that they can be useful as active materials for Hg^{2+} sequestration. Moreover, our present study reveals that these hybrid coacervate droplets have tremendous potential in various sensing and environmental remediation processes along with their useful role in artificial protocell research.

4.3. Conclusions

We present a simple organic-inorganic hybrid nanocomposite-based sensing platform for the ultrasensitive detection and efficient sequestration of Hg^{2+} ions from contaminated water. Intrinsically luminescent membrane-free coacervate droplets (G-Ds and R-Ds) have been fabricated from two different-sized MSA-capped QDs (QD^{523} and QD^{666}) in the presence of PDADMAC in aqueous medium. Significant PL quenching of these hybrid droplets has been observed in the presence of Hg^{2+}. This PL quenching is highly selective towards Hg^{2+} and other metal ions that do not interfere with the sensing process. Our findings demonstrate that Hg^{2+} ions specifically associate with the membrane-less structure of droplets via electrostatic interactions with the free carboxylate groups of MSA ligands at the surface of QDs and undergo ultrafast PET. The estimated LOD for Hg^{2+} sensing with the present system is 1.32 nM (0.26 ppb), which is significantly lower than the maximum allowable contamination level of Hg^{2+} ions in drinking water (2 ppb). Furthermore, we have demonstrated that our present hybrid droplets efficiently sequester trace amounts of Hg^{2+} from contaminated water by simple centrifugation technique. Taken together, our findings reveal that these colloidally stable and intrinsically luminescent hybrid droplets have tremendous potential for practical applications toward Hg^{2+} detection as well as remediation technology.

Note: This is copyrighted material with permission of the American Chemical Society.

4.4. References

1. Fitzgerald W. F., Lamborg C. H., Hammerschmidt C. R. (2007), Marine biogeochemical cycling of mercury, Chem. Rev., 107, 641−662. (DOI:10.1021/cr050353m)

2. Henkel G., Krebs B. (2004), Metallothioneins: zinc, cadmium, mercury, and copper thiolates and selenolates mimicking protein active site features−structural aspects and biological implications, Chem. Rev., 104, 801−824. (DOI:10.1021/cr020620d)

3. Onyido I., Norris A. R., Buncel E. (2004), Biomolecule−mercury interactions: modalities of DNA base−mercury binding mechanisms. remediation strategies, Chem. Rev., 104, 5911−5929. (DOI:10.1021/cr030443w)

4. Wang Q., Kim D., Dionysiou D. D., Sorial G. A., Timberlake D. (2004), Sources and remediation for mercury contamination in aquatic systems–a literature review. Environ. Pollut., 131, 323−336. (DOI:10.1016/j.envpol.2004.01.010)

5. Tchounwou P. B., Ayensu W. K., Ninashvili N., Sutton D. (2003), Environmental exposure to mercury and its toxicopathologic implications for public health, Environ. Toxicol., 18, 149-175. (DOI:10.1002/tox.10116)

6. Harris H. H., Pickering I. J., George G. N. (2003), The chemical form of mercury in fish, Science 301, 1203. (DOI:10.1126/science.1085941)

7. Chen J., Pan J., Chen S. (2017) A naked-eye colorimetric sensor for Hg^{2+} monitoring with cascade signal amplification based on target-induced conjunction of split DNAzyme fragments, Chem. Commun., 53, 10224−10227. (DOI:10.1039/C7CC05445A)

8. Tatay S., Gavina P., Coronado E., Palomares E. (2006), Optical mercury sensing using a benzothiazolium hemicyanine dye, Org. Lett., 8, 3857−3860. (DOI:10.1021/ol0615580)

9. Nazeeruddin M. K., Censo D. D., Humphry-Baker R., Grätzel M. (2006), Highly selective and reversible optical, colorimetric, and electrochemical detection of mercury(II) by amphiphilic ruthenium

complexes anchored onto mesoporous oxide films, Adv. Funct. Mater., 16, 189−194. (DOI:10.1002/adfm.200500309)

10. Nolan E. M., Lippard S. J. (2007), Turn-on and ratiometric mercury sensing in water with a red-emitting probe, J. Am. Chem. Soc., 129, 5910−5918. (DOI:10.1021/ja068879r)

11. Freeman R., Finder T., Willner I. (2009), Multiplexed analysis of Hg^{2+} and Ag^+ ions by nucleic acid functionalized CdSe/ZnS quantum dots and their use for logic gate operations, Angew. Chem. Int. Ed., 48, 7818−7821. (DOI:10.1002/ange.200902395)

12. Piyanuch P., Watpathomsub S., Lee V. S., Nienaber H. A., Wanichacheva N. (2016), Highly sensitive and selective Hg^{2+}-chemosensor based on dithia-cyclic fluorescein for optical and visual-eye detections in aqueous buffer solution, Sens. Actuators B, 224, 201−208. (DOI:10.1016/j.snb.2015.09.131)

13. Ru J., Tang X., Ju Z., Zhang G., Dou W., Mi X., Wang C., Liu W. (2015), Exploitation and application of a highly sensitive Ru (ii) complex-based phosphorescent chemodosimeter for Hg^{2+} in aqueous solutions and living cells, ACS Appl. Mater. Interfaces, 7, 4247−4256. (DOI:10.1021/am508484q)

14. Wu Y., Zhan S., Xu L., Shi W., Xi T., Zhan X., Zhou P. (2011), A simple and label-free sensor for mercury (ii) detection in aqueous solution by malachite green based on a resonance scattering spectral assay, Chem. Commun., 47, 6027−6029. (DOI:10.1039/C1CC10563A)

15. Ding X., Kong L., Wang J., Fang F., Li D., Liu J. (2013), Highly sensitive SERS detection of Hg^{2+} ions in aqueous media using gold nanoparticles/graphene heterojunctions, ACS Appl. Mater. Interfaces, 5, 7072−7078. (DOI:10.1021/am401373e)

16. Shah A. Q., Kazi T. G., Baig J. A., Afridi H. I., Arain M. B. (2012), Simultaneously determination of methyl and inorganic mercury in fish species by cold vapour generation atomic absorption spectrometry, Food Chem., 134, 2345−2349. (DOI:10.1016/j.foodchem.2012.03.109)

17. Wang S. P., Forzani E. S., Tao N. J. (2007), Detection of heavy

metal ions in water by high-resolution surface plasmon resonance spectroscopy combined with anodic stripping voltammetry, Anal. Chem., 79, 4427−4432. (DOI:10.1021/ac0621773)

18. Yang Y.-K., Yook K.-J., Tae J. (2005), A rhodamine-based fluorescent and colorimetric chemodosimeter for the rapid Detection of Hg^{2+} ions in aqueous media, J. Am. Chem. Soc., 127, 16760−16761. (DOI:10.1021/ja054855t)

19. Nolan E. M., Lippard S. J. (2003), A "turn-on" fluorescent sensor for the selective Detection of mercuric ion in aqueous media, J. Am. Chem. Soc., 125, 14270−14271. (DOI:10.1021/ja037995g)

20. Ahamed B. N., Ghosh P. (2011), A chelation enhanced selective fluorescence sensing of Hg^{2+} by a simple quinoline substituted tripodal amide receptor, Dalton Trans., 40, 12540−12547. (DOI:10.1039/C1DT10923E)

21. Gupta A., Chaudhary A., Mehta P., Dwivedi C., Khan S., Verma N. C., Nandi C. K. (2015), Nitrogen-doped, thiol-functionalized carbon dots for ultrasensitive Hg(II) detection, Chem. Commun., 51, 10750−10753. (DOI:10.1039/C5CC03019F)

22. Lan M., Zhang J., Chui Y.-S., Wang P., Chen X., Lee C.-S., Kwong H.-L., Zhang W. (2014), Carbon nanoparticle-based ratiometric fluorescent sensor for detecting mercury ions in aqueous media and living cells, ACS Appl. Mater. Interfaces, 6, 21270−21278. (DOI:10.1021/am5062568)

23. Lou T., Chen Z., Wang Y., Chen L. (2011), Blue-to-red colorimetric sensing strategy for Hg^{2+} and Ag^{+} via redox-regulated surface chemistry of gold nanoparticles, ACS Appl. Mater. Interfaces, 3, 1568−1573. (DOI:10.1021/am200130e)

24. Sumesh E., Bootharaju M. S., Anshup, Pradeep T. (2011), A practical silver nanoparticle-based adsorbent for the removal of Hg^{2+} from water, J. Hazard. Mater., 189, 450−457. (DOI:10.1016/j.jhazmat.2011.02.061)

25. Lee J.-S., Han M. S., Mirkin C. A. (2007), Colorimetric detection of mercuric ion (Hg^{2+}) in aqueous media using DNA-functionalized gold nanoparticles, Angew. Chem. Int. Ed., 46,

4093−4096. (DOI:10.1002/anie.200700269)

26. Li D., Wieckowska A., Willner I. (2008), Optical analysis of Hg^{2+} ions by oligonucleotide−gold-nanoparticle hybrids and DNA-based machines, Angew. Chem. Int. Ed., 47, 3927−3931. (DOI:10.1002/ange.200705991)

27. Ramesh G. V., Radhakrishnan T. P. (2011), A universal sensor for mercury (Hg, Hg^I, Hg^{II}) based on silver nanoparticle-embedded polymer thin film, ACS Appl. Mater. Interfaces, 3, 988−994. (DOI:10.1021/am200023w)

28. George A., Shibu E. S., Maliyekkal S. M., Bootharaju M. S., Pradeep T. (2012), Luminescent, freestanding composite films of Au_{15} for specific metal ion sensing, ACS Appl. Mater. Interfaces, 4, 639− 644. (DOI:10.1021/am201292a)

29. Rudd N. D., Wang H., Fuentes-Fernandez E. M. A., Teat S. J., Chen F., Hall G., Chabal Y. J., Li J. (2016), Highly efficient luminescent metal−organic framework for the simultaneous Detection and removal of heavy metals from water, ACS Appl. Mater. Interfaces, 8, 30294−30303. (DOI:10.1021/acsami.6b10890)

30. Zhang L., Wang J., Du T., Zhang W., Zhu W., Yang C., Yue T., Sun J., Li T., Wang J. (2019), NH_2-MIL-53(Al) metal−organic framework as the smart platform for simultaneous high-performance detection and removal of Hg^{2+}, Inorg. Chem., 58, 12573−12581. (DOI:10.1021/acs.inorgchem.0c01787)

31. Ding S.-Y., Dong M., Wang Y.-W., Chen Y.-T., Wang H.-Z., Su C.-Y., Wang W. (2016), Thioether-based fluorescent covalent organic framework for selective Detection and facile removal of mercury-(II), J. Am. Chem. Soc., 138, 3031−3037. (DOI:10.1021/jacs.5b10754)

32. Cui W.-R., Zhang C.-R., Jiang W., Liang R.-P., Wen S.-H., Peng D., Qiu J.-D. (2019), Covalent organic framework nanosheet-based ultrasensitive and selective colorimetric sensor for trace Hg^{2+} detection, ACS Sustainable Chem. Eng., 7, 9408−9415. (DOI:10.1021/acssuschemeng.9b00613)

33. Li Y., He Y., Guo F., Zhang S., Liu Y., Lustig W. P., Bi S., Williams L. J., Hu J., Li J. (2019), NanoPOP: solution-processable fluorescent porous organic polymer for highly sensitive, selective, and fast naked eye detection of mercury, ACS Appl. Mater. Interfaces, 11, 27394−27401. (DOI:10.1021/acsami.9b06488)

34. Joseph K. A., Dave N., Liu J. (2011), Electrostatically directed visual fluorescence response of DNA-functionalized monolithic hydrogels for highly sensitive Hg^{2+} detection, ACS Appl. Mater. Interfaces, 3, 733−739. (DOI:10.1021/am101068c)

35. Zhu Y.-P., Ma T.-Y., Ren T.-Z., Yuan Z.-Y. (2014), Mesoporous cerium phosphonate nanostructured hybrid spheres as label-free Hg^{2+} fluorescent probes, ACS Appl. Mater. Interfaces, 6, 16344−16351. (DOI:10.1021/am504554h)

36. Yan Z., Xue H., Berning K., Lam Y.-W., Lee C.-S. (2014), Identification of multifunctional graphene−gold nanocomposite for environment-friendly enriching, separating, and detecting Hg^{2+} simultaneously, ACS Appl. Mater. Interfaces, 6, 22761−22768. (DOI:10.1021/am506875t)

37. Chen L.-Y., Ou C.-M., Chen W.-Y., Huang C.-C., Chang H.- T. (2013), Synthesis of photoluminescent Au ND−PNIPAM hybrid microgel for the detection of Hg^{2+}, ACS Appl. Mater. Interfaces, 5, 4383− 4388. (DOI:10.1021/am400628p)

38. Vaishnav J. K., Mukherjee T. K. (2019), Highly photostable and two-photon active quantum dot−polymer multicolor hybrid coacervate droplets, Langmuir, 35, 11764−11773. (DOI:10.1021/acs.langmuir.9b01783)

39. Vaishnav J. K., Mukherjee T. K. (2018), Long-range resonance coupling-induced surface energy transfer from CdTe quantum dot to plasmonic nanoparticle, J. Phys. Chem. C, 122, 28324−28336. (DOI:10.1021/acs.jpcc.8b08757)

40. Wang H., Wang X., Liang M., Chen G., Kong R. M., Xia L., Qu F. (2020), A boric acid-functionalized lanthanide metal-organic framework as a fluorescence "turn-on" probe for selective monitoring of Hg^{2+} and CH_3Hg^+, Anal. Chem., 92, 3366–3372.

(DOI:10.1021/acs.analchem.9b05410)

41. Fu Y., Yu W. G., Zhang W. J., Huang Q., Yan J., Pan C. Y., Yu G. P. (2018), Sulfur-rich covalent triazine polymer nanospheres for environmental mercury removal and detection, Polym. Chem., 9, 4125–4131. (DOI:10.1039/C8PY00419F)

42. Wei-Rong Cui, Wei Jiang, Cheng-Rong Zhang, Ru-Ping Liang, Juewen Liu, Jian-Ding Qiu (2020), Regenerable carbohydrazide-linked fluorescent covalent organic frameworks for ultrasensitive detection and removal of mercury, ACS Sustainable Chem. Eng., 8, 445-451. (DOI:10.1021/acssuschemeng.9b05725)

43. Shiravand G., Badiei A., Mohammadi Ziarani G. (2017), Carboxyl-rich g-C_3N_4 nanoparticles: synthesis, characterization and their application for selective fluorescence sensing of Hg^{2+} and Fe^{3+} in aqueous media, Sensors Actuators B Chem., 242, 244–252. (DOI:10.1016/j.snb.2016.11.038)

44. Long Y. F., Jiang D. L., Zhu X., Wang J. X., Zhou F. M. (2009), Trace Hg^{2+} analysis via quenching of the fluorescence of a CdS-encapsulated DNA nanocomposite, Anal. Chem., 81, 2652–2657. (DOI:10.1021/ac802592r)

45. Choudhury N., Saha B., Ruidas B., De P. (2019), Dual-action Polymeric Probe: Turn-On Sensing and Removal of Hg^{2+} Chemosensor for HSO_4^-. ACS Appl. Polym. Mater., 1, 461–471. (DOI:10.1021/acsapm.8b00162)

46. Lei Wang., Yu Wang., Wenxuan Li., Wenjing Zhi., Yuanyuan Liu., Liang Ni., Yun Wang. (2019), Recyclable DNA-derived polymeric sensor: ultrasensitive detection of Hg(II) ions modulated by morphological changes, ACS Applied Materials & Interfaces, 11, 40575–40584. (DOI:10.1021/acsami.9b13035)

47. Mondal N., Samanta A. (2016), Ultrafast charge transfer and trapping dynamics in a colloidal mixture of similarly charged CdTe quantum dots and silver nanoparticles, J. Phys. Chem. C, 120, 650−658. (DOI:10.1021/acs.jpcc.5b08630)

48. Haram S. K., Kshirsagar A., Gujarathi Y. D., Ingole P. P., Nene O. A., Markad G. B., Nanavati S. P. (2011), Quantum confinement in

CdTe quantum dots: investigation through cyclic voltammetry supported by density functional theory (DFT), J. Phys. Chem. C, 115, 6243−6249. (DOI:10.1021/jp111463f)

49. Singh P. P., Mittal S., Sharma U. (2009), Interaction energy, charge transfer and energy lowering in metal-ligand interaction, Inorg. Chem. Ind. J., 4, 45−58.

Chapter 5

NP-Embedded Hybrid Coacervates as Efficient Nanoreactors for Visible Light Photocatalysis and Dye Degradation

5.1. Introduction

Harvesting of visible light for the generation of charge carriers and their fruitful utilization for chemical transformations have attracted significant research interest in recent past. *[1]* In this context, photocatalytic nanoreactors hold great promise for the efficient utilization of visible light toward chemical and enzymatic transformations. Confinement of catalysts and substrates inside a small volume of nanoreactor alters their chemical reactivity, which results in enhanced reaction kinetics and better conversion yields. *[2]* Steering incompatible reactions to completion inside the nanoreactor finds particular importance in practical applications. Hence, the fabrication of robust artificial photocatalytic nanoreactors for efficient catalytic transformations has attracted a lot of attention in recent times with the goal to imitate the highly efficient natural photosynthetic reaction pathway.

Over the last few decades, photocatalytic nanoreactors have gained significant interest because of their unique microenvironment, robust structure, and the possibility to accommodate multiple catalytic sites in a confined volume. The porous structure of mesoporous silica NPs and zeolite-based nanoreactors have been utilized as porous hosts for various photocatalytic transformations. *[3–6]* In recent times, various structurally flexible photocatalytic nanoreactors have been designed to carry out a wide range of visible-light-driven chemical transformations such as CO_2 reduction, *[7,8]* pollutant degradation, *[9,10]* hydrogen (H_2) production, *[11,12]* oxidation and reduction reactions *[13–16]* etc. These include metal nanocages, *[7, 17]* carbon nanotubes, *[18, 19]* carbon hollow structures, *[20, 21]* yolk-shell NPs, *[22, 23]* metal-organic frameworks (MOFs), *[24, 25]* covalent organic frameworks (COFs) *[26, 27]* and synthetic coordination cages. *[2, 28]* The spatial confinement of catalysts and substrates inside the microenvironment of these nanoreactors can significantly enhance their interactions resulting in improved catalytic efficiency via modulation of intermolecular interactions. Although these earlier

systems provide the fundamental platform to efficiently utilize the visible light source for driving various chemical reactions, they often lack in-built catalytic centers for harvesting the visible light. Externally incorporated NPs often undergo unwanted agglomeration inside these nanoreactors, which limits their efficacy and recyclability. The inclusion of multiple individual catalytic sites inside the same confined space of nanoreactors without any undesirable aggregation and accessibility barrier for reactants remains to be a key challenge. Moreover, the fabrication methods for most of the earlier reported multicomponent photocatalytic nanoreactors are tedious and involve harsh experimental requirements. Recently, we have developed a simple and facile approach for the fabrication of a new and unique class of membrane-free hybrid coacervate droplets using oppositely charged polyelectrolyte and inorganic NPs with multiple in-built catalytic sites.

In the last few years, coacervate droplets have gained a lot of attention due to their confined membrane-less structure. *[29–33]* They are particularly useful as model artificial synthetic cells in protocell research studies. *[31, 34–36]* Various molecules capable of having multivalent electrostatic interactions have been shown to undergo coacervation in aqueous solution. *[37, 38]* In the past decade, massive amount of studies have been conducted to explore the physicochemical properties of various functional coacervates toward enzyme catalysis and drug delivery. *[31, 33]* As a consequence of their biocompatibility, membrane-less architecture, and stimuli-responsive reversible structural rearrangement, coacervate droplets have emerged as an efficient host for biocatalysis and drug delivery vehicles. While significant advancement has been made to understand the mechanism and kinetics of various biocatalytic transformations and intracellular trafficking of functional coacervates, very less is known about their role in photocatalytic reactions. Recently, our group developed a new class of organic-inorganic hybrid coacervates using oppositely charged ligand-capped nanoparticles (NPs) and polyelectrolytes. *[39, 40]* These

155

optically active and structurally robust droplets have been utilized towards environmental remediation, *[41]* theranostic applications, *[40, 42]* and catalytic nanoreactor. *[43]* In our present work, we have fabricated two different types of NP-embedded coacervates namely, QD- and CD-embedded hybrid coacervates (QD- and CD-Ds) and compared their catalytic efficacy by as efficient photocatalytic nanoreactors by carrying out the one-electron photoredox conversion of ferricyanide (Fe^{3+}) to ferrocyanide (Fe^{2+}). Subsequently, the QD-Ds have been utilized for the photocatalytic dye degradation of rhodamine B (RhB) and methylene blue (MB). Both these two types of photocatalytic transformations (Fe^{3+} to Fe^{2+} conversion and environmentally toxic dye degradation) have been utilized extensively to evaluate the catalytic efficacy of various nanocatalysts. *[2, 44–50]* However, bare NPs often exhibit ligand poisoning and unwanted agglomeration during the course of the reaction, which limits their catalytic efficacy and recyclability, respectively. *[47, 48]* Our present nanoreactor comprises of multiple luminescent NPs electrostatically bound with the positively charged polymer PDADMAC (Scheme 5.1).
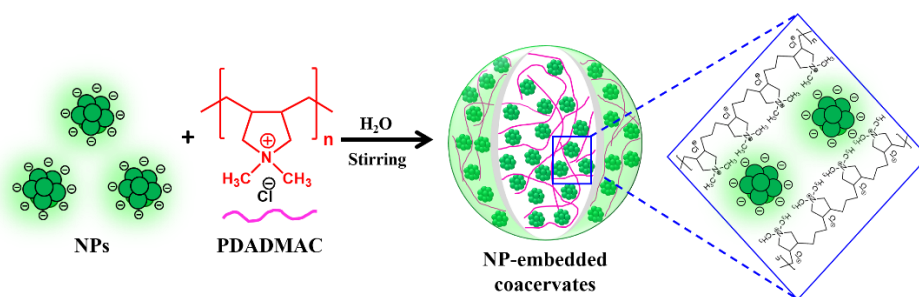
Scheme 5.1. Schematic illustration of NP-embedded coacervates formation via electrostatic interactions between negatively charged NPs and positively charged PDADMAC.

5.2. Results and discussion

5.2.1. Characterization of QD and QD-embedded coacervates

The formation of MSA-functionalized CdTe QDs was confirmed using various microscopic and spectroscopic techniques. *[39]* The as-synthesized CdTe QDs shows an absorption peak at 486 nm with a

corresponding PL maximum at 528 nm (λ_{ex} = 450 nm) (Figure 5.1A). The size distribution and mean size of the QDs were estimated from TEM measurement. The TEM image confirms the presence of well-dispersed spherical QDs with a mean size of ~2.4 ± 0.3 nm (Figure 5.1B,C). The PL quantum yield is estimated to be 0.27, which matches well with the earlier reports. [41]
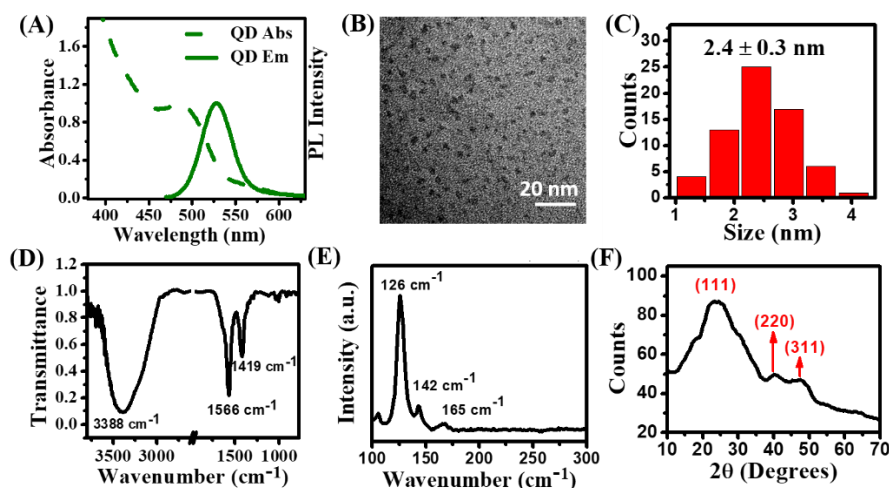
Figure 5.1. (A) Normalized absorption and emission spectra (λ_{ex} = 450 nm) of QDs. (B) TEM image, (C) size distribution histogram, (D) FTIR, (E) Raman spectrum, and (F) PXRD pattern of MSA-capped CdTe QDs.

The covalent attachment of the thiol group of MSA ligands on the surface of QDs was confirmed by FTIR spectroscopy. [39] The different peaks observed at 3388 cm^{-1}, 1566 cm^{-1}, and 1419 cm^{-1} in the FTIR spectrum (Figure 5.1D) can be attributed to the O-H stretching, and asymmetric and symmetric stretching of carboxylate groups of MSA-capped QDs. The Raman spectrum of CdTe QDs reveals two sharp bands at 126 and 142 cm^{-1} which corresponds to tellurium (Te), whereas the broad band observed at 165 cm^{-1} corresponds to the localized longitudinal optical (LO) phonons of CdTe QDs (Figure 5.1E). [54] The ξ potential for QDs at pH 7.4 is estimated to be -25.1 ± 1.2 mV, which indicates the presence of negatively charged surface carboxylate groups. The PXRD pattern of QDs shows three peaks at 2θ values of 24.3, 40.3, and 47.5°, corresponding to the crystalline planes

(111), (220), and (311), respectively (Figure 5.1F). *[39, 49]* Altogether, these findings authenticate the successful synthesis of colloidally stable MSA-functionalized CdTe QDs.

The QD-embedded coacervates (QD-Ds) were fabricated by simple mixing of the negatively charged CdTe QDs (170 nM) and the positively charged polymer PDADMAC (65 μM) in the aqueous medium (pH 7.4) at room temperature (Figure 5.2A). The resulting binary mixture was then equilibrated for 4 h with constant stirring to get homogeneous spherical QD-Ds. The FESEM image showed well-dispersed spherical droplets present inside the binary mixture after 4h of equilibration as shown previously in Chapter 4.
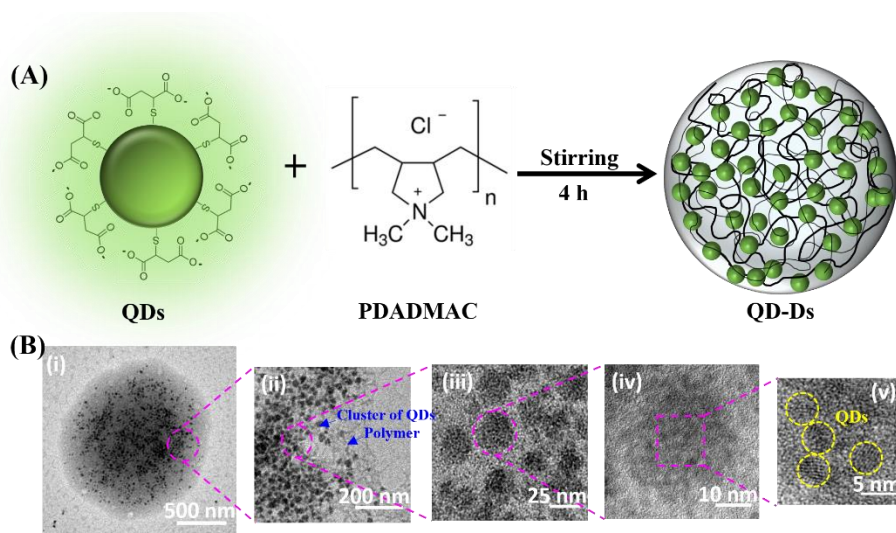
Figure 5.2. (A) Schematic illustration of the formation of QD-Ds. (B) FESEM image, (C) size distribution histogram, (D) confocal microscopy images (DIC and fluorescence), and (E) TEM images of QD-Ds at different magnifications. (F) HR-TEM image of QD-embedded inside the QD-Ds.

Notably, the lack of any QD-D formation in the absence of either PDADMAC or QDs indicates that both QD and PDADMAC are essential for their formation. Moreover, the presence of optically active QDs embedded inside these QD-Ds makes them inherently luminescent. The CLSM images of these QD-Ds further shed some light on the structure and luminescence behavior of these droplets. As

previously observed in Chapter 3, the CLSM images showed well-dispersed spherical morphology with green fluorescence emanating exclusively from the interior of these QD-Ds. To know the spatial distribution of individual QDs inside these droplets, we performed HR-TEM measurements. Figure 5.2E shows the HR-TEM images of a spherical QD-D at different magnifications. It is clearly evident that the spherical QD-D contains several dark spots inside its structure (Figure 5.2Ei). Upon magnification, the image reveals the presence of clusters of QDs entangled in the polymeric networks (Figure 5.2Eii). Upon further magnification, the TEM images reveal the presence of individual QDs inside these entangled clusters (Figure 5.2Eiii-v). The size of these embedded QDs varies in the range of 2-4 nm (Figure 5.2Ev), which matches well with those estimated for individual QDs. Moreover, the magnified image reveals distinct lattice fringes with a d-spacing of 0.324 nm (Figure 5.2F), corresponding to the (200) plane of cubic CdTe (JCPDS Card No. 65-0880). *[55]* Taken together, our findings reveal the presence of multiple entangled QDs in the polymeric networks of PDADMAC inside these QD-Ds.

5.2.2. Characterization of CDs and CD-embedded coacervates

The hydrothermally synthesized CDs were characterized using various spectroscopic and microscopic techniques, as discussed in Chapter 2. *[40]* A distinct absorption peak at 340 nm along with a weak shoulder near 250 nm arise due to the n-π^* transitions from the carbonyl groups (C=O) on the surface of CDs and π-π^* transitions of aromatic sp^2 carbons within the core of CDs, respectively (Figure 5.3A). The PL band of CDs appears at 442 nm upon excitation at 340 nm (Figure 5.3A). The aqueous dispersion of CDs displays intense blue emission upon UV light illumination ($\lambda_{ex} = 365$ nm) (inset, Figure 5.3A).
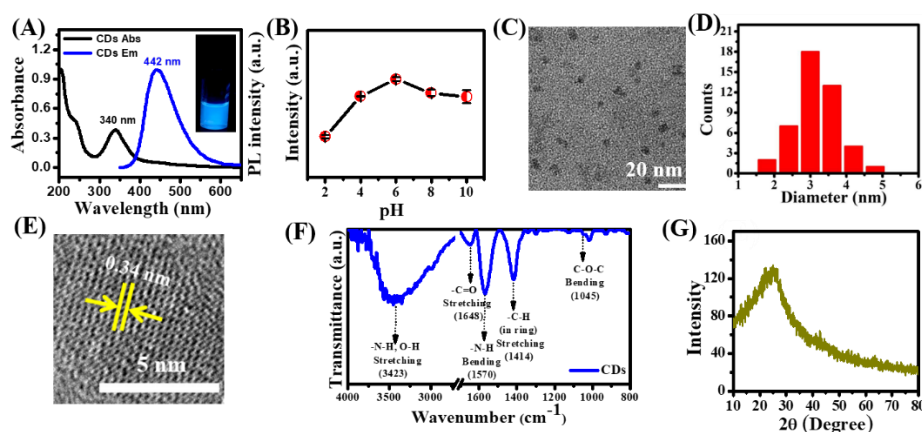
Figure 5.3. (A) Normalized absorption and emission spectra (λ_{ex} = 340 nm) of CDs. (B) Changes in the PL intensity of CDs (λ_{ex} = 340 nm) as a function of pH of the aqueous medium. (C) TEM, (D) size distribution histogram, (E) HRTEM image, (F) FTIR, and (G) PXRD spectra of CDs.

Notably, the PL intensity of CDs changes with the solution pH, indicating the active role of surface functional groups on the PL mechanism (Figure 5.3B). The TEM image reveals the presence of well-dispersed spherical CDs in the size range of 2.1–4.6 nm (Figure 5.3C,D). The HR-TEM image reveals well-resolved lattice fringes with a characteristic d-spacing of 0.34 nm, which matches with the (002) diffraction facets of graphite (Figure 5.3E). The FTIR spectrum of CDs reveals the presence of various functional groups such as hydroxyl (–OH), amine (–NH$_2$), epoxy (–C–O–C–), and carboxylic acid (–COOH) (Figure 5.3F). The estimated zeta potentials (ζ potentials) of CDs at pH 10 and 4.5 are –31.3 $\pm$ 1.8 and +15.4 $\pm$ 0.7 mV, which indicate the deprotonation and protonation of –COOH and –NH$_2$ functional groups at the surface of CDs, respectively. A broad powder XRD peak at $2\theta = 25°$ (d = 0.34 nm) suggests the amorphous nature of these CDs (Figure 5.3G). Taken together, these findings reveal the formation of well-dispersed colloidally stable spherical luminescent CDs.

CD-Ds were formed by mixing aqueous dispersions (pH 10) of CDs (0.06 mg/mL) and PDADMAC (32 μM) at room temperature with

constant stirring (Figure 5.4A). The binary mixtures of CDs and PDADMAC were equilibrated for 12 h before any spectroscopic and microscopic measurements. The TEM image reveals the formation of well-dispersed spherical droplets (Figure 5.4B). The FESEM measurements further substantiates the formation of uniform spherical CD-Ds with a mean size of 411 nm (Figure 5.4C,D). The ζ potential decreases from a value of -31.3 ± 1.8 mV for free CDs to -17.0 ± 0.5 mV upon CD-D formation in the presence of positively charged PDADMAC.[40] This observation can be explained by considering partial surface passivation of negatively charged functional groups of CDs by positively charged PDADMAC via electrostatic association.
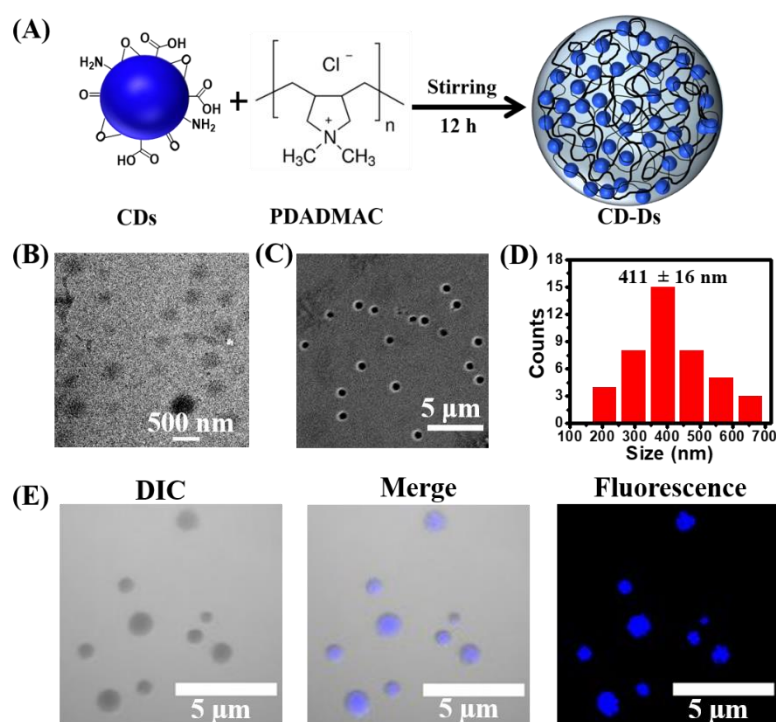
Figure 5.4. (A) Schematic illustration of the fabrication of CD-Ds from CDs and PDADMAC. (B) TEM image, (C) FESEM image, (D) size distribution histogram, and (E) CLSM (DIC, fluorescence, merge) images of CD-Ds.

The CLSM (DIC) image of CD-Ds shows well-dispersed individual spherical droplets (Figure 5.4E). These droplets are intrinsically luminescent in nature and the merged image reveals the

distinct blue emission originating exclusively from the interior of these droplets (Figure 5.4E). This finding indicates that the blue emissive CDs are embedded inside the membrane-less architecture of these droplets, which also matches our earlier observations of the HR-TEM images of QD-Ds. Taken together, these findings unambiguously establish the fabrication of CD-Ds with a uniform distribution of luminescent CDs inside these droplets.

After confirming the successful formation of QD- and CD-Ds, we next aimed to explore the catalytic efficacy of these droplets toward model catalytic conversions by utilizing their unique physicochemical and optoelectronic properties. For the present study, we have utilized the confined structure of optically active QD- and CD-Ds toward visible-light-driven photocatalytic conversion of ferricyanide (Fe^{3+}) to ferrocyanide (Fe^{2+}).

5.2.3. Photoredox conversion of Fe^{3+} to Fe^{2+}

Optically active NPs such as QDs and CDs display unique physicochemical and optoelectronic properties in the UV-vis region and have been often used as efficient photocatalysts toward various catalytic transformations. [*47, 56–60*] To explore the confinement-induced photocatalytic efficacy of our present QD- and CD-D system, we have selected a model visible-light-induced photoredox conversion of Fe^{3+} to Fe^{2+} in the presence and absence of EtOH as a hole scavenger. It is a well-explored single electron photoconversion reaction in the presence of various NPs. *[47, 52, 61, 62]* The key advantage of this photoredox conversion is that the complete reduction process can be easily monitored using UV−vis absorption measurements. Here, our primary objective is to explore the effect of nanoconfinement on the photocatalytic behavior of polymer-bound NPs embedded within the droplets and compare their catalytic efficacy. Toward this goal, we have exploited the membrane-less structure of these droplets for the preferential sequestration of Fe^{3+} to fabricate the Fe^{3+}-loaded droplets (Figure 5.5A).
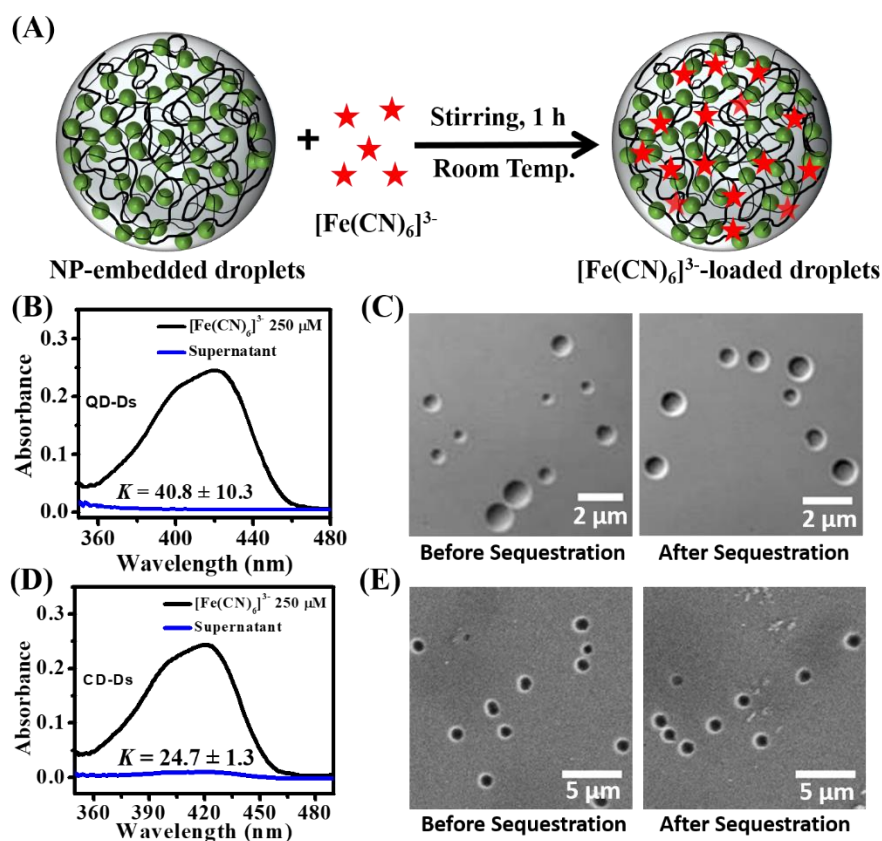
Figure 5.5. (A) Schematic representation of equilibrium partitioning of $[Fe(CN)_6]^{3-}$ inside the NP-embedded droplets. Estimation of equilibrium partition coefficient of $[Fe(CN)_6]^{3-}$ inside (B,D) QD-Ds and CD-Ds, respectively using UV-vis spectroscopy. (C) Confocal (DIC) images of QD-Ds and (E) FESEM images of CD-Ds in the absence and presence of 230 µM $[Fe(CN)_6]^{3-}$.

Earlier, it has been observed that the membrane-free structure of these droplets enables them to sequester a wide range of inorganic and organic molecules within their structure via electrostatic and hydrophobic interactions. *[39–41]* We estimated the equilibrium partition coefficient (K) of Fe^{3+} inside the QD- and CDs using UV-vis spectroscopy. It has been observed that Fe^{3+} shows preferential affinity towards QD- and CD-Ds with a K of 40.8 ± 10.3 and 24.7 ± 1.3, respectively (Figure 5.5B,D). To know the changes in the morphology and structure of Fe^{3+}-loaded droplets, we performed CLSM and FESEM imaging. It is apparent from Figure 5.5C,E that the spherical

architecture and size of both QD- and CD-Ds remain unchanged upon sequestration of Fe^{3+}.

Next, these Fe^{3+}-loaded droplets were utilized for photoredox catalysis using either two 6W blue or green light-emitting diodes (LEDs) as the irradiation source with a λ_{max} of $\sim$ 420 nm and $\sim$520 nm, respectively. The incident light intensity at the surface of the quartz cuvette was estimated to be $\sim$37 mW/cm^2. The reaction kinetics of the photoredox conversion of Fe^{3+} to Fe^{2+} was followed using a UV-vis spectrophotometer by monitoring the changes in the absorbance of Fe^{3+} at 420 nm.
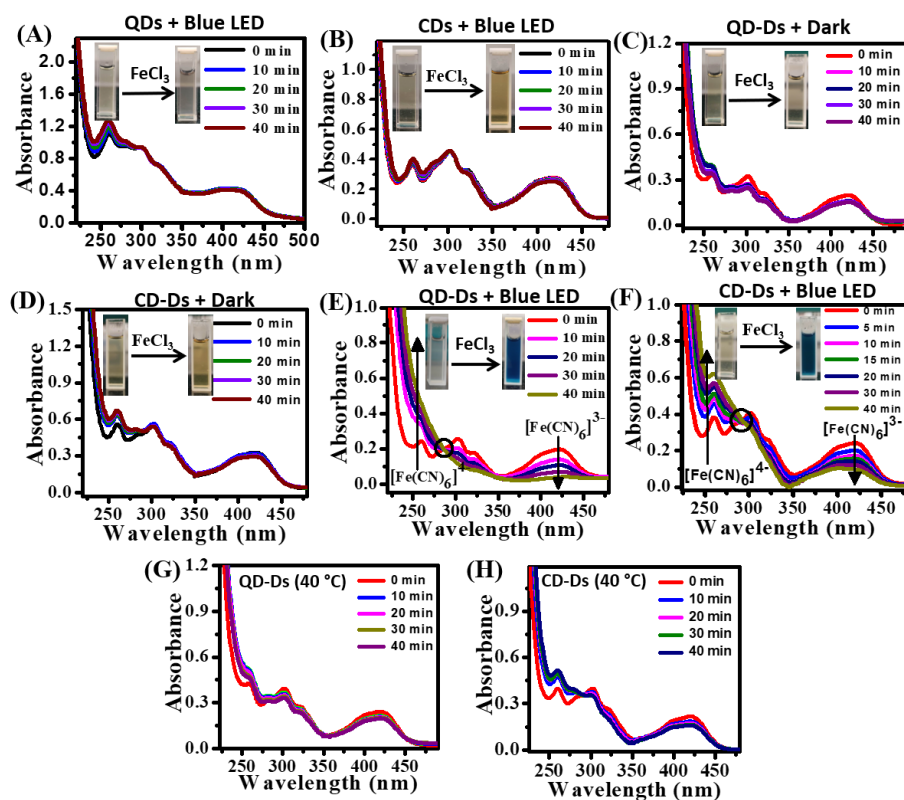
Figure 5.6. Photoconversion of Fe^{3+} to Fe^{2+} under the constant illumination of blue light with (A) bare QDs and (B) bare CDs. Photoconversion of Fe^{3+} to Fe^{2+} with (C) QD-Ds and (D) CD-Ds under dark conditions. Photoconversion of Fe^{3+} to Fe^{2+} with (E) QD-Ds and (F) CD-Ds under blue light irradiation. Photoconversion of Fe^{3+} to Fe^{2+} with (G) QD-Ds and (H) CD-Ds at 313 K. Inset images in (A)–(F) show the Prussian blue test to confirm the formation of Fe^{2+}.

Initially, we checked the photocatalytic activity of the bare QDs and CDs in the aqueous solution under the irradiation of blue LEDs. The absorbance of Fe^{3+} at 420 nm remains virtually unchanged under 40 min of constant illumination in the presence of bare QDs and CDs, indicating the absence of any photocatalytic conversion of Fe^{3+} to Fe^{2+} (Figure 5.6A,B). Furthermore, the Prussian blue test with freshly prepared $FeCl_3$ solution shows no Prussian blue color, which validates the absence of any photocatalytic activity of bare QDs and CDs (Figure 5.6A,B inset). Notably, QD- and CD-Ds were unable to instigate any noticeable spectral changes of Fe^{3+} under dark conditions at 298 K (Figure 5.6C,D). The absence of any isosbestic point along with the negative Prussian blue test indicates a lack of any Fe^{3+} to Fe^{2+} conversion in the absence of light (Figure 5.6C,D inset). In contrast, a continuous decline in the absorbance of Fe^{3+} at 420 nm has been observed with QD- and CD-Ds under the irradiation of blue LEDs with a concurrent increase in the absorbance at 250 nm due to the formation of Fe^{2+}. Moreover, a distinctive isosbestic point at 287 nm appears during the course of the reaction, which signifies the stoichiometric conversion of Fe^{3+} to Fe^{2+} inside these droplets (Figure 5.6E,F).

Interestingly, the reaction mixture turns from colorless to Prussian blue color upon the addition of freshly prepared $FeCl_3$ solution, confirming the photocatalytic conversion of Fe^{3+} to Fe^{2+} inside both the QD- and CD-Ds (Figure 5.6E,F inset). The conversion yield is found to be ~ 85% and ~ 60% for QD- and CD-Ds, respectively under blue light irradiation for 40 min, which is comparable with the other reported nanocatalysts. [43,47,48] To rule out the effect of any photothermal contribution in the photoredox conversion of Fe^{3+} to Fe^{2+}, we kept the Fe^{3+}-loaded QD- and CD-Ds under dark at 313 K and monitored the reaction kinetics for a period of 40 min. The lack of any appreciable changes in the absorption spectrum of Fe^{3+} indicates the absence of any conversion in the absence of light at 313 K (Figure 5.6G,H).

Three fundamental questions arise from these observations. First, how does the present QD- and CD-Ds act as catalysts for this photoredox reaction? As bare QDs and CDs in bulk solution failed to catalyze the conversion, the involvement of PDADMAC in the reaction mechanism could be an important factor. Second, how does the entangled QDs and CDs in the PDADMAC matrix with less exposed surface area become more efficient catalysts compared to the bare QDs and CDs? In general, the catalytic efficacy of NPs is directly proportional to the available surface area and one would expect less efficient conversion inside the droplets. Third, how does the transition state for the photoredox conversion is stabilized inside the droplets compared to the more polar bulk aqueous medium? Considering the preferential solvation of the transition state, one would expect poor catalytic conversion inside the droplets compared to the bulk water medium.
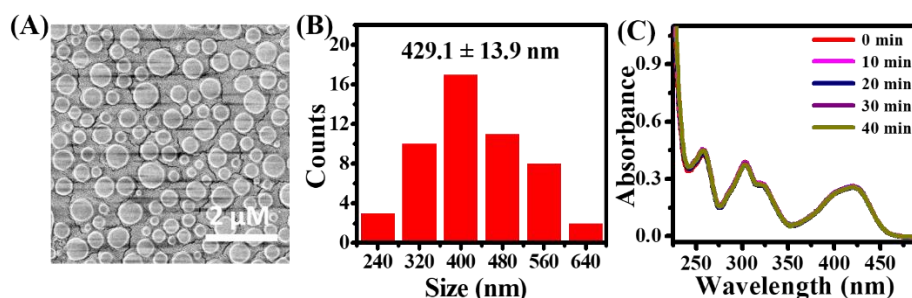
Figure 5.7. (A) FESEM image and (B) size distribution histogram of ATP-Ds. (C) UV-vis spectra of ferricyanide reduction under blue light illumination inside the ATP-Ds in the presence of 0.66 M EtOH.

To address these questions, we performed a few control experiments. To establish the photocatalytic role of embedded NPs inside the droplets, we fabricated ATP coacervates (ATP-Ds) using PDADMAC and ATP. Here it should be noted that these ATP-Ds lack any in built NPs. The fabricated ATP-Ds are spherical with a mean size of 429.1 ± 13.9 nm (Figure 5.7A,B). Notably, no spectral changes were observed in the absorption spectra of Fe^{3+}-loaded ATP-Ds upon blue light irradiation for 40 min (Figure 5.7C), suggesting the absence of any photocatalytic activity of ATP-Ds. This observation authenticates

that the NPs embedded in the hybrid coacervates act as photocatalytic centers for the observed photoredox conversion of Fe^{3+} to Fe^{2+}. Next, we measured and compared the ζ potentials of QDs and QD-Ds. It should be noted that the ζ potential of QDs decreases from a value of -25.1 mV to + 8.2 mV upon QD-D formation.[38] This can be attributed to the partial surface charge passivation of MSA-capped QDs with the positively charged PDADMAC via multivalent electrostatic complexation. This partial charge passivation of individual QDs allows their close proximity with the negatively charged Fe^{3+} complex ($[Fe(CN)_6]^{3-}$). Therefore, the absence of any catalytic activity of bare QDs in the aqueous medium can be attributed to the unfavorable electrostatic repulsion between the negatively charged QDs and $[Fe(CN)_6]^{3-}$. Similar changes in the ζ potential of CDs and CD-Ds from -31.3 $\pm$ 1.8 to -17.0 $\pm$ 0.5 mV were observed, which further points toward the partial surface charge passivation of CDs in CD-Ds to be responsible for efficient photoredox conversion of Fe^{3+} to Fe^{2+}. *[40]* Earlier, it has been shown that liquid-like coacervate droplets contain a significant amount of water inside their membrane-less structure and the interior of these droplets is significantly more polar than DMSO.[30] Taken together, our findings are consistent with a model that consider individual polymer entangled and surface charge passivated NPs as catalytic centers within the coacervate droplets.

The kinetic parameters for the photoredox conversion were estimated by plotting -ln(C_t/C_0) versus reaction time (*t*). The plot follows a linear correlation for the photoredox conversion in both QD- and CD-Ds, which signifies that the reaction follows first-order kinetics. The estimated rate constant for the photoredox conversion of Fe^{3+} to Fe^{2+} inside the QD- and CD-Ds is found to be 3.5×10^{-2} min^{-1} and 3.04×10^{-2} min^{-1}, respectively (Figure 5.8A,D). However, the plots for bare QDs, CDs, and the reaction under dark conditions remain parallel to the X-axis.
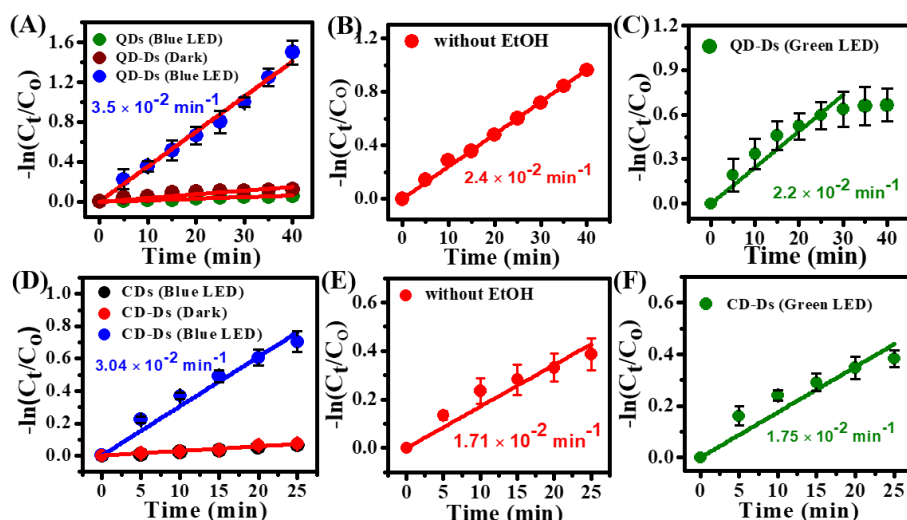
Figure 5.8. The first-order kinetic plots of $-\ln(C_t/C_o)$ versus time in the presence of (A,D) bare QDs, QD-Ds, bare CDs, and CD-Ds under dark and blue LED irradiation in the presence of 0.66 M EtOH. The first-order kinetic plots of $-\ln(C_t/C_o)$ versus time with (B,E) QD- and CD-Ds in the absence of 0.66 M EtOH under blue LED irradiation. The first-order kinetic plots of $-\ln(C_t/C_o)$ versus time with (C,F) QD- and CD-Ds under green light irradiation in the presence of 0.66 M EtOH.

Notably, in the absence of EtOH as a hole scavenger, the rate of the photoconversion decreases slightly to a value of 2.4×10^{-2} min^{-1} and 1.71×10^{-2} min^{-1} for both QD- and CD-Ds, respectively (Figure 5.8B,E), which is similar to that observed earlier for other metal NPs.[43,52] Furthermore, it has been found that the photoreduction of Fe^{3+} inside the QD- and CD-Ds follows a slower kinetics under the green LEDs ($\lambda \sim 520$ nm) with a rate constant of 2.2×10^{-2} min^{-1} and 1.75×10^{-2} min^{-1}, respectively with a corresponding conversion yield of 35 and 44% (Figure 5.8C,F). This observation can be attributed to the drastic reduction of the molar extinction coefficient of QDs and CDs beyond 500 nm, resulting in fewer photoinduced charge carriers.

The morphology and structural stability of the QD- and CD-Ds after the photocatalytic conversion were accessed using FESEM, EDX, and elemental mapping. The FESEM image of QD-Ds after the photoredox conversion shows spherical droplets along with a few fused intermediates (Figure 5.9A). This observation suggests that the

photoreduction of Fe^{3+} to Fe^{2+} does not alter the shape and stability of these QD-Ds. Furthermore, the EDX spectrum confirms the presence of Fe along with all the essential elements of QD-D (Figure 5.9B), which authenticates the presence of Fe^{3+} and Fe^{2+} inside the confined architecture of QD-D.
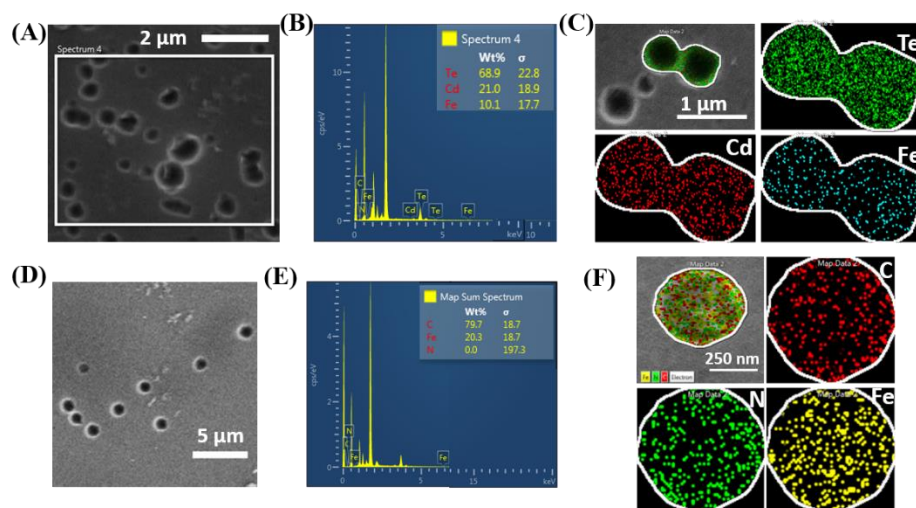
Figure 5.9. (A) FESEM image of Fe^{2+}-loaded QD-Ds after the photocatalytic conversion of Fe^{3+} to Fe^{2+}. (B) EDX spectrum of corresponding QD-Ds. (inset) Weight and atomic % of different elements. Elemental mappings of (C) Te, Cd, and Fe inside QD-Ds and (D) FESEM image of Fe^{2+}-loaded CD-Ds after the photocatalytic conversion of Fe^{3+} to Fe^{2+}. (E) EDX spectrum of corresponding CD-Ds. (inset) Weight and atomic % of different elements. Elemental mappings of (F) C, N, and Fe inside these CD-Ds.

Figure 5.9C displays the corresponding elemental mapping of individual QD-D after the photoredox conversion. The uniform distribution of Fe inside the QD-D further validates the presence of Fe^{3+}/Fe^{2+} inside the individual QD-D. Similar findings were observed in the FESEM, EDX, and elemental mapping of CD-Ds, substantiating the presence of intact spherical CD-Ds after the photoredox conversion with the presence of Fe inside the CD-Ds (Figure5.9D–F). Altogether, these findings suggest that photoreduction of Fe^{3+} to Fe^{2+} occurs exclusively inside the confined structure of NP-embedded droplets.

The recyclability of catalytic nanoreactors for multiple cycles without any compromise on their catalytic efficacy is essential for their practical applications. The recyclability of the QD- and CD-Ds has been explored for multiple consecutive cycles of photoredox conversion of Fe^{3+} to Fe^{2+} under blue light illumination. Here, it is important to note that the product Fe^{2+} remains trapped inside the droplets, as revealed from our elemental mapping measurement, which may adversely affect the recyclability of these droplets. To circumvent this issue, we utilized the pH-triggered assembly/disassembly phenomenon of these droplets. After the first photocatalytic cycle, both the QD- and CD-Ds were disassembled by lowering the pH of the reaction mixture to ~4.5. The obtained mixture was then dialyzed for 2-3 h at constant stirring to separate all the unreacted reactant and product from the solution. After 3 h, a clear solution was obtained from the dialysis bag. Subsequently, the QD- and CD-Ds were reassembled by increasing the pH of this solution to ~7.4 and ~10, respectively. The obtained solution was then equilibrated for 3-4 h for QD-Ds and 12 h for CD-Ds before utilizing it for the second cycle. A similar procedure was followed for all the subsequent cycles.
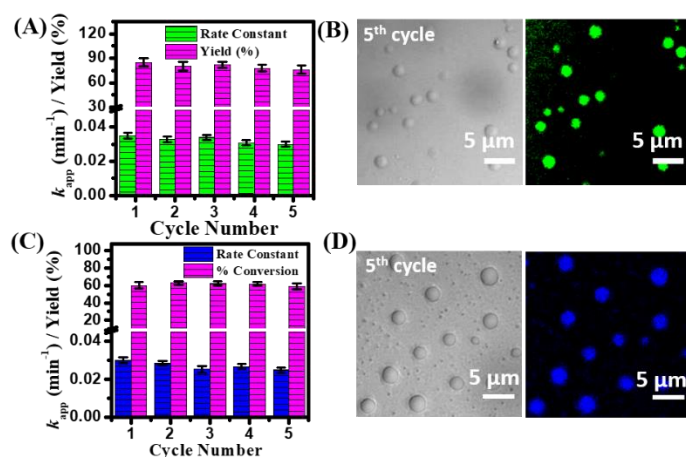
Figure 5.10. Recyclability test of (A) QD-Ds for the photoreduction of Fe^{3+} to Fe^{2+} in the presence of 0.66 M EtOH under the constant illumination of blue LED for five consecutive cycles. Confocal (DIC and fluorescence) images of recycled (B) QD-Ds after 5th photocatalytic cycle. Recyclability test of (C) CD-Ds for the

photoreduction of Fe^{3+} to Fe^{2+} in the presence of 0.66 M EtOH under the constant illumination of blue LED for five consecutive cycles. Confocal (DIC and fluorescence) images of recycled (D) CD-Ds after 5th photocatalytic cycle.

Notably, both the NP-embedded coacervates exhibited good recyclability with negligible changes in k_{app} and conversion yield over multiple successive catalytic cycles. The estimated k_{app} and conversion yield of the fifth cycle for QD-Ds are 3.0 $\times 10^{-2}$ min^{-1} and 76%, respectively (Figure 5.10A), while the k_{app} and conversion yield of the fifth cycle for CD-Ds are 2.4 $\times 10^{-2}$ min^{-1} and 59%, respectively (Figure 5.10C). Furthermore, we utilized CLSM imaging to explore the structural stability of the QD- and CD-Ds after the recyclability assay. The DIC images of regenerated droplets after the 5th cycle reveal the presence of well-dispersed intact spherical droplets without any noticeable morphological changes (Figure 5.10B,D). Moreover, the distinct green and blue signals observed exclusively from the interior of these regenerated QD- and CD-Ds indicate the presence of QDs and CDs inside these intact droplets. These observations reveal that the present droplets can be recycled for multiple consecutive assays without any detrimental effect on their catalytic efficacy. Altogether, our present work demonstrates that the NP-embedded droplets can act as an efficient photocatalytic nanoreactor. Furthermore, the catalytic efficacy of these NP-embedded droplets can be easily tuned by changing the embedded NPs according to the specific requirements.

5.2.4. Mechanistic pathway of the photoredox conversion of Fe^{3+} to Fe^{2+}

To establish the involvement of photo-induced charge carriers for the observed photoredox conversion of Fe^{3+} to Fe^{2+}, we performed PL lifetime measurements at 298 K. The PL decays of embedded QDs were collected at 528 nm upon excitation with a 445 nm laser. All the decays were fitted with a multiexponential decay function. The PL decay of QDs inside the QD-Ds fits satisfactorily (χ^2 = 1.05) with a three exponential function having lifetime components of 0.54 (29%),

3.09 (34%), and 12.90 ns (37%). The mean PL lifetime is calculated to be 5.97 ns (Figure 5.11A).

A noticeable decrease in the mean PL lifetime from 5.97 to 3.42 ns has been observed for QD-Ds in the presence of Fe^{3+} after 40 min of blue light irradiation (Figure 5.11A,C).
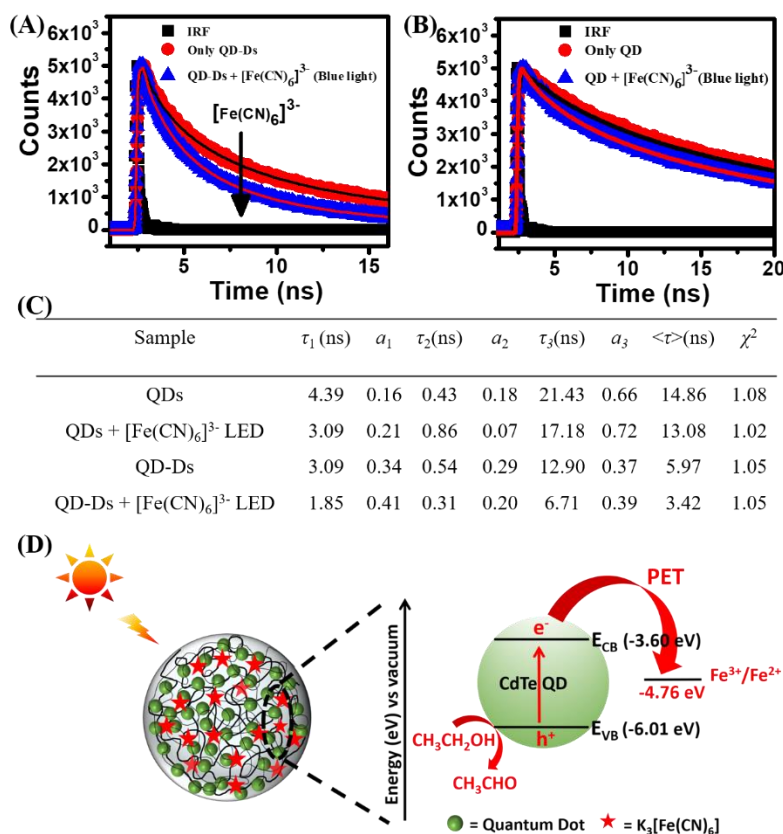
Figure 5.11. (A) Changes in the PL decay traces of only QD-Ds and Fe^{3+} loaded QD-Ds under dark and blue light irradiation for 40 min. (B) Changes in the PL decay traces of bare QDs and QDs with Fe^{3+} under blue light irradiation for 40 min. (C) The PL lifetime decay parameters of QDs and QD-Ds in the presence and absence of $[Fe(CN)_6]^{3-}$ under blue light illumination (D) Schematic representation of the photocatalytic reduction of Fe^{3+} to Fe^{2+} with QD-Ds under blue light irradiation.

Moreover, all the three lifetime components shorten in the presence of Fe^{3+} and blue light exposure having values of 0.31 (20%), 1.85 (41%), and 6.71 ns (39%). These observations signify the involvement of

photogenerated holes and electrons in the reduction process (Figure 5.11A,C). In contrast, the PL lifetime of bare QDs remains unaltered in the presence of Fe^{3+} upon blue light irradiation for 40 min (Figure 5.11B,C), signifying the lack of any charge transfer from bare QDs to Fe^{3+}. Therefore, our present work demonstrates that although the bare QDs are unable to carry out the photoredox conversion in aqueous solution, the membrane-less structure of QD-Ds provides an ideal environment to drive the photoredox conversion via the involvement of photogenerated charge carriers. On the basis of our findings, we proposed a model for the observed photoredox conversion inside the QD-Ds (Figure 5.11D). The photoexcitation of the QDs inside the QD-Ds generates holes and electrons in the valence band and conduction band of QDs, respectively.
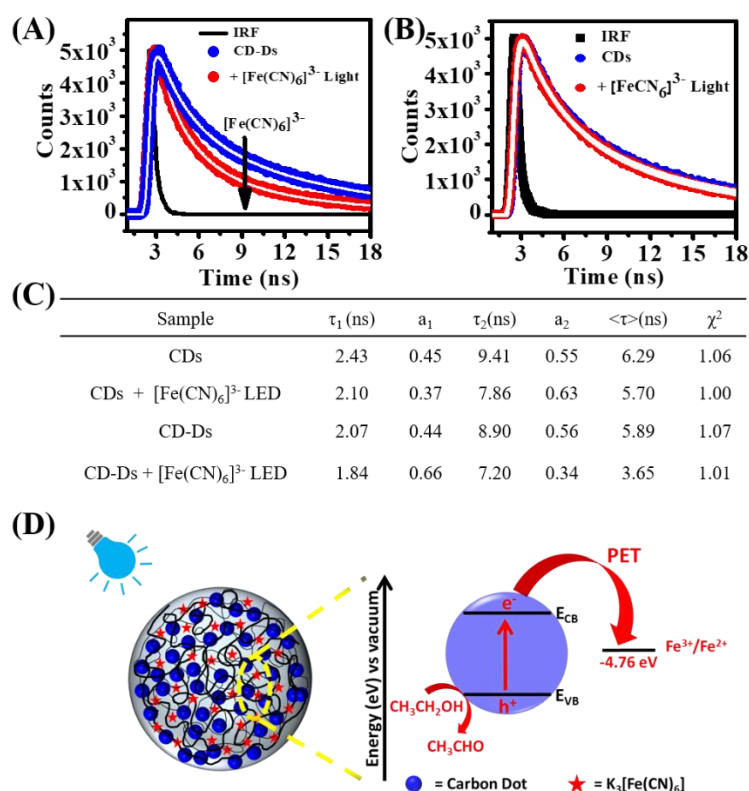
Figure 5.12. (A) Changes in the PL decay traces of only CD-Ds and Fe^{3+} loaded CD-Ds under dark and blue light irradiation for 40 min. (B) Changes in the PL decay traces of bare CDs and CDs with Fe^{3+} upon blue light irradiation for 40 min. (C) The PL lifetime decay parameters of CDs and CD-Ds in the presence and absence of

Sample	τ_1 (ns)	a_1	τ_2 (ns)	a_2	$<\tau>$ (ns)	χ^2
CDs	2.43	0.45	9.41	0.55	6.29	1.06
CDs + $[Fe(CN)_6]^{3-}$ LED	2.10	0.37	7.86	0.63	5.70	1.00
CD-Ds	2.07	0.44	8.90	0.56	5.89	1.07
CD-Ds + $[Fe(CN)_6]^{3-}$ LED	1.84	0.66	7.20	0.34	3.65	1.01

[Fe(CN)$_6$]$^{3-}$ under blue light illumination (D) Schematic representation of the photocatalytic reduction of Fe^{3+} to Fe^{2+} with CD-Ds under blue light irradiation.

The favorable band position of the conduction band of CdTe QDs (-3.60 eV)[41] and the standard reduction potential of [Fe(CN)$_6$]$^{3-}$/[Fe(CN)$_6$]$^{4-}$ couple (-4.76 eV vs vacuum) *[52, 63]* results in the prompt transfer of the photoexcited electrons from the conduction band of CdTe QDs to Fe^{3+}. Consequently, ethanol as a hole scavenger removes the holes from the valence band of QDs to complete the redox cycle (Figure 5.11D).

A similar mechanistic pathway has been observed for the photoredox conversion of Fe^{3+} to Fe^{2+} with CD-Ds. A noticeable decrease has been observed in the PL lifetime of CDs from 5.89 to 3.65 ns inside the CD-Ds during the course of the reaction, signifying the involvement of photogenerated electrons and holes in the reaction mechanism (Figure 5.12A,C). Notably, the PL lifetimes of bare CDs (under dark and light irradiation) as well as those inside the CD-Ds under dark conditions remain almost unchanged, suggesting that the observed ferricyanide to ferrocyanide conversion is exclusively photocatalyzed by embedded CDs inside the CD-Ds (Figures 5.12B,C). Therefore, our present study illustrates that although bare CDs failed to drive the catalytic reduction in aqueous bulk medium, the membrane-less architecture of CD-Ds provides a unique environment to host and drive the photoredox conversion of Fe^{3+} to Fe^{2+} via photogenerated electrons and holes in the CD matrix (Figure 5.12D).

5.2.5. Estimation of thermodynamic parameters

To estimate different thermodynamic parameters associated with the photoredox conversion inside the QD- and CD-Ds, we carried out temperature-dependent (292 to 313 K) kinetic measurements. The morphology and size of both QD- and CD-Ds do not change in this temperature range.[40,41,42] Notably, the rate of reaction increases substantially upon an increase in temperature of the reaction from 292

to 313 K for both the NP-embedded droplets. Similar enhancement of the photochemical rate as a function of temperature has been observed previously in the presence of various metal NPs. *[48, 53, 64]*

The temperature-dependent kinetic results for QD-Ds have been plotted as $-\ln(C_t/C_0)$ versus reaction time (t) in Figure 5.13A. The apparent rate constant (k_{app}) increases from 2.7×10^{-2} to 5.2×10^{-2} min^{-1} upon increasing the temperature from 292 to 313 K (Figure 5.13A).

T (K)	k_{app} x 10^{-2} (min^{-1})	E_a (kJ/mol)	A x 10^2	ΔH (kJ/mol)	ΔS (J/mol K)	ΔG (kJ/mol)
293	2.7					81.41
298	3.5					82.61
		23.01	3.61	21.51	-200	
303	4.0					83.61
313	5.2					85.70

Figure 5.13. (A) The first order kinetic plot of $-\ln(C_t/C_o)$ versus time by observing the absorbance of Fe^{3+} at four different temperatures under the illumination of blue light. (B) Arrhenius plot, and (C) Eyring plot for the photoconversion of Fe^{3+} to Fe^{2+} in the presence of QD-Ds under the illumination of blue light. (D) Thermodynamic parameters for photocatalytic reduction of Fe^{3+} to Fe^{2+} in the presence of QD-Ds at different temperatures.

The pre-exponential factor (A) and the apparent activation energy ($E_{a,kapp}$) were calculated from the linearized Arrhenius plot between ln (k_{aap}) and $1/T$ and were found to be 3.61×10^2 and 23.01 kJ mol^{-1}, respectively (Figure 5.13B,D). The changes in the apparent entropy (ΔS) and enthalpy (ΔH) for the photoconversion of Fe^{3+} were calculated from the linearized Eyring plot between ln (k_{app}/T) and $1/T$ and found to be -200 J mol^{-1} K^{-1} and 21.51 kJ mol^{-1}, respectively

175

(Figure 5.13C,D). The negative ΔS value of the present system can be explained by considering the transfer of photoinduced electrons from the transition state to the localized orbital of the Fe^{3+} complex. The calculated free energy change varies from 81.48 to 84.28 kJ mol^{-1} upon increasing the temperature from 292 to 313 K, respectively.

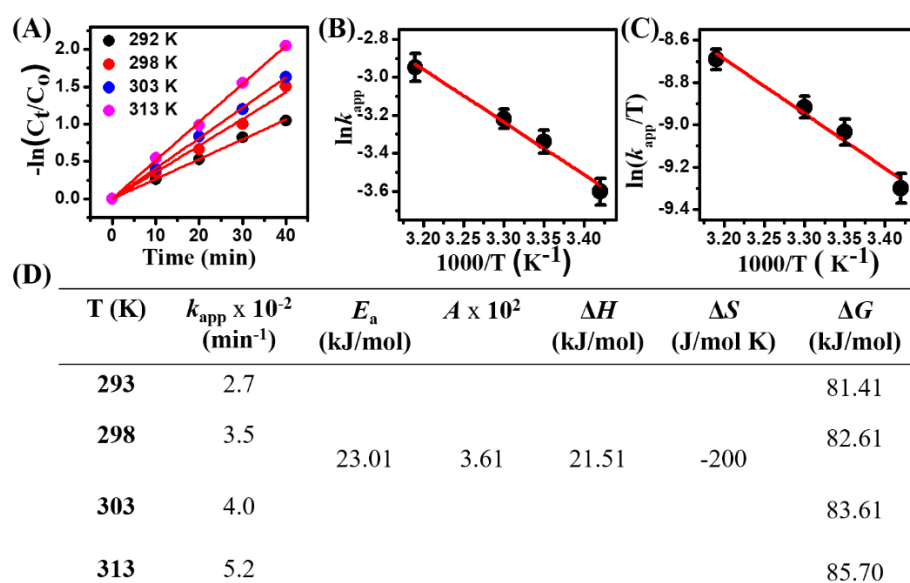| T (K)	k_{app} x 10^{-2} (min^{-1})	E_a (kJ/mol)	A x 10^2	ΔH (kJ/mol)	ΔS (J/mol K)	ΔG (kJ/mol)
293	2.3					80.62
298	3.0					81.60
		25.69	8.71	23.20	-190	
308	3.8					83.56
313	4.7					84.54
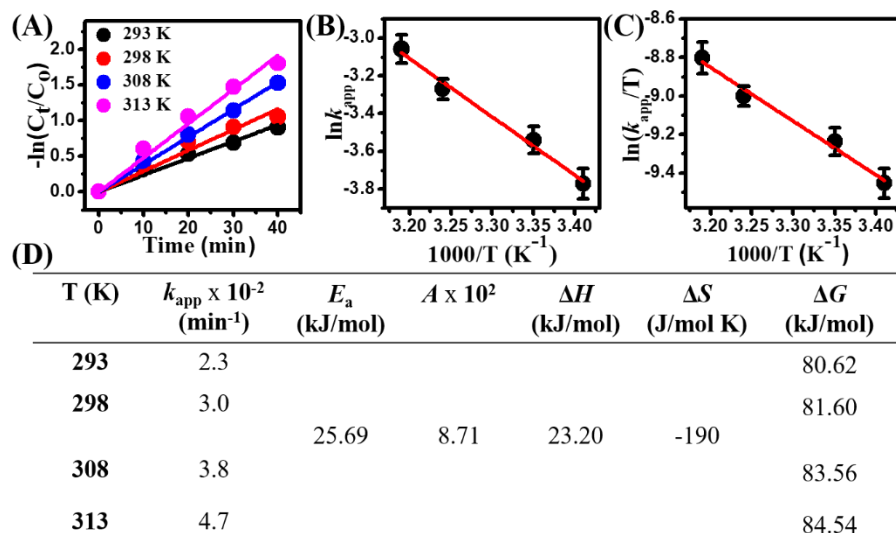
Figure 5.14. (A) The first order kinetic plot of -ln(C_t/C_o) versus time by observing the absorbance of Fe^{3+} at four different temperatures under the illumination of blue light. (B) Arrhenius plot, and (C) Eyring plot for the photoconversion of Fe^{3+} to Fe^{2+} in the presence of CD-Ds under the illumination of blue light. (D) Thermodynamic parameters for photocatalytic reduction of Fe^{3+} to Fe^{2+} in the presence of CD-Ds at different temperatures.

Similar thermodynamic parameters were obtained for the photoredox conversion with CD-Ds. Notably, the estimated k_{app} increases from a value of 2.3×10^{-2} to 4.7×10^{-2} min^{-1} upon increasing the reaction temperature from 293 to 313 K (Figure 5.14A). The linearized Arrhenius plot between ln (k_{aap}) and $1/T$ reveals an apparent activation energy ($E_{a,kapp}$) of 25.69 kJ mol^{-1} with a pre-exponential factor of 8.71×10^2 (Figure 5.14B,D). The apparent activation enthalpy (ΔH) and entropy (ΔS) of the present photoconversion reaction were estimated from the linearized Eyring plot between ln (k_{app}/T) and $1/T$ and found to be 23.20 kJ mol^{-1} and -190 J mol^{-1} K^{-1} (Figure 5.14C,D).

The negative ΔS suggests that the final entropy at the transition state in which a photogenerated electron has been transferred to the localized orbital of the ferricyanide complex has a lower entropy than the initial state where it can delocalize over various excited states of the photoexcited CDs. The obtained thermodynamic parameters estimated in our present study matches well with the previously reported literature for the photoreduction of Fe^{3+} to Fe^{2+} with different photocatalysts. *[48, 53, 64]*

5.2.6. Photocatalytic dye degradation

Next, to further illustrate the efficient visible-light harvesting potential of embedded QDs inside the QD-Ds, we utilized these QD-Ds toward photocatalytic dye degradation in the aqueous solution. Toward this end, RhB and MB were chosen as two model water-soluble organic dyes known to contaminate the water body. *[2, 46, 65, 66]*
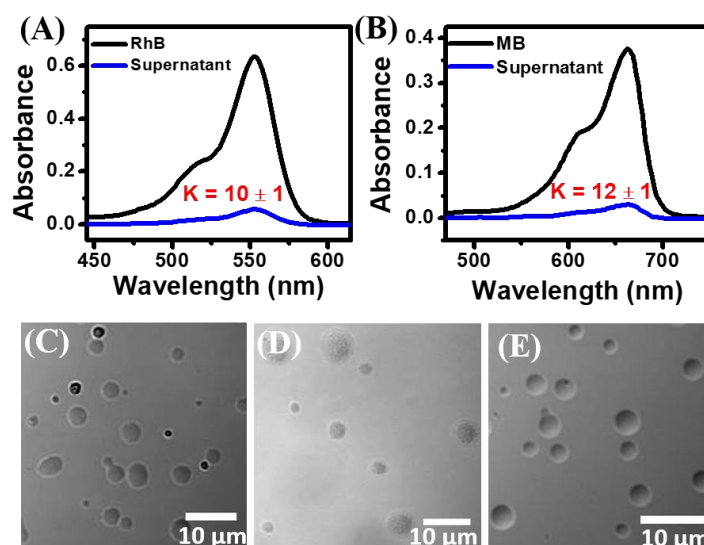
Figure 5.15. Estimation of equilibrium partition coefficient, *K* of (A) RhB and (B) MB inside the QD-Ds using UV-vis spectroscopy. Confocal (DIC) images of (C) QD-Ds, (D) RhB-loaded QD-Ds, and (E) MB-loaded QD-Ds.

The estimated *K* for RhB and MB inside the QD-Ds in pH 7.4 aqueous solution is found to be 10.3 ± 0.4 and 11.9 ± 0.8, respectively (Figure 5.15A,B). Importantly, the mean size and morphologies of dye-loaded

177

QD-Ds remain unaltered upon preferential sequestration (Figure 5.15C–E).

For photocatalytic dye degradation experiments, three 6 W blue LEDs (~420 nm) were utilized to illuminate the samples. All the experiments were carried out at room temperature
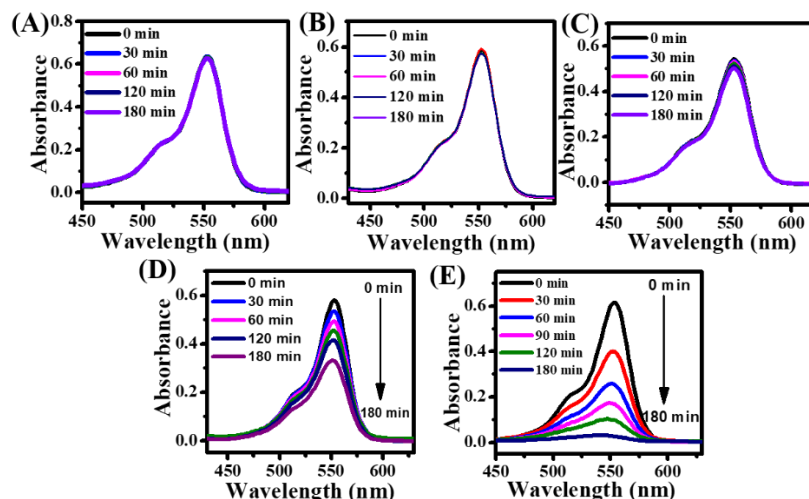
Figure 5.16. Time-dependent absorption spectra of the photocatalytic degradation of RhB in the presence of (A) Only RhB, (B) RhB + H_2O_2, (C) QD + RhB - H_2O_2, (D) QD + RhB + H_2O_2 and (E) QD-Ds + RhB + H_2O_2 under constant blue light irradiation.

. The photocatalytic reaction kinetics were followed using a UV-vis spectrophotometer by monitoring the changes in the absorbance of RhB and MB at their absorption peak maximum of 554 and 654 nm, respectively (Figures 5.16 and 5.17). Control experiments reveal negligible photodegradation of aqueous RhB and MB in the absence and presence of H_2O_2 even after 3 h of constant blue light irradiation (Figure 5.18A,B). This indicates the need for efficient photocatalysts for their degradation. Subsequently, we checked the photocatalytic activity of aqueous MSA-capped QDs towards photocatalytic degradation of RhB and MB in the absence and presence of H_2O_2 under blue light irradiation.
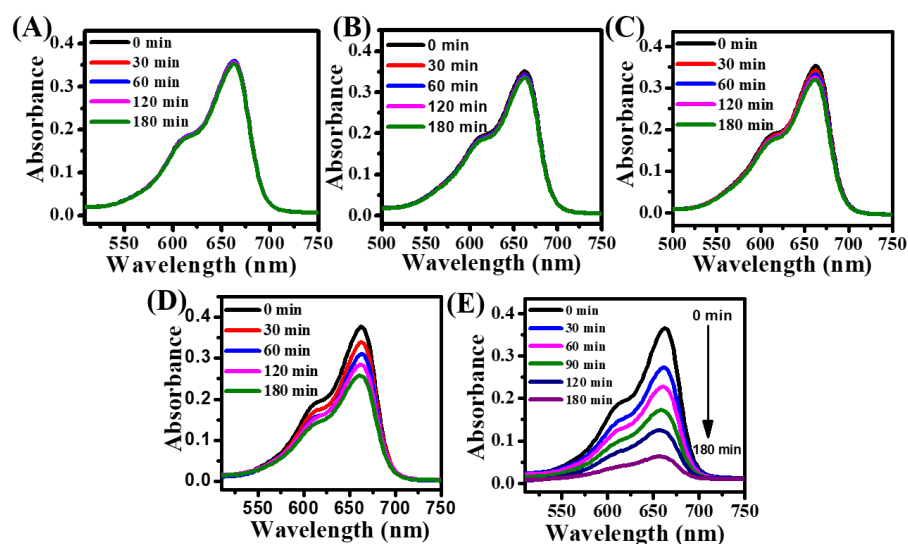
Figure 5.17. Time-dependent absorption spectra of the photocatalytic degradation of MB in the presence of (A) Only MB, (B) MB + H_2O_2, (C) QD + MB - H_2O_2, (D) QD + MB + H_2O_2 and (E) QD-Ds + MB + H_2O_2 under constant blue light irradiation.
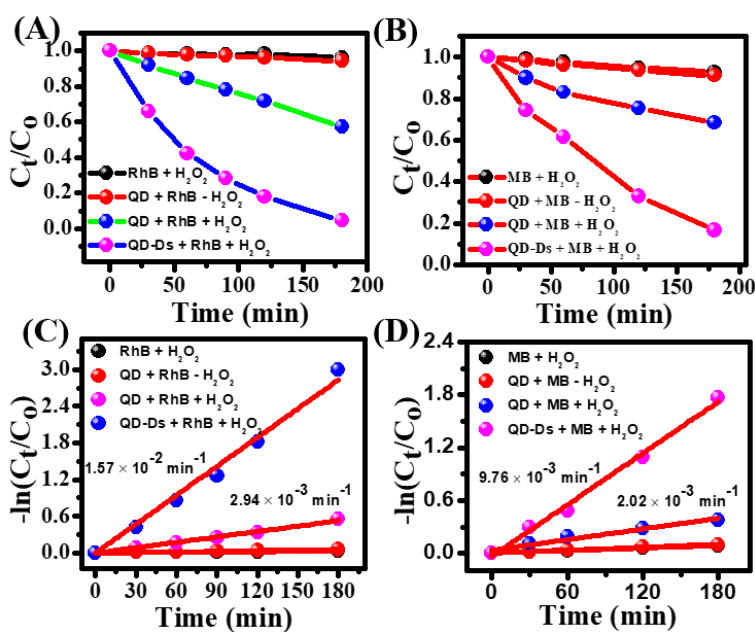
Figure 5.18. C_t/C_o plot of (A) RhB and (B) MB at different conditions under the constant illumination of blue light for 3 h. The first-order kinetic plot of -ln(C_t/C_o) versus time for (C) RhB and (D) MB at different conditions under the constant illumination of blue light for 3 h.

It is evident that aqueous MSA-capped QDs failed to degrade RhB and MB in the absence of H_2O_2 (Figure 5.18A,B). However, an appreciable photodegradation of RhB and MB (43% and 33%, respectively) is observed with MSA-capped QDs in the presence of 80 mM H_2O_2 upon 180 min of light irradiation (Figure 5.18A,B).

These findings indicate that H_2O_2 plays an active role in the photodegradation process possibly via generation of hydroxyl radicals ($^{\bullet}$OH) in the presence of QDs under blue light illumination. Importantly, faster degradation kinetics is observed for dye-loaded QD-Ds in the presence of H_2O_2 under the same experimental conditions with almost 96 and 84% photodegradation for RhB and MB, respectively (Figure 5.18A,B). Similar enhancement in the photodegradation efficacy of different dyes has been observed earlier within caged systems. *[2, 65, 66]* These results can be explained by considering confinement-induced efficient substrate channeling and light harvesting within the QD-Ds.

The experimental data were fitted using the first-order kinetic equation and the rate constants (k) were obtained from the slope of first-order kinetic plots. As seen in Figure 5.18C, RhB shows much faster degradation kinetics within QD-Ds with a corresponding rate constant of 1.57×10^{-2} min^{-1}, which is over 5.3 times higher than that observed in the case of aqueous MSA-capped QDs (2.94×10^{-3} min^{-1}). Similarly, a much higher rate constant of 9.76×10^{-3} min^{-1} for MB degradation inside the QD-Ds has been observed, which is 4.8 times higher than the rate constant (2.02×10^{-3} min^{-1}) estimated in the presence of aqueous MSA-capped QDs (Figure 5.18D). Notably, the significant enhancement in the photocatalytic degradation of RhB and MB with QD-Ds in comparison to the aqueous QDs can be attributed to the confinement of RhB and MB near the surface of embedded QDs inside the QD-Ds.
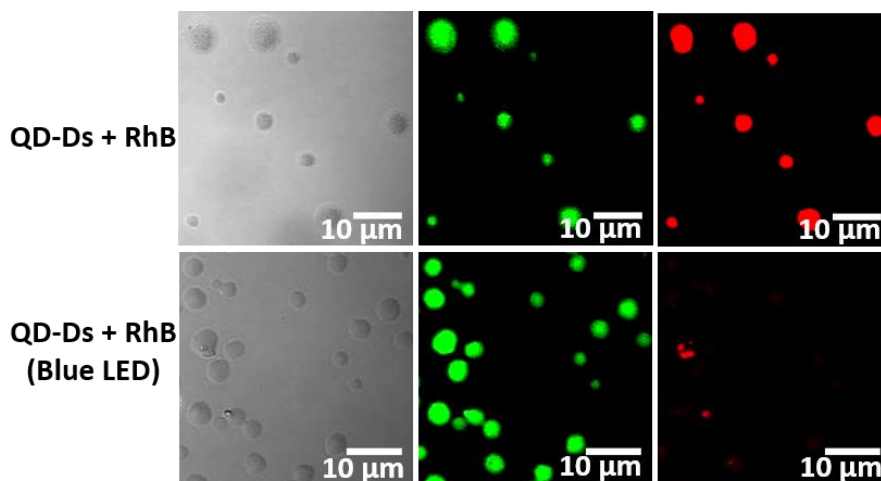
Figure 5.19. Confocal images (DIC, green channel, and red channel) of RhB-loaded QD-Ds before and after blue light irradiation.

To authenticate that the photocatalytic dye degradation occurs exclusively within the QD-D matrix, we utilized CLSM to visualize the luminescence behavior of sequestered RhB before and after light irradiation (Figure 5.19). In the absence of any light irradiation, individual QD-Ds exhibit distinct green (500-560 channel) and red (560-660 channel) signals due to the presence of green-emitting QDs and red-emitting RhB, respectively. Interestingly, upon light irradiation for a period of 3 h, the red signals disappear completely inside the QD-Ds while the green signals remain unaltered. These findings clearly indicate an almost complete photodegradation of RhB present inside the QD-Ds. Here it should be noted that the luminescence properties of embedded QDs remain unchanged before and after the photodegradation process, indicating that the embedded QDs act as photocatalysts for the dye degradation.

5.2.7. Mechanistic pathway of the degradation of RhB and MB

In order to establish the role of $^{\bullet}$OH in the dye degradation mechanism, we monitored its formation from H_2O_2 inside the QD-Ds. The $^{\bullet}$OH formation was studied using terephthalic acid (TA), a common probe for the detection $^{\bullet}$OH radicals. *[67, 68]* It is well known that the TA readily reacts with $^{\bullet}$OH radical to give 2-hydroxyterephthalic acid (TAOH), a fluorescent product ($\lambda_{em} = 430$ nm) which can be easily

detected using conventional fluorescence spectroscopy. Figure 5.20A shows the changes in the fluorescence spectra of TA inside the QD-Ds in the presence of H_2O_2 under constant blue light illumination at different time intervals. Initially, no visible fluorescence has been observed at 430 nm. However, a progressive increase in the PL intensity of TAOH at 430 nm confirms the formation of $^\bullet$OH radicals during the light-harvesting process by QD-Ds in the presence of H_2O_2. To further establish the role of radicals in the dye degradation process, we performed radical scavenger tests.

For this purpose, the photodegradation process of RhB inside the QD-Ds was studied in the presence of silver nitrate ($AgNO_3$) to scavenge electrons (e^-), ethylenediaminetetraacetic acid (EDTA) to scavenge holes (h^+) and benzoquinone (BQ) to scavenge superoxide radicals ($^{\bullet-}O_2$). The extent of photocatalytic degradation of RhB decreases to appreciably to 19% in the presence of $AgNO_3$, which can be due to the efficient scavenging of the photoexcited electrons from the QDs, which are responsible for the generation of $^\bullet$OH. On the other hand, the presence of EDTA results in only 64% degradation of RhB (Figure 5.20B). This decrease in the extent of photocatalytic degradation indicates that the formation of $^\bullet$OH from hydroxyl ions ($^-$OH) is hindered in the presence of EDTA. Notably, 92% degradation was observed in the presence of benzoquinone, indicating that $^{\bullet-}O_2$ does not play any role in the dye degradation process. Taken together, we propose a possible mechanism for the present photocatalytic dye degradation inside the QD-Ds (Figure 5.20C). Notably, embedded QDs inside the QD-Ds get photoexcited upon irradiation with blue light, resulting in the formation of e^- – h^+ pair. Subsequently, photoexcited QD transfers its conduction band electrons to nearby H_2O_2 to generate $^\bullet$OH as the major reactive oxidative species. Notably, a small amount of $^\bullet$OH radicals can also be generated from OH^- by capturing the holes from the valence band of QDs. The photogenerated $^\bullet$OH then directly oxidizes RhB and MB inside the QD-Ds.
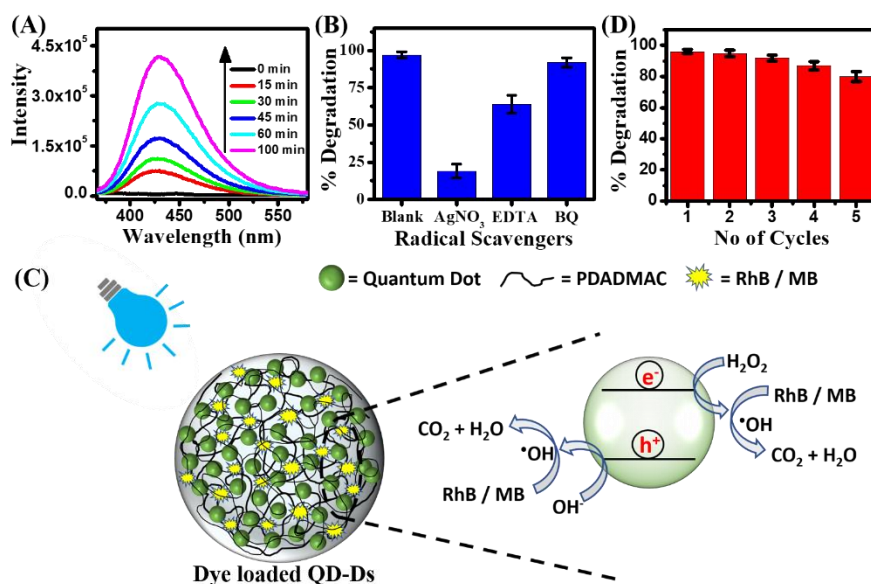
Figure 5.20. (A) Changes in the PL spectrum ($\lambda_{ex} = 310$ nm) of TAOH in presence of QD-Ds and H_2O_2 under blue light illumination. (B) Degradation efficiency of RhB-loaded QD-Ds in the presence of different radical scavengers. (C) Proposed degradation mechanism for RhB and MB degradation. (D) Recyclability test of QD-Ds for photocatalytic dye degradation under the constant illumination of blue LED for five consecutive cycles.

Finally, we explored the recyclability of the dye-loaded QD-Ds for several consecutive photocatalytic cycles. After each photocatalytic cycle, QD-Ds were washed using ethyl acetate for 3-4 times to remove any residual dye or byproducts trapped inside the QD-Ds. Our findings reveal >80% retention of the photodegradation efficiency of RhB even after 5 consecutive cycles (Figure 5.20D).
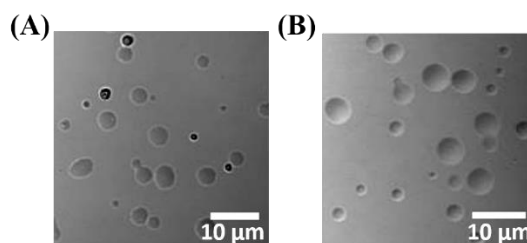
Figure 5.21. Confocal (DIC) images of QD-Ds (A) before the first photocatalytic cycle and (B) after the fifth photocatalytic cycle.

The DIC image of QD-Ds after the 5th photocatalytic cycle reveals intact spherical QD-Ds without any significant structural changes (Figure 5.21). These observations authenticate that the present QD-Ds can be recycled for multiple consecutive runs without any detrimental effect on their catalytic efficacy. In addition, the facile synthetic approach of these structurally stable QD-Ds along with the possibility of having a broad scope for embedded nanocatalysts makes them promising candidates for an efficient photocatalytic nanoreactors towards a broad range of photocatalytic transformations.

5.3. Conclusions

In the present work, we have demonstrated the utilization of a new class of photocatalytic nanoreactor with multiple embedded NPs as catalytic sites for the visible-light-driven photoredox conversion of Fe^{3+} to Fe^{2+} and photocatalytic dye degradation, which are otherwise inefficient with aqueous NPs alone. The membrane-less architecture of these NP-embedded coacervates provides an ideal environment to carry out the photocatalytic conversion inside its confined structure via preferential sequestration of Fe^{3+} and organic dyes. The enhanced photoredox activity of the present QD- and CD-Ds towards Fe^{3+} to Fe^{2+} conversion has been explained on the basis of altered surface charge density of embedded QDs and CDs inside the coacervates and increased concentrations of Fe^{3+}, while the enhanced photodegradation of dyes arises mainly due to the increased local concentrations of sequestered dyes in the close proximity of QDs embedded inside the QD-Ds. Our results indicate the participation of photogenerated electrons and holes from the embedded QDs and CDs for the observed photocatalytic transformations inside these droplets. Moreover, we have illustrated that the present droplets can be recycled for several consecutive cycles without any detrimental effects. Our present work paves the way for next-generation hybrid photocatalytic nanoreactors toward a wide spectrum of photochemical conversions.

5.4. References

1. Prier C. K., Rankic D. A., MacMillan D. W. C. (2013), Visible light photoredox catalysis with transition metal complexes: applications in organic synthesis, Chem. Rev., 113, 5322–5363. (DOI:10.1021/cr300503r)

2. Fang Y., Xiao Z., Kirchon A., Li J., Jin F., Togo T., Zhang L., Zhu C., Zhou H. C. (2019), Bimolecular proximity of a ruthenium complex and methylene blue within an anionic porous coordination cage for enhancing photocatalytic activity, Chem. Sci., 10, 3529–3534. (DOI:10.1039/c8sc05315d)

3. Kumar A., Samanta S., Srivastava R. (2018), Systematic investigation for the photocatalytic applications of carbon nitride/porous zeolite heterojunction, ACS Omega, 3, 17261–17275. (DOI:10.1021/acsomega.8b01545)

4. Fernández-Catalá J., Sánchez-Rubio M., Navlani-García M., Berenguer-Murcia Á., Cazorla-Amorós D. (2020), Synthesis of TiO_2/nanozeolite composites for highly efficient photocatalytic oxidation of propene in the gas phase, ACS Omega, 5, 31323–31331. (DOI:10.1021/acsomega.0c04793)

5. Zhu L., Nguyen D. C. T., Woo J. H., Zhang Q., Cho K. Y., Oh W. C. (2018), An eco-friendly synthesized mesoporous-silica particle combined with WSe_2-graphene-TiO_2 by self-assembled method for photocatalytic dye decomposition and hydrogen production, Sci. Rep., 8, 1–14. (DOI:10.1038/s41598-018-31188-w)

6. Paengjun N., Vibulyaseak K., Ogawa M. (2021), Heterostructural transformation of mesoporous silica–titania hybrids, Sci. Rep., 11, 1–12. (10.1038/s41598-020-80584-8)

7. Su Y., Song Z., Zhu W., Mu Q., Yuan X., Lian Y., Cheng H., Deng Z., Chen M., Yin W., Peng Y. (2021), Visible-light photocatalytic CO_2 reduction using metal-organic framework derived $Ni(OH)_2$ nanocages: a synergy from multiple light reflection, static charge

transfer, and oxygen vacancies, ACS Catal. 11, 345–354. (DOI:10.1021/acscatal.0c04020)

8. Albero J., Peng Y., García H. (2020), Photocatalytic CO_2 reduction to C^{2+} products, ACS Catal., 10, 5734–5749. (DOI:10.1021/acscatal.0c00478)

9. Zhu Z., Tang X., Kang S., Huo P., Song M., Shi W., Lu Z., Yan Y. (2016), Constructing of the magnetic photocatalytic nanoreactor MS@FCN for cascade catalytic degrading of tetracycline, J. Phys. Chem. C, 120, 27250–27258. (DOI:10.1021/acs.jpcc.6b05642)

10. Zhu Z., Yu Y., Huang H., Yao X., Dong H., Liu Z., Yan Y., Li C., Huo P. (2017), Microwave-hydrothermal synthesis of a novel, recyclable and stable photocatalytic nanoreactor for recognition and degradation of tetracycline, Catal. Sci. Technol., 7, 4092–4104. (DOI:10.1039/c7cy01330b)

11. Ding S., Liu X., Shi Y., Liu Y., Zhou T., Guo Z., Hu J. (2018), Generalized synthesis of ternary sulfide hollow structures with enhanced photocatalytic performance for degradation and hydrogen evolution, ACS Appl. Mater. Interfaces, 10, 17911–17922. (DOI:10.1021/acsami.8b02955)

12. Bojja S., Pal U., Yendrapati T. P., Soumya J. (2021), Robust $Co_9S_8@CdIn_2S_4$ cage for efficient photocatalytic H_2 evolution, J. Phys. Chem. C, 125, 5099–5109. (DOI:10.1021/acs.jpcc.0c11554)

13. Mondal B., Mukherjee P. S. (2018), Cage encapsulated gold nanoparticles as heterogeneous photocatalyst for facile and selective reduction of nitroarenes to azo compounds, J. Am. Chem. Soc., 140, 12592–12601. (DOI:10.1021/jacs.8b07767)

14. Zhao X., Liu X., Yi C., Li J., Su Y., Guo M. (2020), Palladium nanoparticles embedded in yolk-shell N-doped carbon nanosphere@void@SnO_2 composite nanoparticles for the photocatalytic reduction of 4-Nitrophenol, ACS Appl. Nano Mater., 3, 6574–6583. (DOI:10.1021/acsanm.0c01038)

15. Xu Q., Feng B., Ye C., Fu Y., Chen D. L., Zhang F., Zhang J., Zhu W. (2021), Atomically dispersed vanadium sites anchored on N-doped porous carbon for the efficient oxidative coupling of amines

to imines, ACS Appl. Mater. Interfaces, 13   15168–15177. (DOI:10.1021/acsami.0c22453)

16. Tan H., Kong P., Zhang R., Gao M., Liu M., Gu X., Liu W., Zheng Z. (2021), Controllable generation of reactive oxygen species on cyano-group-modified carbon nitride for selective epoxidation of styrene, Innov., 2, 100089. (DOI:10.1016/j.xinn.2021.100089)

17. Yen C. W., Mahmoud M. A., El-Sayed M. A. (2009). Photocatalysis in gold nanocage nanoreactors, J. Phys. Chem. A, 113, 4340–4345. (DOI:10.1021/jp811014u)

18. Shaban M., Ashraf A. M., Abukhadra M. R. (2018), TiO_2 nanoribbons/carbon nanotubes composite with enhanced photocatalytic activity; fabrication, characterization, and application, Sci. Rep., 8, 1–17. (DOI:10.1038/s41598-018-19172-w)

19. Zou Y., Xiao K., Qin Q., Shi J. W., Heil T., Markushyna Y., Jiang L., Antonietti M., Savateev A. (2021), Enhanced organic photocatalysis in confined flow through a carbon nitride nanotube membrane with conversions in the millisecond regime, ACS Nano, 15, 6551–6561. (DOI:10.1021/acsnano.0c09661)

20. Sousa-Castillo A., Couceiro J. R., Tomás-Gamasa M., Mariño-López A., López F., Baaziz W., Ersen O., Comesaña-Hermo M., Mascareñas J. L., Correa-Duarte M. A. (2020), Remote activation of hollow nanoreactors for heterogeneous photocatalysis in biorelevant media, Nano Lett., 20, 7068–7076. (DOI:10.1021/acs.nanolett.0c02180)

21. Yu Z., Lu X., Sun L., Xiong J., Ye L., Li X., Zhang R., Ji N. (2021), Metal-loaded hollow carbon nanostructures as nanoreactors: microenvironment effects and prospects for biomass hydrogenation applications, ACS Sustain. Chem. Eng., 9, 2990–3010. (DOI:10.1021/acssuschemeng.0c08422)

22. Li A., Zhu W., Li C., Wang T., Gong J. (2019), Rational design of yolk-shell nanostructures for photocatalysis, Chem. Soc. Rev., 48, 1874–1907. (DOI:10.1039/c8cs00711j)

23. Chen Y. A., Wang Y. T., Moon H. S., Yong K., Hsu Y. J. (2021),

Yolk-shell nanostructures: synthesis, photocatalysis and interfacial charge dynamics, RSC Adv., 11, 12288–12305. (DOI:10.1039/d1ra00803j)

24. Li H., Yang Y., He C., Zeng L., Duan C. (2019), Mixed-ligand metal-organic framework for two-photon responsive photocatalytic C-N and C-C coupling reactions, ACS Catal., 9, 422–430. (DOI:10.1021/acscatal.8b03537)

25. Chen L. W., Hao Y. C., Guo Y., Zhang Q., Li J., Gao W. Y., Ren L., Su X., Hu L., Zhang N., Li S., Feng X., Gu L., Zhang Y. W., Yin A. X., Wang B. (2021), Metal-organic framework membranes encapsulating gold nanoparticles for direct plasmonic photocatalytic nitrogen fixation, J. Am. Chem. Soc., 143, 5727–5736. (DOI:10.1021/jacs.0c13342)

26. Wang H., Wang H., Wang Z., Tang L., Zeng G., Xu P., Chen M., Xiong T., Zhou C., Li X., Huang D., Zhu Y., Wang Z., Tang J. (2020), Covalent organic framework photocatalysts: structures and applications, Chem. Soc. Rev., 49, 4135–4165. (DOI:10.1039/d0cs00278j)

27. Sun D., Kim D. P. (2020), Hydrophobic MOFs@Metal nanoparticles@COFs for interfacially confined photocatalysis with high efficiency, ACS Appl. Mater. Interfaces, 12, 20589–20595. (DOI:10.1021/acsami.0c04537)

28. Jiao J., Tan C., Li Z., Liu Y., Han X., Cui Y. (2018), Design and assembly of chiral coordination cages for asymmetric sequential reactions, J. Am. Chem. Soc., 140, 2251–2259. (DOI:10.1021/jacs.7b11679)

29. Lu T., Spruijt E. (2020), Multiphase complex coacervate droplets, J. Am. Chem. Soc., 142, 2905–2914. (DOI:10.1021/jacs.9b11468)

30. Williams D. S., Koga S., Hak C. R. C., Majrekar A., Patil A. J., Perriman A. W., Mann S. (2012), Polymer/Nucleotide droplets as bio-inspired functional micro-compartments, Soft Matter, 8, 6004–6014. (DOI:10.1039/c2sm25184a)

31. Koga S., Williams D. S., Perriman A. W., Mann S. (2011), Peptide-nucleotide microdroplets as a step towards a membrane-free

protocell model, Nat. Chem., 3, 720–724. (DOI:10.1038/nchem.1110)

32. Pir Cakmak F., Grigas A. T., Keating C. D. (2019), Lipid vesicle-coated complex coacervates, Langmuir, 35, 7830–7840. (DOI:10.1021/acs.langmuir.9b00213)

33. Keating C. D. (2012), Aqueous phase separation as a possible route to compartmentalization of biological molecules, Acc. Chem. Res., 45, 2114–2124. (DOI:10.1021/ar200294y)

34. Krishna Kumar R., Harniman R. L., Patil A. J., Mann S. (2016), Self-transformation and structural reconfiguration in coacervate-based protocells, Chem. Sci., 7, 5879–5887. (DOI:10.1039/c6sc00205f)

35. Li M., Huang X., Tang T. Y. D., Mann S. (2014), Synthetic cellularity based on non-lipid micro-compartments and protocell models, Curr. Opin. Chem. Biol., 22, 1–11. (DOI:10.1016/j.cbpa.2014.05.018)

36. Dora. Tang T. Y., Van Swaay D., DeMello A., Ross Anderson J. L., Mann S. (2015), In vitro gene expression within membrane-free coacervate protocells, Chem. Commun., 51, 11429–11432. (DOI:10.1039/c5cc04220h)

37. Aumiller W. M., Pir Cakmak F., Davis B. W., Keating C. D. (2016), RNA-based coacervates as a model for membraneless organelles: formation, properties, and interfacial liposome assembly, Langmuir, 32, 10042–10053. (DOI:10.1021/acs.langmuir.6b02499)

38. Lu T., Nakashima K. K., Spruijt E. (2021), Temperature-responsive peptide-nucleotide coacervates, J. Phys. Chem. B, 125, 3080–3091. (DOI:10.1021/acs.jpcb.0c10839)

39. Vaishnav J. K., Mukherjee T. K. (2019), Highly photostable and two-photon active quantum dot-polymer multicolor hybrid coacervate droplets, Langmuir, 35, 11764–11773. (DOI:10.1021/acs.langmuir.9b01783)

40. Saini B., Singh R. R., Nayak D., Mukherjee T. K. (2020), Biocompatible PH-responsive luminescent coacervate nanodroplets

from carbon dots and Poly(Diallyldimethylammonium Chloride) toward theranostic applications, ACS Appl. Nano Mater., 3, 5826–5837. (DOI:10.1021/acsanm.0c00995)

41. Singh S., Vaishnav J. K., Mukherjee T. K. (2020), Quantum dot-based hybrid coacervate nanodroplets for ultrasensitive detection of Hg^{2+}, ACS Appl. Nano Mater., 3, 3604–3612. (DOI:10.1021/acsanm.0c00317)

42. Saini B., Singh, R., Mukhopadhyay S., Mukherjee T. K. (2021), Specific loading and in vitro controlled release of a Ru-based hydrophobically encapsulated model anticancer drug inside nanoassemblies toward stimuli-responsive drug delivery, ACS Appl. Nano Mater., 4, 2037–2051. (DOI:10.1021/acsanm.0c03356)

43. Saini B., Singh S., Mukherjee T. K. (2021), Nanocatalysis under nanoconfinement: a metal-free hybrid coacervate nanodroplet as a catalytic nanoreactor for efficient redox and photocatalytic reactions, ACS Appl. Mater. Interfaces, 13, 51117–51131. (DOI:10.1021/acsami.1c17106)

44. Yadav D., Awasthi S. K. (2021), Ni Nanoparticle-immobilized imine-linked microspherical covalent organic polymer for degradation studies of organic dyes, ACS Appl. Polym. Mater., 3, 5460−5469. (DOI:10.1021/acsapm.1c00793)

45. Saini D., Aggarwal R., Sonker A. K., Sonkar S. K. (2021), Photodegradation of azo dyes in sunlight promoted by nitrogen−sulfur−phosphorus codoped carbon dots, ACS Appl. Nano Mater., 4, 9303−9312 (DOI:10.1021/acsanm.1c01810)

46. Huang H., Zhang T., Cai X., Guo Z., Fan S., Zhang Y., Lin C., Gan T., Hu H., Huang Z. (2021), In situ one-pot synthesis of C-decorated and Cl-doped sea-urchin- like rutile titanium dioxide with highly efficient visible-light photocatalytic activity, ACS Appl. Mater. Interfaces, 13, 60337−60350. (DOI:10.1021/acsami.1c17081)

47. Chakraborty I. N., Roy S., Devatha G., Rao A., Pillai P. P. (2019), InP/ZnS quantum dots as efficient visible-light photocatalysts for redox and carbon-carbon coupling reactions, Chem. Mater., 31,

2258–2262. (DOI:10.1021/acs.chemmater.9b00086)

48. Roy S., Roy S., Rao A., Devatha G., Pillai P. P. (2018), Precise nanoparticle-reactant interaction outplays ligand poisoning in visible-light photocatalysis, Chem. Mater., 30, 8415–8419. (DOI:10.1021/acs.chemmater.8b03108)

49. Vaishnav J. K., Mukherjee T. K. (2019), Surfactant-induced self-assembly of CdTe quantum dots into multicolor luminescent hybrid vesicles, Langmuir, 35, 6409–6420. (DOI:10.1021/acs.langmuir.9b00357)

50. Prajapati R., Chatterjee S., Kannaujiya K. K., Mukherjee T. K. (2016), Effect of compartmentalization of donor and acceptor on the ultrafast resonance energy transfer from DAPI to silver nanoclusters, Nanoscale, 8, 13006–13016. (DOI:10.1039/c6nr01792d)

51. Prajapati R., Bhattacharya A., Mukherjee T. K. (2016), Resonant excitation energy transfer from carbon dots to different sized silver nanoparticles, Phys. Chem. Chem. Phys., 18, 28911–28918. (DOI:10.1039/c6cp05451j)

52. Kim Y., Smith J. G., Jain P. K. (2018), Harvesting multiple electron-hole pairs generated through plasmonic excitation of Au nanoparticles, Nat. Chem., 10, 763–769. (DOI:10.1038/s41557-018-0054-3)

53. Kim Y., Torres D., Jain P. K. (2016), Activation energies of plasmonic catalysts, Nano Lett., 16, 3399–3407. (DOI:10.1021/acs.nanolett.6b01373)

54. Vinogradov V. S., Karczewski G., Kucherenko I. V, Mel N. N., Fernandez P. (2008), Raman spectra of structures with CdTe-, ZnTe-, and CdSe-based quantum dots and their relation to the fabrication technology, Phys. Solid State, 50, 164–167. (DOI:10.1134/S1063783408010290)

55. Duan J., Song L., Zhan J. (2009), One-pot synthesis of highly luminescent CdTe quantum dots by microwave irradiation reduction and their Hg^{2+}-sensitive properties, Nano Res., 2, 61–68. (DOI:10.1007/s12274-009-9004-0)

56. Qi M. Y., Li Y. H., Anpo M., Tang Z. R., Xu Y. J. (2020), Efficient photoredox-mediated C-C coupling organic synthesis and hydrogen production over engineered semiconductor quantum dots, ACS Catal., 10, 14327–14335. (DOI:10.1021/acscatal.0c04237)

57. Jouyandeh M., Mousavi Khadem S. S., Habibzadeh S., Esmaeili A., Abida O., Vatanpour V., Rabiee N., Bagherzadeh M., Iravani S., Reza Saeb M., Varma R. S. (2021), Quantum dots for photocatalysis: synthesis and environmental applications, Green Chem., 23, 4931–4954. (DOI:10.1039/d1gc00639h)

58. Wu X., Xie S., Liu C., Zhou C., Lin J., Kang J., Zhang Q., Wang Z., Wang Y. (2019), Ligand-controlled photocatalysis of CdS quantum dots for lignin valorization under visible light, ACS Catal., 9, 8443–8451. (DOI:10.1021/acscatal.9b02171)

59. Jiang Y., Weiss E. A. (2020), Colloidal quantum dots as photocatalysts for triplet excited state reactions of organic molecules, J. Am. Chem. Soc., 142, 15219–15229. (DOI:10.1021/jacs.0c07421)

60. Yuan Y., Jin N., Saghy P., Dube L., Zhu H., Chen O. (2021), Quantum dot photocatalysts for organic transformations, J. Phys. Chem. Lett., 12, 7180–7193. (DOI:10.1021/acs.jpclett.1c01717)

61. Dandapat A., Jana D., De G. (2009), Synthesis of thick mesoporous γ-Alumina films, loading of Pt nanoparticles, and use of the composite film as a reusable catalyst, ACS Appl. Mater. Interfaces, 1, 833–840. (DOI:10.1021/am800241x)

62. Roy S., Rao A., Devatha G., Pillai P. P. (2017), Revealing the role of electrostatics in gold-nanoparticle-catalyzed reduction of charged substrates, ACS Catal., 7, 7141–7145. (DOI:10.1021/acscatal.7b02292)

63. Liang M., Feng K., Karthick R., Zhang L., Shi Y., Hui K. S., Hui K. N., Jiang F., Chen F. (2020), Photocathode-assisted redox flow desalination, Green Chem., 22, 4133–4139. (DOI:10.1039/d0gc01191f)

64. Kim Y., Wilson A. J., Jain P. K. (2017), The nature of plasmonically assisted hot-electron transfer in a donor-bridge-

acceptor complex, ACS Catal., 7, 4360–4365. (DOI:10.1021/acscatal.7b01318)

65. Rasalingam S., Wu C., Koodali R. T. (2015), Modulation of pore sizes of titanium dioxide photocatalysts by a facile template free hydrothermal synthesis method: implications for photocatalytic degradation of rhodamine B, ACS Appl. Mater. Interfaces, 7, 4368−4380. (DOI:10.1021/am508883f)

66. Zhang Y., Hu Y., Zhao J., Park E., Jin Y., Liu Q., Zhang W. (2019), covalent organic framework-supported Fe–TiO$_2$ nanoparticles as ambient-light-active photocatalysts, J. Mater. Chem. A, 7, 16364–16371. (DOI:10.1039/c9ta03649k)

67. Liu J., An T., Chen Z., Wang Z., Zhou H., Fan T., Zhang D., Antonietti M. (2017), Carbon nitride nanosheets as visible light photocatalytic initiators and crosslinkers for hydrogels with thermoresponsive turbidity, J. Mater. Chem. A, 5, 8933–8938. (DOI:10.1039/C7TA02923C)

68. Xia X., Zhang J., Lu N., Kim M. J., Ghale K., Xu Y., Mckenzie E, Liu J., Ye H. (2015), Pd-Ir core-shell nanocubes : a type of highly efficient and versatile peroxidase mimic, ACS Nano, 9, 9994–10004. (DOI: 10.1021/acsnano.5b03525)

Chapter 6

Coacervate-Based Plexcitonic Assembly toward Peroxidase-like Activity and Ultrasensitive Glucose Sensing

6.1. Introduction

Nature utilizes enzymes to drive and boost a variety of biochemical reactions inside the intracellular environments via spatiotemporal regulation. The tremendous potential of enzymes as catalysts has also been recognized for a wide range of applications *[1−3]*. However, due to the fragile nature of these biocatalysts, immobilized enzymes often suffer from various issues including long-term stability, thermal and chemical stability, and recyclability. To circumvent these limitations, various artificial nanozymes have been developed in recent times with comparable activity and improved stability. In general, nanozymes are cost-effective and exhibit tunable enzyme-like activity with improved stability even under harsh environmental conditions *[4]*. These advantages have prompted extensive research interest in developing functional nanomaterials with intrinsic oxidase *[5]*, peroxidase *[6]*, superoxide dismutase *[7]*, and catalase activities *[8]*. Among these, nanozymes with peroxidase-like activity have found great curiosity due to their wide range of applications in clinical and bioanalytical chemistry *[4, 9]*. These nanozymes carry out the oxidation of various colorimetric substrates in the presence of hydrogen peroxide (H_2O_2) either via Fenton-like mechanism *[10, 11]* or a fast electron transfer pathway *[12−14]*. The colorimetric assays of these nanozymes make them suitable for the fabrication of various simple, rapid, and cost-effective immunoassays and biosensors *[11, 15−18]*.

To date, different nanomaterials of transition-metal oxides and chalcogenides (Fe_3O_4, MoS_2, CeO_2, CuO, FeS_2, etc.) *[19−23]*, noble metals (Ag, Au, Pt, Pd) *[11, 15, 24, 25]*, carbon nanomaterials *[26, 27]*, and metal−organic frameworks (MOFs) *[28−30]* have been found to possess intrinsic peroxidase-like activity. The peroxidase-like activity of these nanomaterials has been utilized successfully for the fabrication of low-cost colorimetric assays for the detection of various analytes including glucose *[12, 13]*, H_2O_2 *[18]*, biothiols *[31]*, and dopamine *[32, 33]*. In recent times, researchers have integrated multiple methods and exploited different properties of nanomaterials to

196

enhance the enzyme-mimicking activity *[12, 13, 24]*. Although these previous studies have successfully demonstrated the enzyme-mimicking activities of various integrated hybrid nanozymes with improved activity, their fabrication procedures are often complex and require careful handling. Furthermore, externally incorporated NPs usually suffer from unwanted aggregation which limits their catalytic activity and recyclability. In the present study, we have developed a facile methodology for the fabrication of coacervate-based hybrid plexcitonic material via in situ generation of Au NPs.

Previously our group has explored *[34−36]* and utilized the NP-embedded coacervates for a wide range of applications such as, theranostic applications *[36, 37]*, environmental remediation *[38]*, and catalytic and photocatalytic nanoreactors *[35, 39]*. In the present work, we have utilized quantum dot (QD)-embedded coacervate droplets (QD-Ds) as a scaffold for the fabrication of a new class of coacervate-based plexcitonic assembly via in situ generation of homogeneously dispersed Au NPs at room temperature without any reducing agent. The fabricated Au@QD-Ds have been found to possess intrinsic peroxidase-like activity with excellent storage ability, high recyclability as well as high structural stability at a wide pH and temperature range. Finally, the GOx-loaded Au@QD-Ds have been utilized for rapid and selective colorimetric detection of glucose both in aqueous medium and paper strip.

6.2 Results and discussion

6.2.1. Synthesis and characterization of QDs and QD-Ds

The MSA-capped CdTe QDs were synthesized according to the literature *[34]*. The excitonic peak of these QDs appears at 485 nm with a corresponding PL maximum at 524 nm (Figure 6.1A). The HRTEM image reveals the presence of spherical QDs with a mean size of 2.6 ± 0.2 nm (Figure 6.1B & C). The magnified HRTEM image shows the well-resolved crystal lattice with a d-spacing of 0.28 nm which corresponds to the (102) plane (Figure 6.1D) *[40]*. The zeta (ζ)

potential and PL QY of these QDs are −25.4 mV and 0.28, respectively *[38]*. The FTIR measurements confirm the covalent attachment of the free thiol groups of MSA on the surface of CdTe QDs (Figure 6.1E) *[34]*.
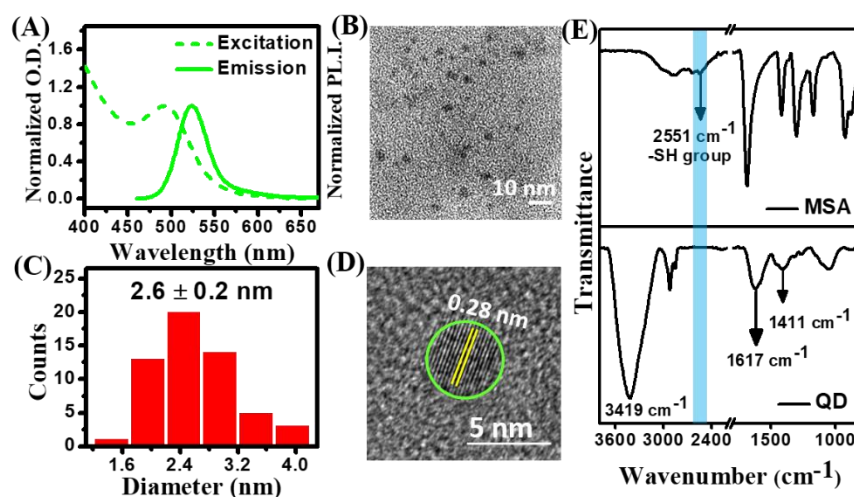

Figure 6.1. (A) Normalized absorption and emission spectra (λ_{ex} = 450 nm) of green emissive CdTe QDs. (B) TEM image, (C) size distribution histogram, and (D) HRTEM image of CdTe QDs. (E) FTIR spectra of MSA and MSA-capped CdTe QDs.

We utilized the as-synthesized QDs for the fabrication of QD-embedded droplets (QD-Ds) via simple mixing of positively charged PDADMAC (65 µM) and negatively charged QDs (170 nM) in aqueous medium under constant stirring (Figure 6.2A). The QD-polymer binary mixture was equilibrated for 4 h before any measurements to obtain homogeneous droplets. The FESEM image shows well-dispersed uniform spherical QD-Ds in the size range of 0.8− 3 µm (Figure 6.2B). These QD-Ds exhibit a ζ-potential of +8 mV *[34]*. Figure 6.2C displays the CLSM images of QD-Ds. The differential interference contrast (DIC) image of QD-Ds shows homogeneously distributed spherical droplets similar to those observed in FESEM measurement (Figure 6.2C). Moreover, the fluorescence image reveals distinct green emissive droplets which clearly indicates that the emission originates exclusively from the interior of these QD-

Ds. This observation unambiguously confirms the presence of QDs inside the droplets.
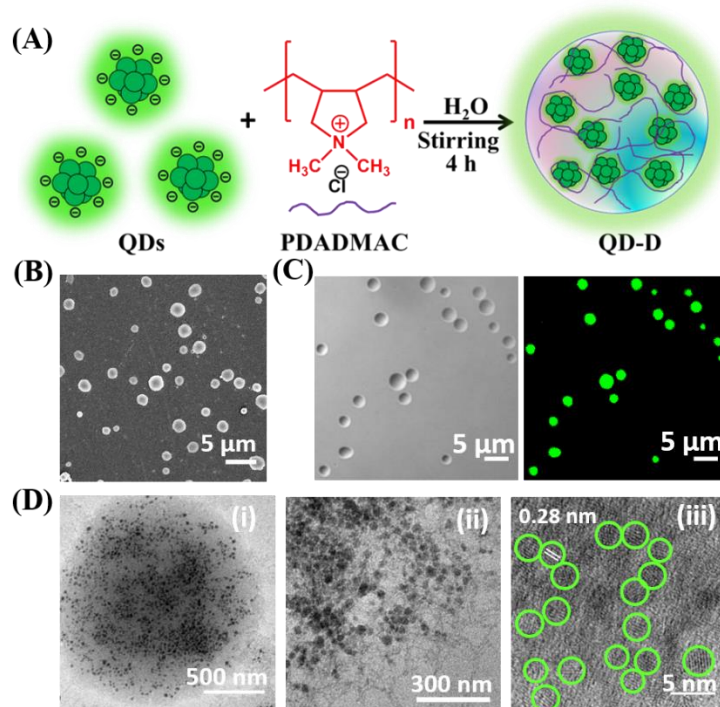

Figure 6.2. (A) Schematic illustration of the fabrication of QD-Ds via simple mixing of QDs and PDADMAC. (B) FESEM and (C) confocal images (DIC and Fluorescence) of QD-Ds. (D) TEM images of QD-D at different magnifications.

Next, we performed HRTEM measurements to know the spatial arrangements of QDs inside the QD-Ds. Figure 1D shows the HRTEM images of a QD-D at different magnification levels. It is evident that QD-D contains uniformly distributed dark spots (Figure 6.2Di). Upon magnification, it is evident that these dark spots consist of a cluster of QDs in the size range of 2–4 nm with a characteristic d-spacing of 0.28 nm entangled in the polymeric network [Figure 6.2D(ii) & (iii)]. Taken together, these findings reveal the formation of well-dispersed QD-Ds.

6.2.2. Synthesis of Au NPs inside the QD-D scaffold

Next, we seek to address whether these membraneless QD-Ds could act as scaffolds for the in situ generation of Au NPs. For this, we added different concentrations of $HAuCl_4$ to QD-D solution. A rapid color

change from colorless to wine red is observed upon the addition of 300 µM HAuCl₄, indicating the formation of Au NPs (Figure 6.3A). To further establish the formation of Au NPs, we recorded the UV−vis absorption spectrum (Figure 6.3B). A distinct localized surface plasmon resonance (LSPR) peak appears at 524 nm upon the addition of 300 µM HAuCl₄.
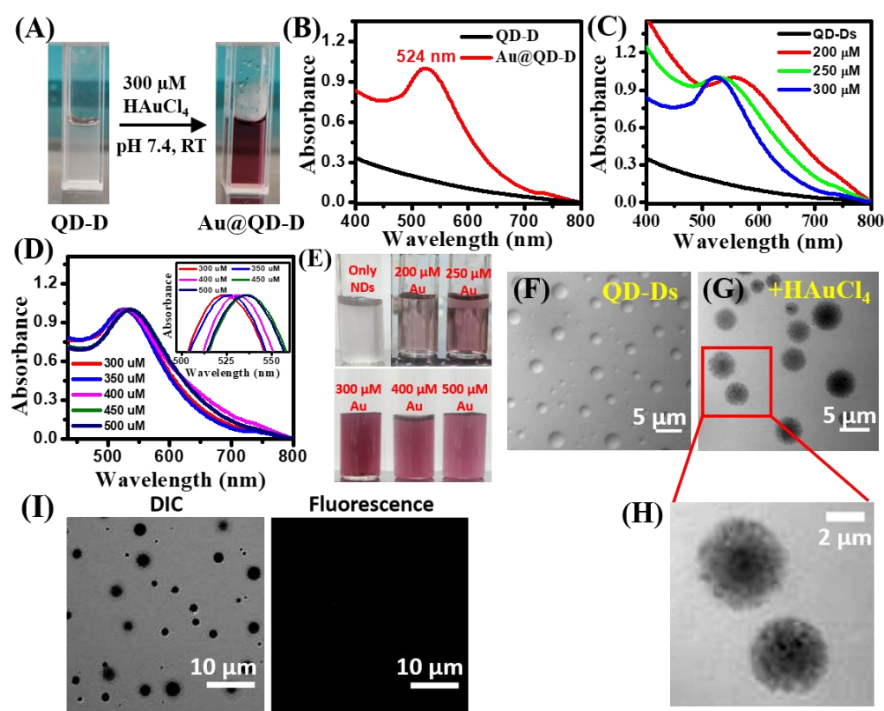

Figure 6.3. (A) Daylight photographs showing the changes in QD-D solution upon the addition of 300 µM HAuCl₄. (B) The UV-vis spectrum of QD-Ds and Au@QD-D showing the formation of Au NPs after the addition of 300 µM HAuCl₄. (C, D) UV-vis spectra and (E) daylight photographs of QD-D upon the addition of different concentrations of HAuCl₄ from 200–500 µM. Changes in the confocal image (DIC) of QD-Ds (F) before and (G) after the addition of 300 µM HAuCl₄. (H) Magnified DIC image of Au@QD-D.

The appearance of this LSPR peak authenticates the formation of spherical Au NPs. Next, we studied the effect of HAuCl₄ concentration (200−500 µM) on the formation of Au NPs inside the QD-Ds. Figure 6.3 shows the absorbance spectra of Au@QD-Ds at different concentrations of HAuCl₄. The LSPR peak of Au NPs shows

a broad structureless feature below 300 μM of $HAuCl_4$, indicating agglomeration of Au NPs (Figure 6.3C). Upon addition of 300 μM $HAuCl_4$, the synthesized Au NPs exhibit a well-resolved characteristic LSPR band at 524 nm. However, this LSPR band shifts to a higher wavelength with increase in the concentrations of $HAuCl_4$, indicating an increase in the mean size of the Au NPs (Figure 6.3D). A maximum red shift of 12 nm has been observed upon increasing the concentration of $HAuCl_4$ from 300 to 500 μM with a corresponding color change from wine red to reddish-purple (Figure 6.3E). To visualize the morphological stability of QD-Ds before and after the formation of Au NPs, we performed CLSM measurements (Figure 6.3F & G). It is evident from the DIC images that the morphology of individual spherical droplets remains intact after the formation of Au NPs. More importantly, the contrast of the droplets increases noticeably after the formation of Au NPs. Magnified DIC image reveals the presence of several dark spots inside the individual droplets (Figure 6.3H). Moreover, a slight increase in the mean size of QD-Ds has been observed after the formation of Au NPs, possibly due to the swelling of the droplet interior. Notably, the luminescence of QD-Ds gets quenched completely after the formation of Au NPs (Figure 6.3I). This observation can be explained by considering nanometal surface energy transfer from photoexcited QDs to nearby Au NPs, which is expected due to the significant spectral overlap between the band-edge emission of QDs and LSPR band of Au NPs. Similar nanometal surface energy transfer between QDs and plasmonic NPs has been reported previously *[41]*.

Next, we performed HRTEM measurements to know the shape and sizes of Au NPs formed inside the QD-Ds. Figure 6.4 shows HRTEM images of spherical Au@QD-Ds at different magnification levels. It is evident that individual Au@QD-D contains several dark spots inside its structure [Figure 6.4A(i)]. The presence of well-dispersed spherical Au NPs is clearly visible upon further magnification of the HRTEM image [Figure 6.4A(ii)]. Here, it is

important to mention that the contrast of Au NPs is higher than the embedded QDs.
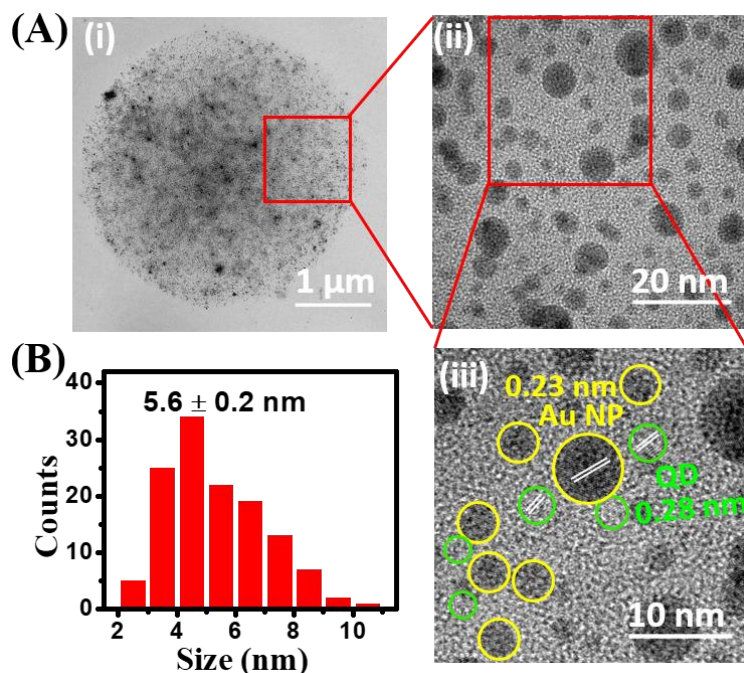

Figure 6.4. (A) TEM images of Au@QD-D at different magnifications and (B) the size distribution histogram of Au NPs formed inside QD-Ds after the addition of 300 µM $HAuCl_4$ estimated from HRTEM image.

Further magnification of the HRTEM image reveals the presence of distinct lattice fringes of QDs and Au NPs with a characteristic d-spacing of 0.28 and 0.23 nm, respectively [Figure 6.4A (iii)] *[12, 39]*. The sizes of the Au NPs are estimated to be in the range of 2−10 nm with a mean diameter of 5.6 ± 0.2 nm (Figure 6.4B). It should be noted that each Au NPs is surrounded by several QDs, indicating the close proximity of QDs and Au NPs inside the QD-D. Taken together, our findings reveal the in situ formation of spherical Au NPs inside the QD-Ds.

The presence of Au NPs inside the Au@QD-D is further confirmed using elemental mapping. Figure 6.5A shows the elemental mapping images of a single Au@QD-D. The presence of all the

essential elements such as Cd, Te, O, C, and Au is clearly evident inside the Au@QD-D.
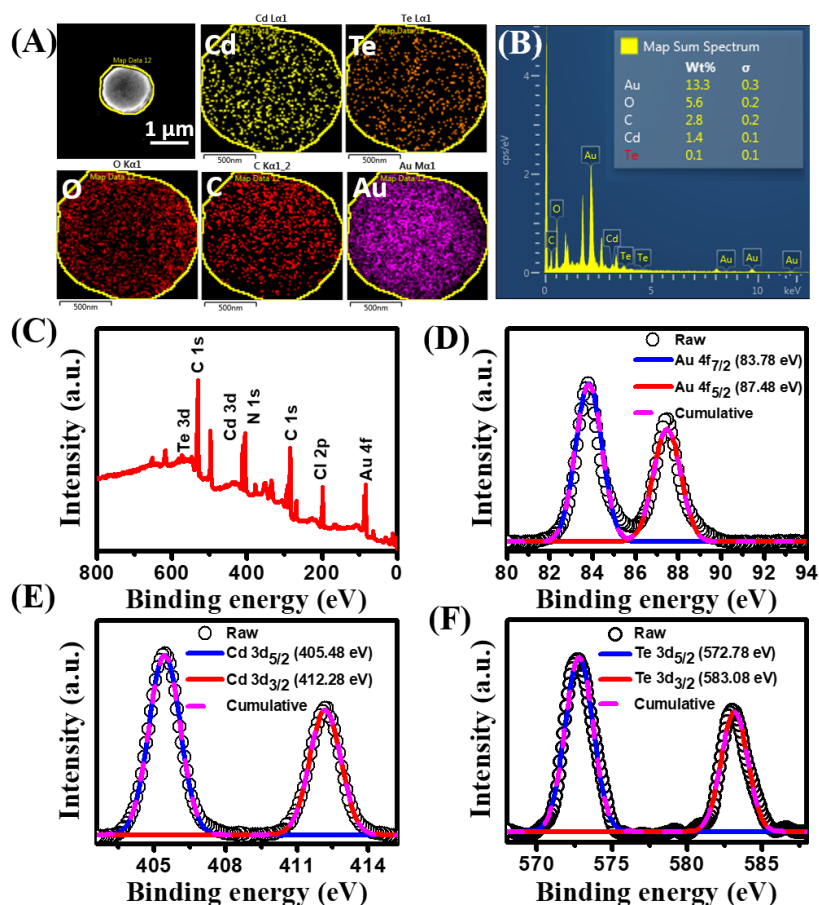

Figure 6.5. (A) Elemental mapping showing the presence of Cd, Te, O, C, and Au inside Au@QD-D. (B) EDX spectrum of Au@QD-D. Inset showing weight and atomic % of different elements. (C) XPS survey spectrum of Au@QD-D. Deconvoluted spectra of (D) Au4f, (E) Cd3d, and (F) Te3d.

Importantly, a uniform distribution of Au inside the Au@QD-D clearly authenticates the presence of Au NPs. The EDX spectrum and XPS survey spectrum of Au@QD-Ds further confirm the presence of Au along with the other elements (Figure 6.5B & C). The high-resolution XPS spectrum of Au 4f exhibits two sharp peaks at 83.78 and 87.48 eV, which can be assigned to Au $4f_{7/2}$ and Au $4f_{5/2}$, respectively (Figure 6.5D) *[12]*. Similarly, Cd 3d spectrum also exhibits two peaks at 405.48 and 412.28 eV which can be attributed to Cd $3d_{5/2}$ and Cd $3d_{3/2}$, respectively (Figure 6.5E) *[42]*. The XPS

spectrum of Te 3d reveals two peaks at 572.78 and 583.08 eV, which can be assigned to $3d_{5/2}$ and $3d_{5/2}$, respectively (Figure 6.5F) *[42]*.

6.2.3. Mechanism of Au NP formation

To know the role of individual constituents of the QD-D assembly on the formation mechanism of Au NPs, we performed different control experiments in the presence of MSA ligands, MSA-capped QDs, and PDADMAC. Notably, no characteristic LSPR peak at 538 nm has been observed neither in the presence of 2.5 mM MSA nor in the presence of 65 μM PDADMAC, indicating that both free MSA ligands and PDADMAC do not take part in the Au NP formation (Figure 6.6A & B).
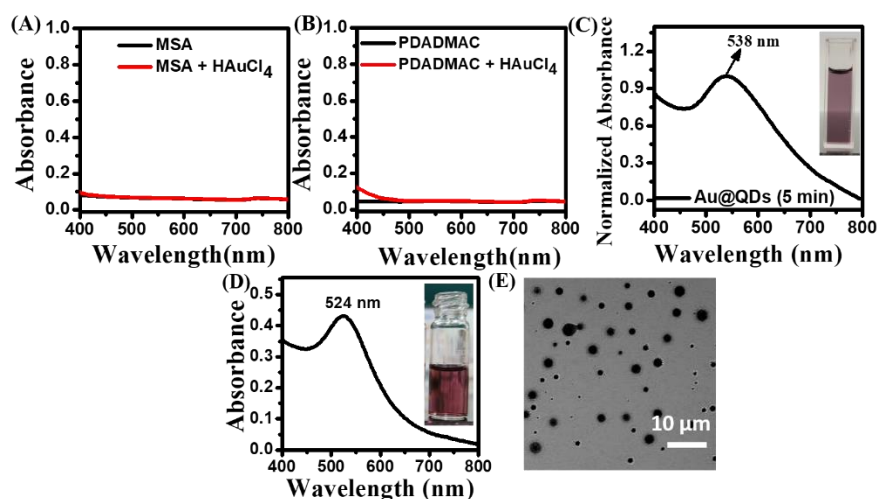

Figure 6.6. Changes in the UV-vis spectra of 300 μM HAuCl4 in the presence of (A) 2.5 mM MSA, (B) 65 μM PDADMAC, and (C) 170 nM QDs. (D) UV-vis spectrum of in situ generated Au NPs after the addition of 300 μM HAuCl4 to QD-D under dark conditions. (E) Confocal DIC image of Au@QD-D fabricated under dark conditions.

In contrast, a distinct LSPR peak appears in the presence of 170 nM MSA-capped QDs, indicating its active role in the Au NP formation (Figure 6.6C). The appearance of this characteristic LSPR peak is also associated with a change in the colorimetric signal from colorless to reddish-purple (Figure 6.6C inset). These observations suggest that the MSA-capped QD alone can reduce Au^{3+} to Au^0. To

know the role of photoexcited excitons of QDs in the reduction process, we performed the reaction under dark conditions (Figure 6.6D & E). The formation of Au NPs in the presence of MSA-capped QDs even under dark conditions rules out the involvement of photoexcited excitons in the reduction process. Therefore, the surface-immobilized MSA ligands on the surface of QDs reduce Au^{3+} to Au^0 and simultaneously stabilize the Au NPs. Similar reduction of metal salt to metal NP in the presence of immobilized surface ligands has been reported previously *[43, 44]*. However, the LSPR band of Au NPs synthesized in the presence of MSA-capped QDs is much broader than that inside the QD-Ds. Moreover, the LSPR band of Au@QD shifts from 538 to 550 nm with a red shift of 12 nm upon incubation for 1 h (Figure 6.7A). Similar changes have also been observed in the colorimetric signals of Au@QD upon incubation for 1 h (Figure 6.7B). These observations indicate that the synthesized Au@QDs are colloidally unstable under ambient conditions possibly due to agglomeration.
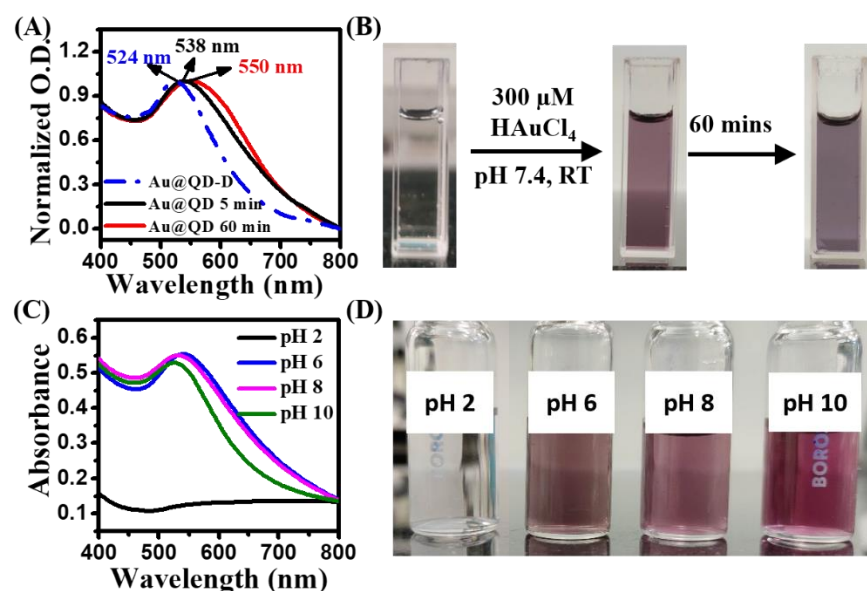

Figure 6.7. (A) UV-vis spectra of Au@QD-D (blue dotted line) and Au@QD (black and red solid lines) as a function of equilibration time. (B) Daylight photographs of Au@QD at different equilibration time. (C) UV-vis spectra, and (B) daylight photographs of Au@QD solution at different pH.

To further ascertain the active role of MSA ligands on the surface of QDs, we investigated the effect of solution pH on the in situ formation of Au NPs (Figure 6.7C & D). MSA has two pKa values of 4.19 and 5.64 [34]. Therefore, at lower acidic pH (<4), it is expected that both the carboxylate groups will be protonated and may not take part in the reduction process. As expected, the formation of Au NPs is inhibited completely at pH = 2 as revealed from UV−vis and colorimetric signals. In contrast, the formation of Au NPs is favorable in the pH range of 6−10, indicating the active role of carboxylate groups of MSA ligands on the surface of QDs (Figure 6.7C & D).

6.2.4 Peroxidase-like activity of Au@QD-Ds

Previously, the optoelectronic properties of plasmonic materials and their composites have been utilized for various catalytic and artificial enzymatic transformations [12, 45, 46] In particular, Au NP-based composites have been shown to exhibit efficient peroxidase-like activity with improved efficacy and stability [12, 13] To explore the peroxidase-like activity of Au@QD-Ds, we have chosen model oxidation reactions involving different chromogenic substrates like TMB, ABTS, and OPD in the presence of H_2O_2 (Figure 6.8A). The enzyme-mimicking activity of Au@QD-Ds was measured using a UV−vis spectrophotometer by monitoring the maximum absorbance of the oxidized products for different substrates. Different substrates were incubated with Au@QD-Ds for a period of 1 h and the reaction kinetics were monitored just after the addition of H_2O_2. Addition of 500 μM TMB and 1 mM H_2O_2 into the aqueous dispersion of Au@QD-Ds results in the appearance of a distinct absorption peak at 652 nm, which is a characteristic peak of oxidized TMB (Figure 6.8B). Additionally, the colorless aqueous dispersion of Au@QD-Ds turns to deep blue within 30 min (Figure 6.8B inset). However, in the absence of Au@QD-Ds, neither TMB nor TMB in the presence of H_2O_2 results in the appearance of the 652 nm peak (Figure 6.8B). These observations indicate that the presence of Au@QD-Ds is essential for the conversion of TMB to oxidized TMB. However, a weak absorption

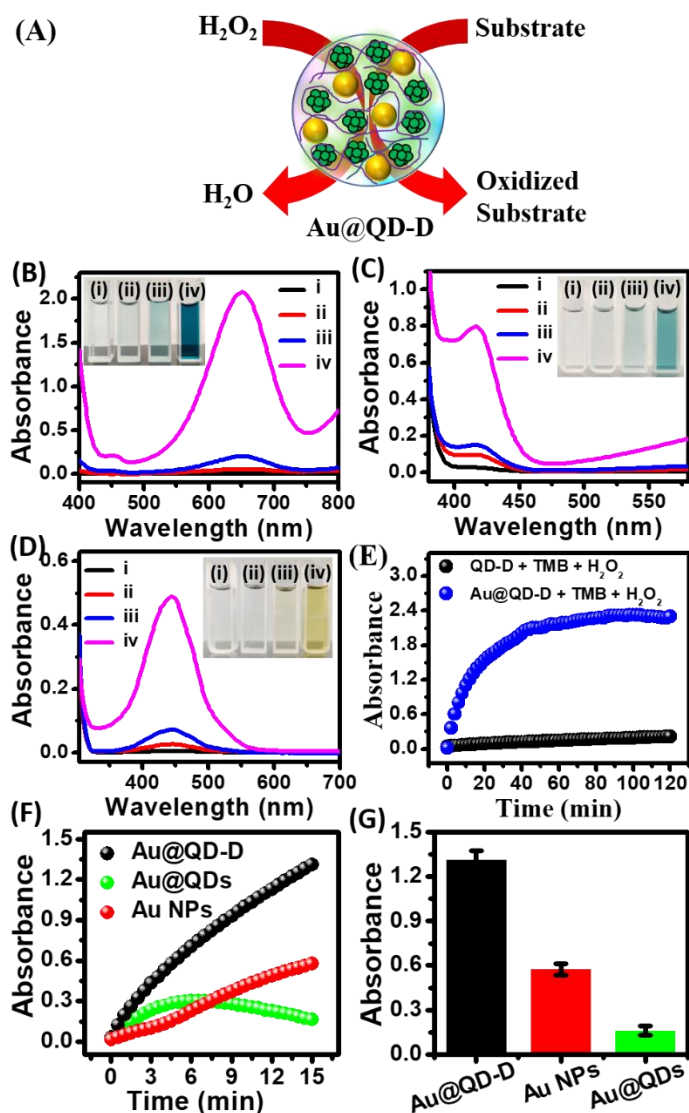peak at 652 nm appears with Au@QD-Ds alone in the absence of H_2O_2.

Figure 6.8. (A) Schematic representation showing the peroxidase-like activity of Au@QD-Ds in the presence of H_2O_2. (B) UV-vis spectra and daylight photographs (inset) of (i) TMB, (ii) TMB + H_2O_2, (iii) Au@QD-Ds + TMB, and (iv) Au@QD-Ds + TMB + H_2O_2. (C) UV-vis spectra and daylight photographs (inset) of (i) ABTS, (ii) ABTS + H_2O_2, (iii) Au@QD-D + ABTS, and (iv) Au@QD-D + ABTS + H_2O_2. (D) UV-vis spectra and daylight photographs of (i) OPD, (ii) OPD + H_2O_2, (iii) Au@QD-D + OPD, and (iv) Au@QD-D + OPD + H_2O_2. (E) Kinetics of TMB oxidation monitored at 652 nm with QD-Ds, and Au@QD-Ds in the presence of H_2O_2. (F) Kinetics of TMB oxidation

monitored at 652 nm with Au@QD-D, Au@QD, and citrate-capped Au NPs in the presence of 1 mM H_2O_2. (G) Relative peroxidase-like activity of Au@QD-Ds, Au@QDs, and citrate-capped Au NPs.

Similar oxidation of ABTS and OPD has also been observed inside the Au@QD-Ds (Figure 6.8C & D). Figure 6.8E shows the changes in the absorbance at 652 nm as a function of time in the presence of 500 μM TMB and 1 mM H_2O_2 in QD-Ds and Au@QD-Ds over a period of 120 min. Notably, QD-Ds alone in the presence of TMB and H_2O_2 show negligible conversion of TMB to oxidized TMB. In contrast, a rapid growth in the absorbance of oxidized TMB has been observed for Au@QD-Ds in the presence of H_2O_2. These observations clearly indicate that the embedded Au NPs in Au@QD-Ds act as catalytic centers for the peroxidase-like activity. Next, we compared the peroxidase activity of Au@QD-Ds, Au@QDs, and citrate-capped Au NPs under similar conditions (Figure 6.8F & G). Notably, Au@QD-Ds exhibit much higher activity toward TMB oxidation relative to Au@QD and citrate-capped Au NPs. The estimated relative activity of Au@QDs and citrate-capped Au NPs is 12 and 43%, respectively.

6.2.5. Optimization of peroxidase-like activity of Au@QD-Ds

To optimize the peroxidase-like activity, we systematically investigated the effect of various reaction parameters such as pH, temperature, and substrate concentrations on the peroxidase-like activity of Au@QD-Ds.
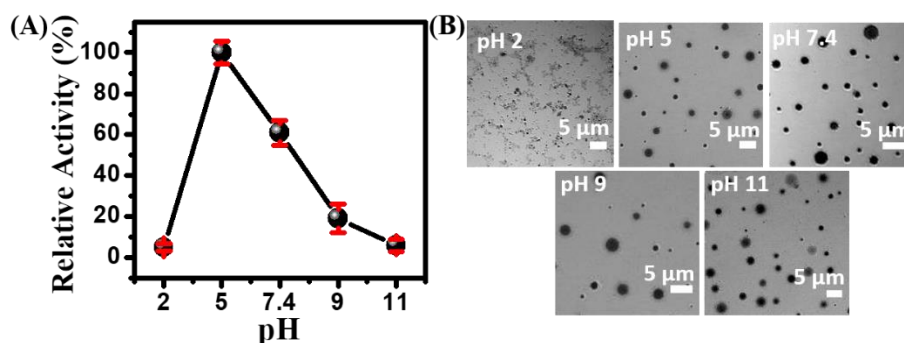

Figure 6.9. (A) Peroxidase-like activity and (B) confocal DIC images of Au@QD-Ds in pH 2, 5, 7.4, 9, and 11.

Figure 6.9A shows the effect of pH in the range of 2−11 on the peroxidase-like activity of Au@QD-Ds. The maximum activity is observed at pH = 5. However, the activity of Au@QD-Ds decreases sharply in both acidic (<5) and basic (>7.4) pH values. Notably, these Au@QD-Ds are unstable at lower acidic pH (<4) due to the protonation of MSA ligands on the surface of QDs. Therefore, the decrease in activity at pH = 2 is due to the disassembly of Au@QD-Ds and subsequent agglomeration of Au NPs (Figure 6.9B) *[39]*. On the other hand, these Au@QD-Ds are stable in the pH range of 5−11 (Figure 6.9B); however, the activity decreases steadily in the basic pH range with a relative activity of 19 and 6% at pH = 9 and 11, respectively. This sharp decrease in the activity can be attributed to the instability of H_2O_2 at highly alkaline pH *[13]*.
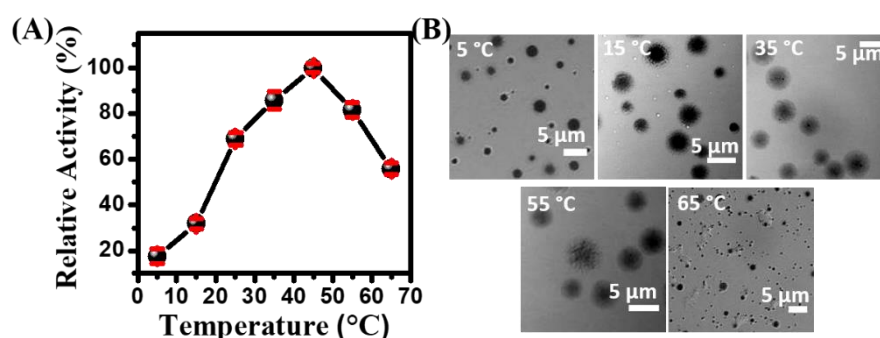

Figure 6.10. (A) Peroxidase-like activity and (B) confocal DIC images of Au@QD-Ds at different temperatures.

To know the effect of temperature on the activity and morphological stability of Au@QD-Ds, we varied the solution temperature in the range of 5−65 °C (Figure 6.10A & B). The temperature-dependent morphological stabilities of Au@QD-Ds were accessed using phase contrast microscopy (Figure 6.10B). It is evident that these Au@QD-Ds are morphologically stable in the temperature range of 5−55 °C. However, the disintegration of these spherical Au@QD-Ds is clearly evident at a higher temperature of 65 °C. Figure 6.10A shows the effect of temperature on the peroxidase-like activity of Au@QD-Ds. While the enzymatic activity of Au@QD-Ds increases steadily in the range of 5−45 °C, it decreases at 55 and 65 °C. The

maximum activity of Au@QD-Ds is observed at 45 °C. The above results indicate good thermal stability of Au@QD-Ds in a broad range of temperatures, which is superior to the natural HRP *[12, 13]*. Next, we evaluated the effect of substrate (TMB and H_2O_2) concentrations on the peroxidase activity of Au@QD- Ds (Figure 6.11A & B). A steady increase in the peroxidase-like activity of Au@QD-Ds as a function of TMB and H_2O_2 concentrations has been observed upon increasing the concentrations up to 0.8 mM. However, beyond 0.8 mM, a slight decrease in the relative activity has been noticed for both TMB and H_2O_2. The observed decrease in the activity is possibly due to the substrate inhibition at higher concentrations as both TMB and H_2O_2 compete for the access of the active sites inside the Au@QD-Ds, which results in the decrease of enzymatic activity. This observation is similar to that observed earlier for other artificial nanozymes and HRP *[13, 47]*.
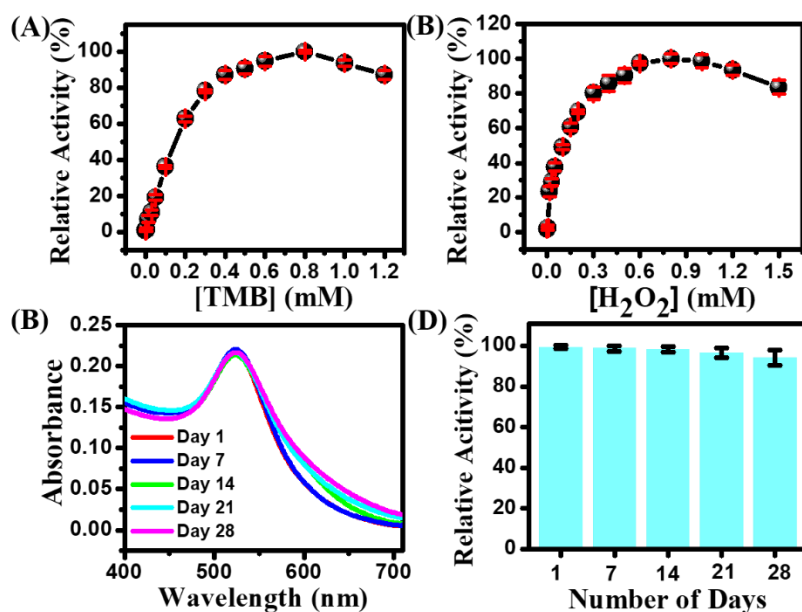

Figure 6.11. Peroxidase-like activity of Au@QD-Ds at different concentrations of (A) TMB and (B) H_2O_2. (C) Changes in the UV-vis spectra of Au@QD-Ds upon aging for 28 days. (D) Time-dependent peroxidase-like activity of Au@QD-Ds upon storing for multiple days. The data represent the mean ± SEM for three (n = 3) independent experiments.

Next, we studied the effect of aging of colloidal Au@QD-Ds on the peroxidase activity for a period of 28 days. The activity of natural peroxidase enzymes such as HRP is known to degrade over time which limits their applicability *[38]*. Notably, no appreciable changes in the LSPR peak for Au@QD-Ds were observed over a period of 28 days (Figure 6.11C). Furthermore, it has been observed that these Au@QD-Ds can retain more than 94% of their initial peroxidase-like activity over a period of 28 days, suggesting excellent storage stability for long durations (Figure 6.11D).

6.2.6. Estimation of kinetic parameters

The kinetic parameters associated with the peroxidase-like activity of Au@QD-Ds were evaluated through detailed kinetic experiments. The kinetic experiments were carried out by varying the concentration of TMB (0−1 mM) and H_2O_2 (0−1.2 mM).
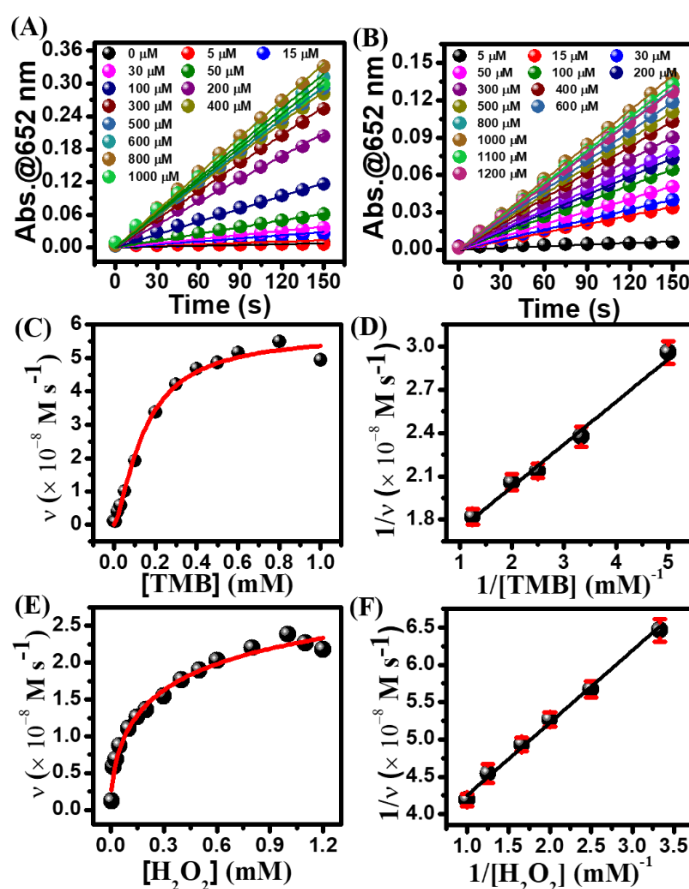

Figure 6.12. Changes in the absorbance of ox-TMB at 652 nm on varying the concentrations of (A) TMB and (B) H_2O_2. (C, E)

Michaelis−Menten plots of Au@QD-D catalyzed TMB oxidations by keeping H_2O_2 and TMB constant, respectively and (D, F) corresponding Lineweaver−Burk plots for TMB and H_2O_2, respectively. The data represent the mean ± SEM for three (n = 3) independent experiments.

The changes in the absorbance at 652 nm were monitored as a function of time (Figure 6.12A & B). The plots of initial reaction rates versus molar concentrations of TMB and H_2O_2 show typical Michaelis−Menten curves for TMB and H_2O_2 (Figure 6.12C & E). This result shows that Au@QD-Ds exhibit a typical Michaelis−Menten behavior similar to those reported previously for other nanozymes and HRP [12, 19]. The Michaelis constant (K_m) and maximum reaction velocity (V_{max}) were obtained using the Lineweaver−Burk plots (Figure 6.12D & F). The K_m value indicates the affinity of different substrates toward the enzymes. A lower value of K_m means a higher affinity while a higher K_m value indicates a lower affinity. The estimated K_m values of TMB and H_2O_2 are 0.21 and 0.28 mM, respectively. These values are either comparable or lower than those estimated for other nanozymes and free HRP [10, 12, 14] indicating that Au@QD-Ds have a much higher affinity for H_2O_2 and TMB than HRP. The enhanced affinity for both the substrates can be explained by considering effective substrate channeling inside the membraneless aqueous microenvironment of Au@QD-Ds. On the other hand, the estimated V_{max} values for TMB and H_2O_2 inside the Au@QD-Ds are 7.04×10^{-8} and 3.01×10^{-8} M s^{-1}, respectively. The estimated kinetic parameters clearly suggest that Au@QD-Ds possess better affinity toward TMB and H_2O_2 and exhibit superior peroxidase-like activity compared to the earlier reported nanozymes.

6.2.7. Mechanism of peroxidase-like activity

The peroxidase-like activity of nanozymes generally proceeds via either the Fenton-like mechanism [10, 11] or the electron-transfer process [12−14]. The Fenton-like mechanism follows the

decomposition of H_2O_2 into reactive oxygen species like hydroxyl radicals (•OH). To know the possibility of the Fenton-like mechanism, the formation of •OH was evaluated using rhodamine B (RhB) and terephthalic acid (TA) as common probes to detect the formation of •OH radicals *[12, 39]*. RhB is known to undergo degradation in the presence of •OH, which can be easily monitored using UV−vis spectroscopy. Figure 6.13A shows the time-dependent absorption spectra of 15 μM RhB in the presence of Au@QD-Ds and H_2O_2 for a duration of 180 min. No appreciable degradation of RhB has been observed under this condition indicating the lack of any •OH radical formation. This argument is further validated using TA as a probe. Figure 6.13B shows the fluorescence spectra of TA in the presence of Au@QD-Ds and H_2O_2 over a period of 180 min. The absence of any characteristic fluorescence peak at 425 nm from 2-hydroxyterephthalic acid (TAOH) further indicates the absence of any •OH radical in the reaction mixture.

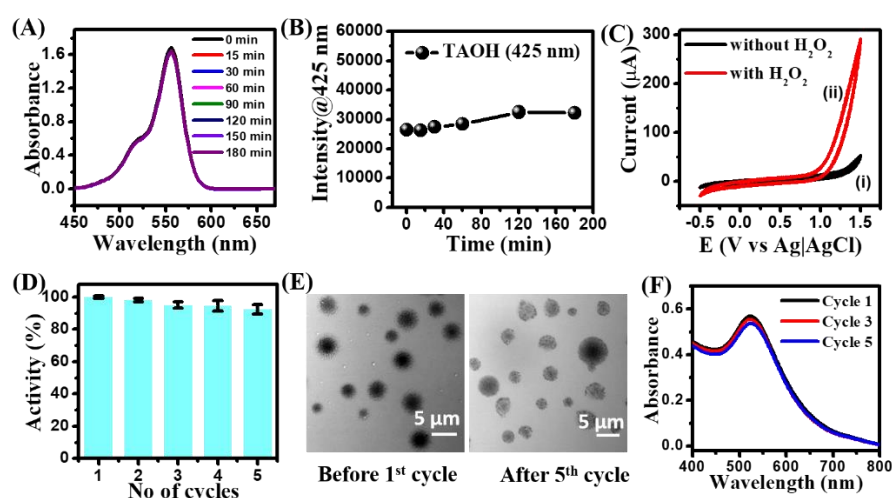**Figure 6.13.** Time-dependent UV-vis spectra of (A) RhB and (B) PL intensity profile of terephthalic acid (TA) (λ_{ex} = 315 nm) in the presence of Au@QD-D and H_2O_2. (C) Cyclic voltammograms of Au@QD-D deposited GC electrode in 10 mM sodium acetate buffer (pH 5.0) in the (i) absence, and (ii) presence of 5 mM H_2O_2. (D) Recyclability test of Au@QD-D for TMB oxidation for several consecutive cycles. The data represent the mean ± SEM for three (n =

3) independent experiments. (E) Confocal images of Au@QD-Ds before 1st cycle and after 5th cycle. (F) UV-vis spectra of Au@QD-Ds before and after different catalytic cycles.

Next, we studied the electrocatalytic behavior of Au@QD-Ds to establish the electron-transfer mechanism. Initially, we modified a GCE with Au@QD-Ds and performed the cyclic voltammetric measurements in the absence and presence of H_2O_2. The cyclic voltammogram of the bare GCE is similar to that of Au@QD-Ds within the same applied potential window in the absence of H_2O_2 [Figure 6.13C(i)]. Notably, no increase in the reduction current was observed for the bare GCE in the absence and presence of H_2O_2. However, the Au@QD-D-modified GCE shows a sharp increase (239 μA) in the electrocatalytic current with a peak at +1.5 V vs Ag|AgCl upon addition of 5 mM H_2O_2 into pH 5 acetate buffer solution [Figure 6.13C(ii)]. This remarkable increase in the electrocatalytic current authenticates that Au@QD-Ds possess excellent electrocatalytic activity and thus can easily facilitate electron transfer between the GC (donor) and H_2O_2 (acceptor) [13, 48]. These findings indicate that the peroxidase-like activity of Au@ QD-Ds proceeds via the electron-transfer mechanism. Taken together, the peroxidase-like activity of Au@QD-Ds mainly proceeds via the electron-transfer mechanism from substrates to Au@QD-Ds and subsequently to H_2O_2, resulting in oxidation of substrates and simultaneous reduction of H_2O_2 to water. Similar peroxidase-like activity of metal-based nanozymes via electron transfer pathways has been reported previously [12].

Recyclability of nanozymes for consecutive cycles is highly desirable in the context of their practical applicability. We checked the recyclability of our composite Au@QD-Ds for several consecutive catalytic cycles. After each catalytic cycle, Au@QD-Ds were first separated from the reaction mixture via centrifugation at 12000 rpm and then washed with water several times to remove any reactants or products from the previous cycle. The separated Au@QD-Ds were then again redispersed in acetate buffer (pH = 5) and used for

subsequent catalytic cycles. Our findings reveal that Au@QD-Ds retain over 92% catalytic activity even after five consecutive cycles (Figure 6.13D). The confocal DIC images of Au@QD-Ds captured before the first catalytic cycle and after the fifth catalytic cycles authenticate the structural integrity of these Au@QD-Ds (Figure 6.13E). The presence of intact spherical Au@QD-Ds even after five consecutive catalytic cycles reveals that the present composite is structurally robust and can be utilized for multiple catalytic cycles without any appreciable loss of catalytic activity. Furthermore, the UV−vis spectra of Au@QD-Ds recorded before and after different cycles authenticate that the dispersion state of colloidal Au NPs inside the QD-Ds remains unchanged (Figure 6.13F).

6.2.8. Selective glucose sensing using Au@QD-Ds

Finally, we utilized the peroxidase-like activity of Au@QD-Ds for the colorimetric detection of glucose in solution and filter paper using an integrated bioplatform in the presence of GOx (Figure 6.14A).
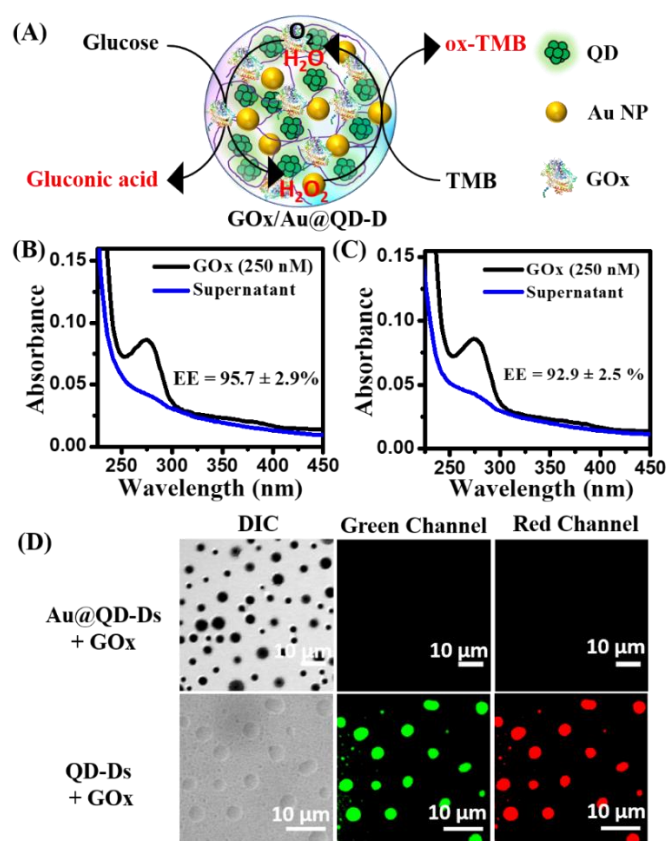
Figure 6.14. (A) Schematic representation of GOx/Au@QD-D composite for glucose detection. Estimation of encapsulation efficiency (EE) of GOx inside (B) QD-Ds and (C) Au@QD-Ds. (D) CLSM (DIC and Fluorescence) images of GOx-loaded Au@QD-Ds and QD-Ds.

The integrated bioplatform was fabricated via preferential sequestration of GOx inside the composite Au@ QD-Ds. To know the affinity of GOx toward QD-Ds and Au@QD- Ds, we estimated the EE from UV−vis spectroscopy. The estimated EE values of GOx are 95.7 ± 2.9 and 92.9 ± 2.5% for QD-Ds and Au@QD-Ds, respectively (Figure 6.14B & C). This high value of EE indicates a high affinity of GOx toward the confined microenvironment of these composite systems. In order to authenticate the presence of GOx inside the QD-Ds and Au@QD-Ds, we utilized RBITC-labeled GOx for their visualization under CLSM.
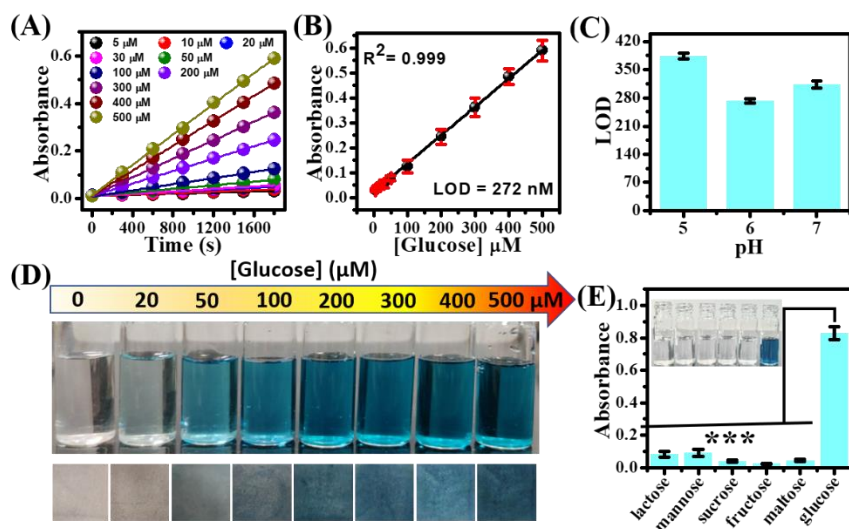

Figure 6.15. (A) Changes in the absorbance of TMB monitored at 652 nm as a function of time and (B) linear plot showing concentration dependent response of Au@QD-D toward TMB oxidation on varying the concentration of glucose (0–500 µM) at pH 6. (C) Bar graph showing LOD of glucose via GOx/Au@QD-D system at different pH. (D) Daylight photographs depicting the colour change in aqueous solution (upper panel) and paper strip (lower panel) for TMB oxidation

on varying the glucose concentration (0–500 μM). (E) Selective response of Au@QD-D toward different sugars. The data represent the mean ± SEM for three (n = 3) independent experiments. Statistical significance was assessed by a two-tailed, unpaired Student's t-test with the three-asterisk symbol (***) representing a P value of < 0.001.

The intrinsic green fluorescence signals from QD-Ds colocalize with the red fluorescence signals from RBITC-labeled GOx, indicating successful sequestration of GOx inside the QD-Ds (Figure 6.14D). Importantly, the DIC image reveals that the morphology of QD-Ds remains unaltered upon GOx sequestration. On the other hand, the presence of Au NPs in Au@QD-Ds results in complete quenching of the fluorescence signals from both QD and RBITC possibly due to the nonradiative energy transfer at the surface of Au NPs (Figure 6.14D). Nevertheless, our findings reveal the successful sequestration of GOx inside the Au@QD- Ds.

The colorimetric assay was performed using TMB as a substrate in the presence of glucose and oxygen inside the GOx-loaded Au@QD-Ds. The time-dependent changes in the absorbance of ox-TMB at 652 nm were monitored in the presence of different concentrations of glucose (0−500 μM) at pH = 6 (Figure 6.15A). Figure 6.15B shows a linear increase in the absorbance at 652 nm over a range of 0−500 μM glucose concentrations with a slope of 1.1×10^{-3} μmol^{-1}L. The estimated LOD of glucose is 272 nM, which is superior or comparable to most of the previously reported nanozymatic systems (Table 6.1) *[12, 18, 26, 28–30, 49–59]*. Earlier, Rana and co-workers fabricated a bioinspired coacervate assembly using polyallylamine and citrate ions and demonstrated efficient peroxidase-mimicking activity of surface-anchored polyoxometalate (POM) nanoclusters with a LOD of 0.31 mM for glucose *[60]*. Our estimated LOD is dependent on the solution pH and the present system shows the highest sensitivity at pH = 6 (Figure 6.15C). These spectral changes are accompanied by a gradual color change of the solution from colorless to blue as a function of glucose concentrations (Figure 6.15D, upper panel).

Table 6.1. List of recently reported nanozymes for glucose detection

S. No.	Nanozymes	Detection Range	LOD	Ref. No.
1	Au_xPd_{100-x} nanocomposites	5–400 µM	0.85 µM	12
2	reduced Co_3O_4 nanoparticles	1–20 µM	0.32 µM	18
3	modified g-C_3N_4	0–1 M	0.8 µM	26
4	MOF-808	5.7–1700 µM	5.7 µM	28
5	Fe-MOF-GOx	1–500 µM	0.487 µM	29
6	BioMOF-NPs	5–25 µM	1.9 µM	30
7	resorcinol–formaldehyde (RF) resins	200–8500 µM	9.2 µM	49
8	B,N-Doped PdRu Aerogels	10–2000 µM	6 µM	50
9	GOx@CuBDC MOF	10–500 µM	4.1 µM	51
10	$CePO_4$–CeO_2 composite nanorods	0–100 µM	4.1 µM	52
11	Au@WSe_2	10–500 µM	3.66 µM	53
12	Mn_2O_3 hollow nanoparticles	100–1000 µM	2.31 µM	54
13	MnO_2 nanoflakes	0–1000 µM	1 µM	55
14	GOx@HP-MIL-88B-BA	2–100 µM	0.98 µM	56
15	Fe-GDY/GOx	5–160 µM	0.89 µM	57
16	Cu^{2+}–C_3N_4 nanosheets	5–1200 µM	0.71 µM	58
17	$Ni_{60}Nb_{40}$ nanoglass	250–4000 µM	0.1 µM	59
18	**GOx/Au@QD-Ds**	**0–500 µM**	**0.27 µM**	**Present Work**

Notably, colorimetric signals appear within 60 s after the addition of glucose. Similar changes in the colorimetric signals have also been observed on composite-loaded Whatman filter paper as a function of glucose concentrations (Figure 6.15D, lower panel). The above findings reveal a rapid and sensitive colorimetric response of GOx-loaded Au@QD-D composites toward glucose sensing in solution as well as on paper strip. Importantly, the spectral and colorimetric responses of the GOx-loaded Au@QD-D composite are highly selective toward glucose (Figure 6.15E). Negligible changes in the spectral and colorimetric signals have been observed in the presence of different analogues of glucose like maltose, lactose, mannose, sucrose, and fructose (Figure 6.15E inset). Taken together, we have developed a robust and facile methodology for the fabrication of a composite bioplatform with inherent peroxidase-mimicking activity for the selective and ultrasensitive detection of glucose in solution as well as

on solid support. The present approach may be further utilized for the fabrication of a wide range of composite systems with inherent enzyme-mimicking activity and may find importance in various analytical and diagnostic applications.

6.3. Conclusions

In summary, we have developed a robust and facile approach for the fabrication of a new class of coacervate-based plexcitonic assembly with inherent peroxidase-mimicking activity. We have utilized QD-Ds both as a scaffold and reducing matrix for the synthesis of 5.6 ± 0.2 nm-sized Au NPs. The in situ fabricated Au@QD-Ds exhibit remarkable peroxidase-mimicking activity for the oxidation of various organic substrates in the presence of H_2O_2. The kinetic analyses reveal typical Michaelis−Menten behavior with K_m values of 0.21 and 0.28 mM for TMB and H_2O_2, respectively. The enhanced peroxidase-like activity of Au@QD-Ds has been accounted by considering efficient substrate channeling as well as due to the ligand-free environment of Au NPs inside the membraneless compartment. Our mechanistic study reveals the active role of fast electron transfer from TMB to H_2O_2 via Au NPs inside the Au@QD-Ds. Finally, we have designed a composite bioplatform with GOx-loaded Au@QD-Ds for the colorimetric sensing of glucose in solution as well as in the solid phase with a LOD of 272 nM. Our present study highlights a facile and efficient strategy for the fabrication of robust nanozymes that may find importance in various analytical, optoelectronic, and biosensing applications.

Note: This is copyrighted material with permission of the American Chemical Society.

6.4. References

1. Knowles J. R. (1991), Enzyme catalysis: not different, just better, Nature, 350, 121−124. (DOI:10.1038/350121a0)
2. Callender R., Dyer R. B. (2015), The dynamical nature of enzymatic catalysis, Acc. Chem. Res., 48, 407−413. (DOI:10.1021/ar5002928)

3. Hauer B. (2020), Embracing nature's catalysts: a viewpoint on the future of biocatalysis, ACS Catal., 10, 8418−8427. (DOI:10.1021/acscatal.0c01708)

4. Wu J., Wang X., Wang Q., Lou Z., Li S., Zhu Y., Qin L., Wei H. (2019), Nanomaterials with enzyme-like characteristics (nanozymes): next-generation artificial enzymes (II), Chem. Soc. Rev., 48, 1004−1076. (DOI:10.1039/C8CS00457A)

5. Qiu N., Liu Y., Guo R. (2020), Electrodeposition-assisted rapid preparation of Pt nanocluster/3D graphene hybrid nanozymes with outstanding multiple oxidase-like activity for distinguishing colorimetric determination of dihydroxybenzene isomers, ACS Appl. Mater. Interfaces, 12, 15553−15561. (DOI:10.1021/acsami.9b23546)

6. Kim M. S., Cho S., Joo S. H., Lee J., Kwak S. K., Kim M. I., Lee J. (2019), N- and B-codoped graphene: a strong candidate to replace natural peroxidase in sensitive and selective bioassays, ACS Nano, 13, 4312−4321. (DOI:10.1021/acsnano.8b09519)

7. Wu G., Berka V., Derry P. J., Mendoza K., Kakadiaris E., Roy T., Kent T. A., Tour J. M., Tsai A. L. (2019), Critical comparison of the superoxide dismutase-like activity of carbon antioxidant nanozymes by direct superoxide consumption kinetic measurements, ACS Nano, 13, 11203−11213. (DOI:10.1021/acsnano.9b04229)

8. Hu M., Korschelt K., Daniel P., Landfester K., Tremel W., Bannwarth M. B. (2017), Fibrous nanozyme dressings with catalase-like activity for H_2O_2 reduction to promote wound healing, ACS Appl. Mater. Interfaces, 9, 38024−38031. (DOI:10.1021/acsami.7b12212)

9. Hu L., Liao H., Feng L., Wang M., Fu W. (2018), Accelerating the peroxidase-like activity of gold nanoclusters at neutral pH for colorimetric detection of heparin and heparinase activity, Anal. Chem., 90, 6247−6252. (DOI:10.1021/acs.analchem.8b00885)

10. Luo L., Su Z., Zhuo J., Huang L., Nian Y., Su L., Zhang W., Wang J. (2020), Copper-sensitized "turn on" peroxidase-like activity of

MMoO$_4$ (M = Co, Ni) flowers for selective detection of aquatic copper ions, ACS Sustain. Chem. Eng., 8, 12568−12576. (DOI:10.1021/acssuschemeng.0c03822)

11. Tan X., Yang Q., Sun X., Sun P., Li H. (2022), PdIr aerogels with boosted peroxidase-like activity for a sensitive total antioxidant capacity colorimetric bioassay, ACS Appl. Mater. Interfaces, 14, 10047−10054. (DOI:10.1021/acsami.1c22625)

12. Cai S., Fu Z., Xiao W., Xiong Y., Wang C., Yang R. (2020), Zero-dimensional/two-dimensional Au$_x$Pd$_{100-x}$ nanocomposites with enhanced nanozyme catalysis for sensitive glucose detection, ACS Appl. Mater. Interfaces, 12, 11616−11624. (DOI:10.1021/acsami.9b21621)

13. Adeniyi O., Sicwetsha S., Mashazi P. (2020), Nanomagnet-silica nanoparticles decorated with Au@Pd for enhanced peroxidase-like activity and colorimetric glucose sensing, ACS Appl. Mater. Interfaces, 12, 1973−1987. (DOI:10.1021/acsami.9b15123)

14. Ding Y., Yang B., Liu H., Liu Z., Zhang X., Zheng X., Liu Q. (2018), FePt-Au ternary metallic nanoparticles with the enhanced peroxidase-like activity for ultrafast colorimetric detection of H$_2$O$_2$, Sens. Actuators B, 259, 775−783. (DOI:10.1016/j.snb.2017.12.115)

15. Cai S., Jia X., Han Q., Yan X., Yang R., Wang C. (2017), Porous Pt/Ag nanoparticles with excellent multifunctional enzyme mimic activities and antibacterial effects, Nano Res., 10, 2056−2069. (DOI:10.1007/s12274-016-1395-0)

16. Li H., Wen Y., Zhu X., Wang J., Zhang L., Sun B. (2020), Novel heterostructure of a MXene@NiFe-LDH nanohybrid with superior peroxidase-like activity for sensitive colorimetric detection of glutathione, ACS Sustain. Chem. Eng., 8, 520−526. (DOI:10.1021/acssuschemeng.9b05987)

17. Xie Y., Qian Y., Li Z., Liang Z., Liu W., Yang D., Qiu X. (2021), Near-Infrared-activated efficient bacteria-killing by lignin-based copper sulfide nanocomposites with an enhanced photothermal effect and peroxidase-like activity, ACS Sustain. Chem. Eng., 9, 6479−6488. (DOI:10.1021/acssuschemeng.1c01589)

18. Lu J., Zhang H., Li S., Guo S., Shen L., Zhou T., Zhong H., Wu L., Meng Q., Zhang Y. (2020), Oxygen-vacancy-enhanced peroxidase-like activity of reduced Co_3O_4 nanocomposites for the colorimetric detection of H_2O_2 and glucose, Inorg. Chem., 59, 3152−3159. (DOI:10.1021/acs.inorgchem.9b03512)

19. Gao L., Zhuang J., Nie L., Zhang J., Zhang Y., Gu N., Wang T., Feng J., Yang D., Perrett S., Yan X. (2007), Intrinsic peroxidase-like activity of ferromagnetic nanoparticles, Nat. Nanotechnol., 2, 577−583. (DOI:10.1038/nnano.2007.260)

20. Zhao H., Dong Y., Jiang P., Wang G., Zhang J. (2015), Highly dispersed CeO_2 on TiO_2 nanotube: a synergistic nanocomposite with superior peroxidase-like activity, ACS Appl. Mater. Interfaces, 7, 6451−6461. (DOI:10.1021/acsami.5b00023)

21. Nagvenkar A. P., Gedanken A. (2016), $Cu_{0.89}Zn_{0.11}O$, a new peroxidase-mimicking nanozyme with high sensitivity for glucose and antioxidant detection, ACS Appl. Mater. Interfaces, 8, 22301−22308. (DOI:10.1021/acsami.6b05354)

22. Ding W., Liu H., Zhao W., Wang J., Zhang L., Yao Y., Yao C., Song C. (2020), A hybrid of FeS_2 nanoparticles encapsulated by two-dimensional carbon sheets as excellent nanozymes for colorimetric glucose detection, ACS Appl. Bio Mater., 3, 5905−5912. (DOI:10.1021/acsabm.0c00605)

23. Ali S. R., De M. (2021), Thiolated ligand-functionalized MoS_2 nanosheets for peroxidase-like activities, ACS Appl. Nano Mater., 4, 12682−12689. (DOI:10.1021/acsanm.1c03242)

24. Deng H. H., Luo B. Y., He S. B., Chen R. T., Lin Z., Peng H. P., Xia X. H., Chen W. (2019), Redox recycling-triggered peroxidase-like activity enhancement of bare gold nanoparticles for ultrasensitive colorimetric detection of rare-earth Ce^{3+} ion, Anal. Chem., 91, 4039−4046. (DOI:10.1021/acs.analchem.8b05552)

25. Chen H., Yuan C., Yang X., Cheng X., Elzatahry A. A., Alghamdi A., Su J., He X., Deng Y. (2020), Hollow mesoporous carbon nanospheres loaded with Pt nanoparticles for colorimetric detection

of ascorbic acid and glucose, ACS Appl. Nano Mater., 3, 4586−4598. (DOI:10.1021/acsanm.0c00638)

26. Zhang P., Sun D., Cho A., Weon S., Lee S., Lee J., Han J. W., Kim D. P., Choi W. (2019), Modified carbon nitride nanozyme as bifunctional glucose oxidase-peroxidase for metal-free bioinspired cascade photocatalysis, Nat. Commun., 10, 940. (DOI:10.1038/s41467-019-08731-y)

27. Fan Y., Zhang W., Liu Y., Zeng Z., Quan X., Zhao H. (2019), Three-dimensional branched crystal carbon nitride with enhanced intrinsic peroxidase-like activity: a hypersensitive platform for colorimetric detection, ACS Appl. Mater. Interfaces, 11, 17467− 17474. (DOI:10.1021/acsami.9b04320)

28. Zheng H. Q., Liu C. Y., Zeng X. Y., Chen J., Lü J., Lin R. G., Cao R., Lin Z. J., Su J. W. (2018), MOF-808: a metal-organic framework with intrinsic peroxidase-like catalytic activity at neutral pH for colorimetric biosensing, Inorg. Chem., 57, 9096−9104. (DOI:10.1021/acs.inorgchem.8b01097)

29. Xu W., Jiao L., Yan H., Wu Y., Chen L., Gu W., Du D., Lin Y., Zhu C. (2019), Glucose oxidase-integrated metal-organic framework hybrids as biomimetic cascade nanozymes for ultrasensitive glucose biosensing, ACS Appl. Mater. Interfaces, 11, 22096− 22101. (DOI:10.1021/acsami.9b03004)

30. Yang Y., Gong Y., Li X., Li M., Wei Q., Zhou B., Zhang J. (2022), Alkaline-stable peroxidase mimics based on biological metal-organic frameworks for recyclable scavenging of hydrogen peroxide and detecting glucose in apple fruits, ACS Sustain. Chem. Eng., 10, 10685−10698. (DOI:10.1021/acssuschemeng.2c03184)

31. Liu C., Cai Y., Wang J., Liu X., Ren H., Yan L., Zhang Y., Yang S., Guo J., Liu A. (2020), Facile preparation of homogeneous copper nanoclusters exhibiting excellent tetraenzyme mimetic activities for colorimetric glutathione sensing and fluorimetric ascorbic acid sensing, ACS Appl. Mater. Interfaces, 12, 42521−42530. (DOI:10.1021/acsami.0c11983)
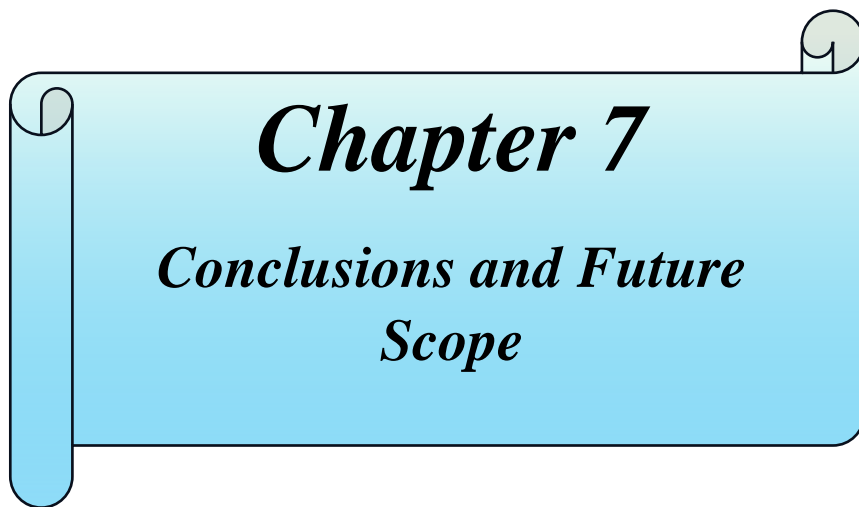
32. Ivanova M. N., Grayfer E. D., Plotnikova E. E., Kibis L. S., Darabdhara G., Boruah P. K., Das M. R., Fedorov V. E. (2019). Pt-decorated boron nitride nanosheets as artificial nanozyme for detection of dopamine, ACS Appl. Mater. Interfaces, 11, 22102−22112. (DOI:10.1021/acsami.9b04144)

33. Wang J., Hu Y., Zhou Q., Hu L., Fu W., Wang Y. (2019), Peroxidase-like activity of metal-organic framework [Cu(PDA)-(DMF)] and its application for colorimetric detection of dopamine, ACS Appl. Mater. Interfaces, 11, 44466−44473. (DOI:10.1021/acsami.9b17488)

34. Vaishnav J. K. Mukherjee T. K. (2019), Highly photostable and two-photon active quantum dot-polymer multicolor hybrid coacervate droplets, Langmuir, 35, 11764−11773. (DOI:10.1021/acs.langmuir.9b01783)

35. Saini B., Singh S., Mukherjee T. K. (2021), Nanocatalysis under nanoconfinement: a metal-free hybrid coacervate nanodroplet as a catalytic nanoreactor for efficient redox and photocatalytic reactions, ACS Appl. Mater. Interfaces, 13, 51117−51131. (DOI:10.1021/acsami.1c17106)

36. Saini B., Singh R. R., Nayak D., Mukherjee T. K. (2020), Biocompatible pH-responsive luminescent coacervate nanodroplets from carbon dots and poly(diallyldimethylammonium chloride) toward theranostic applications, ACS Appl. Nano Mater., 3, 5826−5837. (DOI:10.1021/acsanm.0c00995)

37. Saini B., Singh R., Mukhopadhyay S., Mukherjee T. K. (2021), Specific loading and in vitro controlled release of a Ru-based hydrophobically encapsulated model anticancer drug inside nanoassemblies toward stimuli-responsive drug delivery, ACS Appl. Nano Mater., 4, 2037−2051. (DOI:10.1021/acsanm.0c03356)

38. Singh S., Vaishnav J. K., Mukherjee T. K. (2020), Quantum dot-based hybrid coacervate nanodroplets for ultrasensitive detection of Hg^{2+}, ACS Appl. Nano Mater., 3, 3604−3612. (DOI:10.1021/acsanm.0c00317)

39. Singh S., Rao C., Nandi C. K., Mukherjee T. K. (2022), Quantum dot-embedded hybrid photocatalytic nanoreactors for visible light photocatalysis and dye degradation, ACS Appl. Nano Mater., 5, 7427−7439. (DOI:10.1021/acsanm.2c01446)

40. Jose R., Biju V., Yamaoka Y., Nagase T., Makita Y., Shinohara Y., Baba Y., Ishikawa M. (2004), Synthesis of CdTe quantum dots using a heterogeneous process at low temperature and their optical and structural properties, Appl. Phys. A: Mater. Sci. Process., 79, 1833−1838. (DOI:10.1007/s00339-004-2937-y)

41. Vaishnav J. K., Mukherjee T. K. (2018), Long-range resonance coupling-induced surface energy transfer from CdTe quantum dot to plasmonic nanoparticle, J. Phys. Chem. C, 122, 28324− 28336. (DOI:10.1021/acs.jpcc.8b08757)

42. Shen M., Jia W., You Y., Hu Y., Li F., Tian S., Li J., Jin Y., Han D. (2013), Luminescent properties of CdTe quantum dots synthesized using 3-mercaptopropionic acid reduction of tellurium dioxide directly, Nanoscale Res. Lett., 8, 253. (DOI:10.1186/1556-276X-8-253)

43. Divya K. P., Miroshnikov M., Dutta D., Vemula P. K., Ajayan P. M., John G. (2016), In situ Synthesis of metal nanoparticle embedded hybrid soft nanomaterials, Acc. Chem. Res. 49, 1671−1680. (DOI:10.1021/acs.accounts.6b00201)

44. Zinchenko A., Miwa Y., Lopatina L. I., Sergeyev V. G., Murata S. (2014), DNA hydrogel as a template for synthesis of ultrasmall gold nanoparticles for catalytic applications, ACS Appl. Mater. Interfaces, 6, 3226−3232. (DOI:10.1021/am5008886)

45. Lin G., Xian L., Zhou X., Wang S., Shah Z. H., Edwards S. A., Gao Y. (2020), Design and one-pot synthesis of capsid-like gold colloids with tunable surface roughness and their enhanced sensing and catalytic performances, ACS Appl. Mater. Interfaces, 12, 50152−50160. (DOI:10.1021/acsami.0c14802)

46. Chen L. W., Hao Y. C., Guo Y., Zhang Q., Li J., Gao W. Y., Ren L., Su X., Hu L., Zhang N., Li S., Feng X., Gu L., Zhang Y. W., Yi A. X., Wang B. (2021), Metal-organic framework membranes

encapsulating gold nanoparticles for direct plasmonic photocatalytic nitrogen fixation, J. Am. Chem. Soc., 143, 5727−5736. (DOI:10.1021/jacs.0c13342)

47. Yang Y., Shen D. Long Y., Xie Z., Zheng H. (2017), Intrinsic peroxidase-like activity of ficin, Sci. Rep., 7, 43141. (DOI:10.1038/srep43141)

48. Zhang D., Han Q., Liu W., Xu K., Shao M., Li Y., Du P., Zhang Z., Liu B., Zhang L., Lu X. (2022), Au-decorated N-rich carbon dots as peroxidase mimics for the detection of acetylcholinesterase activity, ACS Appl. Nano Mater., 5, 1958−1965. (DOI:10.1021/acsanm.1c03613)

49. Pramanik K., Sengupta P., Majumder B., Datta P., Sarkar P. (2020), Artificial bifunctional photozyme of glucose oxidase-peroxidase for solar-powered glucose-peroxide detection in a biofluid with resorcinol-formaldehyde polymers, ACS Appl. Mater. Interfaces, 12, 36948–36956. (DOI:10.1021/acsami.0c10973)

50. Zeng Y., Li Y., Tan X., Gong J., Wang Z., An Y., Wang Z., Li H. (2021), B,N-doped PdRu aerogels as high-performance peroxidase mimics for sensitive detection of glucose, ACS Appl. Mater. Interfaces, 13, 36816–36823. (DOI:10.1021/acsami.1c07987)

51. Cheng X., Zheng Z., Zhou X., Kuang Q. (2020), Metal-organic framework as a compartmentalized integrated nanozyme reactor to enable high-performance cascade reactions for glucose detection, ACS Sustain. Chem. Eng., 8, 17783–17790. (DOI:10.1021/acssuschemeng.0c06325)

52. Vinothkumar G., Lalitha A. I., Suresh Babu K. (2019), Cerium phosphate-cerium oxide heterogeneous composite nanozymes with enhanced peroxidase-like biomimetic activity for glucose and hydrogen peroxide sensing, Inorg. Chem., 58, 349–358. (DOI: 10.1021/acs.inorgchem.8b02423)

53. Hong C., Chen L., Wu C., Yang D., Dai J. Y., Huang Z., Cai R., Tan W. (2022), Green synthesis of Au@WSe$_2$ hybrid nanostructures with the enhanced peroxidase-like activity for sensitive

colorimetric detection of glucose, Nano Res., 15, 1587–1592. (DOI: 10.1007/s12274-021-3706-3)

54. Kang Z. W., Kankala R. K., Chen B. Q., Fu C. P., Wang S. B., Chen A. Z. (2019), Supercritical fluid-assisted fabrication of manganese (III) oxide hollow nanozymes mediated by polymer nanoreactors for efficient glucose sensing characteristics, ACS Appl. Mater. Interfaces, 11, 28781–28790. (DOI:10.1021/acsami.9b05688)

55. Han L., Zhang H., Chen D., Li F. (2018), Protein-directed metal oxide nanoflakes with tandem enzyme-like characteristics: colorimetric glucose sensing based on one-pot enzyme-free cascade catalysis, Adv. Funct. Mater., 28, 1–9. (DOI: 10.1002/adfm.201800018)

56. Zhao Z., Huang Y., Liu W., Ye F., Zhao S. (2020), Immobilized glucose oxidase on boronic acid-functionalized hierarchically porous MOF as an integrated nanozyme for one-step glucose detection, ACS Sustain. Chem. Eng., 8, 4481–4488. (DOI: 10.1021/acssuschemeng.9b07631)

57. Liu J., Shen X., Baimanov D., Wang L., Xiao Y., Liu H., Li Y., Gao X., Zhao Y., Chen C. (2019), Immobilized ferrous ion and glucose oxidase on graphdiyne and its application on one-step glucose detection, ACS Appl. Mater. Interfaces, 11, 2647–2654. (DOI: 10.1021/acsami.8b03118)

58. Qu L., Fang X., Xie T., Xu H., Yang G., Liu W. (2022), Nanozyme-catalyzed cascade reactions for high-sensitive glucose sensing and efficient bacterial killing, Sensors Actuators B Chem., 353, 131156. (DOI: 10.1016/j.snb.2021.131156)

59. Bag S., Baksi A., Nandam S. H., Wang D., Ye X., Ghosh J., Pradeep T., Hahn H. (2020), Nonenzymatic glucose sensing using $Ni_{60}Nb_{40}$ nanoglass, *ACS Nano*, *14*, 5543– 5552. (DOI: 10.1021/acsnano.9b09778)

60. Nayak J., Chilivery R., Kumar A. K., Begum G., Rana R. K. (2021), A bioinspired assembly to simultaneously heterogenize polyoxometalates as nanozymes and encapsulate enzymes in a

microstructure endowing efficient peroxidase-mimicking activity, ACS Sustain. Eng., 9, 15819−15829. (DOI:10.1021/acssuschemeng.1c05238)

Chapter 7

Conclusions and Future Scope

7.1. Conclusions

Nature utilizes cellular and subcellular compartmentalization to efficiently drive various complex chemical and biological transformations via spatiotemporal control. In this context, designing of new multifunctional self-assembled structures such as micelles, polymersomes, liposomes, plasmonic dendrimers, vesicles, hydrogels, metal-organic frameworks, polymeric nanoparticles, and coacervate droplets have gained tremendous importance in recent times. Here in this thesis, we have designed optically active micelles by integrating the charged aqueous interfaces of micelles with optically active organic dye, eosin Y (EY). Furthermore, we have also designed and formulated different types of synthetic hybrid coacervate droplets via LLPS between different optically active nanoparticles such as QDs, CDs, and Au NPs and organic polymers such as PDADMAC. The NP-embedded optically active hybrid coacervates were utilized for environmental remediation and catalysis. The overall conclusion of the thesis work is listed below;

Chapter three highlights the tremendous potential of the charged aqueous interface of micelles for boosting the POC of arylamines in aqueous medium. The approach showed a broad substrate scope with excellent yields (up to 100%), fast kinetics (4 h), and 100% selectivity under ambient air atmosphere in aqueous medium without any unwanted byproducts. The CAI not only acts as an efficient host for an ultrafast non-diffusive PET, but also modulates the redox potentials in a favorable manner. The present methodology may find wide-ranging implications in the chemical and pharmaceutical industries.

Chapter four demonstrates a simple organic−inorganic hybrid nanocomposite-based sensing platform for the ultrasensitive detection and efficient sequestration of Hg^{2+} ions from contaminated water. The intrinsically luminescent membraneless coacervate droplets (G-Ds and R-Ds) have been fabricated from two different-sized MSA-capped

QDs (QD^{523} and QD^{666}) in the presence of PDADMAC in aqueous medium. Significant PL quenching of these hybrid droplets has been observed in the presence of Hg^{2+}. This PL quenching is highly selective toward Hg^{2+}, and other metal ions do not interfere in the sensing process. Our findings demonstrate that Hg^{2+} ions specifically associate with the free carboxylate groups of MSA ligands at the surface of QDs embedded inside the droplets via electrostatic interactions and undergo ultrafast PET. The estimated LOD for Hg^{2+} sensing with the present system is 1.32 nM (0.26 ppb), which is significantly lower than the maximum allowable contamination level of Hg^{2+} ions in drinking water (2 ppb). Furthermore, we have demonstrated that our present hybrid droplets efficiently sequester trace amounts of Hg^{2+} from contaminated water by simple centrifugation techniques. Taken together, our findings reveal that colloidally stable and intrinsically luminescent hybrid coacervate droplets have tremendous potential for practical applications toward Hg^{2+} detection as well as remediation technology.

In chapter five, we have demonstrated the utilization of NP-embedded coacervate droplets as a new class of photocatalytic nanoreactor with multiple embedded QDs/CDs as catalytic sites for the visible light-driven photoredox conversion of ferricyanide to ferrocyanide. Notably, the photoredox conversion was incompatible in the presence of bare QDs/CDs, However an efficient conversion of ferricyanide to ferrocyanide was observed in QD- and CD-Ds signifying that these droplets can even drive the incompatible reactions to completion in their unique microenvironment. Interestingly, the QD- and CD-Ds exhibited different photocatalytic activity with 80 and 60% conversion yields, respectively for the photoredox conversion of ferricyanide to ferrocyanide. The change in photocatalytic efficacy of both the droplets signifies the importance of embedded NPs inside the droplets. These results further signifies that the optoelectronic properties of these hybrid coacervates are highly tunable and one can tune them simply by changing the NPs inside the droplets.

Subsequently, the QD-Ds have been utilized for the photocatalytic degradation of RhB and MB. An enhanced photocatalytic degradation of RhB and MB have been achieved inside the QD-Ds in comparision to bare QDs in the presence of H_2O_2. The membrane-less architecture of these droplets provides an ideal environment to carry out the photocatalytic conversion inside its confined structure via preferential sequestration of ferricyanide and organic dyes. The enhanced photoredox activity of the present QD-Ds toward ferricyanide to ferrocyanide conversion has been explained on the basis of altered surface charge density of embedded QDs/CDs inside the droplets and increased concentrations of ferricyanide, while the enhanced photodegradation of dyes arises mainly due to the increased local concentrations of sequestered dyes. Our results indicate the participation of photogenerated electrons and holes from the embedded QDs/CDs for the observed photocatalytic transformations inside the droplets. Moreover, we have illustrated that the present droplets can be recycled for several consecutive cycles without any detrimental effects. This work paves the way for next-generation hybrid photocatalytic nanoreactors toward a wide spectrum of photochemical conversions.

In chapter six, we have developed a robust and facile approach for the fabrication a new class of coacervate-based plexcitonic assembly with inherent peroxidase-mimicking activity. We have utilized QD-Ds both as a scaffold and reducing matrix for the synthesis of 5.6 ± 0.2 nm-sized Au NPs. The in situ fabricated Au@QD-Ds exhibit remarkable peroxidase-mimicking activity for the oxidation of various organic substrates in the presence of H_2O_2. The kinetic analyses reveal typical Michaelis−Menten behavior with K_m values of 0.21 and 0.28 mM for TMB and H_2O_2, respectively. The enhanced peroxidase-like activity of Au@QD-Ds has been accounted by considering efficient substrate channeling as well as due to the ligand-free environment of Au NPs inside the membraneless compartment. Our mechanistic study reveals the active role of fast electron transfer

from TMB to H2O2 via Au NPs inside the Au@QD-Ds. Finally, we have designed a composite bioplatform with GOx-loaded Au@QD-Ds for the colorimetric sensing of glucose in solution as well as in the solid phase with a LOD of 272 nM. Our present study highlights a facile and efficient strategy for the fabrication of robust nanozymes and may find importance in various analytical, optoelectronic, and biosensing applications.

7.2. Scope for future work

The present thesis highlights the photophysical properties of optically active micelles and coacervates toward environmental remediation and catalytic applications. These studies further pave the way for the development of different optically active micelles and coacervates to carry out a wide range of applications.

Chapter three highlights the tremendous potential of the charged aqueous interface of CTAB micelles for boosting the POC of arylamines using EY in the aqueous medium. The present study can be easily extended to different micellar and photocatalyst systems to drive a wide range of organic transformations. Moreover, the role of different shapes of micelles can be explored to boost the photocatalytic efficacy of various organic transformations.

Chapters 3 – 6 highlight the utilization of NP-embedded hybrid coacervates toward environmental remediation and catalytic transformation. These studies pave the way for formulating and studying a wide range of hybrid self-assembled nanostructures with various ligand-capped NPs such as Au, Pd, Pt, CDs, QDs, NCs, etc. The unique properties of these NP-embedded coacervates can expand their applicability in nanocatalysis, enzyme catalysis, biosensing, and bioimaging. Furthermore, their confined and membraneless architecture can be utilized for the in situ synthesis of a wide variety of NPs and tune the optoelectronic properties of these hybrid coacervates towards catalytic and enzymatic applications.

Appendix A

List of ^{1}H and ^{13}C NMR data
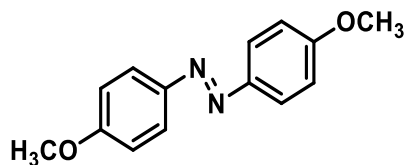
The isolated product was red solid, 11.5 mg, 94% yield. ^{1}H NMR (500 MHz, Chloroform-*d*) δ 7.95 (d, *J* = 8.9 Hz, 4H), 7.02 (d, 4H), 3.90 (s, 6H).^{13}C NMR (126 MHz, CDCl$_3$) δ 161.82, 146.55, 124.59, 114.25, 55.59.
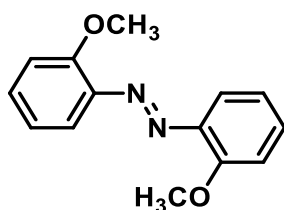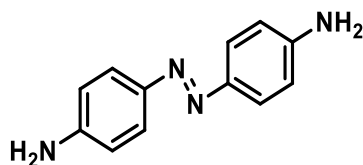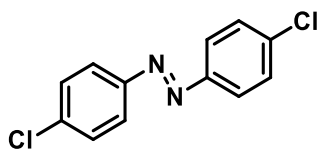

The isolated product was red solid, 11.0 mg, 90% yield. ^{1}H NMR (400 MHz, Chloroform-*d*) δ 7.63 (d, *J* = 7.8 Hz, 2H), 7.43 (t, *J* = 7.6 Hz, 2H), 7.08 (d, *J* = 8.3 Hz, 2H), 7.00 (t, 2H), 4.01 (s, 6H). ^{13}C NMR (101 MHz, CDCl$_3$) δ 156.57, 142.69, 131.92, 120.55, 117.28, 112.25, 56.06.
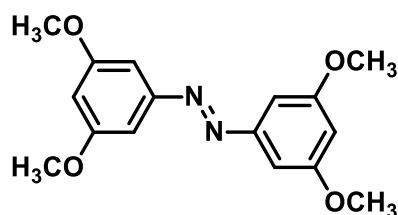
The isolated product was red solid, 14.1 mg, 92% yield. ^{1}H NMR (500 MHz, Chloroform-*d*) δ 7.15 (s, 4H), 6.60 (s, 2H), 3.88 (s, 12H). ^{13}C NMR (126 MHz, CDCl$_3$) δ 160.82, 154.01, 103.77, 100.67, 55.34.
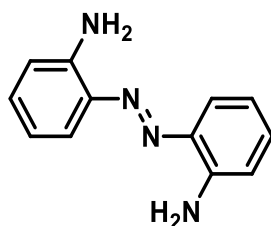

The isolated product was yellow solid, 9.2 mg, 86% yield. ^{1}H NMR (500 MHz, Chloroform-*d*) δ 7.69 (d, *J* = 8.0 Hz, 2H), 7.19 (t, 2H), 6.80 (t, 2H), 6.77 (d, 2H), 5.49 (s, 4H). ^{13}C NMR (126 MHz, CDCl$_3$) δ 142.89, 137.50, 131.16, 124.07, 117.43, 116.82.

The isolated product was a reddish-orange solid, 9.6 mg, 89% yield. ^{1}H NMR (500 MHz, Chloroform-*d*) δ 7.74 (d, *J* = 8.7 Hz, 4H), 6.74 (d, *J* = 8.7 Hz, 4H). ^{13}C NMR (126 MHz, CDCl$_3$) δ 148.75, 146.04, 124.59, 115.02.
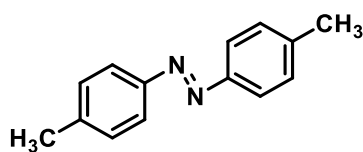
The isolated product was a yellow solid, 10 mg, 94% yield. ^{1}H NMR (500 MHz, Chloroform-*d*) δ 7.83 (d, *J* = 8.3 Hz, 4H), 7.32 (d, *J* = 8.1 Hz, 4H), 2.44 (s, 6H). ^{13}C NMR (126 MHz, CDCl$_3$) δ 151.09, 141.48, 129.98, 122.99, 21.75.
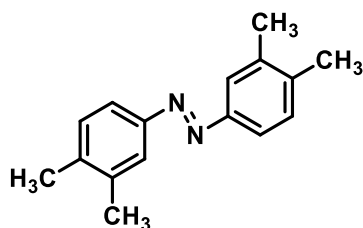
The isolated product was an orange solid, 10.8 mg, 89% yield. ^{1}H NMR (500 MHz, Chloroform-*d*) δ 7.61 (s, 2H), 7.59 (d, *J* = 8.0 Hz, 2H), 7.19 (d, *J* = 7.8 Hz, 2H), 2.28 (s, 6H), 2.26 (s, 6H). ^{13}C NMR (126 MHz, CDCl$_3$) δ 150.79, 139.45, 136.95, 129.82, 122.90, 120.31, 19.46.
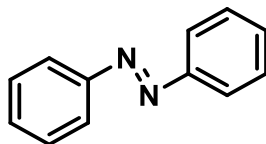
The isolated product was an orange solid, 8.2 mg, 89% yield. ^{1}H NMR (500 MHz, Chloroform-*d*) δ 7.94 (d, *J* = 8.5 Hz, 4H), 7.54 – 7.51 (m, 4H), 7.49 – 7.46 (m, 2H). ^{13}C NMR (126 MHz, CDCl$_3$) δ 152.53, 130.85, 128.95, 122.71.

The isolated product was yellow solid, 11.3 mg, 89% yield. ^{1}H NMR (500 MHz, Chloroform-d) δ 7.87 (d, J = 8.7 Hz, 4H), 7.50 (d, 4H). ^{13}C NMR (126 MHz, CDCl$_3$) δ 150.78, 137.22, 129.39, 124.18.
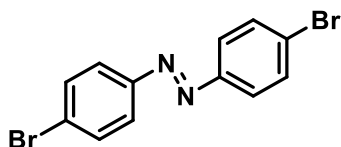
The isolated product was an orange solid, 14.6 mg, 85% yield. ^{1}H NMR (500 MHz, Chloroform-d) δ 7.80 (d, J = 8.7 Hz, 4H), 7.66 (d, J = 8.7 Hz, 4H). ^{13}C NMR (126 MHz, CDCl$_3$) δ 151.13, 132.39, 125.75, 124.40.
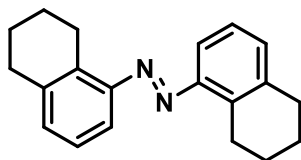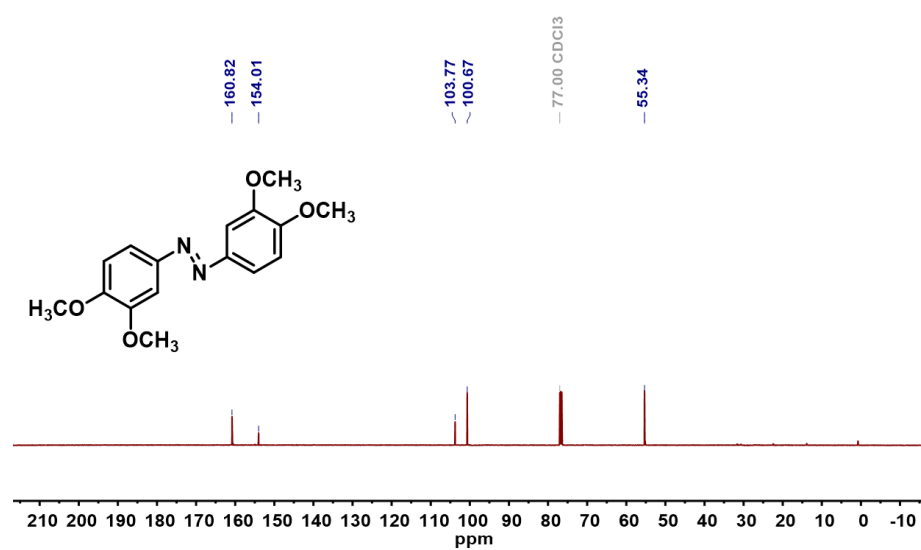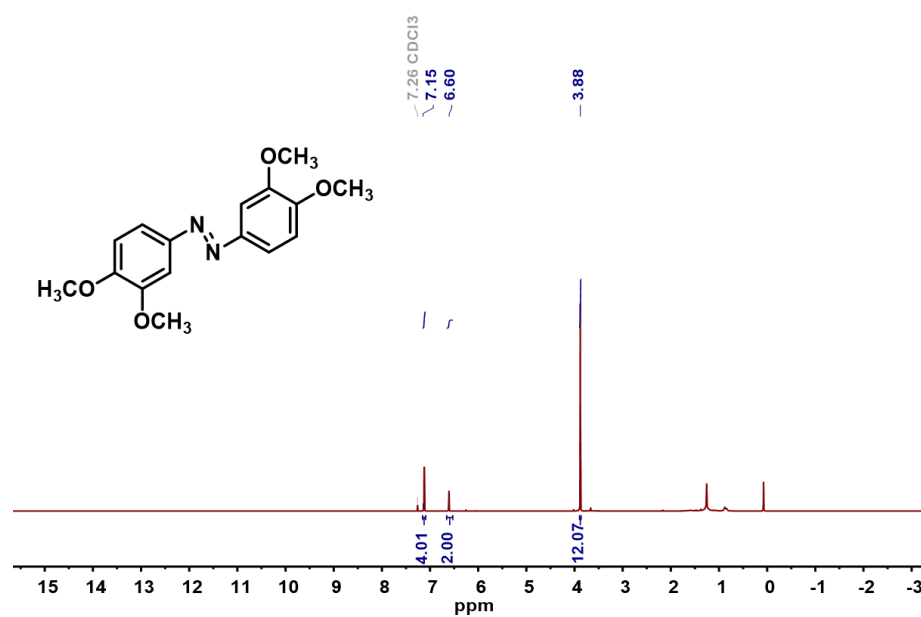
The isolated product was a reddish-orange solid, 13.1 mg, 89% yield. ^{1}H NMR (500 MHz, Chloroform-d) δ 7.64 (d, J = 8.3 Hz, 2H), 7.61 (d, J = 5.5 Hz, 2H), 7.19 (d, J = 8.2 Hz, 2H), 2.85 (d, J = 17.4 Hz, 8H), 1.86 – 1.82 (m, 8H). ^{13}C NMR (126 MHz, CDCl$_3$) δ 150.70, 140.33, 137.76, 129.60, 123.16, 119.73, 29.41, 22.93.
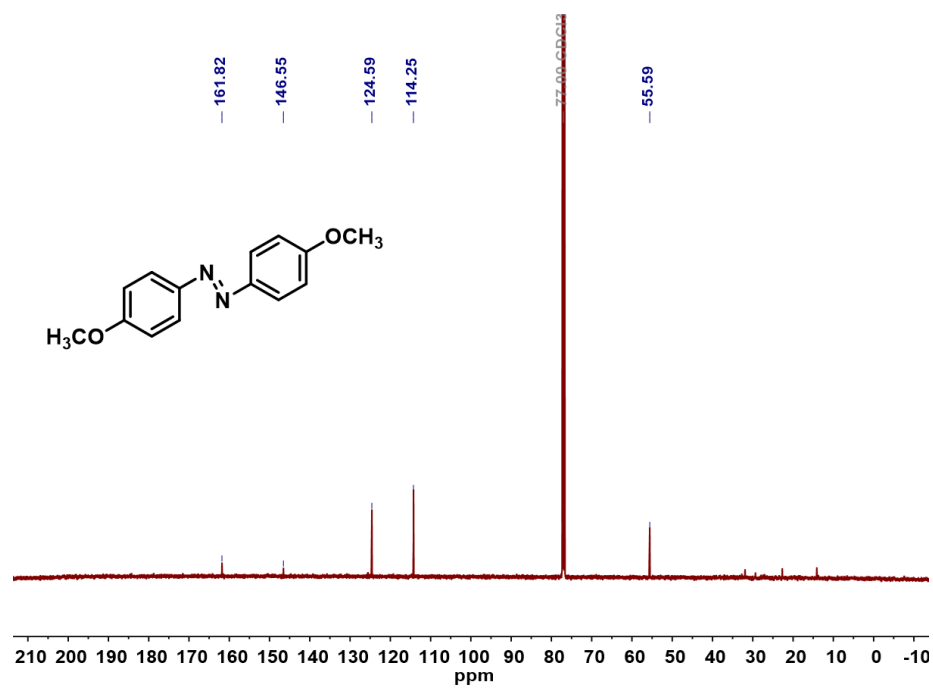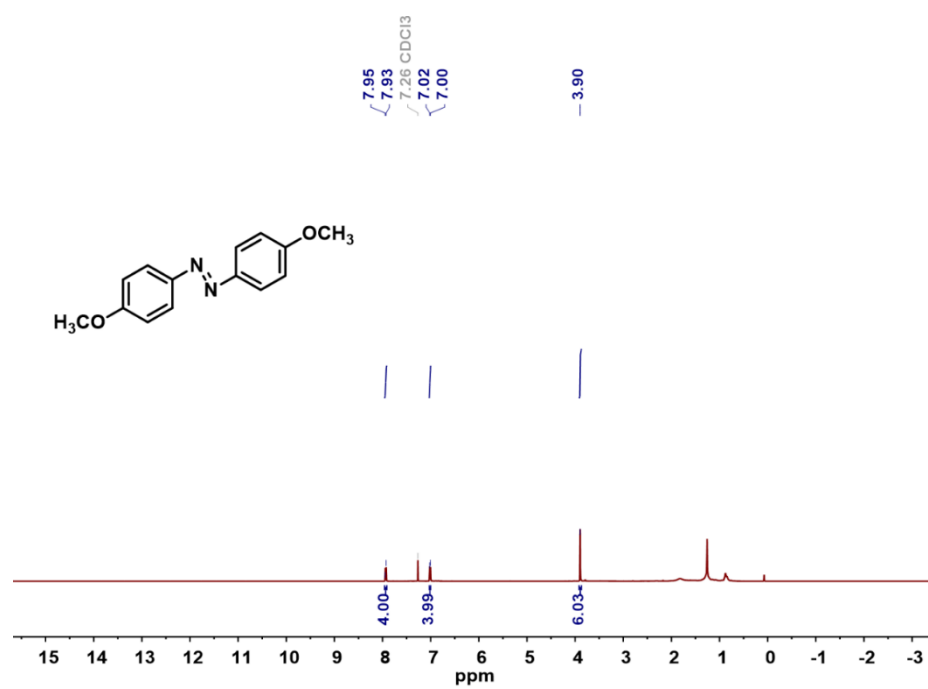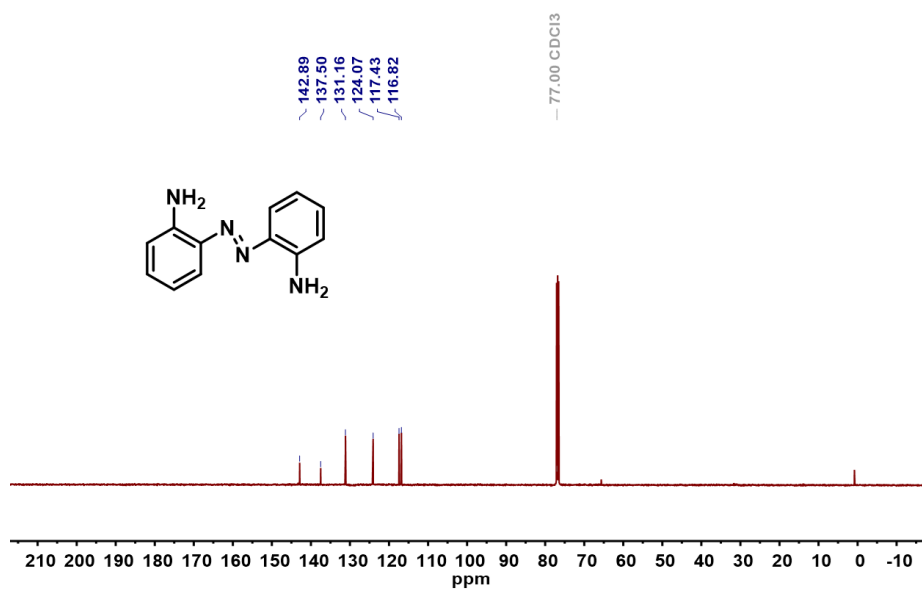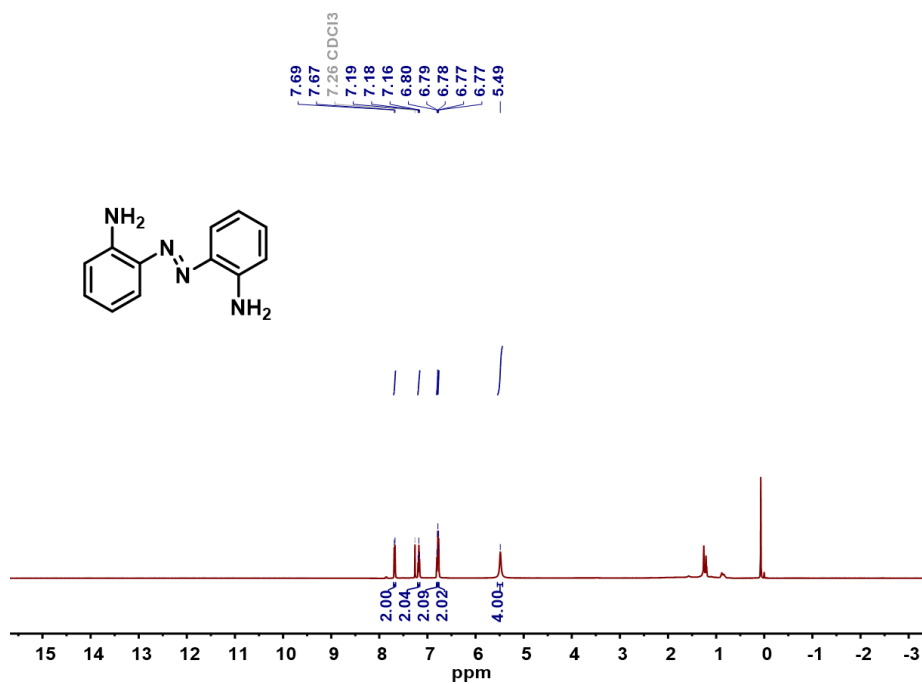
A 1. ^{1}H and ^{13}C NMR spectra of 1,2-bis(4-methoxyphenyl)diazene.
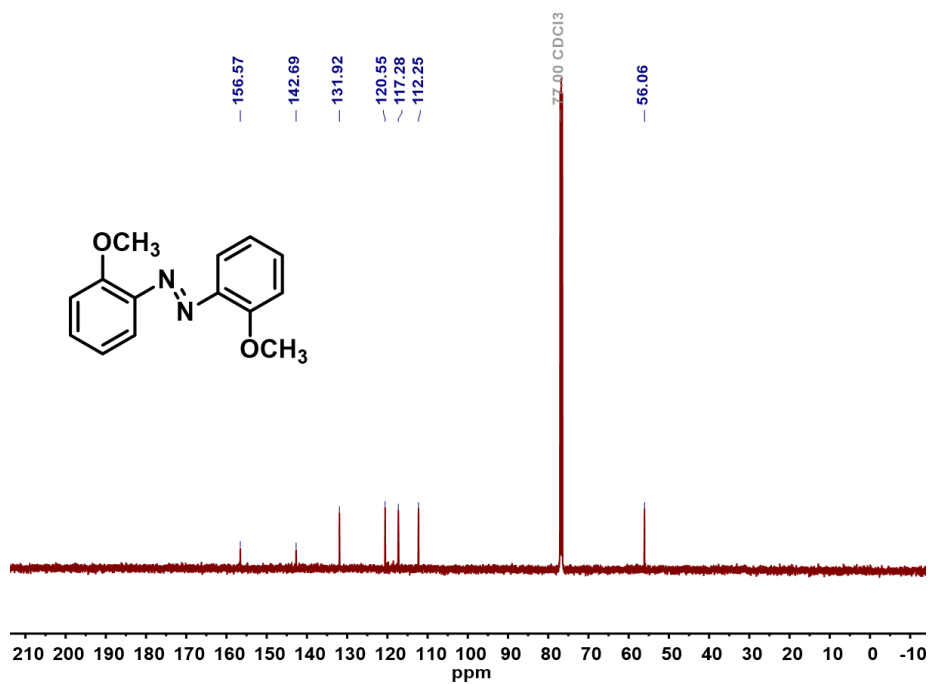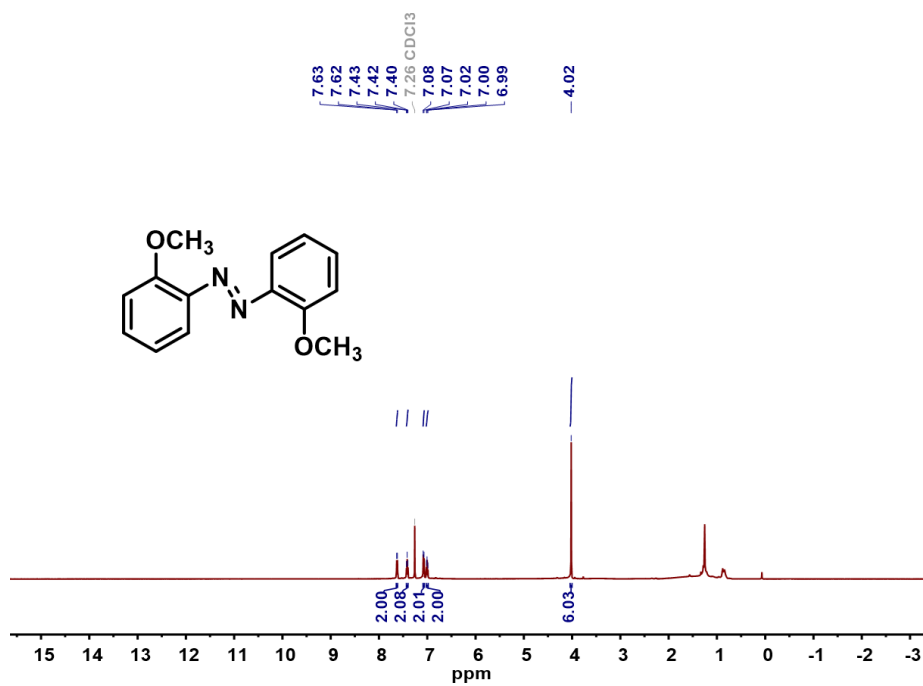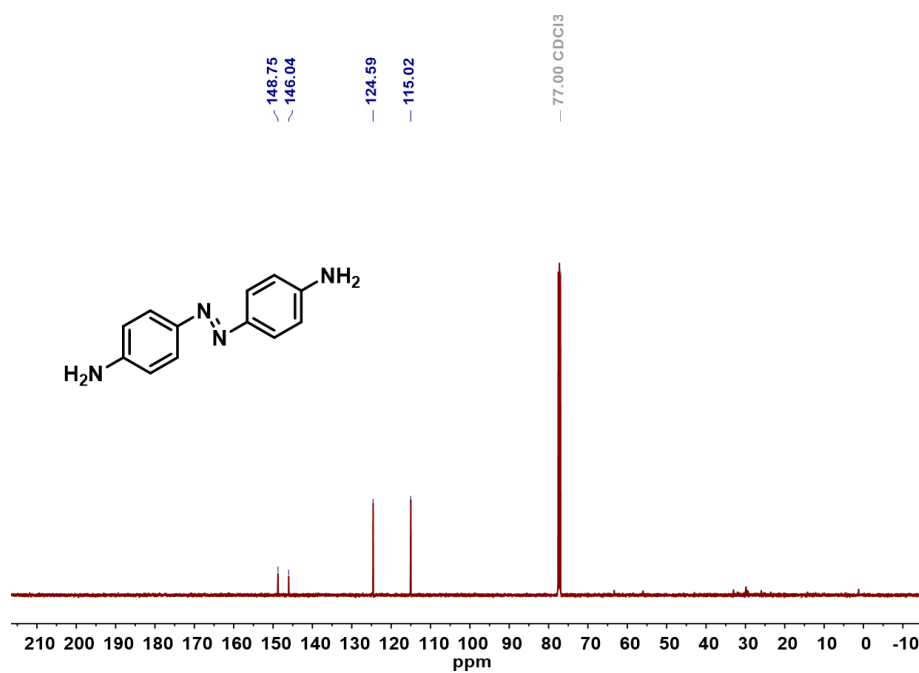
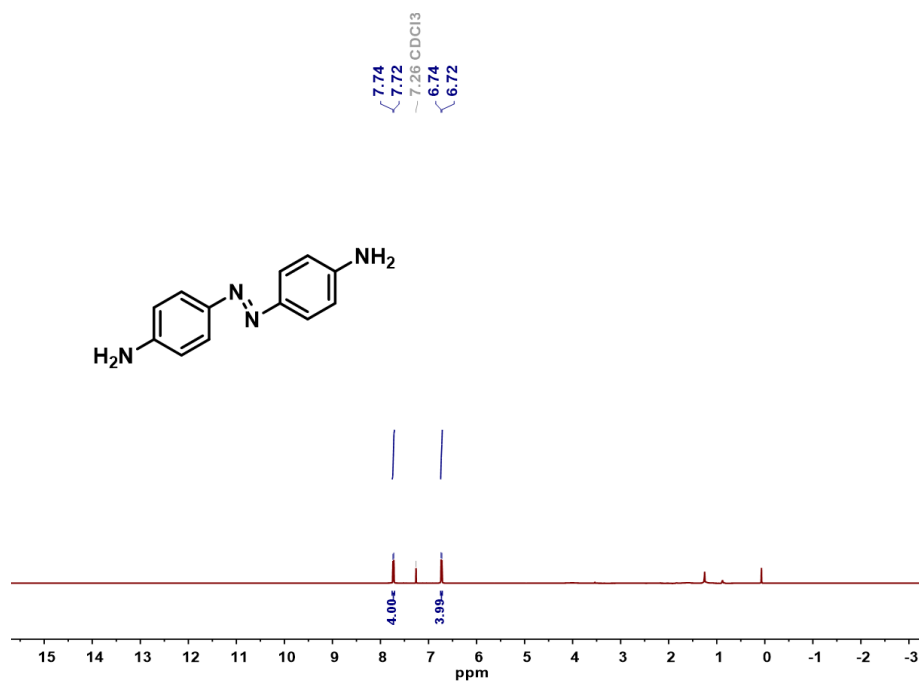**A 2.** ^{1}H and ^{13}C NMR spectra of 1,2-bis(2-methoxyphenyl)diazene.
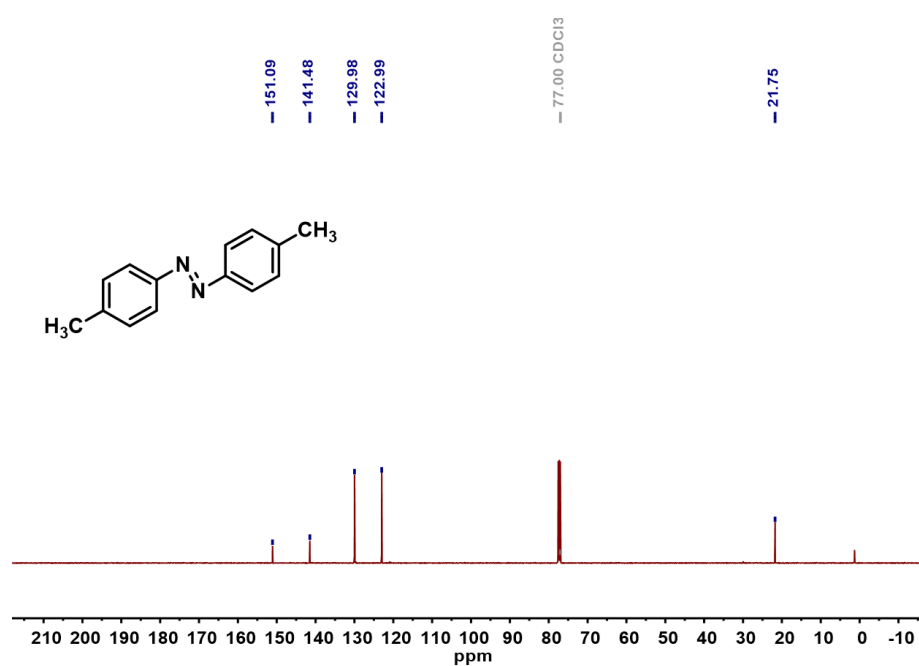
A **23.** ¹H and ¹³C NMR spectra of 1,2-bis(3,5-dimethoxyphenyl)diazene.

A 4. ^{1}H and ^{13}C NMR spectra of 1,2-bis(2-aminophenyl)diazene.

A 5. ^{1}H and ^{13}C NMR spectra of 1,2-bis(4-aminophenyl)diazene.

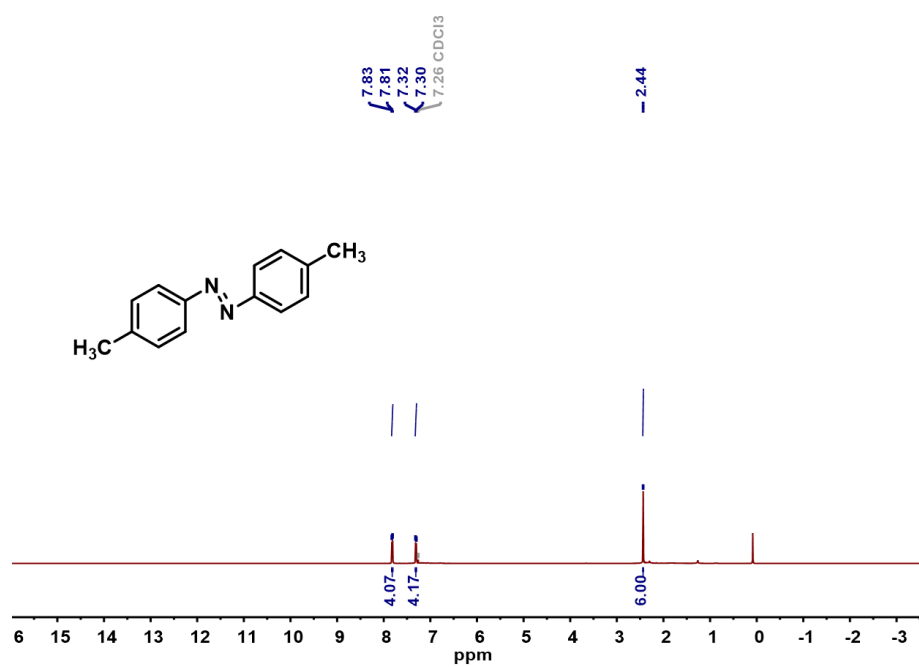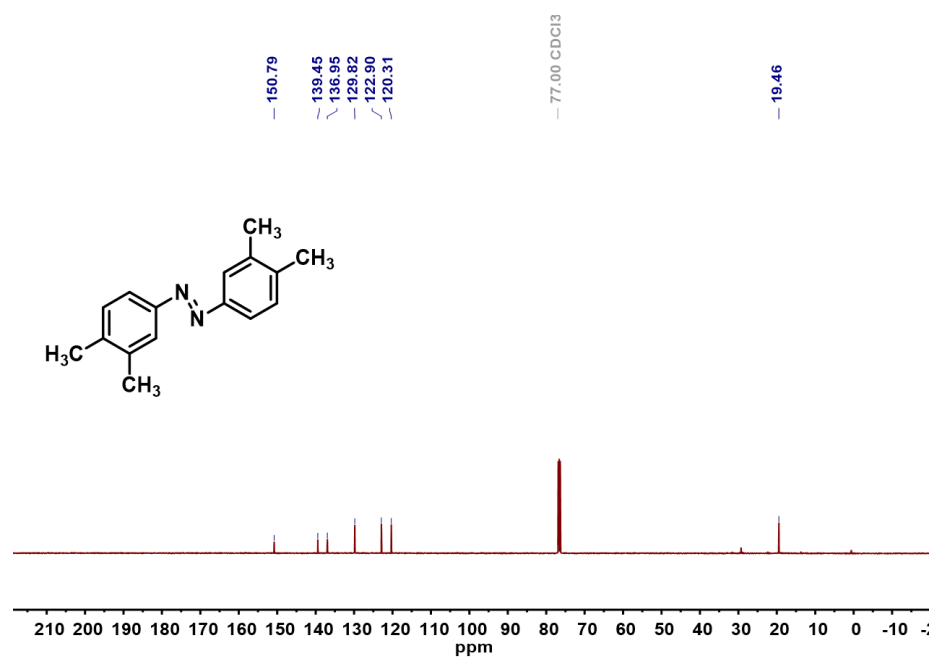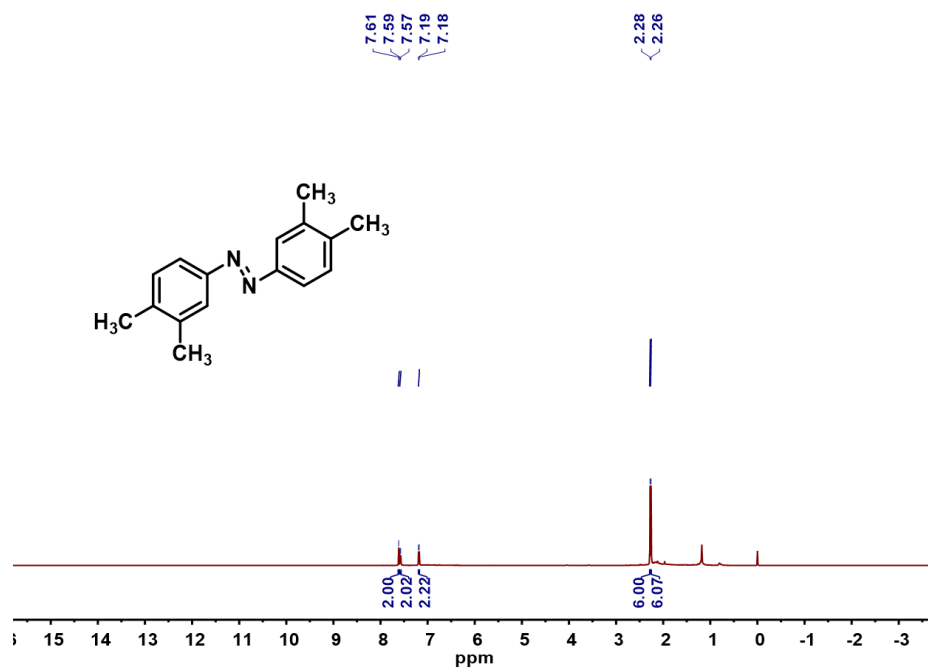**A 6.** ¹H and ¹³C NMR spectra of 1,2-bis(4-methylphenyl)diazene.

A 7. ^{1}H and ^{13}C NMR spectra of 1,2-bis(3,4-dimethylphenyl)diazene.

7.94
7.92
7.54
7.53
7.51
7.49
7.48
7.46
7.26 CDCl3

4.00
4.15
2.01

16 15 14 13 12 11 10 9 8 7 6 5 4 3 2 1 0 -1 -2 -3
ppm

152.53

130.85
128.95
122.71

77.00 CDCl3

210 200 190 180 170 160 150 140 130 120 110 100 90 80 70 60 50 40 30 20 10 0 -10
ppm
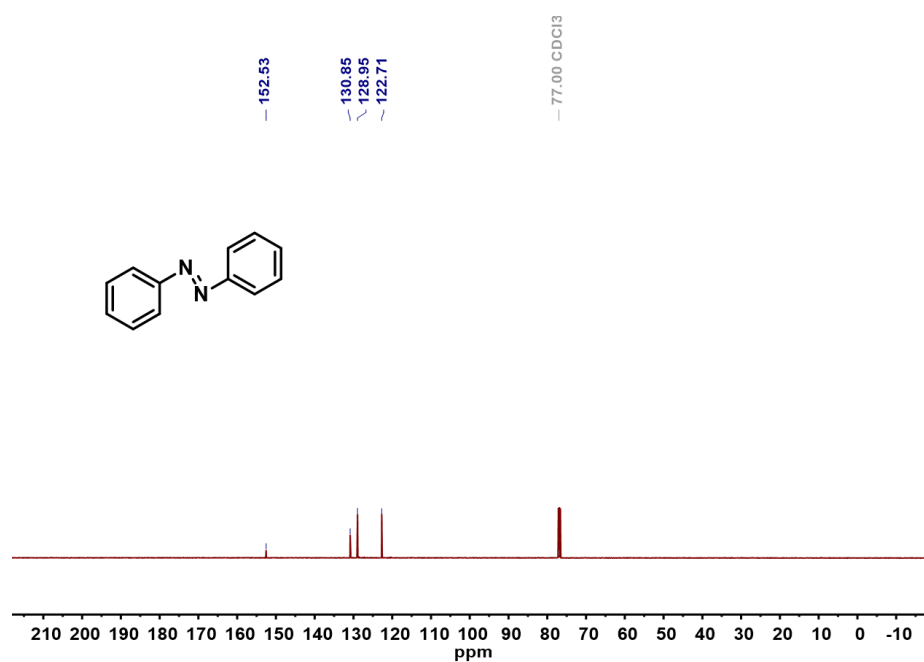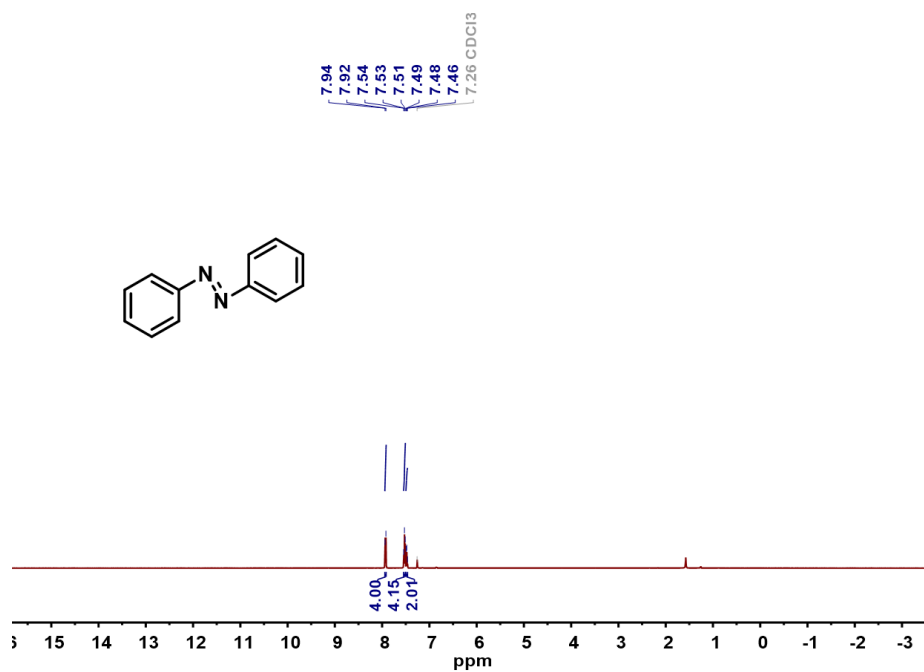
A 8. ^{1}H and ^{13}C NMR spectra of 1,2-diphenyldiazene.
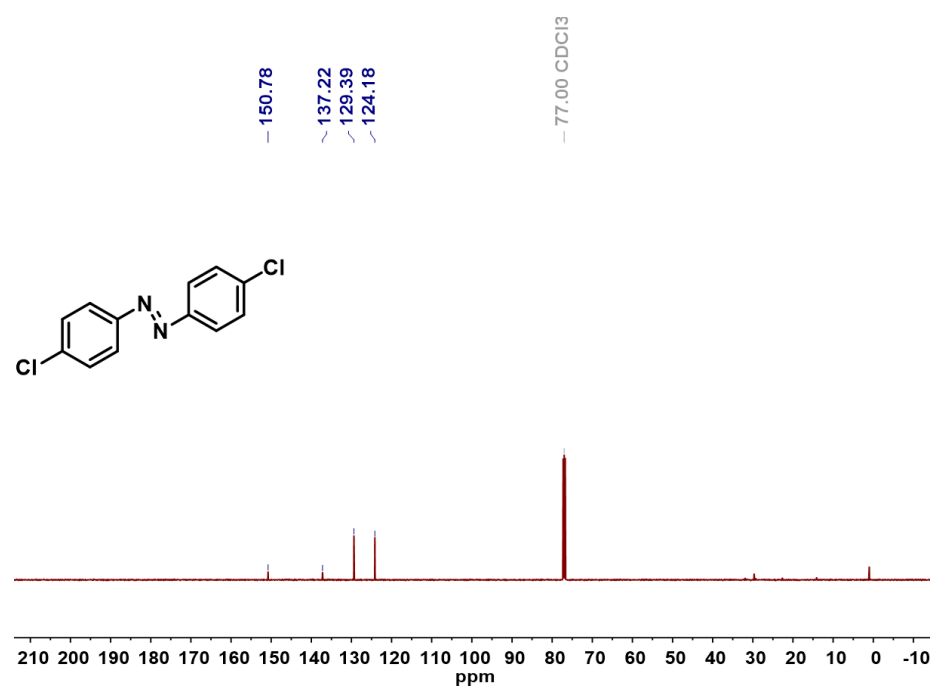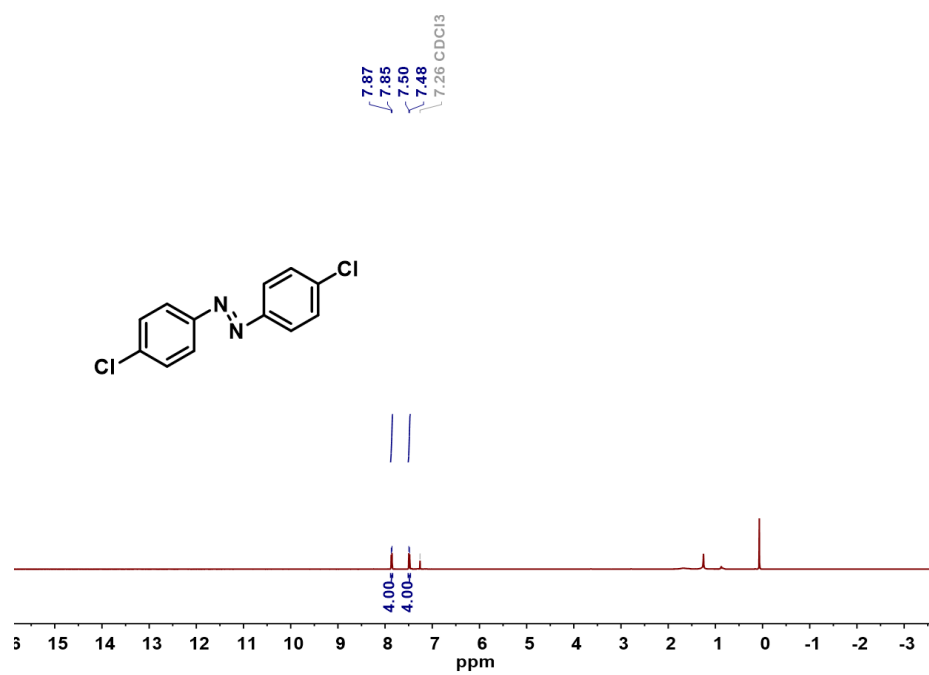
A 9. ^{1}H and ^{13}C NMR spectra of 1,2-bis(4-chlorophenyl)diazene.
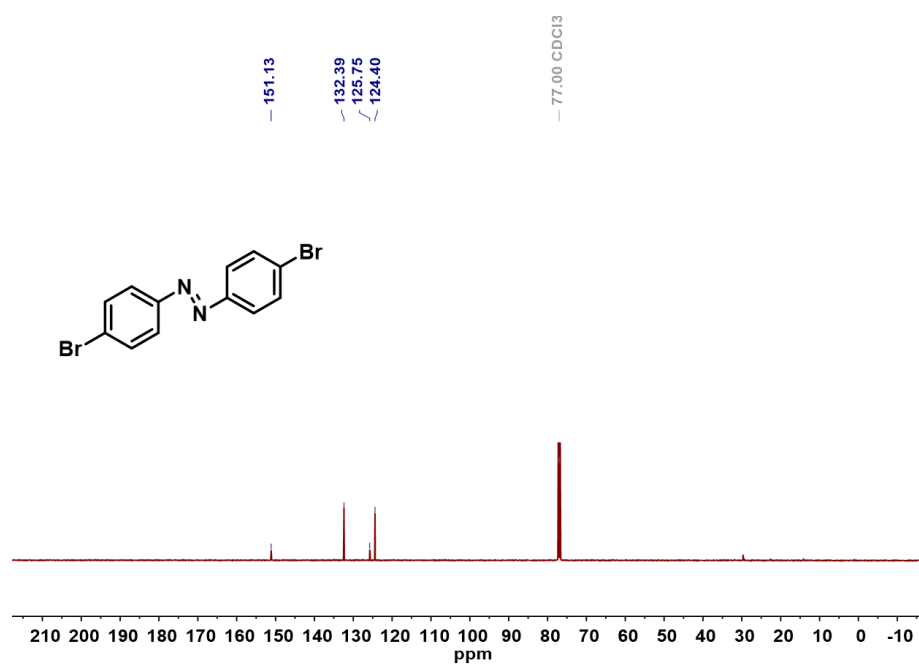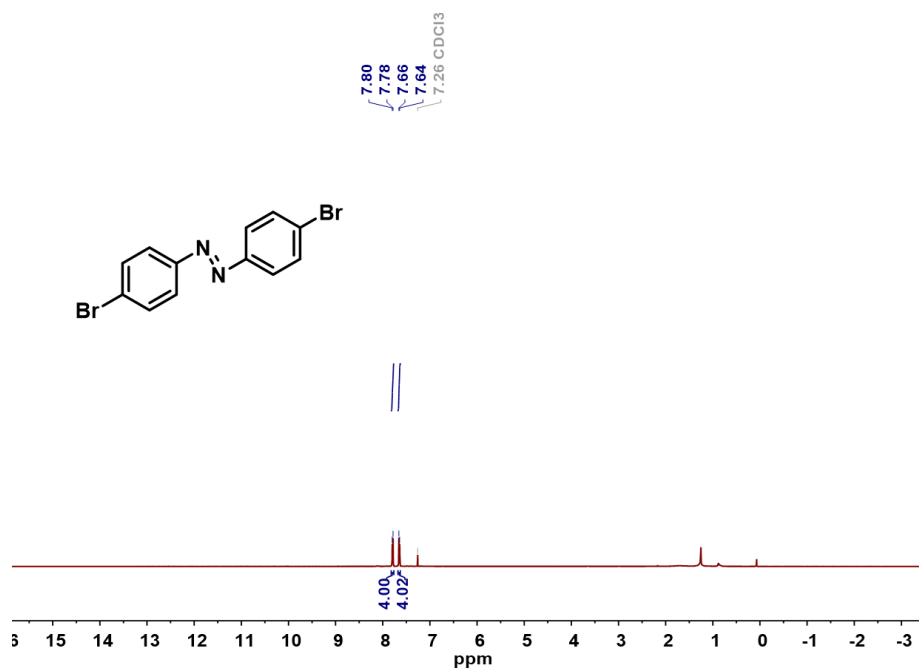
A 10. ^{1}H and ^{13}C NMR spectra of 1,2-bis(4-bromophenyl)diazene.
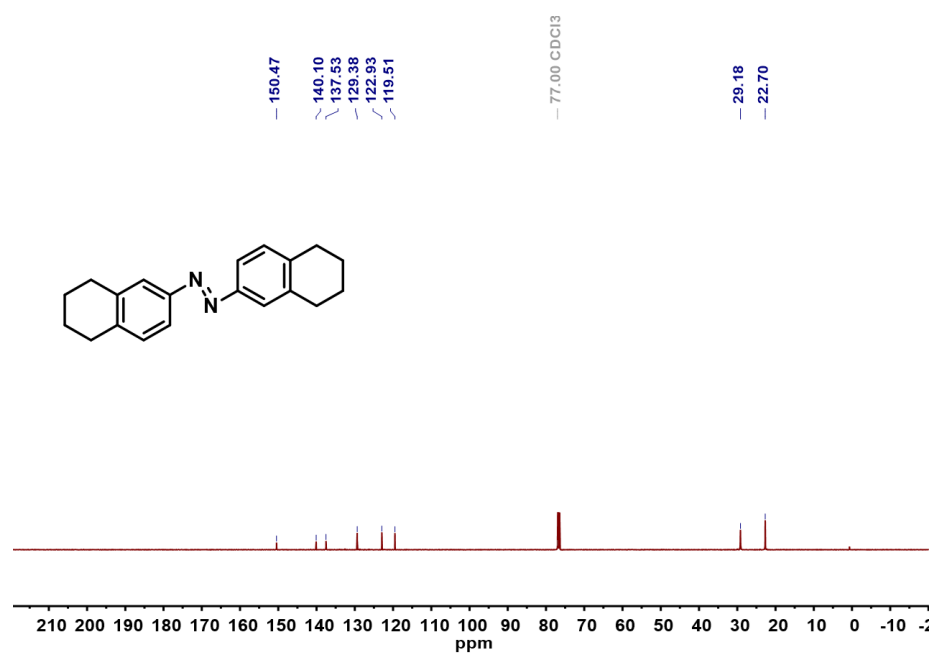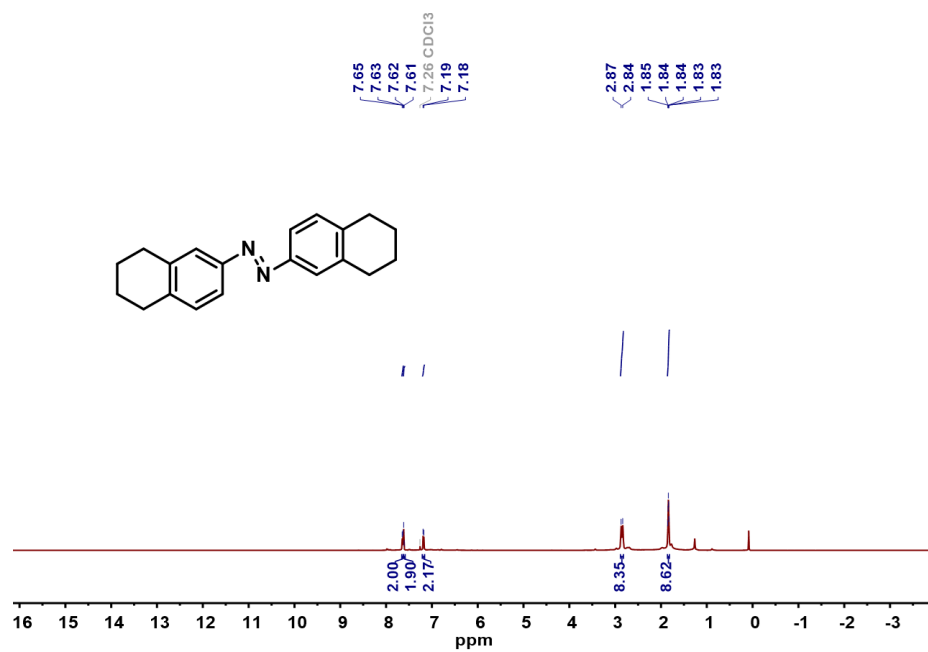
A 11. ^{1}H and ^{13}C NMR spectra of 1,2-bis(5,6,7,8-tetrahydronaphthalen-1-yl)diazene.
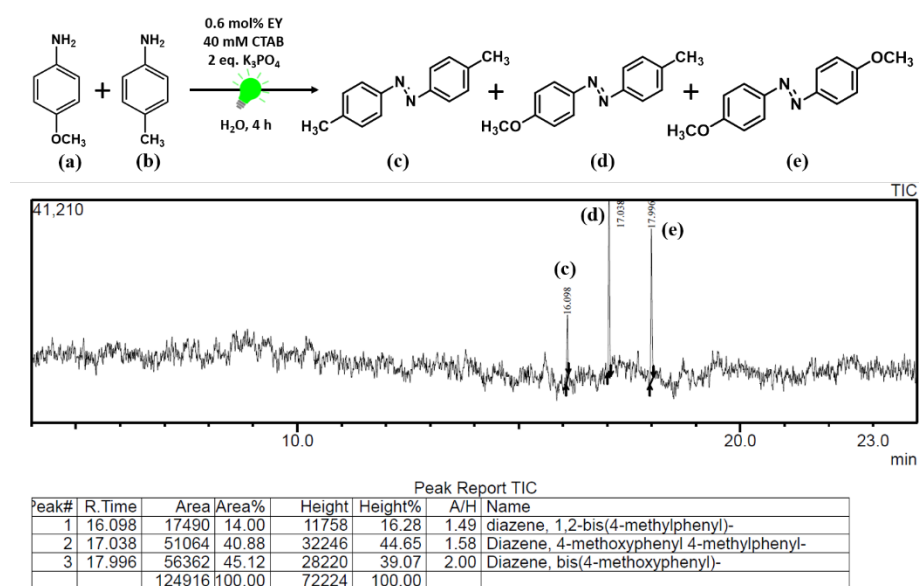
A 12. GC-MS spectrum for the photocatalytic oxidative coupling of *p*-anisidine and *p*-toluidine.
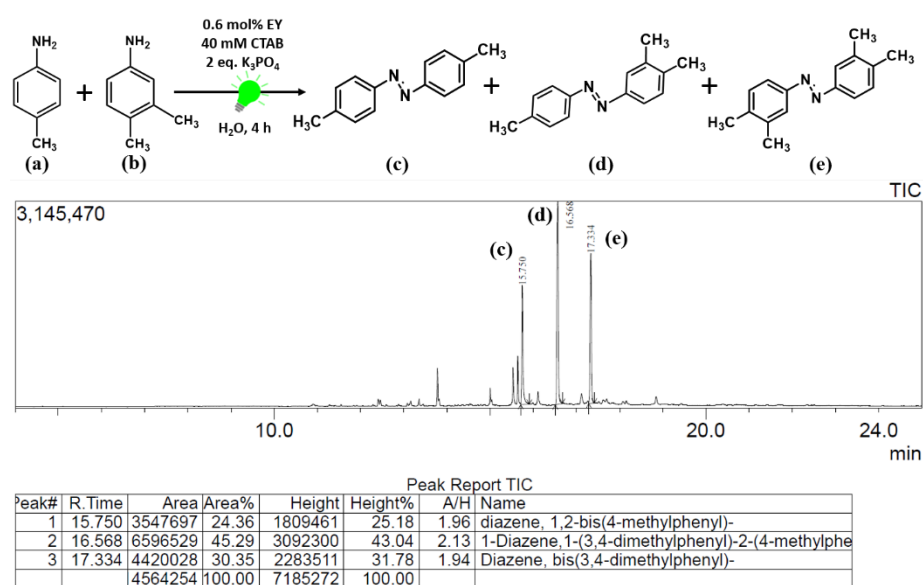
A 13. GC-MS spectrum for the photocatalytic oxidative coupling of *p*-toluidine and 3,4-dimethylaniline.

250
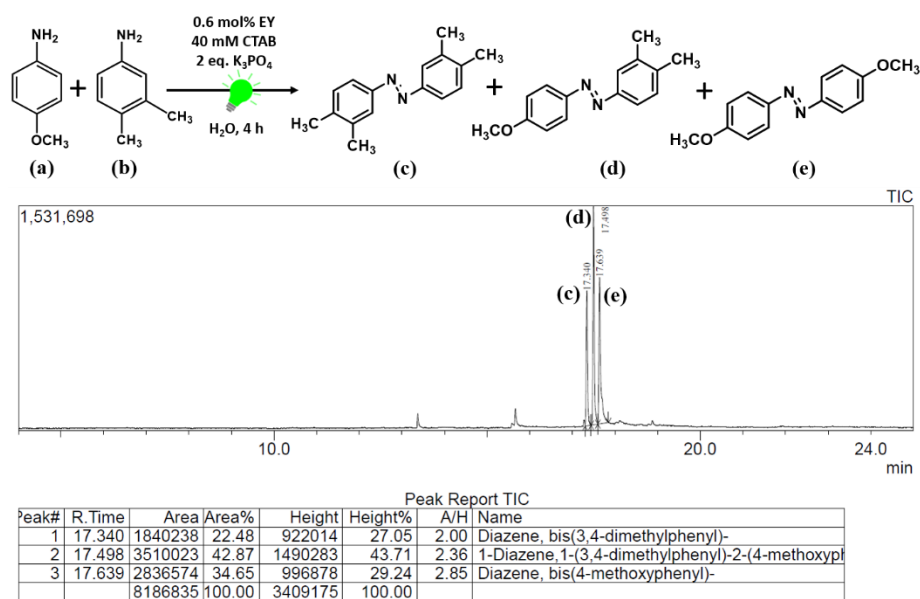
A 14. GC-MS spectrum for the photocatalytic oxidative coupling of *p*-anisidine and 3,4-dimethylaniline.

Peak#	R.Time	Area	Area%	Height	Height%	A/H	Name
1	17.340	1840238	22.48	922014	27.05	2.00	Diazene, bis(3,4-dimethylphenyl)-
2	17.498	3510023	42.87	1490283	43.71	2.36	1-Diazene,1-(3,4-dimethylphenyl)-2-(4-methoxyph
3	17.639	2836574	34.65	996878	29.24	2.85	Diazene, bis(4-methoxyphenyl)-
		8186835	100.00	3409175	100.00		
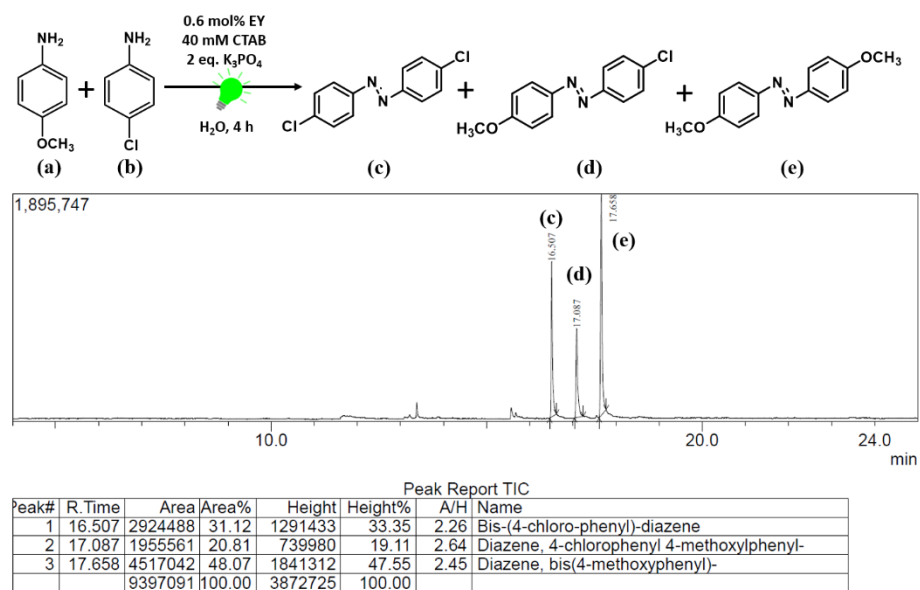
A 15. GC-MS spectrum for the photocatalytic oxidative coupling of *p*-anisidine and *p*-chloroaniline.

Peak#	R.Time	Area	Area%	Height	Height%	A/H	Name
1	16.507	2924488	31.12	1291433	33.35	2.26	Bis-(4-chloro-phenyl)-diazene
2	17.087	1955561	20.81	739980	19.11	2.64	Diazene, 4-chlorophenyl 4-methoxylphenyl-
3	17.658	4517042	48.07	1841312	47.55	2.45	Diazene, bis(4-methoxyphenyl)-
		9397091	100.00	3872725	100.00		

251

Peak#	R.Time	Area	Area%	Height	Height%	A/H	Name
1	14.256	2087577	35.42	536153	32.03	3.89	Azobenzene
2	15.412	2678592	45.45	892815	53.33	3.00	Diazene, 1-(4-chlorophenyl)-2-(phenyl)-
3	16.552	1127228	19.13	245054	14.64	4.60	Diazene, 1,2-bis-(4-chlorophenyl)-
		5893397	100.00	1674022	100.00		

A 16. GC-MS spectrum for the photocatalytic oxidative coupling of aniine and *p*-chloroaniline.

Peak#	R.Time	Area	Area%	Height	Height%	A/H	Name
1	15.777	4781430	54.26	2205897	61.95	2.17	diazene, 1,2-bis(4-methylphenyl)-
2	16.124	2709092	30.74	1049759	29.48	2.58	diazene, 1-(4-chlorophenyl)-2-(4-methylphenyl)-
3	16.528	1322123	15.00	305375	8.58	4.33	diazene, 1,2-bis-(4-chlorophenyl)-
		8812645	100.00	3561031	100.00		

A 17. GC-MS spectrum for the photocatalytic oxidative coupling of *p*-toluidine and *p*-chloroaniline.

Peak#	R.Time	Area	Area%	Height	Height%	A/H	Name
1	16.508	1387892	14.92	532633	13.64	2.61	Diazene, 1,2-bis-(4-chlorophenyl)-
2	16.906	2721142	29.26	1204309	30.85	2.26	Diazene, 1-(4-chlorophenyl)-2-(3,4-dimethylpheny
3	17.357	5191628	55.82	2166869	55.51	2.40	Diazene, bis(3,4-dimethylphenyl)-
		9300662	100.00	3903811	100.00		

A 18. GC-MS spectrum for the photocatalytic oxidative coupling of *p*-chloroaniline and 3,4-dimethylaniline.

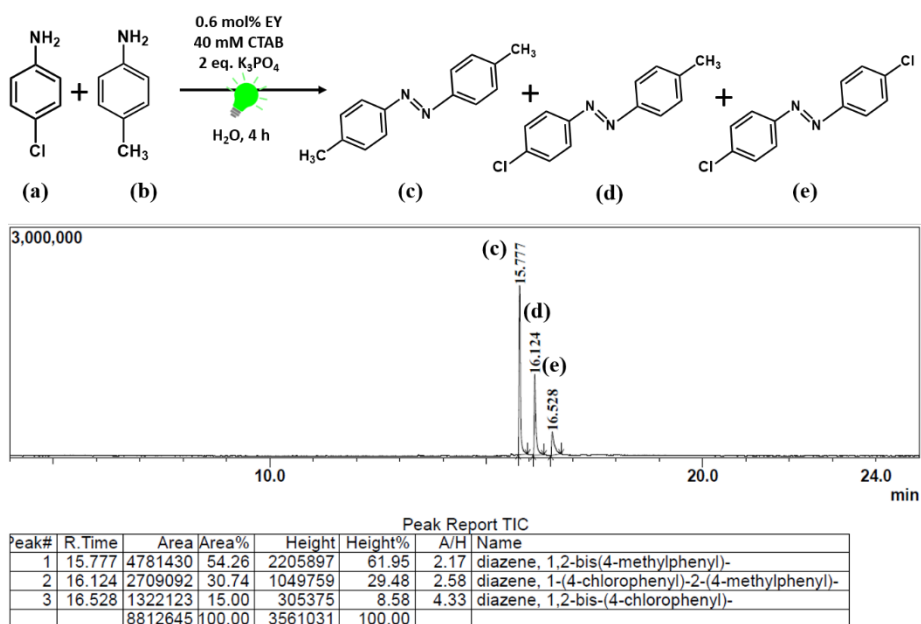| Peak#	R.Time	Area	Area%	Height	Height%	A/H	Name
1	14.238	7231313	42.00	3063225	42.25	2.36	Azobenzene
2	15.876	4278326	24.85	1808754	24.95	2.37	Diazene, 1-(3,4-dimethylphenyl)-2-(phenyl)-
3	17.361	5706418	33.15	2378509	32.80	2.40	Diazene, bis(3,4-dimethylphenyl)-
		7216057	100.00	7250488	100.00		

A 19. GC-MS spectrum for the photocatalytic oxidative coupling of aniline and 3,4-dimethylaniline.

253

A 20. GC-MS spectrum for the photocatalytic oxidative coupling of *p*-toluidine and 3,5-dimethoxyaniline.
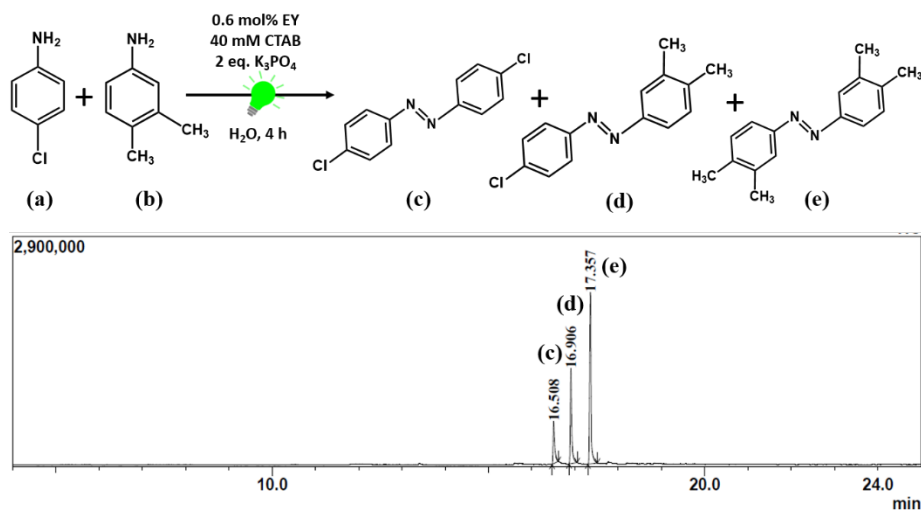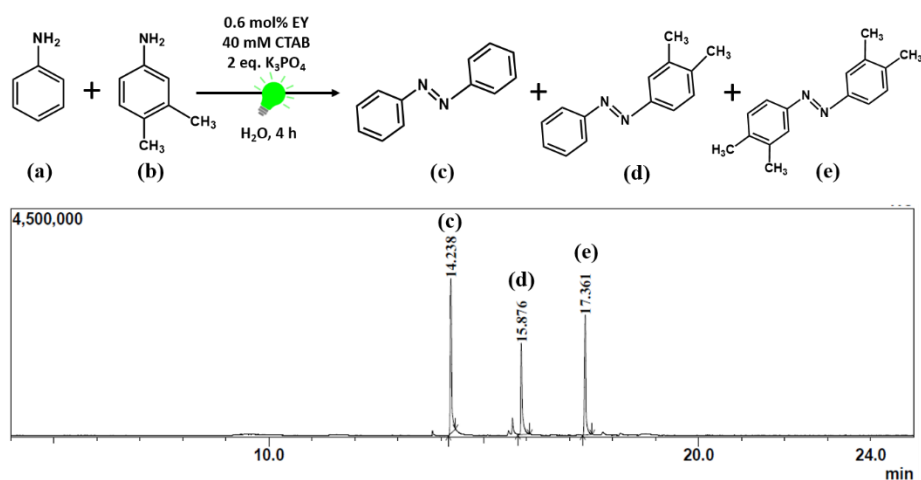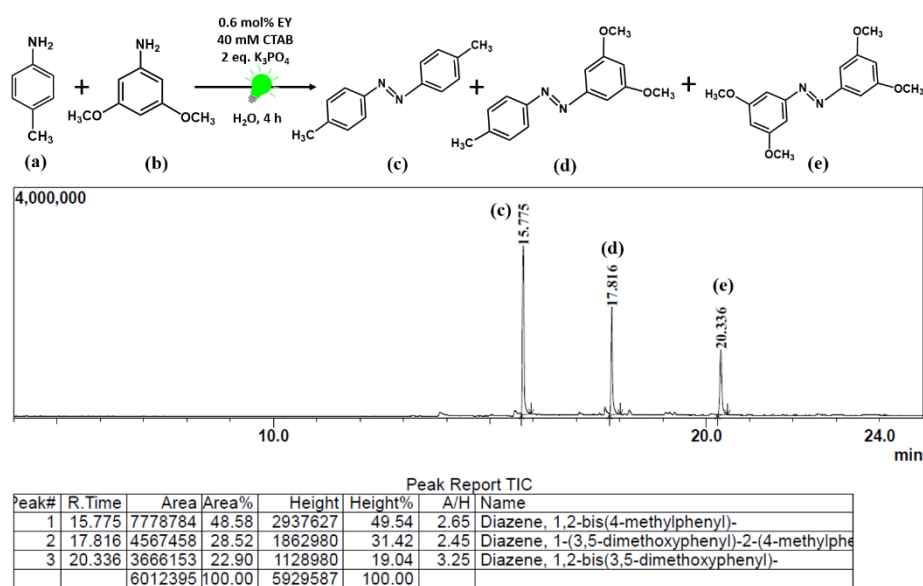
Peak Report TIC

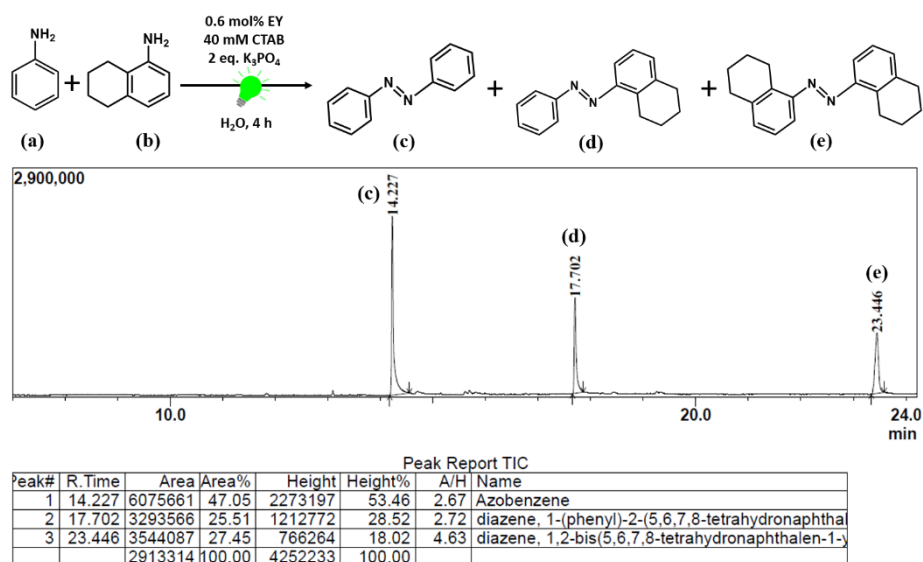| Peak#	R.Time	Area	Area%	Height	Height%	A/H	Name
1	15.775	7778784	48.58	2937627	49.54	2.65	Diazene, 1,2-bis(4-methylphenyl)-
2	17.816	4567458	28.52	1862980	31.42	2.45	Diazene, 1-(3,5-dimethoxyphenyl)-2-(4-methylphe
3	20.336	3666153	22.90	1128980	19.04	3.25	Diazene, 1,2-bis(3,5-dimethoxyphenyl)-
		6012395	100.00	5929587	100.00		
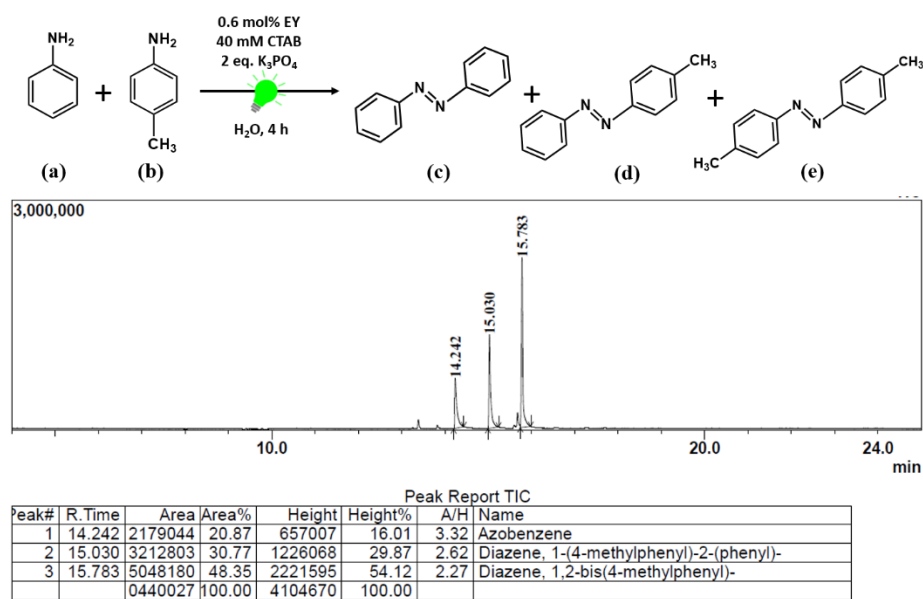
A 21. GC-MS spectrum for the photocatalytic oxidative coupling of aniline and *p*-toluidine.

Peak Report TIC

Peak#	R.Time	Area	Area%	Height	Height%	A/H	Name
1	14.242	2179044	20.87	657007	16.01	3.32	Azobenzene
2	15.030	3212803	30.77	1226068	29.87	2.62	Diazene, 1-(4-methylphenyl)-2-(phenyl)-
3	15.783	5048180	48.35	2221595	54.12	2.27	Diazene, 1,2-bis(4-methylphenyl)-
		0440027	100.00	4104670	100.00		

254

A 22. GC-MS spectrum for the photocatalytic oxidative coupling of aniline and 5,6,7,8-tetrahydronaphthalene.
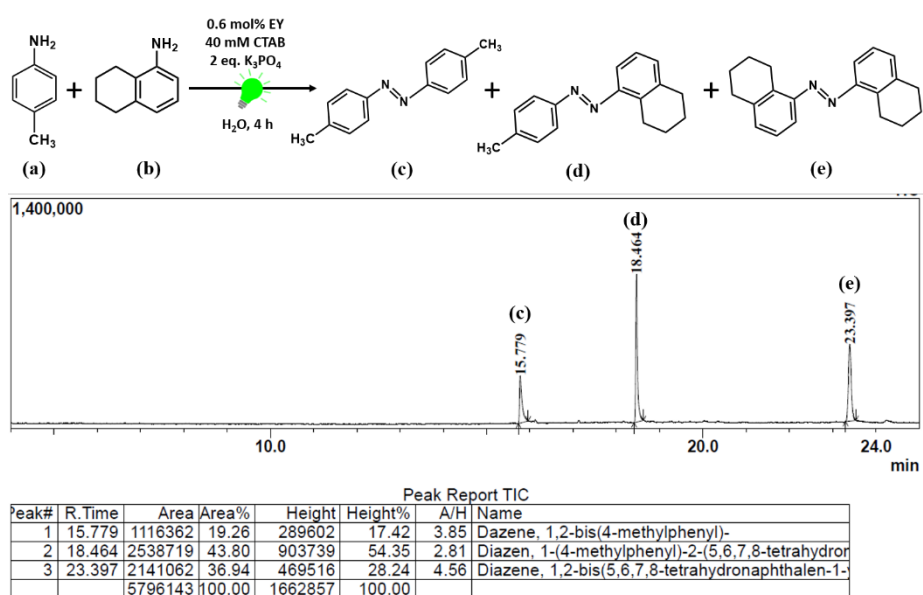
A 23. GC-MS spectrum for the photocatalytic oxidative coupling of *p*-toluidine and 5,6,7,8-tetrahydronaphthalene.

Peak Report TIC

Peak#	R.Time	Area	Area%	Height	Height%	A/H	Name
1	14.232	4349028	53.35	1176344	51.07	3.70	p-Nitroaniline
2	17.659	3803240	46.65	1126939	48.93	3.37	Diazene, bis(4-methoxyphenyl)-
		8152268	100.00	2303283	100.00		
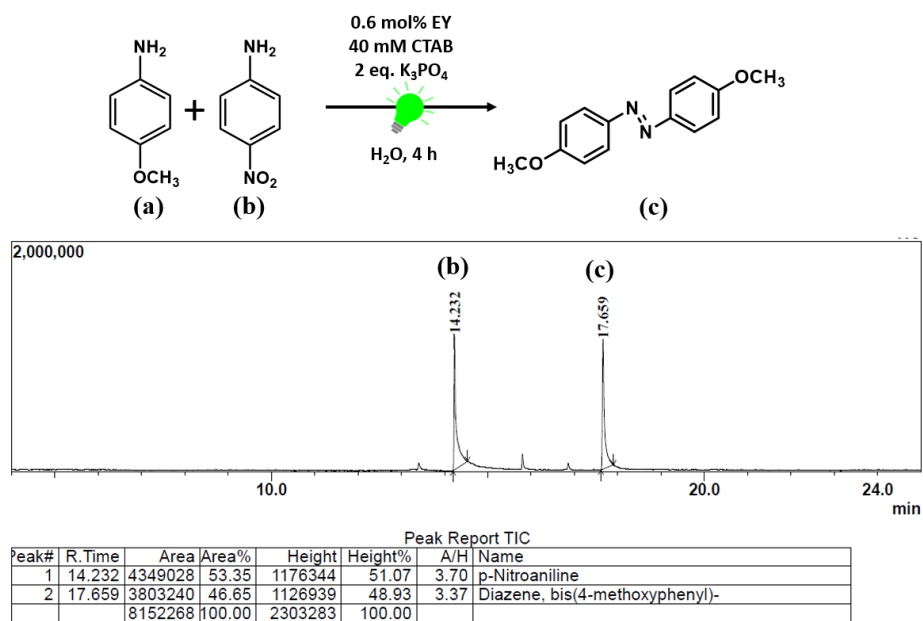
A 24. GC-MS spectrum for the photocatalytic oxidative coupling of *p*-nitroaniline and *p*-anisidine.